Mathematical Methods for Modelling Biological Heterogeneity

Arran Hodgkinson

Méthodes Mathématiques pour Modéliser l'Hétérogénéité Biologique

Mathematical Methods for Modelling Biological Heterogeneity

Arran Bryan Joseph HODGKINSON

10^{th} December 2019

This thesis was submitted to the Université de Montpellier in partial fulfilment of the requirements for the degree of Doctor of Philosophy

Sous la direction de Ovidiu RADULESCU et Laurent LE CAM

Devant le jury composé de

Ovidiu RADULESCU Prof, Université de Montpellier

Laurent LE CAM Dr, Directeur de recherche INSERM

Helen BYRNE Prof, Oxford University

Benoît PERTHAME Prof, Sorbonne-Université

Nathalie THÉRET Dr, Directeur de recherche INSERM

Gilles UZÉ Dr, Directeur de recherche CNRS

Dumitru TRUCU Dr, University of Dundee

Résumé

Vulgarisé

L'hétérogénéité biologique est à l'origine d'importants problèmes de santé publique tels que la résistance des agents pathogènes et des cellules cancereuses à l'immunité et aux traitements. Au travers de méthodes mathématiques adaptées à l'étude de l'hétérogénéité biologique des cellules cancéreuses, nous avons constaté que les tumeurs à évolution génétique étaient capables de développer une résistance aux thérapies ciblées autant que celles présentant une plasticité métabolique, mais que seules ces dernières pouvaient être ré-sensibilisées au traitement. De plus, en se demandant pourquoi l'immunité évolue avec des analogues de forte et faible affinité de la même protéine, nous montrons que l'addition d'analogues de faible affinité peut réduire l'infection virale de 23%. Dans la théorie de l'évolution darwinienne, nous avons constaté que les femelles pouvaient sélectionner des caractéristiques sexuellement désirables chez les mâles, allant même à l'encontre de la sélection naturelle. Enfin, nos modèles mathématiques permettant d'étudier des problèmes encore plus complexes tels que la dynamique d'invasion des cellulaires cancéreuses.

Prolongé

Les processus biologiques sont des phénomènes complexes, multi-échelles, présentant une hétérogénéité importante à travers l'espace, la structure et la fonction.

De plus, ils impliquent des événements fortement corrélés et présentent des boucles de rétroaction à travers les échelles. Dans cette thèse, nous utilisons des représentations spatio-structuro-temporelles en grande dimension pour étudier l'hétérogénéité biologique à travers l'espace, la fonction biologique et le temps, et appliquons cette méthode à divers problèmes importants en biologie et en clinique.

Nous commençons par introduire un nouveau cadre spatio-structuro-temporel, basé sur équations aux dérivées partielles, pour le cas d'un système biologique dont la fonction dépend de la dynamique dans le temps et l'espace des récepteurs membranaires, des ligands et du métabolisme. Afin d'étudier les solutions de ces équations, nous utilisons un schéma numérique de différences finies ainsi que divers résultats analytiques. Pour tester la validité de nos approches numériques nous prouvons un théorème sur la stabilité de notre schéma.

Le cancer est un problème croissant pour la population mondiale, car ses taux d'incidence et sa résistance aux médicaments augmentent. D'abord nous modélisons l'invasion du cancer du sein agressif via sa capacité à produire des enzymes dégradant la matrice extracellulaire, et nous montrons la génération de structures spatiales anatomo-pathologiques difficiles à enlever par la chirurgie. Ensuite, nous développons des modèles mathématiques de tumeurs résistantes au traitement et appliquons ces modèles à la résistance aux thérapies ciblées (inhibiteurs de BRAF et de MEK) du mélanome cutané. Nous constatons que les tumeurs développent une résistance à la fois à travers des processus d'adaptations génétiques ou par le remodelage de leur métabolisme, mais montrons que seules les tumeurs métaboliquement plastiques manifestent une resensibilisation à ces thérapies. Enfin, via une approche basée sur des données d'expression en cellule unique (RNA-seq), nous montrons que la dynamique spatiale contribue à l'hétérogénéité tumorale et à la résistante aux traitements de façon liée au statut prolifératif des cellules cancéreuses.

Nous appliquons nos méthodes à deux autres systèmes. Dans le contexte de la réponse immunitaire à l'infection virale, nous étudions la production et la dynamique spatiale de l'interféron (IFN) et l'apparent paradoxe de la conserva-

tion de molécules d'IFN avec affinités faibles et fortes. Nous constatons que les molécules IFN de faible affinité sont plus capables de se propager dans l'espace, alors que les molécules de haute affinité sont capables de maintenir le signal localement. L'addition de ligands de faible affinité à un système ne comprenant que des ligands de moyenne ou grande affinité peut entraîner une diminution de la charge virale d'environ 23%. Ensuite, nous explorons le contexte de la sélection sexuelle de l'apparence masculine dans l'évolution darwinienne. Nous constatons que les systèmes biologiques conservent les traits sélectionnés sexuellement, même si cela entraîne une diminution générale de la population.

Enfin, nous introduisons deux autres techniques de modélisation: pour augmenter la dimensionnalité de notre approche, nous développons une approche pseudo-spectrale basée sur les polynômes de Chebyshev et l'appliquons au même scénario de résistance aux médicaments phénotypiques que ci-dessus. Ensuite, pour étudier un scénario coopératif dans lequel des cellules cancéreuses prolifératives et invasives sont co-injectées, induisant des comportements invasifs dans les cellules prolifératives, nous développons une nouvelle méthode de simulation combinant des automates cellulaires et systèmes d'agents. Nous trouvons que cette méthode est capable de reproduire les résultats de l'expérience de coinjection et d'autres expériences dans lesquelles des cellules ont été placées dans des micropistes de collagène.

Summary

Simplified

Biological heterogeneity is responsible for important public health problems ranging from resistance of pathogens and cancer cells to human immunity. We develop mathematical methods, coping with the complexity of biological heterogeneity, and numerical techniques for solving biological problems. By modelling cancer resistance, we found that simulated genetically and metabolically evolving tumours were capable of developing resistance but that only metabolically evolving tumours could be re-sensitised to treatment. Moreover, asking why immune systems concomitantly evolve strong and weak binding analogues of the same protein, we found that the addition of weak binding analogues to a system could decrease viral infection by up to 23%. In Darwinian evolutionary theory, we found that sexually desirable traits in males were selected for by females, even contradicting selection by predation. We finally introduce further techniques for yet more complex problems and single-cell invasion dynamics.

Extended

Biological processes are complex, multi-scale phenomena displaying extensive heterogeneity across space, structure, and function. Moreover, these events are highly correlated and involve feedback loops across scales, with nuclear transcription being effected by protein concentrations and vice versa, presenting

a difficulty in representing these through existing mathematical approaches. In this thesis we use higher-dimensional spatio-structuro-temporal representations to study biological heterogeneity through space, biological function, and time and apply this method to various scenarios of significance to the biological and clinical communities.

We begin by deriving a novel spatio-structuro-temporal, partial differential equation framework for the general case of a biological system whose function depends upon dynamics in time, space, surface receptors, binding ligands, and metabolism. In order to simulate solutions for this system, we present a numerical finite difference scheme capable of this and various analytic results connected with this system, in order to clarify the validity of our predictions. In addition to this, we introduce a new theorem establishing the stability of the central differences scheme.

Despite major recent clinical advances, cancer incidence continues to rise and resistance to newly synthesised drugs represents a major health issue. To tackle this problem, we begin by investigating the invasion of aggressive breast cancer on the basis of its ability to produce extracellular matrix degrading enzymes, finding that the cancer produced a surgically challenging morphology. Next, we produce a novel structure in which models of cancer resistance can be established and apply this computational model to study genetic and phenotypic modes of resistance and re-sensitisation to targeted therapies (BRAF and MEK inhibitors). We find that both genetic and phenotypic heterogeneity drives resistance but that only the metabolically plastic, phenotypically resistant, tumour cells are capable of manifesting re-sensitisation to these therapies. We finally use a data-driven approach for single-cell RNA-seq analysis and show that spatial dynamics fuel tumour heterogeneity, contributing to resistance to treatment accordingly with the proliferative status of cancer cells.

In order to expound this method, we look at two further systems: To investigate a case where cell-ligand interaction is particularly important, we take the scenario in which interferon (IFN) is produced upon infection of the cell by a virus and ask why biological systems evolve and retain multiple different

affinities of IFN. We find that low affinity IFN molecules are more capable of propagating through space; high affinity molecules are capable of sustaining the signal locally; and that the addition of low affinity ligands to a system with only medium or high affinity ligands can lead to a $\sim 23\%$ decrease in viral load. Next, we explore the non-spatial, structuro-temporal context of male elaboration sexual and natural selection in Darwinian evolution. We find that biological systems will conserve sexually selected traits even in the event where this leads to an overall population decrease, contrary to natural selection.

Finally, we introduce two further modelling techniques: To increase the dimensionality of our approach, we develop a pseudo-spectral Chebyshev polynomial-based approach and apply this to the same scenario of phenotypic drug resistance as above. Next, to deal with one scenario in which proliferative and invasive cancer cells are co-injected, inducing invasive behaviours in the proliferative cells, we develop a novel agent-based, cellular automaton method and associated analytic theorems for generating numerical solutions. We find that this method is capable of reproducing the results of the co-injection experiment and further experiments, wherein cells migrate through artificially produced collagen microtracks.

Contents

0 Introduction **xv**

1 Derivation of an Higher-Dimensional Modelling Framework and Associated Numerical Methods **1**

1.1 Introduction to Higher-Dimensional Modelling 1

1.2 Higher-Dimensional Derivation 3

1.2.1 Structural Fluxes 8

1.3 Higher-Dimensional Source Terms 10

1.3.1 Derivation of a Structural Source Term for Systems with Receptors 10

1.3.2 A Reproductive Source Term for Evolutionary Dynamics 12

1.4 Approaches and Stability for Numerical Simulations 15

1.4.1 Central Difference Stability 17

1.4.2 Numerical Ball Integrals 24

2 Modelling Urokinase Plasminogen Activator (uPA) Dynamics in Breast Cancer **29**

2.1 Introduction to uPA Systems 29

2.2 Computational Approaches for uPA Systems 32

2.2.1 Description and Brief Justification of the Mathematical System 32

2.2.2 Computational Approach and Analysis for the Discretisation of the Spatio-Structural-Temporal Tumour Model . . 39
2.2.3 Numerical Results and Simulations in 1D-Spatial Case . . 47
2.2.4 Numerical Results in 2D-Spatial Cases 50
2.2.5 Discussion & Conclusions 58

3 Novel Approaches to Modelling Drug Resistance in Melanoma 65
3.1 Introduction to Drug Resistance Modelling 65
3.2 Modelling Resistance & Resensitisation 68
3.2.1 Mathematical Background 68
3.2.2 Presentation of the General Model 69
3.2.3 Mutational Evolution and the Establishment of Drug Resistance 78
3.2.4 Results for the Mutational System 87
3.2.5 Metabolic Remodeling and the Re-Establishment of Drug Sensitivity 98
3.2.6 Results for the Metabolic System 106
3.2.7 Discussion 113
3.3 Data-Driven Drug Resistance Modelling 116
3.3.1 Introduction 116
3.3.2 Spatio-Structuro-Temporal Modelling of Single-Cell RNA-seq Data 117
3.3.3 Results 123
3.3.4 Discussion 128

4 Modelling Ligand-Activated Signalling Processes Applied to Interferon 131
4.1 Introduction to IFN Dynamics 131
4.1.1 Ligand-Activated Sensing and Reciprocating Systems . . 132
4.1.2 An Example of a SAR System: Cellular Interferon (IFN) System 135

4.2 Modelling Signal Propagation in SARs 137
4.2.1 A Simple Spatio-Temporal Model of SARs 137
4.2.2 General SAR Model Within the Spatio-Structuro-Temporal Framework 139
4.2.3 Particularised IFN-Based Model 146
4.2.4 Numerical methods 152
4.2.5 Results from Numerical Simulations 155
4.2.6 Discussion 165
4.3 Antiviral Multi-Affinity IFN Systems 168
4.3.1 Further Biological Details of the Interferon (IFN) System 168
4.3.2 A Mathematical Model for IFN Dynamics 170
4.3.3 Numerical Methods 173
4.3.4 Results & Discussion 175

5 Multi-Dimensional Analysis of Theoretical Problems in Evolution 189

5.1 Introduction to Evolutionary Modelling 189
5.1.1 Current Evolutionary Theory & Modelling 190
5.2 Darwinian Trait Evolution 192
5.2.1 An Evolutionary Mathematical Model 192
5.2.2 Equilibrium Analysis 199
5.2.3 Numerical Methods 218
5.2.4 Results 219
5.2.5 Discussion 229

6 Further Methods in Multi-Scale Modelling of Cancer Invasion 233

6.1 Introduction to Pseudo-Spectral and CA Methods 233
6.1.1 Brief Recap of Multi-Scale Drug Resistance 234
6.1.2 Oncological co-invasion 236
6.2 Pseudo-Spectral Chebyshev Approaches 237
6.2.1 The Mathematics of Chebyshev Polynomials 237

6.2.2 An Algorithm for Pseudo-Spectral Chebyshev Polynomial Methods 243
6.2.3 Results & Conclusions 246
6.3 Cellular Automata Modelling of Cell Invasion 250
6.3.1 Development of a Novel Cellular Automata Model 250
6.3.2 Numerical Aspects of Cellular Automata Modelling 254
6.3.3 Results & Conclusions 258

7 Conclusion **263**
7.1 Particular Conclusions 263
7.2 Perspectives 270

List of Figures

1.1 Set theoretic diagram for generating source terms 13

1.2 Components involved in the calculation of the ball integral . . . 25

2.1 Numerical 1D-spatial 1D-structural results 49

2.2 Numerical 2D-spatial 1D-structural results for homogeneous ECM, plotted at times $t \in \{3, 15\}$ 52

2.3 Numerical 2D-spatial 1D-structural results for homogeneous ECM, plotted at times $t \in \{35, 50\}$ 53

2.4 Numerical 2D-spatial 1D-structural results for heterogeneous ECM, plotted at times $t \in \{3, 9\}$ 55

2.5 Numerical 2D-spatial 1D-structural results for heterogeneous ECM, plotted at times $t \in \{15, 20\}$ 56

2.6 Numerical 2D-spatial 1D-structural results for heterogeneous ECM, plotted at times $t \in \{30, 50\}$ 57

2.7 Numerical 2D-spatial 2D-structural results for (2.3) for heterogeneous ECM, plotted at times $t \in \{3, 9\}$ 59

2.8 Numerical 2D-spatial 2D-structural results for (2.3) for heterogeneous ECM, plotted at times $t \in \{12, 20\}$ 60

2.9 Numerical 2D-spatial 2D-structural results for (2.3) for heterogeneous ECM, plotted at times $t \in \{25, 35\}$ 61

3.1 Diagrams comparing discrete and continuous resistance paradigms 66

3.2 Normalized structural velocity functions for genetic mutation . . 85
3.3 Distributions of drug effectiveness functions in y 87
3.4 Punctuated evolution is more consistent with biological results than gradual evolution 91
3.5 The sequencing of treatments is crucial to success 93
3.6 Oscillatory tumour volumes can emerge in the absence of re-sensitisation 95
3.7 Spatial heterogeneity eradicates treatment success, $t \in \{5, 40, 80, 120\}$ 96
3.8 Spatial heterogeneity eradicates treatment success, $t \in \{160, 200, 240, 280\}$ 98
3.9 Visual reinterpretation of the structural y variable to account for the metabolism of glucose 100
3.10 Distributions for the drug effectiveness functions in y 105
3.11 Resistance and re-sensitisation dynamics are captured by *in silico* modelling 107
3.12 Tumours use oxphos metabolic pathways to resist targeted inhibition of glycolytic pathways by BRAFi and MEKi therapies, $\{50, 100, 150\}$ 108
3.13 Tumours use oxphos metabolic pathways to resist targeted inhibition of glycolytic pathways by BRAFi and MEKi therapies, $\{200, 220, 240\}$ 109
3.14 Tumours use oxphos metabolic pathways to resist targeted inhibition of glycolytic pathways by BRAFi and MEKi therapies, $\{245, 250, 255\}$ 110
3.15 Tumours use oxphos metabolic pathways to resist targeted inhibition of glycolytic pathways by BRAFi and MEKi therapies, $\{260, 280, 300\}$ 111
3.16 tNSE data becomes principal axis map (PrAM). 117
3.17 Time resolved tNSE scatter plots for Phases $t_0 - t_3$. 118
3.18 Numerical simulations of the initial conditions and tumour volume over time 124

3.19 Numerical simulations of tumour growth and drug particle dynamics prior to and during treatment, $t \in \{-8, 0, 10\}$ 125

3.20 Numerical simulations of tumour growth and drug particle dynamics during treatment, $t \in \{20, 30, 40\}$ 126

3.21 Numerical simulations of tumour growth and drug particle dynamics prior to and during treatment, $t \in \{50, 60\}$ 128

3.22 Simulation of *in silico* sample collection for the tumour at regions of high cancer cell density and low drug particle concentration, and *vice versa* 129

4.1 Multi-cluster results in the concentration of molecular species for varying affinities of IFN, $t \in \{0, 25, 50, 75, 100\}$ 138

4.2 Diagram describing the simplified IFN cell-regulatory system . . 148

4.3 Single-cluster results from simulation of IFN model for low affinity IFN, $t \in \{0, 5, 10, 15\}$ 156

4.4 Single-cluster results from simulation of IFN model for low affinity IFN, $t \in \{20, 25, 30, 35\}$ 157

4.5 Multi-cluster results from simulation of IFN model for low affinity IFN, $t \in \{0, 15, 30\}$ 158

4.6 Multi-cluster results from simulation of IFN model for low affinity IFN, $t \in \{45, 60, 75\}$ 159

4.7 Spatially static, multi-cluster results from simulation of IFN model for high affinity IFN, $t \in \{0, 15, 30\}$ 160

4.8 Spatially static, multi-cluster results from simulation of IFN model for high affinity IFN, $t \in \{45, 60, 75\}$ 161

4.9 Spatially dynamic, multi-cluster results from simulation of IFN model for high affinity IFN, $t \in \{0, 10, 20\}$ 162

4.10 Spatially dynamic, multi-cluster results from simulation of IFN model for high affinity IFN, $t \in \{30, 40, 50\}$ 163

4.11 Temporal dynamics of the IFN binding system upon artificial stimulation with IFNβ, in an High/Low affinity system system with inhibited low affinity IFN production 176
4.12 Temporal dynamics of the IFN binding system upon artificial stimulation with IFNβ, in an High/Low affinity system 177
4.13 Temporal dynamics of the IFN binding system upon artificial stimulation with IFNβ, in a virally infected High/Low affinity system with inhibited low affinity IFN production 178
4.14 Temporal dynamics of the IFN binding system upon artificial stimulation with IFNβ, in a virally infected High/Low affinity system 179
4.15 temporal dynamics of the interferon binding system after the mimesis of the artificial stimulation of a central cell cluster with IFNβ, in a High/Low IFN system, $t \in \{100, 120, 140, 160, 180, 200\}$ 180
4.16 Temporal dynamics of the IFN binding system upon artificial stimulation with IFNβ, in an High/Medium/Low affinity system infected with a slowly diffusing virus and with inhibited low affinity IFN production 183
4.17 Temporal dynamics of the IFN binding system upon artificial stimulation with IFNβ, in an High/Medium/Low affinity system infected with a slowly diffusing virus 184
4.18 Temporal dynamics of the IFN binding system upon artificial stimulation with IFNβ, in an High/Medium/Low affinity system infected with a quickly diffusing virus and with inhibited low affinity IFN production 185
4.19 Temporal dynamics of the IFN binding system upon artificial stimulation with IFNβ, in an High/Medium/Low affinity system infected with a quickly diffusing virus 186
4.20 Total viral concentration over time for an infected system where low affinity IFN production is inhibited and for a fully functional system 187

4.21 Percentage change in total viral concentration for a system without low affinity IFN 188

5.1 Diagram displaying the interactions between traits survival, beauty, and selectivity within the prey population and between the prey and predator populations 195

5.2 Population dynamics for a system with advantage parameters $q = 1.6$ and $\beta = 0.4$ 220

5.3 Time series colour-maps representing 2-dimensional distribution of prey populations, $t \in \{0, 2, 4\}$ 221

5.4 Time series colour-maps representing 2-dimensional distribution of prey populations, $t \in \{6, 8, 10\}$ 223

5.5 Female sexual selection drives male elaboration 224

5.6 Advantageous elaboration gives rise to augmented male success . 225

5.7 Modelling predicts a steep drop-off in elaboration as costs exceed orthogonal compensations 226

5.8 Shifting elaboration costs causes elaborate-selective and inconspicuous-non-selective phenotypic selection 227

5.9 Beauty is an evolutionary end in itself 228

6.1 Pictorial representation of successive Chebyshev polynomial expansions 238

6.2 Schematic representation of the numerical Chebyshev polynomial scheme implemented 244

6.3 Results of the numerical simulations for the phenotypically evolving tumour model, using pseudo-spectral methods, are given, $t \in \{0, 30, 60\}$ 246

6.4 Results of the numerical simulations for the phenotypically evolving tumour model, using pseudo-spectral methods, are given, $t \in \{90, 100, 110\}$ 247

6.5 Results of the numerical simulations for the phenotypically evolving tumour model, using pseudo-spectral methods, are given, $t \in \{120, 150, 180\}$ 248
6.6 Snapshots of simulated cells migrating through the ECM 258
6.7 Results of cell microtrack experiments 259
6.8 Experimental *in silico* injection of $\text{MITF}^{\text{HIGH}}$ cells; MITF^{LOW} cells; or both cell types 260

List of Tables

2.1 Table of parameters for use in simulating (2.3) 48

3.1 List of parameters used for numerical simulations of the model. Parameters are defined within a non-dimensionalised system (excepting for time measured in days) and, as such, are defined in terms of units days^{-1}. 89

4.1 Table of parameters 155
4.2 Table of parameters for a model SAR system 155
4.3 Parameters used in generating numerical results for the full IFN system 174

5.1 Table of constants for the evolutionary sexual selection model . . 218

6.1 Example of the first 6 Chebyshev polynomials and their approximated functions, calculated using (6.5). 239

List of Abbreviations

ATP	Adenosine triphosphate
BRAFi	B-rapidly activated fibrosarcoma gene
COM	Centre of mass
DNA	Deoxyribonucleic acid
ECM	Extra-cellular matrix
ECNE	Extra-cellular nutritional environment
EGFR	Epidermal growth factor receptor
ERK	Extracellular signalling-related kinase
HP	Handicap principle
HSH	Honest signalling hypothesis
ICAM	Intercellular adhesion molecule
IFN	Interferon
IFNAR	Interferon α/β receptor
IRF	Interferon regulatory [transcription] factor
ISG	Interferon stimulated gene
ISGF	Interferon stimulated gene [transcription] factor
JAK	Janus kinase
LHS	Left-hand side
MAPK	Mitogen activated protein kinase
MEKi	MAPK/ERK kinase
MITF	Microphthalmia-associated transcription factor
MMP	Matrix metalloproteinase
mRNA	Messenger ribonucleic acid
NF-κB	Necrosis factor κB
NRAS	Neuroblastoma-associated rat sarcoma gene
OD	Orthogonal disadvantage
ODE	Ordinary differential equation
oxphos	Oxidative phosphorylation

PAMP	Pathogen-associated molecular pattern
PCA	Principle component analysis
PDE	Partial differential equation
PDF	Probability density function
PDX	Primary derived xenograft
PE	Punctuated equilibrium
PG	Phyletic gradualism
PI3K	Phosphoinositide 3-kinase
PrAM	Principle axis map
PRR	Pattern recognition receptor
PTEN	Phosphatase and tensin homolog
RHS	Right-hand side
RK4	4^{th} order Runge-Kutta
RNA	Ribonucleic acid
SAR	Sensing and reciprocating
scuPA	Single-chain urokinase plasminogen activator
SST	Spatio-structuro-temporal
STAT	Signal Transducer and Activator of Transcription
tSNE	t-distributed stochastic neighbour embedding
uPA	Urokinase plasminogen activator
uPAI	Urokinase plasminogen activator inhibitor
uPAR	Urokinase plasminogen activator receptor
UPH	Unprofitable prey hypothesis
USP	Ubiquitin specific peptidase

List of Publications

Herein I present a list of 'first author' publications emanating from the undertaking of this thesis and published within a mixture of mathematical and biological journals. (All other authors to these papers played a supervisory role in their completion.)

1. Hodgkinson A, Chaplain M A J, Domschke P, Trucu D (2018) Computational approaches and analysis for a spatio-structural-temporal invasive carcinoma model. *Bulletin of Mathematical Biology* **80**(4): 701-737

2. Hodgkinson A, Radulescu O, Uzé G, Trucu D (2018) Signal propagation in sensing and reciprocating cellular systems with spatial and structural heterogeneity. *Bulletin of Mathematical Biology* **80**: 1900-1936

4. Hodgkinson A (2018) Cellular Automata, chap. A Novel Cellular Automata Modelling Framework for Micro-Environmental Interaction and Co-Invasion. Springer

3. Hodgkinson A, Le Cam L, Trucu D, Radulescu O (2019) Spatio-genetic and phenotypic modelling elucidates resistance and re-sensitisation to treatment in heterogeneous melanoma. *Journal of Theoretical Biology* **466**: 84-105

5. Hodgkinson A, Uzé G, Radulescu O (2019) Both high and low affinity inter- ferons are necessary for effective immune response. *Submitted*

6. Hodgkinson A (2019) Beauty and Survival Traits are Evolutionarily Symbiotic. *Submitted*

Acknowledgements

I send my gratitude to the Laboratoire des Intéractions Hôte-Pathogène (LIHP) of the Université de Montpellier and the Institut de Rechrche en Cancerologie de Montpellier (IRCM) of the Institut National de Santé et de le Rechrche Médicale (INSERM), who facilitated my studies, and to the École Doctorale de l'Université de Montpellier, for funding my PhD studies in their entirety. I should also extend special thanks to Prof. Ovidiu Radulescu for the support and funding provided in order to allow me to travel to conferences and effectively engage with the international scientific community.

My deepest and warmest thanks are extended to Prof. Ovidiu Radulescu – who assisted in correcting and clarifying the mathematics within my thesis and who indulged innumerable conversations on life, mathematics, and the nature of the universe – and Dr. Laurent Le Cam – for his unending patience in explaining the biological realities of any given problem. Likewise, Prof. Gille Uzé lent significant time and expertise in relation to answering the biological questions, herein, pertaining to immunology; Prof. Jean-Christophe Marine and Dr. Florient Rambow were kind enough to share with me their manuscript, without which the higher-dimensional data-driven modelling would have been impossible; and Dr. Alain Jean-Marie indulged me for several hours, first as my lecturer and latterly as my collaborator, on an exciting project in Markov chain analyses.

Finally, I would like to thank my dearest wife – whose support has been invaluable and unwavering – and my family for their continued support throughout my undergraduate, postgraduate, and doctoral studies – without whom the completion of this thesis would have been immeasurably more challenging.

To my family, friends, and the pursuit of truth...

Chapter 0

Introduction

The genesis, sustenance, behaviour, and eradication of cancers are complex, multi-scale processes, involving a coalescent mixture of biological, chemical, and physical mechanisms. Over the past three decades or so, the processes involved in cancer growth and spread received significant mathematical attention through novel and increasingly sophisticated modelling approaches [277, 235, 243, 15, 9, 113], leading to a deeper understanding of key aspects in cancer development with potential therapeutical importance [99, 32].

While being sometimes regarded as a paradigm of local tissue remodelling, cancer invasion is a crucially important process in the overall cancer development where complex, heterotypic, cell population-scale processes, combined with a cascade of molecular signalling mechanisms, lead to the degradation of healthy tissue and its concomitant repopulation by migratory cancer cells [74, 144]. This phenomenon attracted a wide range of spatio-temporal modelling at either one spatial scale [15, 117, 14, 54, 55, 57] or in a multi-scale approach [9, 47, 319, 264].

It became increasingly apparent, however, that the context of macro-scale spatio-temporal modelling was not sufficient to take into account the intricate behaviour of cancer cell processes. To that end, with insights from important concepts in structural modelling of biological systems (considering age, size, etc.) [91, 194, 239, 63, 92, 27, 212], the various spatio-temporal modelling approaches

for cancer invasion have been recently complemented by structural models [60, 96], which enable a more detailed description of the involved biological processes, to a certain extent, by implicitly accounting for single cell-dynamics.

The need for considering both the spatial and structural heterogeneity of cell populations in tissues has been proven by recent advances in single cell mRNA and DNA sequencing and in spatially resolved proteomics [278]. These new experimental techniques unravelled a complex picture where cancer heterogeneity occurs at multiple scales: inter-individual, inter-tumoural, intra-tumoural, spatial, inter-cellular, *et cetera*. The understanding of this complex landscape becomes particularly important for predicting the tumour's response to targeted treatment. As a matter of fact, in order to resist treatment cancer develops strategies exploiting underlying heterogeneity at all scales.

The proposal for this work was to explore the ways in which we may increase our understanding of the biological phenomena involved in cancer invasion, through appreciating this process across a variety of scales considered important by the biological and clinical communities. Our primary and most fundamental goal, therefore, is to shed light on these processes by utilising and developing novel mathematical approaches, capable of enhancing the level of resolution at which we may appreciate the underlying and superordinate dynamics of tumour-, cell-, and protein-scale events.

We begin, in Chapter 1, by introducing the most formal and fundamental aspects of this modelling technique through a mathematical derivation of the higher-dimensional modelling framework, used throughout this thesis, from the first principles of the continuity equation [161]. Alongside this work, we present a derivation of complex source terms necessary for biologically relevant mathematical representations of population-scale proliferation – avoiding temporal discontinuities introduced in earlier works on modelling cancer heterogeneity [96] – and the phenotypic alterations resulting from disparate parent lineages producing offspring, as well as temporally local mutation events in a model of evolution of traits with a negative influence on fitness [157].

It was also important to us that the numerical methods that we were intending to use did not interfere with the efficacy of our solutions to align themselves with the descriptive mathematical systems. In order to do so, we begin by presenting a theorem establishing the stability of the central differences operator, frequently used in finite difference-driven numerical simulators. Likewise, the introduction of nonlocal adhesion terms for amending the spatial flux of cell populations by Domschke *et al.* [96] required a novel method for implementing ball integrals on the spatial domain, for which no error-bound theorems yet exist. This is given as our final, global numerical result.

The first application of these numerical methods, covered in Chapter 2, was then to an existing system of equations [96], which focussed on a novel modelling framework which aimed to take account of the urokinase plasminogen receptor's binding dynamics, at the cell surface, during the invasion of heterogeneous breast cancer species. To do this, we used PDEs over a multi-dimensional structure space, upon which cell populations were defined and permitted to evolve under certain assumption about their biological dynamics. This allowed for a coupling of dynamics between spatial and binding characteristics belonging to the population. The project largely involved the development of a numerical scheme for the computation of approximate solutions in 3- and 4-dimensions, as well as several error-bound theorems for these approximations [158].

The multi-dimensional nature of this framework was considered significant for its ability to postulate that certain features and dynamics of the cell occurred through hypothetical biologically structured dimensions which could describe the changes taking place within the cell, and on the level of the population. In other words, it gave rise to the possibility to consider cellular dynamics on multiple scales, simultaneously, such that the fullest resolution of the biological context could be appreciated and accounted for mathematically. The purpose of this doctoral study, then, was to build on this work and extend the utility of the multi-dimensional methods that were beginning to be introduced to oncological modelling.

Chapter 3 involves the explication of a yet more biologically involved modelling project, aiming to clarify many of the ambiguities around the mechanism for the development of resistance to targeted drug treatments in melanoma. The first example of this is no more apparent than in the experimental work of Perna *et al.* [267], who showed the clear manifestation of a 4-stage growth and resistance process in melanoma responding to BRAF inhibitor (BRAFi) treatment. These stages of initial growth, sensitivity, tolerance, and resistance occur throughout the literature, while the mechanisms and dynamics of this process remained mysterious. We attempt to provide a paradigm in which to explain this data by postulating a population of cells whose spatio-temporal dynamics are coupled to a cell-scale metabolic dynamic, in which cells may take on a metabolic status between glycolytic or oxidative phosphorylative phenotypes – two modes of metabolising glucose to produce adenosine triphosphate (ATP) and acidic molecules. We find that cells which take on a genetically disfavourable phenotype, by means of random fluctuation, may be preferentially selected for by targeted therapies and may return to their original states upon the alleviation of therapy [160].

The second research section in drug resistance covers the results of a more laborious data-driven project to discover the clinical and biological implications of an intriguing set of *in vivo* single-cell RNA-seq data produced by Rambow *et al.* [278]. This temporally resolved RNA-seq data displayed the dynamics of the cell population during the course of BRAFi + MEKi therapy and resulted in a far more cumbersome system of PDEs than the theoretically derived system, but which was able to recapitulate the RNA expression dynamics, to some extent. Coupling this to a spatially dynamic system, we then generated solutions for this 5-dimensional problem and found that tumours may express highly resistant phenotypes on the perimeter of the tumour, where drug concentrations are high, and protect the inner core of the tumour which remains highly proliferative and sensitive to treatment throughout. The current intention is to test this biological hypothesis and, hopefully, provide validation for this approach.

As a further attempt to validate the approach of higher dimensional spatio-structuro-temporal modelling, in Chapter 4 we present several of the result that we have generated within the field of immunology, including an important hypothesis around the evolution of cytokines. We begin, within this work, by presenting a comparison between a more simple, spatio-temporal PDE model, capable of exploring the difference in the ability of high- and low-affinity ligands to propagate a signal across space, and a more complex spatio-structuro-temporal model, which accounts for the proportionate binding of each ligand and its subsequent affect on the underlying IFN production dynamics within the cell. We found that low affinity IFN ligands were capable of propagating a signal, whereas only high affinity IFN ligands were capable of reliably maintaining the activity of the cell [161].

In an extension to this work, we increased the relevance of our model by coupling viral dynamics with the IFN dynamics to explore their affect on one another. Biologically, viruses will activate the IFN signalling cascade whereas IFN signalling aims to stall the activity of infected cells. Given this hypothesis, therefore, we found that systems that contained both low- and high-affinity IFN would destroy and contain an infection more rapidly than would those systems which contained only one or the other ligand, suggesting that evolution would conserve such multiplicitous systems over uniform ones. Moreover, in a humanoid system, containing 13 IFN ligands of differing affinities for its receptors, we found that systems containing low affinity ligands resulted in a 23% lower viral yield during local infection period than those without. This shows not only the importance of low affinity IFN ligands but also the opportunity for using higher-dimensional techniques for the exploration of fundamental scientific questions [159].

On top of these motivations, immuno-oncology is an exceptionally important subdomain within oncology and new developments, taking advantage of our knowledge of the IFN pathway and its dynamics, are increasingly looking to exploit this system for the treatment of resistant tumours [142, 352, 313]. This is perhaps most true in the case of oncolytic viral therapies, which aim to

degrade the tumour by inducing a local viral infection, but which often fail due to the interruption of the IFN signalling cascade which seeks to shut-down viral proliferation and isolate infections [308, 223, 226].

This then bring us to a statement made by Theodosius Dobzhansky of which every biologist is aware: "Nothing in biology makes sense expect in the light of evolution." The process by which our *in silico* cancer populations eventually survive is through an evolutionary and natural selective process and, likewise, to ask why our IFN systems contained low affinity ligands necessarily invoked the discussion of evolution, itself. Then, in light of this, it only makes sense to ask if survival is the only trait which evolution conserves or whether there are traits which the natural universe is willing to conserve despite their survival disadvantages.

Chapter 5 of this thesis seeks to ask this question by addressing one of the few existing problems of evolutionary biology; that of why elaboration is conserved even when it appears only to decrease the hosts survival opportunities. Herein, we postulate a system wherein the biological organism may acquire survival traits, either beneficial to survival or otherwise, or sexually desirable traits, such as æsthetic qualities, from the parents and ask whether or not these traits will be acquired or conserved, in spite of the assumption that the sexually selected traits negatively influence survival. We find that, in accordance with expectation, when the negative influence of a beauty trait is small, the trait is acquired and conserved by a population and that there is a critical threshold under which this trend is conserved. Moreover, when the negative influence of a beauty trait is sufficiently high, the beauty trait itself will actually contribute to selection for more highly adaptive survival traits, since the selective pressure on the population will increase. Therefore, beauty, despite being a negative influence on survival, will aid the selection of traits which will aid survival and may be an evolutionary end in itself [157].

Finally, and in order to fully explore alternative description of reality in a multi-scale paradigm, we use Chapter 6 to explore a pseudo-spectral method

of solving systems of PDEs in higher-dimensional spaces and adopt a cellular automata model to explore a previously intractable problem for continuous methods. Orthogonal polynomial methods are commonly used in the solution of continuous PDEs due to their low memory requirements; near-analytic solutions; and infinite resolution on the calculated domain. We employ, in particular, Chebyshev polynomials in pursuit of a methodology to expand the number of dimensions across which we may simulate our system and apply this to our drug resistance problem, for the sake of comparison. We find that the results are somewhat disparate, although reconcilable, and that the continuity of the Chebyshev polynomials, themselves, may hinder the ability of the numerical solutions to reflect the semi-discrete quality of biological metabolic systems. Our pseudo-spectral method, in contradiction to our earlier results, fail to predict the pre-resistance disappearance of the tumour population and may, therefore, only be appropriate for use in very particular problems.

Our cellular automata method, on the other hand, is employed to model a significantly different problem, wherein separately non-invasive proliferating cells become invasive when co-injected with highly invasive, but non-proliferative, cells. We develop, from scratch, a continuous agent-based cellular automaton capable of accounting for micro-environmental changes at the cell-membrane and use this to simulate the co-injection experiment. We found that the adaptive nature of the cells in our model were able to recapitulate the results of this experiment and other, individual cell-based, experiments where cells were placed within microtracks and their speed measured on the basis of extra-cellular matrix (ECM) density and microtrack width [156]. This, partially discrete model is yet another paradigm in which the fully continuous system was not quite able to replicate the behavioural mechanics of biological experiment and points to a quasi-continuous reality.

In essence, the continuous representation of reality makes a fundamental claim about the nature of reality, as a continuous and indivisible entity, which we wished to more fully explore and test the limitations thereof. Firstly, it

is clear that reality has discrete features at the microscopic level of molecular and cellular interactions and modifications. At a low resolution, macroscopic, level all these discrete features are approximated by continuous distributions. Although most aspects of the biological function are insensitive to individual discrete details and are well rendered in coarse-grained representations of reality, it is possible that some microscopic events have inter-scale effects. Reality may exist somewhere between these two interpretations – a meso-resolution with continuous and discrete elements.

Chapter 1

Derivation of an Higher-Dimensional Modelling Framework and Associated Numerical Methods

1.1 Introduction to Higher-Dimensional Modelling

There exists an increasing difficulty in the field of bio-mathematics, in that the ability of models to account for the vast and sophisticated data sets emanating from the fields of biological enquiry require ever-more sophisticated approaches. For example, the realisation that the dynamics of cancer could not merely be considered at a population level and required spatial consideration, in order to

appreciate the complexity and precise mechanics of this process, yielded several impressive spatio-temporal PDE-based modelling approaches [117, 15, 54, 55]. Modern results in cancer and beyond, however, mean that spatial resolution, alone, may not be sufficient to increasingly account for the micro-scale chemical events which give rise to macro-scale tumour behaviours or events.

One recently developed method showed particular promise for application to and the analysis of intricately detailed biological systems [96]. This method showed an additional advantage in that it is able to cope with cell population heterogeneity, i.e. with the existence, in the same spatial location, of cells of the same type but having a distribution of states and behaviours. This was made possible by characterising the cell populations by distributions in spatial and structural dimensions. The structural dimensions represent biochemical variables characterising the intracellular dynamics. These high dimensional distributions of cells follow Liouville equations including source terms and various spatial and structural fluxes. Moreover, and given that chemical events rely on physical components (such as proteins or enzymes) that are partitioned during cell division, the source terms, that describe proliferation, require special attention.

We deal with these source terms in two entirely differing scenarios: The first of these scenarios was covered in Domschke *et al.* [96] but led to critical instabilities for the numerical apparatus which calculated solutions to this system [158]. In this systems, bound ligands on the cell's surface must be distributed between resultant daughter cells during proliferation and we propose an amendment to the original form of this term to rectify the instabilities and respect the continuity of the proliferative process, on the population scale. The second case is that wherein mutation occurs during proliferation and gives rise to daughters which differ significantly to their parents. We consider the cases both wherein this mutation is random and wherein the resultant phenotype falls mid-way between the parents' phenotypes, as a combined phenotype.

As we have mentioned, the employment of novel mathematical modelling methods often requires the development of novel numerical strategies for the

calculation, and approximation, of their solutions. We begin by producing a theorem which establishes the stability of the oft-used central difference operator in finite difference schemes, to maintain our confidence in the ability of our system to generate reliable solutions. Given that the errors for gradients calculated using central differences are of the order $\mathcal{O}(\delta_x^2)$, the addition of this stability theorem justifies our particular numerical scheme. Finally, we present a numerical approach to the calculation of nonlocal ball integral, across short radii, and approximate this solution for easy application to problems involving these operations.

It is important to note that the frameworks and theorems established within the following sections will be employed extensively, throughout this thesis. The establishment of a higher-dimensional framework for modelling will be used in each of the following chapters and establishes a general approach which may be applied to a wide range of biological problems beyond, where the source terms will be utilised as appropriate within this framework. Since I will rely heavily on finite difference methods for the approximation of spatio-structuro-temporal solutions to models generates, the numerical calculations will also be used in every following chapter (with additional theorems being given in Section 6.3 for the sake of approximations to the agent-based cellular automata solutions).

1.2 Multi-Dimensional & Multi-Scale Modelling

In order to introduce this technique, mathematically, we now indulge the presentation of its derivation as set out in [161]:

For mathematical formality, let $\mathcal{D} \subset \mathbb{R}^d$ with $d \in \{1, 2, 3\}$ be a bounded spatial domain, $\mathcal{I} = [0, T] \subset \mathbb{R}$, with $T > 0$ be an arbitrary time interval. Thus, the variables $x \in \mathcal{D}$ represent space and $t \in \mathcal{I}$ represents time. Further, let $\mathcal{P} \subset \mathbb{R}^p$ be a domain containing variables characterising the available binding sites of transmembrane receptors and their occupation state. The variables $(\xi, y) \in \mathcal{P}$ represent the total concentrations of various receptors and the parts of the receptor binding sites occupied by ligands. For instance, if there are p

different transmembrane receptors and each one has only one binding site that can bind only one ligand, $\xi = (\xi_1, \ldots, \xi_p)$, $y = (y_1, \ldots, y_p)$, where ξ_i is the total concentration of the receptor of i and $0 \leq y_i \leq \xi_i$ is the concentration of bound rceptors, for $1 \leq i \leq p$. In this case the domain $\mathcal{P}$ is a cone. Finally, let $\Gamma \subset \mathbb{R}^\gamma$ with $\gamma \in \mathbb{N}$ be a domain containing the metabolic states. More precisely, $(\alpha_1, \ldots, \alpha_\gamma) \in \Gamma$ represent the internal biochemical state of a cell : α_i can be species concentrations, convex coordinates of metabolic fluxes in the convex basis of extreme currents, data driven PCA (principal component analysis) reduced variables, etc.. Rather, generally, the domains $\mathcal{P}$ and Γ can be considered convex.

In the model given by Hodgkinson *et al.* [161, 159] the structural variable y is used as described above; in order to describe the binding of ligands to available receptors on the cell surface. This was also the way in which the structural variable was conceived in its original derivation and exposition in [96], where the derivation to follow constitutes a significant extension of this modelling framework's scope and functionality. In later uses of this modelling framework, however, we chose to interpret this y variable as a genetic or phenotypic variable, in order to interpret either the evolution of cancer cells [160] or even species of bird [157], whilst we had also used this to represent the temporally variable single-cell RNA-seq profiles of PDX tumours *in vivo*. I will explain these various utilities of the structural variable in their relevant contexts, as appropriate.

Following the same form as the derivation given in Domschke *et al.* [97], we derive of a spatio-structural-temporal model that was utilised throughout the exploration and explication of the hypotheses set out herein.

Further, let U, V, W be rectangles in $\mathcal{D}$, $\mathcal{P}$, and Γ respectively (i.e. $U \times V \times W \subseteq \mathcal{D} \times \mathcal{P} \times \Gamma$). Then the total amount of cells at a given time t is given by

$$\hat{c}(t) \quad = \quad \int_W \int_V \int_U c(t, x, (\xi, y), \alpha)\, dx\, d(\xi, y)\, d\alpha \tag{1.1}$$

the change in $\bar{c} := \hat{c}(t, x, (\xi, y), \alpha)$ per unit time in the spatio-metabolo-receptoro-

binding region $U \times V \times W$ is given by

$$\begin{aligned}
\tfrac{d\bar{c}(t)}{dt} &= \int_W \int_V \int_U \hat{S}(t,x,(\xi,y),\alpha)\,dx\,d(\xi,y)\,d\alpha \\
&\quad - \int_W \int_V \int_{\partial U} \hat{F}(t,x,(\xi,y),\alpha)\cdot\mathfrak{n}(x)\,d\sigma_{d-1}(x)\,d(\xi,y)\,d\alpha \\
&\quad - \int_W \int_U \int_{\partial V} [\hat{G}(t,x,(\xi,y),\alpha),\hat{H}(t,x,(\xi,y),\alpha)]^T\cdot\mathfrak{n}(\xi,y)\,d\sigma_{v+p-1}(\xi,y)\,dx\,d\alpha \\
&\quad - \int_V \int_U \int_{\partial W} \hat{K}(t,x,(\xi,y),\alpha)\cdot\mathfrak{n}(\alpha)\,d\sigma_{\gamma-1}(y)\,dx\,d(\xi,y)\,d\alpha
\end{aligned} \tag{1.2}$$

where σ_{d-1}, σ_{2r-1}, and $\sigma_{\gamma-1}$ are surface measures on $\partial\mathcal{D}$, $\partial\mathcal{P}$, and $\partial\Gamma$, respectively. Supposing, now, that F, G, H, and J, are in the class of continuously differentiable vector fields, $\mathcal{C}^1$, one can use Stokes' Theorem to write

$$\begin{aligned}
\tfrac{d\bar{c}(t)}{dt} &= \int_W \int_V \int_U \hat{S}(t,x,(\xi,y),\alpha)\,dx\,d(\xi,y)\,d\alpha \\
&\quad - \int_W \int_V \int_U \nabla_x\cdot\hat{F}(t,x,(\xi,y),\alpha)\,dx\,d(\xi,y)\,d\alpha \\
&\quad - \int_W \int_U \int_V \nabla_{(\xi,y)}\cdot[\hat{G}(t,x,(\xi,y),\alpha),\hat{H}(t,x,(\xi,y),\alpha)]^T\,d(\xi,y)\,dx\,d\alpha \\
&\quad - \int_U \int_V \int_W \nabla_\alpha\cdot\hat{K}(t,x,(\xi,y),\alpha)\,d\alpha\,d(\xi,y)\,dx
\end{aligned} \tag{1.3}$$

and using Lebesgue's Dominated Convergence Theorem, one can move the time derivative within the integral for $\hat{c}$

$$\begin{aligned}
\int_W \int_V \int_U \tfrac{\partial\hat{c}}{\partial t}\,dx\,d(\xi,y)\,d\alpha &= \int_W \int_V \int_U \hat{S}(t,x,(\xi,y),\alpha)\,dx\,d(\xi,y)\,d\alpha \\
&\quad - \int_W \int_V \int_U \nabla_x\cdot\hat{F}(t,x,(\xi,y),\alpha)\,dx\,d(\xi,y)\,d\alpha \\
&\quad - \int_V \int_U \int_W \nabla_{(\xi,y)}\cdot\begin{pmatrix}\hat{G}(t,x,(\xi,y),\alpha)\\ \hat{H}(t,x,(\xi,y),\alpha)\end{pmatrix} d(\xi,y)\,dx\,d\alpha \\
&\quad - \int_U \int_V \int_W \nabla_\alpha\cdot\hat{K}(t,x,(\xi,y),\alpha)\,d\alpha\,d(\xi,y)\,dx\,,
\end{aligned} \tag{1.4}$$

which can be written

$$\begin{aligned}
&\int\limits_{\mathbb{R}^{d+\upsilon+p+\gamma}} [\tfrac{\partial \hat{c}}{\partial t}]\mathbf{1}_{U\times V\times W}(x,(\xi,y),\alpha)\,dx\,d(\xi,y)\,d\alpha \\
&\quad = \int\limits_{\mathbb{R}^{d+\upsilon+p+\gamma}} [\hat{S}(t,x,(\xi,y),\alpha)]\mathbf{1}_{U\times V\times W}(x,(\xi,y),\alpha)\,dx\,d(\xi,y)\,d\alpha \\
&\qquad - \int\limits_{\mathbb{R}^{d+\upsilon+p+\gamma}} [\nabla_x \cdot \hat{F}(t,x,(\xi,y),\alpha)]\mathbf{1}_{U\times V\times W}(x,(\xi,y),\alpha)\,dx\,d(\xi,y)\,d\alpha \\
&\qquad - \int\limits_{\mathbb{R}^{d+\upsilon+p+\gamma}} \left[\nabla_{(\xi,y)} \cdot \begin{pmatrix} \hat{G}(t,x,(\xi,y),\alpha) \\ \hat{H}(t,x,(\xi,y),\alpha) \end{pmatrix}\right] \mathbf{1}_{U\times V\times W}(x,(\xi,y),\alpha)\,dx\,d(\xi,y)\,\alpha \\
&\qquad - \int\limits_{\mathbb{R}^{d+\upsilon+p+\gamma}} [\nabla_\alpha \cdot \hat{K}(t,x,(\xi,y),\alpha)]\mathbf{1}_{U\times V\times W}(x,(\xi,y),\alpha)\,dx\,d(\xi,y)\,d\alpha\,.
\end{aligned} \tag{1.5}$$

Then, since we have that

$$\{U\times V\times W \;\mid\; U,V,W \text{ - compact with piecewise smooth boundaries}\}$$

is a family of generators for the Borelian σ-algebra on $U\times V\times W$ we can denote $\mathbf{1}_A$ as the indicator function for any arbitrary $A \subseteq \mathcal{D}\times\mathcal{P}\times\Gamma$ and write

$$\begin{aligned}
&\int\limits_{\mathbb{R}^{d+\upsilon+p+\gamma}} [\tfrac{\partial \hat{c}}{\partial t}]\mathbf{1}_{A}(x,(\xi,y),\alpha)\,dx\,d(\xi,y)\,d\alpha \\
&\quad = \int\limits_{\mathbb{R}^{d+\upsilon+p+\gamma}} [\hat{S}(t,x,(\xi,y),\alpha)]\mathbf{1}_{A}(x,(\xi,y),\alpha)\,dx\,d(\xi,y)\,d\alpha \\
&\qquad - \int\limits_{\mathbb{R}^{d+\upsilon+p+\gamma}} [\nabla_x \cdot \hat{F}(t,x,(\xi,y),\alpha)]\mathbf{1}_{A}(x,(\xi,y),\alpha)\,dx\,d(\xi,y)\,d\alpha \\
&\qquad - \int\limits_{\mathbb{R}^{d+\upsilon+p+\gamma}} \left[\nabla_{(\xi,y)} \cdot \begin{pmatrix} \hat{G}(t,x,(\xi,y),\alpha) \\ \hat{H}(t,x,(\xi,y),\alpha) \end{pmatrix}\right] \mathbf{1}_{A}(x,(\xi,y),\alpha)\,dx\,d(\xi,y)\,d\alpha \\
&\qquad - \int\limits_{\mathbb{R}^{d+\upsilon+p+\gamma}} [\nabla_\alpha \cdot \hat{K}(t,x,(\xi,y),\alpha)]\mathbf{1}_{A}(x,(\xi,y),\alpha)\,dx\,d(\xi,y)\,d\alpha
\end{aligned} \tag{1.6}$$

for any arbitrary Borelian set A in the σ-algebra on $\mathcal{D}\times\mathcal{P}\times\Gamma$. Then we can

replace $\mathbf{1}_A$ with any simple function, as so

$$\begin{aligned}
&\int\limits_{\mathbb{R}^{d+2r+\gamma}} [\tfrac{\partial \hat{c}}{\partial t}]\nu(x,(\xi,y),\alpha)\,dx\,d(\xi,y)\,d\alpha \\
&\qquad = \int\limits_{\mathbb{R}^{d+\upsilon+p+\gamma}} [\hat{S}(t,x,(\xi,y),\alpha)]\nu(x,(\xi,y),\alpha)\,dx\,d(\xi,y)\,d\alpha \\
&\qquad\quad - \int\limits_{\mathbb{R}^{d+\upsilon+p+\gamma}} [\nabla_x \cdot \hat{F}(t,x,(\xi,y),\alpha)]\nu(x,(\xi,y),\alpha)\,dx\,d(\xi,y)\,d\alpha \\
&\qquad\quad - \int\limits_{\mathbb{R}^{d+\upsilon+p+\gamma}} \left[\nabla_{(\xi,y)} \cdot \begin{pmatrix} \hat{G}(t,x,(\xi,y),\alpha) \\ \hat{H}(t,x,(\xi,y),\alpha) \end{pmatrix}\right] \nu(x,(\xi,y),\alpha)\,dx\,d(\xi,y)\,d\alpha \\
&\qquad\quad - \int\limits_{\mathbb{R}^{d+\upsilon+p+\gamma}} [\nabla_\alpha \cdot \hat{K}(t,x,(\xi,y),\alpha)]\nu(x,(\xi,y),\alpha)\,dx\,d(\xi,y)\,d\alpha \\
&\qquad\qquad\qquad\qquad\qquad\qquad\qquad\qquad \forall \nu \in \mathcal{C}_0^\infty(\mathcal{D}\times\mathcal{P}\times\Gamma)\,.
\end{aligned} \tag{1.7}$$

Then, since this relation holds for any $\mathcal{C}^\infty$ test function, $\nu(x,(\xi,y),\alpha)$, we obtain the equation

$$\begin{aligned}
\frac{\partial \hat{c}}{\partial t} &= \hat{S}(t,x,(\xi,y),\alpha) - \nabla_x \cdot \hat{F}(t,x,(\xi,y),\alpha) \\
&\quad - \nabla_{(\xi,y)} \cdot [\hat{G}(t,x,(\xi,y),\alpha), \hat{H}(t,x,(\xi,y),\alpha)]^T - \nabla_\alpha \cdot \hat{K}(t,x,(\xi,y),\alpha)\,,
\end{aligned} \tag{1.8}$$

where the functions on the right-hand side describe fluxes in the cellular population density.

It is also worth noting that such a technique is better conceived as dealing with joint probability distributions across the product of several correlated sets, rather than attempting to simulate true or absolute physical dynamics of populations across this space. Conceived in this way, this framework introduces a significant opportunity for nuance in the discussion of current spatio-temporaly dependent biomathematical paradigms. Where once we were forced to consider the spatial dynamics of structurally discretised subpopulations (such as those cancer populations who are either 'sensitive' or 'resistant' in an absolute sense), we now have a framework capable of handling the discussion of the probabilities of being within these states or, indeed, some intermediate state. In saying this, we also acknowledge that these systems provide significant obstacles to analysis

and the drawing of firm conclusions; perhaps making them more reflective of the non-propositional nature of reality.

This note is added not solely for the purpose of advertising this model but, rather, for the purposes of clarifying its results and conclusions. The results of simulations produced using this framework should be interpreted through this probabilistic lens such that, although we may produce and interpret spatial results as real concentrations, structural results (in the absence of overwhelming evidence) should be read as probability density functions over the relevant structural space. That is, the full continuum of the structural space may not, indeed, be represented as shown but rather some discrete sample across the continuum of points in this space would be a more true representation of reality. All points on the continuum are, therefore, relevant but the cells that we attempt to simulate are, of course, discrete and should be interpreted as inhabiting some discreet set of points on that space, relatively with the given probability density function.

1.2.1 Structural Fluxes

We consider here the dynamics of a cell population in structure space. Each cell of the population is characterised by its structure state vector $s = (\xi, y, \alpha)$ and by its location $x \in \mathcal{D}$. We consider that cells in the same location follow a dynamics defined by the vector field Ψ on $s \in \mathcal{P}\times\Gamma$, with $c(t,x)$, $m(t,x)$, $v(t,x)$ as parameters defining the local environment

$$\frac{ds}{dt} = \Psi(s; c(t,x), m(t,x), v(t,x)). \tag{1.9}$$

Different cells have different initial conditions at $t = t_0$, whose distribution is given by $\hat{c}(t_0, x, s)$. Let $s(t) = \Phi_{t,t_0}(s_0)$ be the unique solution of (1.9) starting from s_0 at t_0.

Let us consider the cell sub-population located in the bounded spatial $V \subset \mathcal{D}$ and structural $U \subset \mathcal{P}\times\Gamma$ boxes. A population in which each cell follows (1.9)

fulfils the continuity equation, namely

$$\int_V \int_{\Phi_{t,t_0}(U)} \hat{c}(t,x,s)\,ds\,dx = \int_V \int_U \hat{c}(t_0,x,s)\,ds\,dx - \int_{t_0}^{t} \int_{\partial V} \int_{\Phi_{t',t_0}(U)} \hat{F}(t',x,s)\cdot \mathfrak{n}(x)\,ds\,d\sigma(x)\,dt' + \int_{t_0}^{t} \int_V \int_{\Phi_{t',t_0}(U)} \hat{S}(t',x,s)\,ds\,dx\,dt'\,, \tag{1.10}$$

where $\Phi_{t,t_0}(U)$ is the image of U by Φ_{t,t_0}, ∂V is the boundary of V, $\mathfrak{n}(x)$ is the normal vector, and $d\sigma(x)$ is the surface measure on this boundary. Performing a change of variables in the left hand side of (1.10) we get

$$\int_{\Phi_{t,t_0}(U)} \hat{c}(t,x,s)\,ds = \int_U \hat{c}(t,x,\Phi_{t,t_0}(s))J_{t,t_0}\,ds\,, \tag{1.11}$$

where $J_{t,t_0} = |\det \frac{d\Phi_{t,t_0}}{ds}|$ is the Jacobian determinant.

Using Stokes theorem and the first fundamental theorem of calculus in (1.10) and further using (1.11) it follows that

$$\int_V \int_U \frac{d}{dt}[\hat{c}(t,x,\Phi_{t,t_0}(s))J_{t,t_0}]\,ds\,dx = -\int_V \int_{\Phi_{t,t_0}(U)} \nabla_x \cdot \hat{F}(t,x,s)\,ds\,dx + \int_V \int_{\Phi_{t,t_0}(U)} \hat{S}(t,x,s)\,ds\,dx. \tag{1.12}$$

After changing the structure variables in the two integrals in the right hand side of (1.12) we get

$$\frac{d}{dt}[\hat{c}(t,x,\Phi_{t,t_0}(s))J_{t,t_0}] = -\nabla_x \cdot \hat{F}(t,x,s)J_{t,t_0} + \hat{S}(t,x,s)J_{t,t_0}. \tag{1.13}$$

Using $\frac{1}{J}\frac{dJ}{dt} = \nabla_s \cdot \Psi(s, c(t,x), m(t,x), v(t,x))$, from (1.13) we obtain the

Liouville equation

$$\frac{\partial \hat{c}(t,x,s)}{\partial t} = -\nabla_s \cdot (\hat{c}(t,x,s)\Psi(s, c(t,x), m(t,x), v(t,x))) - \nabla_x \cdot \hat{F}(t,x,s) + \hat{S}(t,x,s). \tag{1.14}$$

Comparing this result to (4.3) it follows that the structural fluxes $\hat{G}$, $\hat{H}$, $\hat{K}$ are advection fluxes

$$\hat{G} = \hat{c}\Psi_\xi(\xi, y, \alpha; c(t,x), m(t,x), v(t,x)), \tag{1.15}$$

$$\hat{H} = \hat{c}\Psi_y(\xi, y, \alpha; c(t,x), m(t,x), v(t,x))), \tag{1.16}$$

$$\hat{K} = \hat{c}\Psi_\alpha(\xi, y, \alpha; c(t,x), m(t,x), v(t,x)), \tag{1.17}$$

where Ψ_ξ, Ψ_y, Ψ_α are the components of the vector Ψ on the directions ξ, y, α, respectively.

1.3 Deriving Relevant Source Terms for Intricate Replicative Dynamics

1.3.1 Derivation of a Structural Source Term for Systems with Receptors

We proceed similarly to derive the source term in the case when the dynamics of the receptors is also accounted for. Consider again that mitosis is a time dependent process that occurs on a normalised micro-temporal scale, $\tau \in [0, 1)$ and that we have uniform splitting of the receptors on the cell surface during cell differentiation, at a given spatio-temporal node (t, x). Then the amount of cells whose receptoral-binding structure reside within an arbitrary rectangle $V \times W \in \mathcal{P}$ is given by the difference between the cells that arrived within $V \times W$ due to mitosis and those that leave $V \times W$ through mitosis, which can be

expressed as

$$\int_{V\times W} \hat{S}(t,x,\xi,y,\alpha)\,d(\xi,y) = 2\int_{[0,1)}\int_{(2-\tau)V\times W} \phi((\tilde{\xi},\tilde{y}),c,v)\hat{c}(t,x,\xi,\tilde{y},\alpha)\,d(\tilde{\xi},\tilde{y})\,d\tau - \int_{V\times W} \phi((\xi,y),c,v)\hat{c}(t,x,\xi,y,\alpha)\,d(\xi,y). \tag{1.18}$$

This equation can be understood as follows: We are considering extensive structure variables that, during the cell cycle, follow the cell volume homothetically; after symmetric mitosis they split, in half, their values. The decision to commit to mitosis, however, is not taken at maximum volume but before. Let us denote by $\phi((\xi,y),c,v)$ the growth rate, representing the birth probability or equivalently the probability to commit to mitosis. The growth rate is not necessarily constant, as the decision to commit to mitosis generally depends on the cell increasing its structure variables. After the decision to commit to mitosis the cell continues to grow and at the termination of mitosis it splits into two equal daughter cells. Then, letting $\tau \in [0,1]$ be a normalised variable describing the cell cycle progression at the microscale. At macroscopic time t two cells having structure variables in $V\times W$ originate from a mother cell with structure variables in $(2-\tau)V\times W$ at the microscale moment when the mother cell took the decision to commit to mitosis (this justifies the factor 2 in the positive source terms). This domain is $V\times W$ when the mitotic decision was taken at the beginning of the cell cycles, or $2V\times W$ when the decision was taken at the end. Our choice to cover the entire $[0,1]$ interval was dictated by regularity requirements, in reality the mitotic decision is taken within a smaller interval. Let us note that more complex source terms can be considered. For instance, instead of symmetric mitosis one may consider asymmetric mitosis. In this case, a second micro-scale variable can be used to describe the fragmentation process; a second integration with respect to a probability measure describing the distribution of this variable is then needed. Furthermore, structure variables can be extensive and not proportional to the cell volume. We should in this case consider a different micro-scale dynamics for them instead of simple homothetic

expansion.

Using the change of variable

$$\begin{aligned}(\tilde{\xi},\tilde{y})(\xi,y) &= (2-\tau)(\xi,y)\\ d(\tilde{\xi},\tilde{y}) &= (2-\tau)\,d(\xi,y)\end{aligned} \tag{1.19}$$

we obtain

$$\begin{aligned}&\int_{V\times W}\hat{S}(t,x,\xi,y,\alpha)\,d(\xi,y)\\ &\quad= 2\int_{[0,1)}(2-\tau)^{(p+\gamma)}\int_{V\times W}\phi((2-\tau)(\xi,y),c,v)\hat{c}(t,x,(2-\tau)(\xi,y),\alpha)\,d(\xi,y)\,d\tau\\ &\qquad-\int_{V\times W}\phi((\xi,y),c,v)\hat{c}(t,x,\xi,y,\alpha)\,d(\xi,y)\\ &\quad=\int_{V\times W}2\int_{[0,1)}(2-\tau)^{(p+\gamma)}\phi((2-\tau)(\xi,y),c,v)\hat{c}(t,x,(2-\tau)(\xi,y),\alpha)\,d\tau\,d(\xi,y)\\ &\qquad-\int_{V\times W}\phi((\xi,y),c,v)\hat{c}(t,x,\xi,y,\alpha)\,d(\xi,y)\,.\end{aligned} \tag{1.20}$$

Since this relation holds for any rectangle $V\times W$, then using the standard measure theory density argument as in the 2 preceding appendix sections, we arrive at our final expression of source flux for the total population as

$$\begin{aligned}&S(t,x,\xi,y,\alpha)\\ &\qquad= 2\int_{[0,1)}(2-\tau)^{(p+\gamma)}\phi((2-\tau)(\xi,y),c,v)\hat{c}(t,x,(2-\tau)(\xi,y),\alpha)\,d\tau\\ &\qquad\quad-\phi((\xi,y),c,v)\hat{c}(t,x,\xi,y,\alpha)\,.\end{aligned} \tag{1.21}$$

1.3.2 A Reproductive Source Term for Evolutionary Dynamics

To derive the reproductive source term, $R:\mathcal{I}\times\Upsilon^2\times\mathcal{Z}$, from our modelling assumptions, we follow the procedure set out in a previous study of cellular

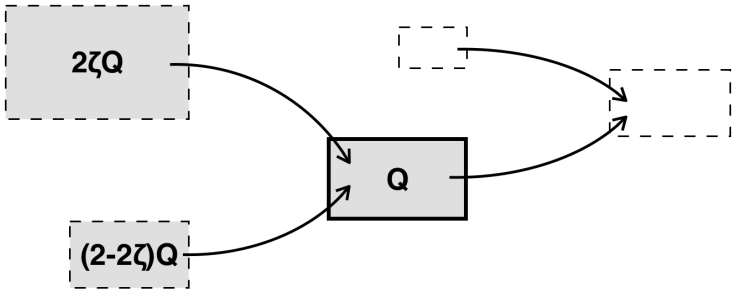

Figure 1.1: Diagram showing the creation of offspring in the set $\mathcal{Q}$ from the parental sets $2\zeta\mathcal{Q}$ and $(2-2\zeta)\mathcal{Q}$, where $\zeta \in [0,1]$.

mitotic reproduction [96]. Since we have that the resultant genetic position, z, for two parents of genetic positions, $z^{\dagger}$ and $z^{\ddagger}$, is definitionally given by the average position between these two genetic states, such that $z = \frac{1}{2}(z^{\dagger} + z^{\ddagger})$. Therefore, given the state $z \in \mathcal{Q}$, where $\mathcal{Q} \subset \mathcal{Z}$ is an arbitrary compact subset, we may say that the set $\mathcal{Q}$ is contributed to by the reproduction of pairs in subsets $2\zeta\mathcal{Q}$ and $(2-2\zeta)\mathcal{Q}$, for some $\zeta \in [0,1]$ (Fig. 1.1).

Therefore, we begin by writing that the total integral of the reproductive source term is given by the product of the unembellished female population with its choice kernel, $\kappa(\mathbf{y})$, and the indecisive male population integrated over the contributory subsets and over all values of ζ, such that

$$\begin{aligned}\iint\limits_{\mathcal{Q}\times\mathcal{Q}} & R(t,\mathbf{y},z)\,d(z,z) \\ & = \frac{\alpha}{2}\int\limits_{[0,1]}\int\limits_{(2-2\zeta)\mathcal{Q}}\int\limits_{2\zeta\mathcal{Q}}\kappa(\mathbf{y})\int\limits_{\Upsilon} f(t,\mathbf{y},z^{\dagger})\,dy_2\int\limits_{\Upsilon} m(t,\mathbf{y},z^{\ddagger})\,dy_1\,dz^{\dagger}\,dz^{\ddagger}\,d\zeta\,.\end{aligned} \tag{1.22}$$

Then, using the change of variables $z^{\dagger}(z) = 2\zeta z$, we may rewrite the above proposition as

$$\begin{aligned}\iint\limits_{\mathcal{Q}\times\mathcal{Q}} & R(t,\mathbf{y},z)\,d(z,z) \\ & = \frac{\alpha}{2}\int\limits_{[0,1]}\int\limits_{(2-2\zeta)\mathcal{Q}}\int\limits_{\mathcal{Q}}\kappa(\mathbf{y})\int\limits_{\Upsilon} 2\zeta f(t,\mathbf{y},2\zeta z)\,dy_2\int\limits_{\Upsilon} m(t,\mathbf{y},z^{\ddagger})\,dy_1\,dz\,dz^{\ddagger}\,d\zeta\end{aligned} \tag{1.23}$$

Use the change of variables $z^{\ddagger}(z) = (2-2\zeta)z$

$$\begin{aligned}&\iint\limits_{\mathcal{Q}\times\mathcal{Q}} R(t,\mathbf{y},z)\,d(z,z)\\ &= \alpha \int\limits_{[0,1]} \int\limits_{\mathcal{Q}} \int\limits_{\mathcal{Q}} 2\zeta(1-\zeta)\kappa(\mathbf{y}) \int\limits_{\Upsilon} f(t,\mathbf{y},2\zeta z)\,dy_2 \int\limits_{\Upsilon} m(t,\mathbf{y},(2-2\zeta)z)\,dy_1\,dz\,dz\,d\zeta\,.\end{aligned} \tag{1.24}$$

Using Fubini's theorem, with the observation that $f(t,\mathbf{y},z)$ and $m(t,\mathbf{y},z)$ are finite, bounded functions on the closed domain $\mathcal{I}\times\Upsilon\times\Upsilon\times\mathcal{Z}$, we have that the source term may be expressed as

$$R(t,\mathbf{y},z) = \alpha \int\limits_{[0,1]} 2\zeta(1-\zeta)\kappa(\mathbf{y}) \int\limits_{\Upsilon} f(t,\mathbf{y},2\zeta z)\,dy_2 \int\limits_{\Upsilon} m(t,\mathbf{y},(2-2\zeta)z)\,dy_1\,d\zeta\,. \tag{1.25}$$

The derivation of the latter form for this term – including mutational dynamics which cause a spreading of the reproductive solution across the domain – is much simpler. Firstly, recall that the mutational kernel, which indicates the proportion of of a given population at $(\mathbf{y}',z')$ who will be displaced to location $(\mathbf{y},z)$ in the state space, is given by $\mu(\mathbf{y},z,\mathbf{y}',z')$. Postulate a further test space, where in y may reside, such that $y\in\mathcal{W}\subset\Upsilon$. Therefore, we must integrate over the entire test domain $\mathcal{W}^2\times\mathcal{Q}$, since the final population may originate at any point in this space proportionally with $\mu(\mathbf{y},z,\mathbf{y}',z')$, and multiply this with our kernel evaluated at each such point $(\mathbf{y}',z')\in\mathcal{W}^2\times\mathcal{Q}$:

$$\begin{aligned}R(t,\mathbf{y},z) = \alpha \iiint\limits_{\mathcal{W}^2\times\mathcal{Q}} \mu(\mathbf{y},z,\mathbf{y}',z') \int\limits_{[0,1]} \Bigg[&2\zeta(1-\zeta)\kappa(\mathbf{y})\\ &\int\limits_{\Upsilon} f(t,\mathbf{y},2\zeta z)\,dy_2 \int\limits_{\Upsilon} m(t,\mathbf{y},(2-2\zeta)z)\,dy_1\Bigg]\,d\zeta\,d(\mathbf{y}',z')\end{aligned} \tag{1.26}$$

and then, simply recognise that the relationship for this arbitrary subspace $\mathcal{W}^2\times\mathcal{Q}\subset\Upsilon^2\times\mathcal{Z}$ may be extended to the entire space to achieve (5.7).

1.4 Approaches and Stability for Numerical Simulations

With the exception of the results generated through the application of pseudo-spectral, Chebyshev orthogonal polynomial-based methods in section 6.2, all of the numerical results within this manuscript generated for the higher-dimensional approaches outlined by Hodgkinson *et al.* [158, 161, 160] and in section 1.2 were obtained by the use of the following finite difference scheme:

On an atemporal basis, or for each evaluation of the right-hand side (RHS) of a given differential equation, the domain, $\mathcal{D}$ over which the solutions were to be generated was evenly divided into point-like masses with a distance of $\delta_x = \frac{1}{100}|\max(D) - \min(\mathcal{D})|$ between each adjacent point. Each of these points was treated as an individual entity throughout and for the entire duration of the solution generation. If, for example, the domain, $\mathcal{D} = [0, 1]$, were 1-dimensional then the solution was generated at the points in the domain given by $\bar{\xi} = [0, \frac{1}{100}, \frac{2}{100}, \ldots, 1]'$. Likewise, if the solution domain were 2-dimensional then the solutions would be generated across a matrix of points and were generated across a discrete tensor of points for 3- or higher-dimensional domains.

Therefore, local and non-local terms were handled very differently from one another. Local terms could be evaluated by treating the entire system of PDEs as a system of ODEs, where the RHS for any given PDE was identical to the RHS of each of the ODEs within the analogous system. Nonlocal terms, however, required operations across a distribution of discrete points within the domain. For one dimensional systems, these operations could be achieved by taking the product of the vector of discrete points and the appropriate matrix product (such as that discussed in the following subsection 1.4.1). In particular, nonlocal derivative terms were calculated using the standard central differences formula, which is known to have an error of the order $\mathcal{O}(\delta_x^2)$, with Neumann boundary conditions to guarantee no flux.

The temporal dynamics of this system were handled uniformly across all

cases and with an acute attention to detail, in terms of how the choice of scheme would affect the numerical solutions to the system. Newton stepping is know to introduce rather significant errors into any given numerical scheme and, as such, we chose to use the far more complicated but sophisticated Runge-Kutta 4 (RK4) method to move between time points of the solution. The RK4 method is so called because it is a fourth order approximation to any given initial value problem and, thusly, introduces an error on the order $\mathcal{O}(\delta_t)$, where δ_t is the length of the time step [196].

In order to further augment the accuracy of the scheme, and further guarantee the stability of the numerical scheme we choose to implement a higher level predictor-corrector method [276]. Since McCormack predictor-corrector schemes, described by the general iteration of the equations if the governing PDE is given generically by

$$\frac{\partial}{\partial t}c = F(c, \dots) \tag{1.27}$$

then given that we wish to know the value of c at a time point $\tau + 1$ (named $c^{\tau+1}$) given c^{τ} we use

$$c_*^{\tau+1} = \delta_t \cdot F(c^{\tau}, \dots), \qquad c^{\tau+1} = \frac{1}{2}(c^{\tau} + c_*^{\tau+1}) + \frac{1}{2}\delta_t \cdot F(c^{\tau+1}, \dots), \tag{1.28}$$

were deemed to give the greatest stability to biased advective systems of equations, these were used across the consecutive RK4 iterations to increase accuracy and stability [221].

1.4.1 Stability of the Central Difference Operator, J_r

In numerical analysis, the central difference operator, given by

$$J_r = \begin{pmatrix} -2 & 2 & 0 & \dots & 0 & 0 & 0 \\ -1 & 0 & 1 & \dots & 0 & 0 & 0 \\ 0 & -1 & 0 & \ddots & 0 & 0 & 0 \\ \vdots & \vdots & \ddots & \ddots & \ddots & \vdots & \vdots \\ 0 & 0 & 0 & \ddots & 0 & 1 & 0 \\ 0 & 0 & 0 & \dots & -1 & 0 & 1 \\ 0 & 0 & 0 & \dots & 0 & -2 & 2 \end{pmatrix} \tag{1.29}$$

for particular boundary conditions, and is well known to have an error of $\mathcal{O}(\delta_x^2)$. This means that it is often utilised for generating numerical solutions to PDEs, despite the fact that its stability has not yet been established in the literature. In order to assess the stability of the central difference operator J_r utilised throughout the generation of solution by means of finite difference numerical schemes, we will prove a series of technical results that will ultimately completely characterise the eigenvalues of J_r [158].

Lemma 1.4.1. *Let $\mathcal{Q}$ be the following set of polynomials with real coefficients*

$$\mathcal{Q} := \left\{ P_k(x) = a_k x^k + \cdots + a_1 x + a_0 \;\middle|\; \begin{array}{l} k \geq 4, \\ a_{k-1-2i} = 0, \ \forall i \in 0, \dots, \left[\frac{k-1}{2}\right] \end{array} \right\} \tag{1.30}$$

where by $[\cdot]$ we understand the usual integer part. Further, let $P_{N-2}, P_{N-1} \in \mathcal{Q}$ be polynomials of degree $N-2$ and $N-1$ respectively, then the iterative relation $P_N = P_{N-2} - xP_{N-1}$ gives rise to a polynomial of degree N with $P_N \in \mathcal{Q}$.

Proof. If one writes the considered polynomials as

$$P_{N-2} : a_{N-2}x^{N-2} + a_{N-4}x^{N-4} + ... + \max_{i\in\{0,...,[\frac{k-1}{2}]\}} a_{N-i-3}x^{N-i-3} = 0$$

$$P_{N-1} : a_{N-1}x^{N-1} + a_{N-3}x^{N-3} + ... + \max_{i\in\{0,...,[\frac{k-1}{2}]\}} a_{N-i-2}x^{N-i-2} = 0, \tag{1.31}$$

then the proof is trivial. □

Theorem 1.4.2. *Considering the set of polynomials $\mathcal{Q}$ defined in* (1.30)*, for any natural $N \geq 6$, let $P_N \in \mathcal{Q}$ be a polynomial of degree N such that the polynomials $P_{N-2}, P_{N-1} \in \mathcal{Q}$ that give P_N via the recurrence relation $P_N = P_{N-2} - xP_{N-1}$ satisfy the following properties:*

1) *denote $\{u_1, u_2, ..., u_{N-2}\}$ and $\{v_1, v_2, ..., v_{N-1}\}$ the ordered set of roots of the polynomials P_{N-2} and P_{N-1}, respectively*

2) *the roots of these two polynomials are only imaginary, namely:*

$$\begin{aligned} Re(u_i) &= 0 \quad \forall i \in \{1, \dots, N-2\} \\ Re(v_j) &= 0 \quad \forall j \in \{1, \dots, N-1\} \end{aligned}$$

3) *finally, the roots of these two polynomials satisfy the additional relations:*

$$v_{N-1}^2 \geq u_{N-2}^2$$

and

$$u_i^2 \geq v_i^2 \geq u_{i-2}^2 \geq v_{i-2}^2, \quad \forall i \in \{i = 2j \,|\, j \in \{1, \dots, \left[\tfrac{N-2}{2}\right]\}\},$$

where for any $i \in \{i = 2j \,|\, j \in \{1, \dots, \left[\frac{N-2}{2}\right]\}\}$ we have that $u_{j-1} := \bar{u}_j$ and $v_{j-1} := \bar{v}_j$.

Then, if we let $\{w_1, w_2, ..., w_N\}$ denote the ordered set of roots for P_N, we have that

1) *all the roots of P_N are imaginary, i.e.,*

$$Re(w_i) = 0, \quad \forall i \in \{1..N\},$$

ii) the roots of P_N and P_{N-1} satisfy the relations:

$$w_{N-1}^2 \geq v_{N-2}^2$$

and

$$v_i^2 \geq w_i^2 \geq v_{i-2}^2 \geq w_{i-2}^2, \quad \forall i \in \{i = 2j \,|\, j \in \{1, \ldots, \left[\tfrac{N-1}{2}\right]\}\},$$

where for any $i \in \{i = 2j \,|\, j \in \{1, \ldots, \left[\tfrac{N-1}{2}\right]\}\}$ we have that $w_{j-1} := \bar{w}_j$.

Proof. First, we notice that there are 2 different cases:

(1) N is even or

(2) N is odd.

Take case (1) and let $N = 2n$, $n \in \mathbb{N}$. We can use the conjugate root theorem to write the polynomials as

$$\begin{aligned} P_{N-2}(x) &= (x^2 - u_2^2)(x^2 - u_4^2)...(x^2 - u_{N-2}^2) \\ P_{N-1}(x) &= -x(x^2 - v_2^2)(x^2 - v_4^2)...(x^2 - v_{N-2}^2), \end{aligned} \tag{1.32}$$

where $u_{2i-1} = \overline{u_{2i}}$, $u_{2i}^2 = u_{2i-1} \cdot u_{2i}$ and $v_{2i-1} = \overline{v_{2i}}$, $v_{2i}^2 = -|\mathrm{Im}(v_{2i})^2|$. We then have that P_N can be written as

$$P_N(x) = (x^2 - u_2^2)(x^2 - u_4^2)...(x^2 - u_{N-2}^2) + x^2(x^2 - v_2^2)(x^2 - v_4^2)...(x^2 - v_{N-2}^2). \tag{1.33}$$

Now, by Descartes' rule of signs and Lemma 1.4.1, we can say that none of the roots of P_N are positive and that at most N of these roots are negative.

Use the substitution $z = x^2$, the initial polynomial P_N induces

$$\bar{P}_N(z) = (z - u_2^2)(z - u_4^2)...(z - u_{N-2}^2) + z(z - v_2^2)(z - v_4^2)...(z - v_{N-2}^2). \tag{1.34}$$

Evaluating $\bar{P}_N(z)$ at $\pm\infty$ and at a selection roots of $P_{N-1}(x)$ given by

$$S_a := \{v_{2j}^2 \,|\, j = 1, n-1\},$$

we have two different cases:

(1a) $n-1$ is odd or

(1b) $n-1$ is even.

In case (1a), we have that

$$\lim_{z\to\pm\infty} \bar{P}_N(z) = +\infty.$$

Further, as the elements of S_a are solutions of P_{N-1}, using their properties that $u_{2j}^2 \geq v_{2j}^2$, $j = 1, n$, we obtain

$$\bar{P}_N(v_{2j}^2) \quad = \quad (-1)^j |v_i^2 - u_2^2||v_i^2 - u_4^2|...|v_i^2 - u_{N-2}|, \qquad j = 1, n-1, \tag{1.35}$$

and so

$$\text{sign}(\bar{P}_N(v_{2j}^2)) = (-1)^j, \qquad j = 1, n-1$$

Therefore, denoting $S_a' := \{-\infty\} \cup S_a \cup \{+\infty\}$, we have

$$\text{sign}(\bar{P}_N(S_a')) \quad = \quad \{+, -, +, -, ..., -, +\}, \tag{1.36}$$

which yields n intervals where the values of polynomial changes, and so by Intermediate Value Theorem we must have n real non-positive roots for $\bar{P}_N(z)$. Thus, reversing now the change of variable $z = x^2$, we obtain that the initial polynomial $P_N(x)$ has only imaginary roots with

$$\text{Re}(w_i) = 0 \quad with \quad w_i \geq v_i, \quad i = 1, N$$

For case (1b), we have that

$$\lim_{z\to\pm\infty} \bar{P}_N(z) = \pm\infty$$

Further, denoting by with S_b the following set of squares of the roots of $P_{N-2}(x)$,

namely

$$S_b := \{u_{2j}^2 \,|\, j = 1, n-1\},$$

$$\text{sign}(\bar{P}_N(u_{2j}^2)) = (-1)^{n-j}, \quad j = 1, n-1$$

Therefore, denoting $S_b' := \{-\infty\} \cup S_b \cup \{+\infty\}$, we have

$$\text{sign}(\bar{P}_N(S_b')) \quad = \quad \{-, +, -, +, ..., -, +\}, \tag{1.37}$$

and by the Intermediate Value Theorem, we again get $\text{Re}(w_i) = 0$ with $w_i \geq v_i$.

For case (2), we consider odd values of N and let $N = 2n + 1$, $n \in \mathbb{N}$ such that we again use the conjugate root theorem to write

$$\begin{aligned} P_{N-2}(x) &= -x(x^2 - v_2^2)(x^2 - v_4^2)...(x^2 - v_{N-2}^2) \\ P_{N-1}(x) &= (x^2 - u_2^2)(x^2 - u_4^2)...(x^2 - u_N^2) \\ P_N(x) &= -x(x^2-u_2^2)(x^2-u_4^2)...(x^2-u_{n-2}^2) - x(x^2-v_2^2)(x^2-v_4^2)...(x^2-v_N^2). \end{aligned} \tag{1.38}$$

Further, factoring out the common multiple $-x$ and using the substitution $z = x^2$ to augment the remainder of the polynomial, we can now test the polynomial with the set, S', in the same way as in case (1). □

Theorem 1.4.3. *Assuming that N is the number of discretisation points and $N \geq 6$, the characteristic polynomials $P_N(\lambda)$ of the central differences matrices J_N satisfy the following recurrence relation*

$$P_N(\lambda) = P_{N-2}(\lambda) - \lambda P_{N-1}(\lambda).$$

Proof. Let's denote P_N is the characteristic polynomial of the $N \times N$ dimensional central differences matrix, J_N, we observe first that desired the recurrence relation $P_N = P_{N-2} - \lambda P_{N-1}$ is trivially satisfied by the characteristic polyno-

mials of J_4, J_5, and J_6, which are given by

$$\begin{aligned} P_4 &= \lambda^4 + \lambda^2 \\ P_5 &= -\lambda^5 - 2\lambda^3 \\ P_6 &= \lambda^6 + 3\lambda^4 + \lambda^2 \,. \end{aligned} \tag{1.39}$$

To prove that this relation is satisfied in general for any natural number $N \geq 6$, we proceed as follows. First, $\forall l \in \mathbb{N} \setminus \{0,1,2,3\}$, for the matrix $\hat{J}_l := J_l - \lambda I_l$, and let us denote by A^o_l and A'_l the following determinants of the $(l-1)\times(l-1)$ submatrices of $\hat{J}_l$, namely

$$\begin{aligned} A^o_{l-1} &= \begin{vmatrix} \hat{J}_{2,2} & \hat{J}_{2,3} & \hat{J}_{2,4} & \dots & \hat{J}_{2,l} \\ \hat{J}_{3,2} & \hat{J}_{3,3} & \hat{J}_{3,4} & \dots & \hat{J}_{3,l} \\ \hat{J}_{4,2} & \hat{J}_{4,3} & \hat{J}_{4,4} & \dots & \hat{J}_{4,l} \\ \vdots & \vdots & \vdots & \dots & \vdots \\ \hat{J}_{l,2} & \hat{J}_{l,3} & \hat{J}_{l,4} & \dots & \hat{J}_{l,l} \end{vmatrix}, \\ A'_{l-1} &= \begin{vmatrix} \hat{J}_{2,1} & \hat{J}_{2,3} & \hat{J}_{2,4} & \dots & \hat{J}_{2,l} \\ \hat{J}_{3,1} & \hat{J}_{3,3} & \hat{J}_{3,4} & \dots & \hat{J}_{3,l} \\ \hat{J}_{4,1} & \hat{J}_{4,3} & \hat{J}_{4,4} & \dots & \hat{J}_{4,l} \\ \vdots & \vdots & \vdots & \dots & \vdots \\ \hat{J}_{l,1} & \hat{J}_{l,3} & \hat{J}_{l,4} & \dots & \hat{J}_{l,l} \end{vmatrix}, \end{aligned} \tag{1.40}$$

and let's observe that these have the properties that

$$\begin{aligned} A^o_{l-1} &= -\lambda A^o_{l-2} - A'_{l-2} \\ A'_{i-1} &= -A^o_{l-2} \end{aligned} \tag{1.41}$$

Then, using (1.41) we have that

$$|\hat{J}_{N-2}| = (-2-\lambda)A^o_{N-3} - 2A'_{N-3} \tag{1.42a}$$

$$\begin{aligned} |\hat{J}_{N-1}| &= (-2-\lambda)A^o_{N-2} - 2A'_{N-2} \\ &= (-2-\lambda)(-\lambda A^o_{N-3} - A'_{N-3}) - 2(-A^o_{N-3}) \\ &= (-2-\lambda)(-\lambda)A^o_{N-3} + (2+\lambda)A'_{N-3} + 2A^o_{N-3} \\ &= ((-2-\lambda)(-\lambda)+2)A^o_{N-3} + (2+\lambda)A'_{N-3} \end{aligned} \tag{1.42b}$$

$$\begin{aligned} |\hat{J}_{N}| &= (-2-\lambda)A^o_{N-1} - 2A'_{N-1} \\ &= (-2-\lambda)(-\lambda A^o_{N-2} - A'_{N-2}) - 2(-A^o_{N-2}) \\ &= (-2-\lambda)(-\lambda(-\lambda A^o_{N-3} - A'_{N-3}) - (-A^o_{N-3})) + 2A^o_{N-2} \\ &= (-2-\lambda)(-\lambda(-\lambda A^o_{N-3} - A'_{N-3}) - (-A^o_{N-3})) + 2(-\lambda A^o_{N-3} - A'_{N-3}) \\ &= (-2-\lambda)(-\lambda)^2 A^o_{N-3} + (-2-\lambda)(-\lambda)A'_{N-3} + (-2-\lambda)A^o_{N-3} \\ &\qquad - 2\lambda A^o_{N-3} - 2A'_{N-3} \\ &= ((-2-\lambda)(-\lambda)^2 + (-2-\lambda) - 2\lambda)A^o_{N-3} + ((-2-\lambda)(-\lambda) - 2)A'_{N-3} \end{aligned} \tag{1.42c}$$

From (1.42a)-(1.42c) we obtain immediately by direct calculation that

$$|\hat{J}_N| = |\hat{J}_{N-2}| - \lambda|\hat{J}_{N-1}| \tag{1.43}$$

which can finally be equivalently expressed as

$$P_N(\lambda) = P_{N-2}(\lambda) - \lambda P_{N-1}(\lambda). \tag{1.44}$$

□

Therefore, we finally obtain the following central result for our analysis.

Theorem 1.4.4. *The eigenvalues of the central differences matrix J_r are either*

0 or imaginary.

Proof. Using Theorem 1.4.3 we have that the characteristic polynomial of J_r is given by $P_r(\lambda)$ and that $u_i^2 \geq v_i^2 \geq u_{i-2}^2 \geq v_{i-2}^2$ for all $i \in \{i = 2j \,|\, j \in \{1, \ldots, \left[\frac{r-2}{2}\right]\}\}$. Then, by invoking Theorem 1.4.2, we immediately obtain by induction that the roots, denoted w_i, of characteristic polynomial of J_r are imaginary with $\mathrm{Re}(w_k) = 0$, $\forall k \in \{1, ..., r\}$. □

1.4.2 Calculation of Numerical Ball Integrals and Associated Errors

The primary mathematical operator for which we require a novel numerical instrument is that of the ball integral around a given discrete grid point $f_{i,j}$. Assume, firstly, that $d = 2$ such that we are calculating the ball integral on a 2-dimensional plane. Given a sensing radius $r : [0, 2\pi) \to \mathbb{R}_+$ and a spatial discretisation step of δ, we assume that this radius fall within the interval $r \in [\frac{1}{\sqrt{2}}\delta, \frac{3}{2}\delta]$ such that it captures at least the totality of the grid region $[f_{i,j} - \frac{1}{2}\delta, f_{i,j} + \frac{1}{2}\delta]^2$ and does not extend beyond the regions described by the adjacent points $f_{i-1,j}$, $f_{i+1,j}$, $f_{i,j-1}$, $f_{i,j+1}$ (Fig. 1.2). Then we divide this ball into three separate groups of subregions given by 4 'axial' regions who are situated along one of the major axes, whose body is defined by the adjacent grid points to $f_{i,j}$, and whose area is denoted A_a (Fig. 1.2, *blue*); 4 'bowed' regions who are situated in the corners of the ball with only three vertices, whose body is defined by the diagonal grid points to $f_{i,j}$, and whose area is denoted A_b (Fig. 1.2, *red*); and 1 'central' region who is situated in the centre of the ball, whose body is defined by the central point $f_{i,j}$, and whose area is denoted A_c (Fig. 1.2, *green*). The numerical integral for any given one of these subregions is then approximated by taking the value of the function f at the centre of mass for the given region (where a linear interpolation to this point would analogise to the trapezoidal method), multiplied by the area of the region.

The area of the axial regions, then, may be calculated as the sum of two integrals; that of the rectangular segment and that of the arched segment. Firstly,

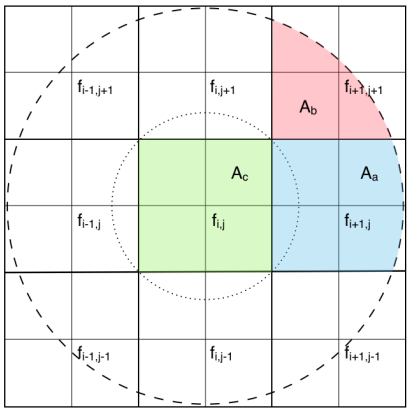

Figure 1.2: Components involved in the calculation of the ball integral, centred at the point $f_{i,j}$ for sensing radii of $r \in [\sqrt{2}\delta, \frac{3}{2}\delta]$, where balls at the upper (- - -) and lower ($\cdot\ \cdot\ \cdot$) bounds of this interval are shown. The region can be split into three separate groups of subregions; axial (*blue*), bowed (*red*), and central (*green*).

the rectangular interval over the region between the point $\frac{1}{2}\delta$ and that where the circle intersects with the perpendicular line at a distance of $\frac{1}{2}\delta$ (Fig. 1.2). The arched segment's integral is then calculated by integrating between this same point of intersection and the distance of the arc from the centre of the ball, $\sqrt{r^2 - x^2}$. Thusly, we have

$$\begin{aligned} A_a &= \int_{-\frac{1}{2}\delta}^{\frac{1}{2}\delta} \int_{\sqrt{r^2-\frac{1}{4}\delta^2}}^{\sqrt{r^2-x^2}} 1\, dy\, dx + \int_{-\frac{1}{2}\delta}^{\frac{1}{2}\delta} \int_{\frac{1}{2}\delta}^{\sqrt{r^2-\frac{1}{4}\delta^2}} 1\, dy\, dx \\ &= \left[\frac{1}{2}r^2(z + \frac{1}{2}\sin 2z)\right]_{z=\sin^{-1}\left(-\frac{\delta}{2r}\right)}^{z=\sin^{-1}\left(\frac{\delta}{2r}\right)} - \frac{1}{2}\delta^2\,. \end{aligned} \tag{1.45}$$

The bowed region, however, has only one arched integral to be computed between $\frac{1}{2}\delta$ and the arc distance in each dimension, x and y, so that it is given by

$$\begin{aligned} A_b &= \int_{\frac{1}{2}\delta}^{\sqrt{r^2-\frac{1}{4}\delta^2}} \int_{\frac{1}{2}\delta}^{\sqrt{r^2-x^2}} 1\, dy\, dx \\ &= \left[\frac{1}{2}r^2(z + \frac{1}{2}\sin 2z)\right]_{\sin^{-1}\left(\frac{\delta}{2r}\right)}^{\sin^{-1}\left(1-\frac{\delta^2}{4r^2}\right)^{\frac{1}{2}}} - \frac{1}{2}\delta\sqrt{r^2 - \frac{1}{4}\delta^2} + \frac{\delta^2}{4}\,. \end{aligned} \tag{1.46}$$

It is entirely trivial to give the area of the central region but we present it here for completeness:

$$A_c = \delta^2 \,. \tag{1.47}$$

In the case of the axial and bowed regions, also, we have an additional assumption that must be accounted for; we assume that the value of the function, f, across any given region is uniform, constant. This assumption may surely only be substantiated so long as we at least reframe the assumption to say that the considered value at f is considered an average across the region. Then, we must at least endeavour to calculate the value of the function at the centre of mass (assuming uniform density) for the region. The centre of mass for the axial region is given by

$$\begin{aligned} CM_a &= \frac{1}{A_a} \int_{\frac{1}{2}\delta}^{r} \int_{\frac{1}{2}\delta}^{\sqrt{r^2-x^2}} y \, dy \, dx \\ &= \frac{1}{A_a} \int_{\frac{1}{2}\delta}^{r} \frac{1}{2}(r^2 - x^2) - \frac{1}{8}\delta^2 \, dx \\ &= \frac{1}{A_a} \left(\frac{1}{2} r^2 - \frac{1}{8}\delta^2 \right) \left(r - \frac{1}{2}\delta \right) - \frac{1}{24 A_a} \left(r - \frac{1}{2}\delta \right)^3 . \end{aligned} \tag{1.48}$$

Similarly, the centre of mass for the bowed region is given by

$$\begin{aligned} CM_b &= \frac{1}{A_b} \int_{\frac{1}{2}\delta}^{\sqrt{r^2-\frac{1}{4}\delta^2}} \int_{\frac{1}{2}\delta}^{\sqrt{r^2-x^2}} y \, dy \, dx \\ &= \frac{1}{A_b} \int_{\frac{1}{2}\delta}^{\sqrt{r^2-\frac{1}{4}\delta^2}} \frac{1}{2}(r^2 - x^2) - \frac{1}{8}\delta^2 \, dx \\ &= \frac{1}{A_b} \left(\frac{1}{2} r^2 - \frac{1}{8}\delta^2 \right) \left(\sqrt{r^2 - \frac{1}{4}\delta^2} - \frac{1}{2}\delta \right) - \frac{1}{24 A_b} \left(\sqrt{r^2 - \frac{1}{4}\delta^2} - \frac{1}{2}\delta \right)^3 . \end{aligned} \tag{1.49}$$

Now, if we assume that we are given the biologically determined parameter, r, which defines the sensing radius of a given cell, for example, then we should

choose to implement the numerical scheme such that $\delta := \frac{2}{3}r$. Assuming that we do so, we can substitute this value into A_a and achieve an approximation for the area of the axial regions:

$$\begin{aligned}\tilde{A}_a &= \left(\frac{3}{2}\delta\right)^2\left(\sin^{-1}\frac{1}{3} + \frac{1}{2}\sin\left(2\sin^{-1}\frac{1}{3}\right)\right) - \frac{1}{2}\delta^2 \\ &\approx 0.9717\delta^2\,.\end{aligned} \tag{1.50}$$

Likewise, substituting our value for δ into the relation for the bowed regions, we arrive at

$$\begin{aligned}\tilde{A}_b = &\frac{1}{2}\left(\frac{3}{2}\delta\right)^2\left(\sin^{-1}\frac{2\sqrt{2}}{3} + \frac{1}{2}\sin\left(2\sin^{-1}\frac{2\sqrt{2}}{3}\right)\right) \\ &- \frac{1}{2}\left(\frac{3}{2}\delta\right)^2\left(\sin^{-1}\frac{1}{3} + \frac{1}{2}\sin\left(2\sin^{-1}\frac{1}{3}\right)\right) - \frac{\sqrt{2}\delta^2}{4} + \frac{\delta^2}{4} \\ &\approx 0.5454\delta^2\,.\end{aligned} \tag{1.51}$$

Moreover, it is worth noting that the substitution of $\delta := \frac{2}{3}r$ into the relation for the centre of mass for the axial regions yields $CM_a = \frac{23}{24}\delta$, which is sufficiently close to δ so that the function value may be approximated thereon. Given all of these constraints and relationships, we may then write the total ball intergal as being given by

$$\begin{aligned}I_B = &\tilde{A}_c f_{i,j} + \tilde{A}_a\left(f_{i-1,j} + f_{i+1,j} + f_{i,j-1} + f_{i,j+1}\right) \\ &+ \tilde{A}_b\left(f_{i-1,j-1} + f_{i-1,j+1} + f_{i+1,j-1} + f_{i+1,j+1}\right)\,.\end{aligned} \tag{1.52}$$

Chapter 2

Modelling Urokinase Plasminogen Activator (uPA) Dynamics in Breast Cancer

2.1 Introduction to Spatio-Structuro-Temporal Modelling for the uPA System

Cancer is primarily a multi-facetted mistake in the cell's ability to regulate its own proliferation but is perhaps most devastating due to its ability to invade the local stroma and become increasingly difficult to excise from the patient. In order to invade the surrounding tissue, the cancer cell will employ several strategies, stemming from their dysregulation, including the production of matrix-metalloproteinases (MMPs); the alteration of cell morphology, to squeeze through unusually small passages between cells; and the direct degradation of the extra-cellular matrix (ECM) through any means available to it. We

begin [158] by employing our spatio-structuro-temporal framework to explore a system set out in several previous studies [57, 96].

This particular biological system, important to cancer invasion, has received an increase attention in recent years and has been termed the urokinase plasminogen activator (uPA) system [264, 301, 268]. The uPA protein has long been noted as a marker of various cancer types, such as colorectal, gastric, œsophageal, lung, cervical, ovarian, renal, pancreatic, and hepatocellular, with its greatest prognostic evidence being derived from strains of breast cancer [100]. The reduction in uPA expression in peritumoural tissue also causes this protein to be of great clinical significance, such that expression remains localised to the cancerous tissue [34, 206].

Urokinase plasminogen activator receptor (uPAR) is a protein anchored to the cell surface and, bound with high affinity to uPA [309], aids the degradation of the extra cellular matrix (ECM) [192, 207]. X-ray analysis of the uPA-uPAR complex has revealed that uPA binds its receptor on a subsurface encapsulated by all three of its major interactive domains [168, 24]. Neither uPAR nor unbound uPA are intrinsically active within the human tissue due to their folding being unfavourable to binding plasminogen, until formation of the uPA-uPAR complex [104]. However, regardless the biological paradigm, uPA retains its high specificity for plasminogen [283].

Further to this, the binding structure of these proteins allows the binding regions of the uPAR protein to become available for plasminogen protein interactions. Moreover, bound uPA is susceptible to being further bound by the class of inhibitory proteins referred to as uPA inhibitor-1 (uPAI-1). The ability of the cell to advantageously manipulate its environment and achieve local dominance, is further altered by this chemical adaptation. This process is mediated through changes to cellular capabilities when bound to activated uPA-uPAR complexes, enabling greater survival, adhesion, and migration [36]. It has been shown that even modest increases in the presence of this surface-bound complex are sufficient to greatly increase the prolific and proteolytic activities of invasive tumour cells [307].

The cancer invasive process is further augmented through integrin-mediated signalling pathways utilised by the uPA-uPAR complex [185]. Perhaps most significant is the activation of the protein class known as $\alpha 5 \beta 1$ integrin, which actively recruits the epidermal growth factor receptor (EGFR), an upstream signalling protein whose presence has been an indicator for high levels of extracellular signal-regulated kinases (ERKs) [210]. As an essential upregulator of mitotic activity in cancerous cells, ERKs enhance the proteolytic dynamics of the cancer cell population [61].

Furthermore, the complex formed between uPA and uPAR also increases the avidity of uPAR for vitronectin, an important protein for cell-ECM adhesion [336]. Vitronectin is a protein found primarily within plasma or deposited within the ECM, where it weakly binds the intra-matrix vitronectin receptor [339]. The unbound receptor, uPAR, will further selectively bind vitronectin and increase cellular adhesion to the ECM [335] whereas bound uPAR is an exceptionally high affinity receptor for vitronectin [339, 335].

Cancer cells migration is enhanced through the downstream synthesis of matrix metalloproteinases (MMPs), after the activation of conformal pro-MMP proteins by locally activated plasminogen, which degrade the ECM and enable local tumour invasion [74]. The growth of the tumour, however, then activates a negative feedback loop through the downstream upregulation of PAI-1 synthesis [125, 204].

There is significant evidence that proteolytic enzymes (which degrade the collagen of the ECM) can be activated by an increased presence of activated plasminogen [224, 73]. Primarily, the function of uPA is the conversion of plasminogen to plasmin; known to be a key regulator of these proteolytic proteins [73]. In this context, matrix metalloproteinase 2 (MMP2) is a major target for plasmin, causing increased degradation of the ECM and incorporation of the degraded collagen into localised plaques [265, 224].

Finally, a specifically prolific feature of the the uPA-uPAR complex (in relation to with its environment) is that in its active conversion of plasminogen to plasmin it encourages the production of the proenzyme single-chain uroki-

nase plasminogen activator (scuPA). This scuPA protein is the precursor of uPA and therefore closes a positive feedback loop which is integral to the success of cancer cells in their invasive pursuit [36]. Plasmin is also capable of activating scuPA by cleaving a bond named Lys158 [283], contributing to the feedback mechanism. There is mounting evidence that the majority of these feedback mechanisms are localised to the cancer's invading edge [336, 74].

2.2 Computational Approaches and Analysis for a Spatio-Structural-Temporal Invasive Carcinoma Model

2.2.1 Description and Brief Justification of the Mathematical System

Based upon the biological evidence discussed so far, it is therefore crucially important to account for the molecular binding of the uPA components in modelling cancer dynamics. To that end, the general modelling approach introduced in Domschke *et al.* [97], where a novel spatio-temporal-structural model was derived for a general tissue dynamics involving of cells, ECM, and several accompanying populations of potentially membrane binding molecules, offers therefore an appropriate framework.

The model proposed by Domschke *et al.* [97] is a recent advancement within the well established area of a structured population modelling, uniquely utilising the structural dynamics to describe spatio-chemical-temporal processes in the tumour cell population. With a history stretching over almost six decades, however, structured-population models address a whole range of research challenges arising across many bio-medical and ecological areas, including epidemiology, collective movement either within cell population (such as those in cancer invasion or embryogenesis) or within social crowd dynamics. Varying in scope and purpose, these range from temporal-structural approaches (where space

is ignored, and time is coupled for instance with "age" or "size" structure) [316, 317, 298, 139, 91, 194, 140, 141, 320, 90, 92, 175, 49, 285, 70, 27, 60], to spatio-structural models were (where time is ignored) [137, 220, 93, 115, 169, 282, 198, 199, 21, 83, 11], and finally to more complex approaches that couple time, space, and structure [89, 45, 198, 109, 302, 8, 71, 87, 97, 318]. Specifically, important examples of structured approaches in cancer modelling include size-structured models [138] (which account for cell size in order to understand cell cycle dynamics), age-structured models [33, 101, 102] (which account for the age distribution of the population), as well as more specific models taking into account various other aspects such as RNA content [187], mutational state [85, 214, 86], popular altruism [166] and more. For a more extensive introduction to and analysis of these structured cancer development models, one may refer to the review papers by Bellomo *et al.* [31, 30] as well as to a number of relevant books on this topic [4, 70, 269, 225].

Thus, adopting here the notations from Domschke *et al.*[97], in this paper we propose appropriate computational approaches and resulting simulation alongside associated analysis to explore the spatio-temporal-structural modelling of a cancerous tissue consisting of:

- a structured cancer cell density $c(t, x, y)$, with $(t, x, y) \in \mathcal{I} \times \mathcal{D} \times \mathcal{P}$, where $\mathcal{I} := [0, T]$ is a time interval, $\mathcal{D} \in \mathbb{R}^d$, $d = 1, 2$, is the spatial tumour domain, and $\mathcal{P} \subset \mathbb{R}^p$ is a cone of appropriate dimension $p \leq 2$ representing the set of all admissible membrane-binding structures for the uPA System;

- ECM density $v(t, x)$, with $(t, x) \in \mathcal{I} \times \mathcal{D}$;

- $q \leq 3$ components of the uPA system (uPA, PAI-1, and plasmin), which are appropriately grouped in binding and unbinding classes of molecular species represented here by $m_b := [m_{b,1}(t, x), \ldots, m_{b,p}(t, x)]^T \in \mathbb{R}^p$ and $m_f := [m_{f,1}(t, x), \ldots, m_{f,q-p}(t, x)]^T \in \mathbb{R}^{q-p}$, respectively.

Using on the theoretical framework derived in Domschke *et al.* [97], we explore the dynamics of a cancerous tissue of the resulting spatio-temporal-

structural uPA modelling system, which we briefly describe here as follows. Per unit time, under the presence of a cell proliferation law, we generally assume that the spatial dynamics of the cancer cell population is dictated by diffusion, chemotaxis, haptotaxis, and cell-adhesion. The molecular binding and unbinding of the uPA components (uPA or PAI-1) is accounted for in this framework[97] in terms of an appropriately derived structural cone $\mathcal{P}$ (detailed on specific cases in the following sections), and the resulting dynamics leads not only to a spatio-temporal migration but also to a structural movement of the cancer population $c(t, x, y)$. The influence of cell-adhesion over the spatial dynamics at x is considered here in non-structured fashion and, similar to other previous approaches[95, 120], this is captured via a non-local term that represents the cell-cell and cell matrix adhesion interactions within a sensing region of radius R. This non-local term is of the form

$$\mathcal{A}(t, x, y, \mathbf{u}(t, \cdot)) = \tfrac{1}{R} \int\limits_{B(0,R)} \mathbf{n}(\tilde{x}) \mathcal{K}(\parallel \tilde{x} \parallel_2) g(t, y, \mathbf{u}(t, x + \tilde{x})) \chi_D(x + \tilde{x})\, d\tilde{x} \tag{2.1}$$

where, for any $\tilde{x} \in B(0, R)$, $\mathbf{n}(\tilde{x})$ represents the unit vector pointing from x to $x + \tilde{x}$, $\mathcal{K}(\cdot)$ is a smooth spatial kernel, and the adhesion function $g(t, y, \mathbf{u}(t, x + \tilde{x}))$ accounts for the cell-cell and cell-matrix adhesion strengths S_{cc} and S_{cv}, respectively, this being given by

$$g(t, y, \mathbf{u}) \quad = \quad [S_{cc}(t) \int\limits_{\mathcal{P}} c\, dy + S_{cv}(t) v] \cdot (1 - \rho(\mathbf{u}))^+ . \tag{2.2}$$

with the convenience vector notation

$$\mathbf{u}(t, x) := \left[\int\limits_{\mathcal{P}} c(t, x, y) dy\, ,\ v(t, x) \right]^T$$

and $(\cdot)^+ := \max\{0, \cdot\}$. Furthermore, as the ECM density $v(t, x)$ is only degraded and remodelled by the cancer cells and that the unbound (free) part of the considered components of the uPA System that are produced by the cancer cells are only diffusing in the tumour domain, the structured system that is

obtained via the general modelling framework from Domschke *et al.*[97] is as follows:

$$\begin{cases} \frac{\partial c}{\partial t} &= \nabla_x \cdot \left[D_c \nabla_x c - c(1-\rho(\mathbf{u})) \left(\sum\limits_{k=1}^{q} \xi_k \nabla_x m_k + \xi_v \nabla_x v \right) + c\mathcal{A} \right] \\ & \quad -\nabla_y \cdot [(\mathbf{b}(y,\mathbf{m}) - \mathbf{d}(y))c] \\ & \quad +2^{p+1}\phi(2y,c,v)c(t,x,2y) - \phi(y,c,v)c(t,x,y) \\ \frac{\partial v}{\partial t} &= -\gamma_v^T \mathbf{r} v + \psi_v(t,\mathbf{u}) \\ \frac{\partial \mathbf{m}}{\partial t} &= \nabla_x \cdot [\mathbf{D_m} \nabla_x \mathbf{m}] - \int\limits_{\mathcal{P}} \left(\hat{\mathbf{b}}(y,\mathbf{m}) - \hat{\mathbf{d}}(y) \right) \varepsilon c(t,x,y)\, dy \\ & \quad +\psi_{\mathbf{m}}(\mathbf{u},\mathbf{r}) - \mathrm{diag}\,(\gamma_{\mathbf{m}})\,\mathbf{m}\ . \end{cases} \tag{2.3}$$

where the vector notations are used here to represent

- the molecular population of unbound (free) part of the considered components of uPA system via $\mathbf{m} := [m_b^T, m_f^T]^T$;
- the total molecular population (both bound and unbound part) of the considered components of uPA system via $\mathbf{r} := \left[\int\limits_{\mathcal{P}} y\varepsilon c(t,x,y)\, dy,\ \mathbf{m}(t,x) \right]^T$,

whereas ε stands for the ratio between cell-surface density and cancer cell density. Furthermore, to simplify the context, the cell cancer proliferation law $\phi(y,c,v)$ is chosen here to be of a non-structured logistic form, namely

$$\phi(y,\mathbf{u}) = \mu_c(1-\rho(\mathbf{u})) \tag{2.4}$$

where $\rho(\mathbf{u})$ quantifies the space occupied by the ECM and total cancer cell density

$$C(t,x) := \int\limits_{\mathcal{P}} c(t,x,y)\, dy, \tag{2.5}$$

and is defined by

$$\rho(\mathbf{u}(t,x)) := \mathfrak{v}_c C(t,x) + \mathfrak{v}_v v(t,x) \tag{2.6}$$

with $\mathfrak{v}_c$ and $\mathfrak{v}_v$ denoting the volume fraction for c and v at the same spatio-temporal point (t, x), respectively. Moreover, the ECM remodelling term $\psi_v(t, \mathbf{u})$ assumes here the volume filling form

$$\psi_v(t, \mathbf{u}) := \mu_v(1 - \rho(\mathbf{u}))^+. \tag{2.7}$$

Finally, for the uPA binding components given by $m_b := [m_{b,1}, \ldots, m_{b,p}]^T$, the cell surface binding and unbinding rates are represented here by $\mathbf{b}(y, \mathbf{m})$ and $\mathbf{d}(y)$, respectively. Therefore, since for the free components m_f we do not have any binding or unbinding, to unify the notation, we use here the extended binding and unbinding rates vectors $\hat{\mathbf{b}}(y, \mathbf{m})$ and $\hat{\mathbf{d}}(y)$ in $\mathbb{R}^q$ given by

$$\hat{\mathbf{b}}(y, \mathbf{m}) := [(\mathbf{b}(y, \mathbf{m}))^T, 0, \ldots, 0]^T \text{ and } \hat{\mathbf{d}}(y) := [(\mathbf{d}(y))^T, 0, \ldots, 0]^T.$$

The molecular source $\psi_{\mathbf{m}}$ is assumed to depend here only on $\mathbf{u}$ and the total molecular population $\mathbf{r}$ while the constant vector $\gamma_{\mathbf{m}} \in \mathbb{R}^q$ represents the natural degradation rate of $\mathbf{m}$.

The dynamics of uPA System with and without PAI-1

Assuming that a total amount M of uPAR receptors is uniformly distributed on the surface of each cancer cell, in the following we explore the form and dynamics of the spatio-temporal-structural system (2.3) when considering uPA binding and unbinding to uPAR both in the presence and in the absence of binding PAI-1 inhibitor molecules. These will result in different structural dimensionalities that will be addressed below as appropriate.

uPA System in the absence of PAI-1

The first case that we consider here accounts only for the uPA bounding and unbinding molecules while ignoring the presence of PAI-1. In this context, the total number of considered uPA System components is $q = 2$, and consists of

- a binding molecular species (*i.e.*, uPA) represented by $m_b(t, x) := m_{b,1}(t, x)$;

- a free molecular species (*i.e.*, plasmin) represented by $m_f(t,x) := m_{f,1}(t,x)$.

The amount of those uPA molecules among $m_{b,1}(t,x)$ that are exercising binding to the available uPAR receptors is denoted here with y, and represents the binding structure of the cancer cell population distributed at the spatio-temporal node (x,t). Thus, under the assumption of a certain level of membrane-binding saturation, after eventual normalisation, the collection of all the binding structures $\mathcal{P}$ is given here by the interval $[0,1]$, so the dimension of $\mathcal{P}$ is in this case $p=1$. Furthermore, after a brief calculation[97], the uPA binding rate $\mathbf{b}(y,\mathbf{m})$ is given by

$$\mathbf{b}(y,\mathbf{m}) = (1-y)m_{b,1}, \tag{2.8}$$

while the uPA unbinding rate $\mathbf{d}(y)$ has a form

$$\mathbf{d}(y) = d_{m_{b,1}}. \tag{2.9}$$

Furthermore, assuming that the unbound uPA is produced by the cancer cells $C(t,x)$ at the rate $\alpha_{m_{b,1}}$ and that plasmin is produced only by those cells which are bound by uPA at a rate $\alpha_{m_{f,1}}$, the molecular source term $\psi_{\mathbf{m}}(C,\mathbf{r})$ is given here by

$$\psi_{\mathbf{m}}(C,\mathbf{r}) = \begin{bmatrix} \alpha_{m_{b,1}} C \\ \alpha_{m_{f,1}} \int\limits_{\mathcal{P}} y\varepsilon c(t,x,y)\,dy \end{bmatrix} \tag{2.10}$$

uPA System in the presence of PAI-1

Building on the first modelling case assumed in subsection 2.2.1, we consider now a second situation in which, besides the binding uPA, also the inhibitor PAI-1 is brought into the picture, this being able to bind to cell surface-bound uPA molecules, this way inhibiting their action. In this new context, the total number of the uPA System considered is $q=3$, this consisting of

- two binding molecular species (*i.e.*, uPA and PAI-1) represented by $m_b(t,x) := [m_{b,1}(t,x), m_{b,2}(t,x)]^T$, with $m_{b,1}(t,x)$ standing for the uPA density and $m_{b,2}(t,x)$ denoting the PAI-1 inhibitor density;

- a free molecular species (*i.e.*, plasmin) represented by $m_f(t,x) := m_{f,1}(t,x)$.

While proceeding as in subsection 2.2.1 and denoting amount of those uPA molecules among $m_{b,1}(t,x)$ that are exercising binding to the available uPAR receptors is denoted here with y_1, we denote with y_2 the amount of PAI-1 receptors that binds to bound uPA, causing the inhibition of these uPA molecules. Thus, given the binging possibilities for PAI-1 onto receptor-bound uPA versus the binding possibilities of the free uPA on the uPAR receptors, it is always the case that $y_2 \leq y_1$, and so after an eventual normalisation due to reaching saturation levels of cell-surface uPA binding, we obtain that that maximal set of binding structures $\mathcal{P}$ is two-dimensional in this case and is given by $\mathcal{P} := \{(y_1, y_2) \in \mathbb{R}^2 \,|\, y_1 \in [0,1] \text{ and } y_2 \in [0, y_1]\}$. Thus, using a measure theoretical argument[97] for the binding components for the uPA and PAI-1, the vector of binding rates $\mathbf{b}(y, \mathbf{m})$ is given by

$$\mathbf{b}(y, \mathbf{m}) = \begin{bmatrix} (1-y_1)\beta_1 m_{b,1} \\ (y_1 - y_2)\beta_2 m_{b,2} \end{bmatrix} \tag{2.11}$$

and similarly, we obtain that the vector of unbinding rates $\mathbf{d}(y)$ is

$$\mathbf{d}(y) = \begin{bmatrix} (y_1 - y_2) d_{y_1} \\ y_2 d_{y_2} \end{bmatrix} \tag{2.12}$$

Assuming that the uPA density $m_{b,1}$ is produced in the presence of cells expressing uPAR (namely the total cell density C) at a rate $\alpha_{m_{b,1}}$, $m_{b,2}$ is produced in the presence of activated plasminogen (namely the plasmin density $m_{f,1}$) at a rate $\alpha_{m_{b,2}}$, and plasmin density $m_{f,1}$ is activated by cells expressing uPA density $m_{b,1}$ but not also inhibitor PAI-1 density $m_{b,2}$ at a rate $\alpha_{m_{f,1}}$, we obtain

that the molecular source term $\psi_{\mathbf{m}}$ is given by

$$\psi_{\mathbf{m}}(C,\mathbf{r}) = \begin{bmatrix} \alpha_{m_{b,1}} C \\ \alpha_{m_{b,2}} m_{f,1} \\ \alpha_{m_{f,1}} \int\limits_{\mathcal{P}} (y_1 - y_2)\varepsilon c(t,x,y)\, dy \end{bmatrix}. \tag{2.13}$$

2.2.2 Computational Approach and Analysis for the Discretisation of the Spatio-Structural-Temporal Tumour Model

Throughout this section, we consider only the case of one dimension both in space and structure for system (2.3). Thus, assuming equal spatial and structural step size $\delta_x = \delta_y$ and an equal number $r \in \mathbb{N} \setminus \{0,1,2,3\}$ of collocation points in both x and y dimensions, in the following we will proceed to discretise c, v, and $\mathbf{m}$ at any given time node $n\delta_t$, with $n \in \mathbb{N}$. At each discretised spatial location in x, let c_x^n denote the vector of the discretisation of the distribution of the cancer cell population over the structural dimension y, explicitly given by $c_x^n := [c_{x,y_1}^n, ..., c_{x,y_r}^n]^T$. Likewise, at each discretised structural location in y, let c_y^n denote the vector of the discretisation of the distribution of the cancer cell population over the spatial dimension x, explicitly given by $c_y^n := [c_{x_1,y}^n, ..., c_{x_r,y}^n]^T$. In a similar way, the spatial discretisation of the ECM concentration is denoted by $v^n := [v_{x_1}^n, \ldots, v_{x_r}^n]^T$. Further, to simplify the notation for the components of $\mathbf{m}$, in this section we will drop the indices $_b$ and $_f$ and orderly relabel the involved molecular species simply upon their position in the vector $\mathbf{m}$, namely as $\mathbf{m} = [m_1, \ldots, m_q]^T$. In this context, the discretisation of $\mathbf{m}$ is simply denoted by $\mathbf{m}^n := [(m_1^n)^T, \ldots, (m_q^n)^T]^T \in \mathbb{R}^{qr}$, with $m_i^n := [m_{i,x_1}^n, \ldots, m_{i,x_r}^n]^T$, $\forall\, i \in \{1, \ldots, q\}$.

Finally, for appropriately designed $r \times r$ diagonal matrices Γ (aimed to serve for approximating expectations of the various structurally distributed variables that are involved in system (2.3)), let us denote $C^n(\Gamma) := [C_{x_1}^n(\Gamma), ..., C_{x_r}^r(\Gamma)]^T \in$

$\mathbb{R}^r$, with each component defined by

$$C^n_{x_i}(\Gamma) \quad := \quad \tfrac{\delta_y}{2}[c^n_{x_i}]^T \Gamma [1,2,2,...,2,2,1]^T, \tag{2.14}$$

and note that for instance the total cell density is given by $C(I_r)$, where I_r is the $r \times r$ identity matrix.

Discretisation of the 1D-Spatial 1D-Structural uPA Model

The iterative time step for the cancer population equation in (2.3) is then given by

$$c^{n+1} = c^n + \delta^n_c \quad \text{with} \quad \delta^n_c = \left(A_x c^n_x + (A_y + A_\phi)\, c^n_y\right) \cdot \delta_t \tag{2.15}$$

where

$$\begin{aligned} A_x = & \quad \tfrac{1}{4\delta_x^2} J^2 + \tfrac{1}{2\delta_x} J \tilde{f} \\ \tilde{f} := & \quad \mathrm{diag}([f_1, ..., f_r]), \end{aligned} \tag{2.16}$$

with J_r being the $r \times r$ central difference derivative matrix given by

$$J_r = \begin{pmatrix} -2 & 2 & 0 & \dots & 0 & 0 & 0 \\ -1 & 0 & 1 & \dots & 0 & 0 & 0 \\ 0 & -1 & 0 & \ddots & 0 & 0 & 0 \\ \vdots & \vdots & \ddots & \ddots & \ddots & \vdots & \vdots \\ 0 & 0 & 0 & \ddots & 0 & 1 & 0 \\ 0 & 0 & 0 & \dots & -1 & 0 & 1 \\ 0 & 0 & 0 & \dots & 0 & -2 & 2 \end{pmatrix}, \tag{2.17}$$

and the components of $\tilde{f}$ being given by

$$f_i := f_i(c^n_{x_i}, v^n_{x_i}, \mathbf{m}^n_{x_i}) = \left(1 - \rho(c^n_{x_i}, v^n_{x_i})\right) \left(\sum_k \xi_k \mathrm{row}_i(J_r^2) \mathbf{m}^n_{k,x_i} + \xi_v \mathrm{row}_i(J_r^2) v^n_{x_i} \right), \tag{2.18}$$

where $\text{row}_i(J_r^2)$ indicates the i^{th} row of the matrix given by J_r^2, for all $i \in \{1, ..., r\}$. Furthermore, we have that

$$\begin{aligned} A_y = &\quad -\tfrac{1}{2\delta_y} J_r \tilde{g} \\ \tilde{g} := &\quad \text{diag}([(b_1 - d_1), ..., (b_r - d_r)]), \end{aligned} \tag{2.19}$$

where $b_i := b(\mathbf{m}^n, y_i)$ and $d_i := d(y_i)$, $\forall i \in \{1, ..., r\}$ stands for the discretised binding and unbinding rates, and

$$A_\phi = A_{\phi_y} + A_{\phi_{2y}} \tag{2.20}$$

with

$$\begin{aligned} A_{\overline{\phi_y}} = &\quad -\tilde{\phi}_y & \qquad A_{\overline{\phi_{2y}}} = &\quad 2^{P+1} \hat{I}^T \tilde{\phi}_{2y} \hat{I} \\ \tilde{\phi}_y = &\quad \text{diag}([\phi_1, ..., \phi_r]) & \qquad \tilde{\phi}_{2y} = &\quad \sum_{i=1}^{r} \phi_{2i} E_{i,2i} \qquad \hat{I} = \begin{pmatrix} I_r \\ \emptyset_r \end{pmatrix}, \end{aligned} \tag{2.21}$$

where $\emptyset_r$ is the $r \times r$ zero matrix, $E_{i,2i}$ is the standard elementary matrix; $\phi_i := \phi(y_i, c^n_{y_i}, v^n)$ and $\phi_{2i} := \phi(2y_i, c^n_{2y_i}, v^n), \forall i \in \{1, ..., r\}$.

Similarly iterative time step for the ECM equation in (2.3) is given by

$$v^{n+1} = v^n + \delta_v^n \quad \text{with} \quad \delta_v^n = (B_x v^n + \tilde{\psi}_v) \cdot \delta_t \,, \tag{2.22}$$

where

$$B_x = -\gamma_{v,c} \varepsilon \text{diag}(C^n(\tilde{y})) - \sum_{i=1}^{q} \gamma_{v,m_i} \text{diag}(m_i^n) \,, \tag{2.23}$$

with $\tilde{y} := \text{diag}([y_1, \ldots, y_r])$, the ECM degradation rates vector γ_v organised as $\gamma_v := [\gamma_{v,c}, \gamma_{v,m_1}, \ldots, \gamma_{v,m_q}]^T$. Furthermore, $\tilde{\psi}_v$ denotes here the remodelling vector given by

$$\tilde{\psi}_v := \quad [\psi_{v,1}, ..., \psi_{v,r}]^T \,, \tag{2.24}$$

where we use the reduced notation $\psi_{v,i} := \psi_v(c_i^n, v_i^n)$, $\forall i \in \{1, ..., r\}$.

Finally, the iterative time step for uPA components equation in (2.3) is given by

$$\mathbf{m}^{n+1} = \mathbf{m}^n + \delta^n_{\mathbf{m}} \quad \text{with} \quad \delta^n_{\mathbf{m}} = (D_x(\mathbf{m}^n) + D_\phi) \cdot \delta_t \,, \tag{2.25}$$

where we used the operator notation $D_x(\mathbf{m}^n) := [(D_{m_1} J_r^2 m_1^n)^T, \ldots, (D_{m_q} J_r^2 m_q^n)^T]^T$, and

$$D_{\phi_i} \quad := \psi_{m_i} - \varepsilon C^n(\tilde{g}) - \gamma_{m_i} m_i^n \tag{2.26}$$

where $\psi_{m_i} := [\psi_{m_i}(C^n_{x_1}(I_r), C^n_{x_1}(\tilde{y})), \ldots, \psi_{m_i}(C^n_{x_r}(I_r), C^n_{x_r}(\tilde{y}))]^T, \forall i \in \{1, \ldots, q\}$, where we used the operator notation $D_\phi(\mathbf{m}^n) := [D^T_{\phi_1}, \ldots, D^T_{\phi_q}]^T$.

Therefore, the first iteration of the resulting discrete *global operator* for an arbitrary discrete spatio-structural points (x, y), and time node $n = 0$, which appears when computing given by $(c^1, v^1, \mathbf{m}^1)^T$, leads to the following *relations*:

$$\begin{aligned}
\delta^0_c &= \Big(\tfrac{1}{4\delta_x^2} J_r^2 c^0_y + \tfrac{1}{2\delta_x} J_r \tilde{f} c^0_y - \tfrac{1}{2\delta_y} J_r \tilde{g} c^0_x \\
&\qquad + \Big(2^{P+1} \hat{I}^T \tilde{\phi}_{2y} \hat{I} - \tilde{\phi}_y \Big) c^0_y \Big) \delta_t \\
\delta^0_v &= \left(-\gamma_{v,c} \varepsilon \mathrm{diag}(C^n(\tilde{y})) v^0 - \sum_{k=1}^{q} \gamma_{v,m_k} \mathrm{diag}(m^n_k) v^0 + \tilde{\psi}_v \right) \delta_t \\
\delta^0_{m_k} &= \left(D_{m_k} J_r^2 m^n_k + \psi_{m_k} - \varepsilon C^0(\tilde{g}) - \gamma_{m_k} m^n_k \right) \delta_t \,.
\end{aligned} \tag{2.27}$$

The stability of the primary term in these discrete time differences is dependent upon the operator J_r, whose analysis was the focus of section 1.4.1.

Stability Analysis of the Global Numerical Scheme

Returning now to the stability analysis of the global numerical scheme associated to 1D-spatio 1D-structural case of (2.3), we will focus now only those operators occurring in (2.28) that have eigenvalues $\mathrm{Re}(\lambda) > 0$. Therefore, as J_r was proved to be stable, of interest for the stability analysis remains the behaviour of the following remainders of the operators from (2.28) without those terms involving

J_r that we indicate with $\bar{}$, namely:

$$\begin{aligned}
\bar{\delta}_c^0 &= \Big(2^{P+1}\hat{I}^T\tilde{\phi}_{2y}\hat{I} - \tilde{\phi}_y\Big)c_y^0\delta_t \\
\bar{\delta}_v^0 &= \Big(-\gamma_{v,c}\varepsilon\mathrm{diag}(C^n(\tilde{y}))v^0 - \sum_{k=1}^{q}\gamma_{v,m_k}\mathrm{diag}(m_k^n)v^0 + \tilde{\psi}_v\Big)\delta_t \\
\bar{\delta}_{m_k}^0 &= \Big(\psi_{m_k} - \varepsilon C^0(\tilde{g}) - \gamma_{m_k}m_k^n\Big)\delta_t\,.
\end{aligned} \tag{2.28}$$

We begin by assessing the stability of the structural dimension by considering the mitotic operator for the 2^{nd} and 3^{rd} such iterations on c, wherein we have:

$$\bar{\delta}_c^1 = (A_{\overline{\phi_y}} + A_{\overline{\phi_{2y}}})c_y^0\delta_t + (A_{\overline{\phi_y}} + A_{\overline{\phi_{2y}}})^2c_y^0\delta_t^2\,, \tag{2.29}$$

$$\begin{aligned}
\bar{\delta}_c^2 &= (A_{\overline{\phi_y}} + A_{\overline{\phi_{2y}}})c_y^0\delta_t + (A_{\overline{\phi_y}} + A_{\overline{\phi_{2y}}})^2c_y^0\delta_t^2 \\
&\quad +(A_{\overline{\phi_y}} + A_{\overline{\phi_{2y}}})^3c_y^0\delta_t^3\,,
\end{aligned} \tag{2.30}$$

such that the n^{th} iteration is given by

$$\bar{\delta}_c^n = \sum_{i=1}^{n+1}(A_{\overline{\phi_y}} + A_{\overline{\phi_{2y}}})^i\delta_t^ic_y^0\,. \tag{2.31}$$

The basic criterion for stability is that a small perturbation in the solution will decrease or remain constant in value through time, $t \to \infty$. Now, since in the above sum, the order of the terms (with respect to δ_t) increases with i, we can form a preliminary estimate of the perturbation's growth using only the first $i = 1$ terms, namely

$$c_{x_i,y_j}^1 = c_{x_i,y_j}^0 + \Big(-\phi_{y_j}c_{x_i,y_j}^0 + 2^{P+1}\phi_{2y_j}c_{x_i,2y_j}^0\Big)\cdot\delta_t \tag{2.32}$$

and so we get the following condition for stability

$$\phi_{y_j}c_{x_i,y_j}^n \geq 2^{P+1}\phi_{2y_j}c_{x_i,2y_j}^n\,. \tag{2.33}$$

Given that $0 \leq \phi \leq 1$, we have that for stability

$$\begin{aligned} \lim_{\delta_{y_j}\to 0}\lim_{y_j\to 0} c^n_{x_i,y_j} &= \infty, \qquad \forall n \in [0, N), \\ \lim_{\delta_{y_j}\to 0}\lim_{y_j\to \infty} c^n_{x_i,y_j} &= 0, \qquad \forall n \in [0, N). \end{aligned} \tag{2.34}$$

Further, concerning the structural dynamics, denoting now by $\bar{\bar{\delta}}^n_{c;x_i,y_j}$ the change in the cancer cell distribution c due to the y-flux of the system at a given spatio-structural position (x_i, y_j) during a time interval $[n\delta_t, (n+1)\delta_t]$, we have that

$$\begin{aligned} \bar{\bar{\delta}}^0_{c;x_i,y_j} &:= A_y c^0_y \cdot \delta_t \\ &= \left(\frac{1}{2\delta_y}(b_{y_{j-1}} - d_{y_{j-1}})c^0_{x_i,y_{j-1}} - \frac{1}{2\delta_y}(b_{y_{j+1}} - d_{y_{j+1}})c^0_{x_i,y_{j+1}} \right) \cdot \delta_t \,. \end{aligned} \tag{2.35}$$

Therefore, if we have that b, d are proportional to y, then we can extract the modified binding and unbinding rates $\bar{b}$ and $\bar{d}$ as

$$b^n_{y_j}(y_j, \mathbf{m}^n) = \bar{b}(\mathbf{m}^n) \cdot y_j \text{ and } d_{y_j}(y) = \bar{d} \cdot y_j, \tag{2.36}$$

and so we can then write

$$\bar{\bar{\delta}}^0_{c;x_i,y_j} = \left(y_{j-1} c^0_{x_i,y_{j-1}} - y_{j+1} c^0_{x_i,y_{j+1}} \right) \cdot \tfrac{1}{2\delta_y}(\bar{b}^0 - \bar{d}^0) \cdot \delta_t, \tag{2.37}$$

whose stability is ensured by having either

$$\bar{b} \leq \bar{d}, \tag{2.38a}$$

or

$$c^0_{x_i,y_{j-1}} \leq \frac{y_{y_{j+1}}}{y_{y_{j-1}}} c^0_{x_i,y_{j+1}}, \qquad \forall x_i, y_j \,. \tag{2.38b}$$

Thinking biologically about the ramifications of the former constraint, (2.38a),

this would mean that the unbinding of the molecular species involved was more frequent than the binding of these species which would imply a relationship of affinity that approaches 0. Although these exist biologically, the considered system is one in which the binding of molecular species plays a major role in the metabolic processes of the cell and one can thusly disregard (2.38a) from consideration as trivial. Therefore, we consider here only (2.38b) as viable.

From (2.33), (2.34), and (2.38b), however, we have a contradiction and therefore, the system must be unstable with neither an absolute nor a convective instability. The instability present is absolute in its source but convective in its requirement and behaviour.

For the stability of the equation in v of the discretised 1D-spatio 1D-structural system (2.3), from (2.28) we observe first that $0 \leq c^n_{x_i,y_j} \leq 1$ and $0 \leq m^n_{k;x_i,y_j}$, $\forall k \in \{1, ..., q\}$. It is then trivial to show the following eigenvalues relations

$$\begin{aligned} &\lambda_{\mathrm{diag}(c^n_{x_i,y_j})} = c^n_{x_i,y_j} \geq 0, \\ &\lambda_{\mathrm{diag}(m^n_{k;x_i})} = m^n_{k;x_i} \geq 0, \forall k \in \{1, ..., q\}, \\ &\lambda_{B_x} \leq 0 \end{aligned} \tag{2.39}$$

where $\lambda_{\mathrm{diag}(c^n_{x_i,y_j})}$ denote the eigenvalues of $\mathrm{diag}(c^n_{x_i,y_j})$, $\lambda_{\mathrm{diag}(m^n_{k;x_i})}$ are the eigenvalues of $\mathrm{diag}(m^n_{k;x_i})$, and λ_{B_x} represent the eigenvalues of B_x. Therefore, using a similar notation, since for the eigenvalues of B_ϕ, we have that $\lambda_{B_\phi} \geq 0$, given smooth solutions for c^n_x and m^n_x, we finally obtain that the solutions for v^n_x will remain smooth and stable.

Finally, using the similar eigenvalue notation, for the stability in the equations for $\mathbf{m}$, we obtain that the eigenvalues for $C^n(\tilde{g})$, δ_m and $\tilde{\psi}_m$ have the properties

$$\begin{aligned} \lambda_{C^n(\tilde{g})} &\geq 0, \\ \lambda_{\delta_{\mathbf{m}}} &= \gamma_{\mathbf{m}}, \\ \lambda_{\tilde{\psi}_{\mathbf{m}}} &\geq 0. \end{aligned} \tag{2.40}$$

Moreover, we can also observe that eigenvalues of D_ϕ have the property that

$$\lambda_{D_\phi} \leq 0 \quad \text{iff} \quad \lambda_{\tilde{\psi}_{\mathbf{m}}} \leq \gamma_{\mathbf{m}} + \varepsilon \lambda_{C^n(\tilde{g})}. \tag{2.41}$$

where for convenience we used the vector convention in writing the above inequality, which simply means that the inequality is respected per each component. Thus, we have that either (1) $\tilde{\psi}_{\mathbf{m}}$ is proportional to $\varepsilon C^n(\tilde{g})$ or (2) $\tilde{\psi}_{\mathbf{m}}$ is proportional to $C^n(I_r)$. For case (1), if we let $k_{\psi,1}$ be the proportionality constant within the relation $\psi_{\mathbf{m}}$, then we can write that there must exist some values for $C_x^n(\tilde{g})$ at which

$$\begin{aligned} k_{\psi,1}\varepsilon\lambda_{C^n(\tilde{g})} &\leq \gamma_{\mathbf{m}} + \varepsilon\lambda_{C^n(\tilde{g})} \\ (k_{\psi,1}-1)\varepsilon\lambda_{C^n(\tilde{g})} &\leq \gamma_{\mathbf{m}} \\ (k_{\psi,1}-1)\varepsilon C^n(\tilde{g}) &\leq \gamma_{\mathbf{m}}\,, \end{aligned} \tag{2.42}$$

where we used the same vector convention as in (2.41). Thus, using integration by parts, we can write

$$(k_{\psi,1}-1)\varepsilon\left(\tilde{g}C^n(I) - (\bar{b}-\bar{d})y_r C^n(I_r)\right) \leq \gamma_{\mathbf{m}}. \tag{2.43}$$

For case (2), if we let $k_{\psi,2}$ be the proportionality constant within the relation $\psi_{\mathbf{m}}$ then we can write that there must exist some values for $C^n(I_r)$ at which

$$\begin{aligned} k_{\psi,2}\lambda_{C^n(I_r)} &\leq \gamma_{\mathbf{m}} + \varepsilon\lambda_{C^n(\tilde{g})} \\ k_{\psi,2}C^n(I) &\leq \gamma_{\mathbf{m}} + \varepsilon\left(\tilde{g}C^n(I) - (\bar{b}-\bar{d})y_r C^n(I_r)\right) \\ k_{\psi,2}C^n(I_r) &\leq \gamma_{\mathbf{m}} + \varepsilon\left(\tilde{g} - (\bar{b}-\bar{d})y_r\right)C^n(I_r) \end{aligned} \tag{2.44}$$

where $\tilde{g} \geq (\bar{b}-\bar{d})y_r$. Therefore, given sufficiently large values for $C^n(I_r)$, given by

$$C^n(I_r) \leq \frac{\gamma_{\mathbf{m}}}{k_{\psi,2} - \varepsilon\left(\tilde{g} - (\bar{b}-\bar{d})y_r\right)}\,, \tag{2.45}$$

the solutions for m_i^n will be unstable with

$$\lim_{n\to\infty} m_i^n = \infty \quad \forall i \text{ where } \psi_{m_i} = \psi_{m_i}(c_x^n, \cdot)\,. \tag{2.46}$$

For sufficiently low values of $C^n(I_r)$, given by the contrary argument to (2.45), the solutions for m_i^n will be stable with $m_i^n = 0$.

2.2.3 Numerical Results and Simulations in 1D-Spatial Case

The parameters considered throughout this work are chosen to be consistent with those set out in Domschke *et al.* [97], and other previous models [120], and are detailed in 2.1.

Numerical results generated by running the test case, and finite difference scheme for the system, through MATLAB are given below (Fig. 2.1-2.9). Several different cases are simulated in order to numerically verify the validity of proposed changes to the system and in order to perform analyses of the system using numerically generated graphic results:

For the 1D-spatial, 1D-structural case the associated model (2.3), was explored numerically in the presence of initial conditions for $c(t, x, y)$ for $t = 0$, given by

$$c_0(x, y) \quad := \quad c(0, x, y) = \exp\left[-100\left(x^2 + 4(y - \tfrac{1}{4})^2\right)\right]\,, \tag{2.47}$$

and the *homogeneous* ECM conditions

$$v_0(x) \quad := \quad v(0, x) = 1 - \int_{\mathcal{P}} c(0, x, y)\, dy\,. \tag{2.48}$$

uPA in the absence of PAI-1: 1D-Spatial 1D-Structural Results

One characteristic of the numerical solution, which has not previously been observed, is that of the partial travelling wave translation in the structural

c	:	$D_c = 10^{-4}$	$\xi_v = 5 \times 10^{-2}$	$\xi_1 = 1 \times 10^{-3}$	$\mu_c = 0.1$
		$S_{cc} = 10^{-4}$	$S_{cv} = 10^{-4}$	$\mathfrak{v}_c = 0.524$	$\mathfrak{v}_v = 0.476$
i-state	:		$\varepsilon = 0.1$	$\beta = 0.5$	$\gamma_y = 0$
v	:		$\gamma_v = 10$	$\mu_v = 0.05$	
$m_{b,1}$	:	$D_{m_{b,1}} = 10^{-3}$	$\alpha_{m_{b,1}} = 0.1$	$\gamma_{m_{b,1}} = 0.1$	
$m_{b,1}$	:	$D_{m_{b,1}} = 10^{-3}$	$\alpha_{m_{b,1}} = 0.1$	$\gamma_{m_{b,2}} = 0.1$	
$m_{f,1}$	:	$D_{m_{f,1}} = 10^{-3}$	$\alpha_{m_{f,1}} = 0.5$	$\gamma_{m_{f,1}} = 0.1$	

Table 2.1: Table of parameters for use in simulating (2.3)

dimension (Fig. 2.1). That is to say that the proliferative terms lead to the travelling wave being depleted and replaced, to a greater extent at a lower value for y. These features shall be henceforth referred to as structural "y-waves" and is an essential feature in understanding the dynamics of such systems, given their recurrence in all domains. There is not sufficient evidence in the biological literature to verify that this is the case or to contradict this result.

The hyper-affinity binding also results in the behaviour of "replicative y-trapping" (referring to the behaviour of c collection at the upper y boundary as y-trapping and the proliferative duplication at $\frac{1}{2}y$ as replicative of this y-trapping) behaviour producing a discontinuity that fails to allow the system to continue the migration of c through $\mathcal{P}$ and raises significant questions of the biological efficacy of this system when coupled to assumptions of equal mitosis. Again, this results from the binding a production of these species occurring at far higher rates than the unbinding or degradation of these species.

The y-waves actually caused a resultant x-resolved profile, $C(t, x)$, which was itself not smooth (Fig. 2.1); this is a ramification of the proliferative contribution to the replication of steep gradient profiles. One must observe that, within the discrete space, the proliferative term necessarily means that any gradient is replicated with a proliferative constant, μ_c.

Further, one observes an sharp spiking behaviour that occurs only at the boundary, which can be directly observed for $t = 50$ (Fig. 2.1c). The source of this spiking is not clear, since it occurs to a lesser extent for other values of

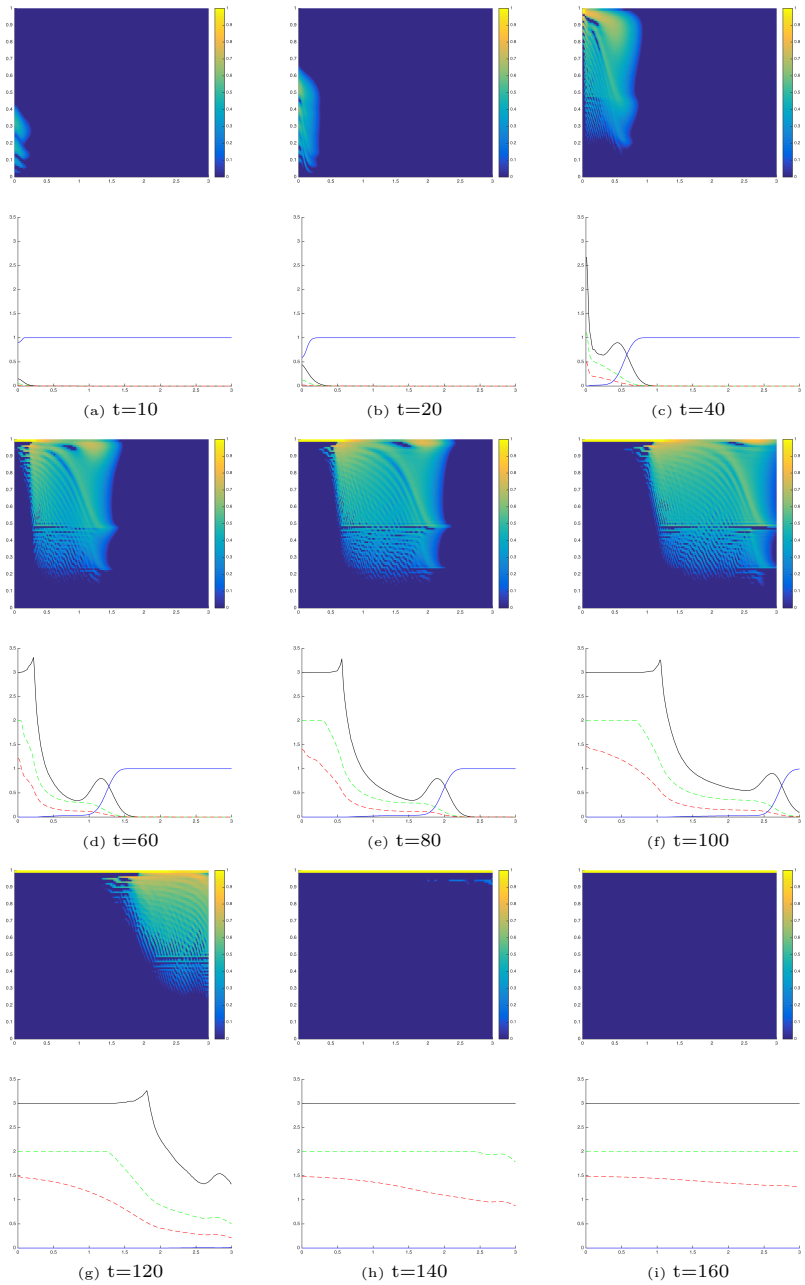

(a) t=10 (b) t=20 (c) t=40

(d) t=60 (e) t=80 (f) t=100

(g) t=120 (h) t=140 (i) t=160

Figure 2.1: Numerical 1D-spatial 1D-structural results generated from simulation of the system (2.3), with c plotted in the x- and y-dimension (*top*), with values for C (*black*), v (*blue*), $m_{b,1}$ (*green dashed*), and $m_{f,1}$ (*red dashed*) plotted spatially (*bottom*).

(t, x), but could be due to the gradient-guided dissipation occurring only one side of the spike. In other words, the accuracy of the estimate of the double derivative is lessened by the fact that the peak occurs on the boundary and one can obtain information about the local features on only one side of the peak. It is also possible that this results from the contribution of the chemotaxis to the molecular species, on the bulk of the population, and the haptotaxis, on the exterior of the population.

There exists, however, some biological evidence to corroborate this behaviour as a natural process occurring due to the difference between forces between cell-cell junctions and cell-ECM based motility. For instance, Yamaguchi *et al.* [342] report the phenomenon of differential behaviours between 'leader' and 'follower' cells during collective cell migration, often resulting in a clustered cell subpopulation leading the migration of the tumour's boundary. Likewise, *in vivo* experimentation (necessarily invoking the heterogeneity of the underlying migratory substrate) has demonstrated breakaway clusters of cells which develop anterior to the invasive front [58].

2.2.4 Numerical Results in 2D-Spatial Cases

Proceeding in a similar manner to the 1D-spatial case, also in the 2D-spatial cases, with the appropriate 1D- or 2D-structural domain $\mathcal{P}$, we we assume equal spatial and structural step size $\delta_{x_i} := \delta_{y_j} := \delta_x$, $i, j \in \{1, 2\}$ and an equal number $r \in \mathbb{N}^*$ of collocation points in both spatial and structural dimensions, and in the following we will proceed to discretise c, v, and $\mathbf{m}$ at any given time node $n\delta_t$, with $n \in \mathbb{N}$.

For the 2D-spatial 1D-structural model, numerical results have been obtained for the initial condition for $c(t, x, y)$ which are the extension of (2.47), and in this case are given by

$$c_0(x, y) := c(0, x, y) = \exp\left[-100\left(\| x \|_2^2 + 4(y - \tfrac{1}{4})^2\right)\right], \tag{2.49}$$

Furthermore, for the ECM, we use both the *homogeneous* initial conditions

given in (2.48) and a new set of *heterogeneous* initial conditions given as in [13], namely:

$$\begin{gathered}(x_1, x_2) := \tfrac{1}{3}\left(x + \tfrac{3}{2}\right) \in [0,1]^2 \text{ for } x \in \mathcal{D}\,, \quad \zeta := 6\pi, \\ h(x_1, x_2) := \tfrac{1}{2} + \tfrac{1}{2}\sin\left(\tfrac{\zeta x_1}{x_2+1}\right)\sin\left(\zeta x_1 x_2\right)\sin\left(\tfrac{\zeta(1-x_1)}{x_2+1}\right)\sin\left(\zeta(x_1-1)(x_2-1)\right), \\ v_0(x) := v(0,x) = \min\left\{h(x_1,x_2), \tfrac{1-\mathfrak{v}_c C(0,x)}{\mathfrak{v}_v}\right\}.\end{gathered} \tag{2.50}$$

Finally, for the 2D-spatial 2D-structural model, numerical results have been obtained for the appropriate extension of the initial conditions for $c(t,x,y)$ considered in (2.47) and (2.49) which in this case recast as follows:

$$c_0(x,y) := c(0,x,y) = \exp\left[-100\left(\|\,x\,\|^2 + 4\,\|\,(y - [\tfrac{1}{4},\tfrac{1}{4}]^T)\,\|^2\right)\right], \tag{2.51}$$

as well as the homogeneous and heterogeneous ECM initial conditions given in (2.48) and (2.50).

uPA in the absence of PAI-1: 2D-Spatial 1D-Structural Results

Results from the simulations were consistent with the 1D-spatial 1D-structural case but varied widely due to the effect of the ECM on the cancer species.

Results for the 2D-spatial 1D-structural system for lower binding values are given (Fig. 2.2 & 2.3). For c, the the spatial distribution of the tumour in 2-spatial dimensions and isosurface figure in a 2D-spatial 1D-structural domain (in the absence of PAI-1) are displayed to attempt to give the fullest impression of the progress of the cancer through the spatial and structural domains in time. One can see, again, the y-wave behaviour in the 2D-spatial system with mushroom-like forms replicating themselves at progressively lower values for y. A typical symmetric cancer cluster grows into the spatial domain, giving higher values for concentration at the upper boundary of $\mathcal{P}$ towards the epicentre of the cancer cluster.

In biological terms, this indicates that the more established, inner, portion of the tumour will likely have a higher bound population of molecules that

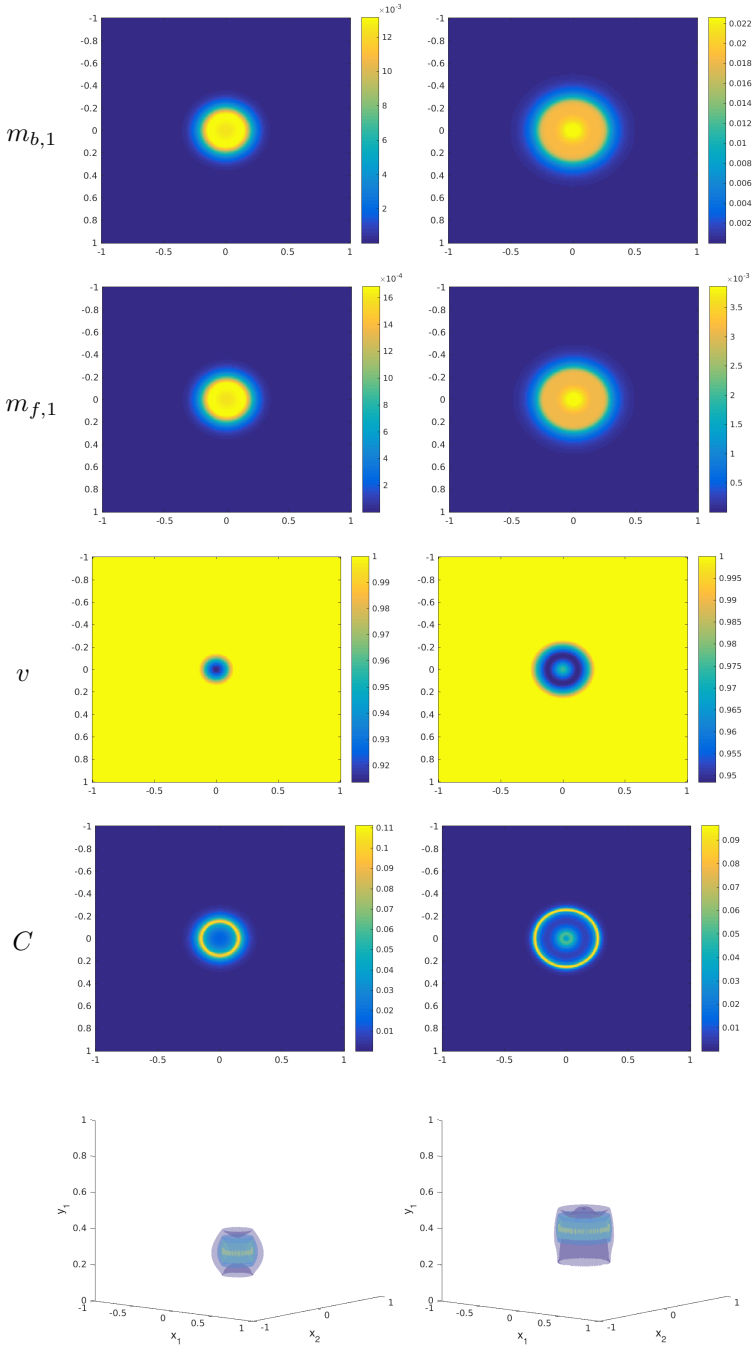

(a) t=3 (b) t=15

Figure 2.2: Numerical 2D-spatial 1D-structural results for (2.3) for homogeneous ECM, plotted at times $t \in \{3, 15\}$: $m_{b,1}$ (*row 1*), $m_{f,1}$ (*row 2*) v (*row 3*), C (*row 4*), and c (*row 5*) as an isosurface on the 2D x-plane.

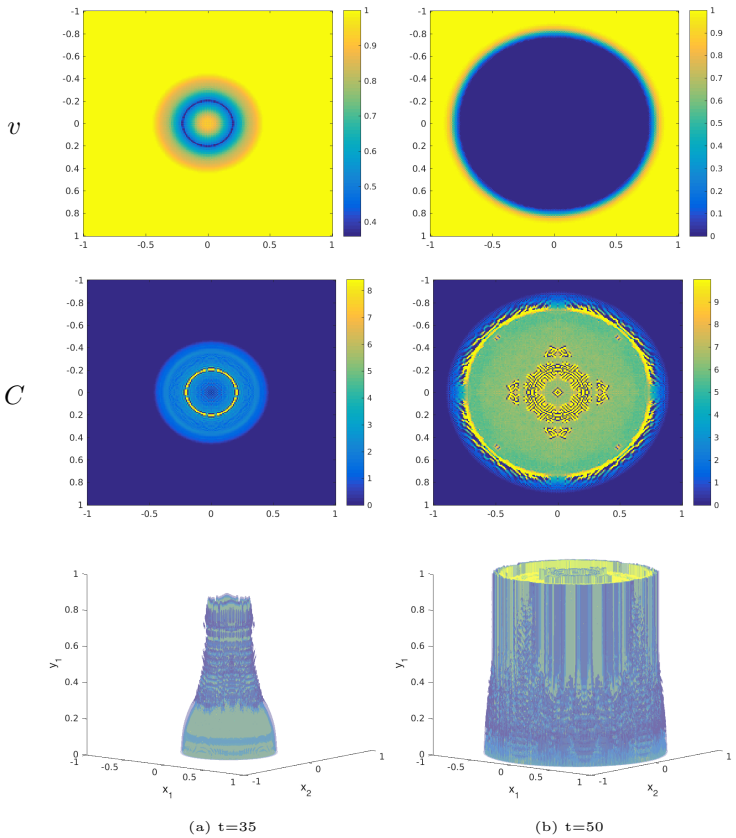

Figure 2.3: Numerical 2D-spatial 1D-structural results for (2.3) for homogeneous ECM, plotted at times $t \in \{35, 50\}$: v (*row 1*), C (*row 2*), and c (*row 3*) as an isosurface on the 2D x-plane.

the boundary, outer, portion. This result is counter-intuitive since, given that these bound species are more effective at degrading the extracellular matrix, a theoretical postulation might lead one to believe that these species would exist to a greater extent on the boundary. This is either a flaw within the application of the model or may provide an interesting observation about the efficiency of natural biological cancers.

Biological evidence does exist, on the other hand, to support the claim that both uPAR, and consequently surface bound uPA, are more highly concentrated towards the interior of invasive cell structures. Invading T lyphocytes have been reported to exhibit such internally high expression levels, with only individuated

exterior cells expressing high levels of uPARs [35]. A biological spatio-temporal model of tumour invasion reported high levels of uPA of the tumour's leading edge but also found extremely high levels on the invading mass' interior [5].

The y-waves occur within the 2D-spatial model also (Fig. 2.2–2.3), where one may observe graduated levels of binding for c. One can observe that the largest concentration of c begins and remains at the epicentre of the population.

All results show a significant correlative relationship between the ECM levels, $v(t,x)$, and the destructive molecular species, $m_{f,1}(t,x)$, and therefore a wave of ECM destruction follows closely behind the travelling wave of the cancer cell population. This is an indicator of the indirect relationship between the cancer growth mechanism and the cancer population itself (i.e. acting through the intermediate degradative protein species $m_{f,1}$).

Results generated using a heterogeneous initial ECM density (Fig. 2.4–2.6) varied from the previously observed results with similar behaviour, nonetheless. One observes the spiking behaviours developing into a particularly defined wave front for the growing cancer population. Here, the boundary wave-like solution may be caused by the high affinity between the cancer cell population and the ECM.

Although it is difficult to depict this behaviour, one again observes y-waves in the numerics for the behaviour at the interior of the cancer population. This is masked by the isosurface for the spiking shell of the cancer population. The y-waves play an important role in determining the initial behaviour of the cancer population, during growth and establishment of the perimeter. It is unclear wether these waves contribute to the dramatic change in behaviour and form $t \in (9, 15)$.

Just as in the 1D- and 2D-spatial homogeneous-ECM cases, one can observe the initial spatial splitting of the cancer population. Unlike in the homogeneous case (Fig. 2.2–2.3), however, the heterogeneity appears to mediate the consolidation of the cancer subpopulations (Fig. 2.4b–2.5b) into the characteristic tumour that one associates with the biological paradigm.

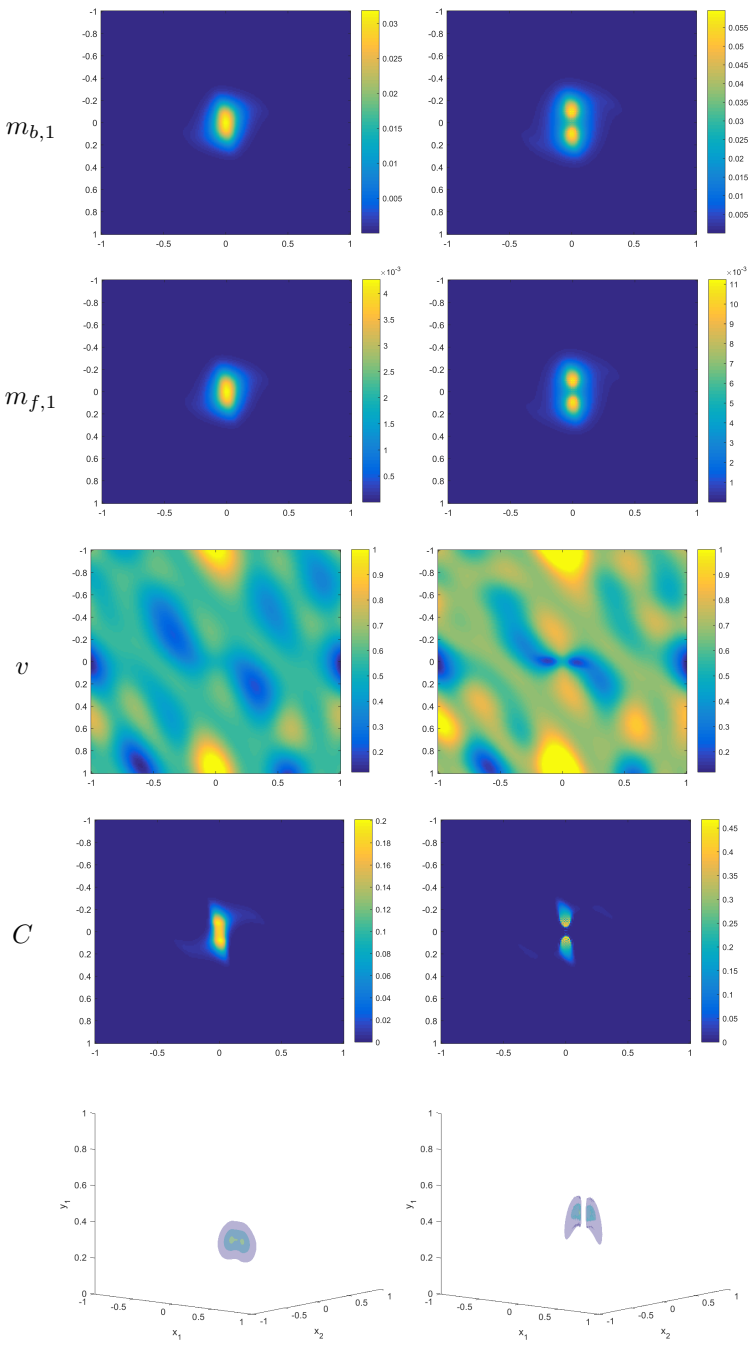

(a) t=3 (b) t=9

Figure 2.4: Numerical 2D-spatial 1D-structural results for (2.3) for heterogeneous ECM, plotted at times $t \in \{3, 9\}$: $m_{b,1}$ (*row 1*), $m_{f,1}$ (*row 2*) v (*row 3*), C (*row 4*), and c (*row 5*) as an isosurface on the 2D x-plane.

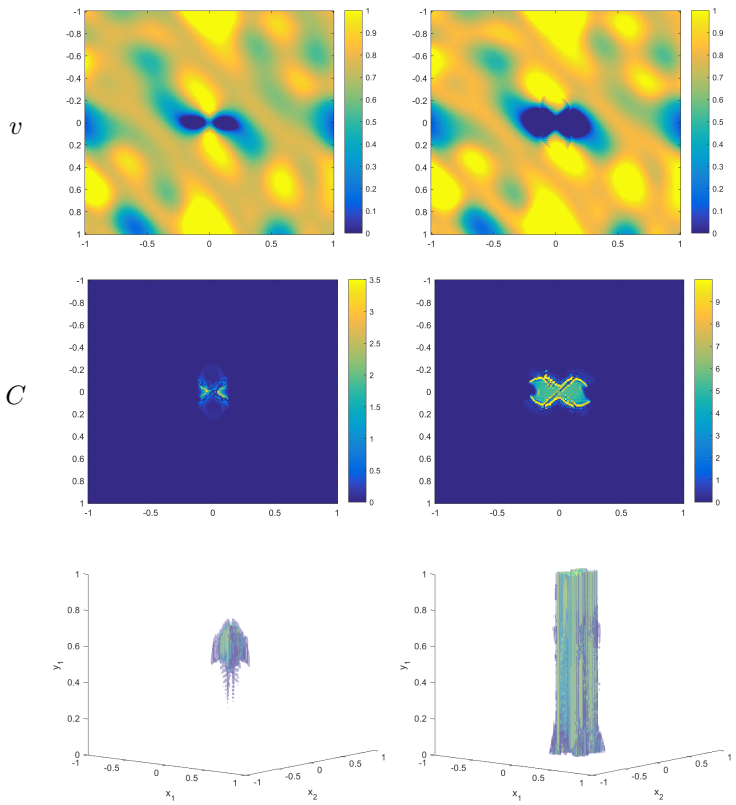

Figure 2.5: Numerical 2D-spatial 1D-structural results for (2.3) for heterogeneous ECM, plotted at times $t \in \{15, 20\}$: v (*row 1*), C (*row 2*), and c (*row 3*) as an isosurface on the 2D x-plane.

Given that a periodic function is used to generate the ECM heterogeneity, it is not terribly surprising that the result produced ($t \leq 20$) resembles that of a cyclic environment, with 180° turn symmetry. Further results (not shown) were generated with an asymmetric, or with non radial symmetry with respect to the initial positioning of the tumour. These results again displayed an asymmetric splitting of the population (typically into two spatially distinct subpopulations) with the larger portion of the subpopulation migrating to those regions with the steepest ECM gradients. Given that all of these environments were normalised with respect to their overall nutritional capacity, the underlying ECM patterning has no significant bearing on the invasive success of the tumour.

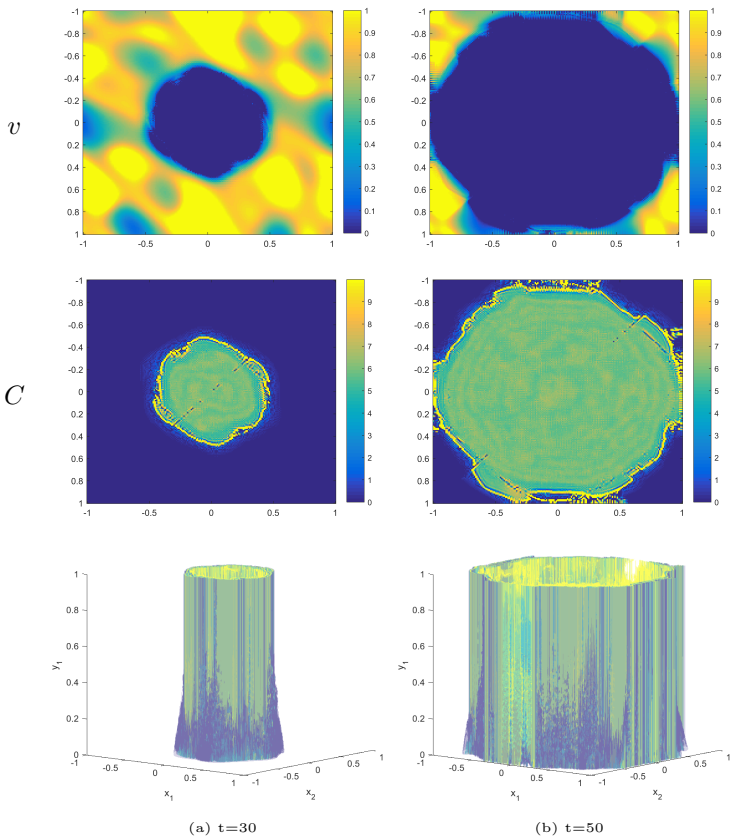

Figure 2.6: Numerical 2D-spatial 1D-structural results for (2.3) for heterogeneous ECM, plotted at times $t \in \{30, 50\}$: v (*row 1*), C (*row 2*), and c (*row 3*) as an isosurface on the 2D x-plane.

Moreover, the cancer, in this 2D-spatial 1D-structural heterogeneous case, is particularly exploitative of its environment, protruding into areas of low ECM density before the diffusion of the molecular species through the more dense sections of the ECM allows the remainder of the population to follow. This feature of the cancer behaviour is repeated until total permeation of the spatial domain occurs. This also leads to the boundary of the cancer population becoming somewhat amorphous, as one observes with cancer in the natural, biological environment of the human tissue. It may be interesting to consider the case in which molecular species are more free to diffuse into areas of lower ECM density.

uPA in the presence of inhibitor PAI-1: 2D-Spatial 2D-Structural Results

Results generated using a heterogeneous initial ECM density were similar to those generated for the system with 1-structural dimension (in the absence of PAI-1, Fig. 2.7–2.9). One observes again that the spiking behaviours developing into a particularly defined wave front for the growing cancer population. Again, this is likely to be due to the attractive forces, leading to haptotaxis, between the cellular population and the ECM causing cells to chemotactically self-aggregate on the boundary of the tumour. This is also likely accentuated by the local inhibition of invasion (through PAI-1 binding), which contrasts the advancement of the tumour boundary and encourages hyper-localised behaviours.

All of those significant features, appearing in the case of 1D-structural dimension (in the absence of PAI-1), appear in those for 2-structural dimensions (in the presence of PAI-1), with the important difference being that the nature of the tumour in this 2D-structural case develops at a much slower rate. This is expected behaviour given that the introduction of a 2^{nd} structural dimension, in this case, corresponds to the introduction of an inhibitor to the degradative activation protein, uPA. The apparent rate of change in tumour growth can be approximately given by $\alpha_{m_{f,1}} - \gamma_{m_{f,1}}$ such that the rate by which the tumour is slowed down is equal to the binding ability of the inhibitor. This can be clearly seen in the differences in morphology at $t < 20$ (Fig. 2.7–2.8).

2.2.5 Discussion & Conclusions

In the case where we consider a homogeneous cancer population and ECM density (Fig. 2.2-2.3) one observes a logistic boundary that expands, unimpeded, to its maximal radius within the given domain. Within this one observes a lower peak that clearly continues to expand throughout the space with the y-wave behaviour (which can be observed within the raw data), although at much lower values for C. This is likely due to the initial conditions remaining constant with the addition of a spatial dimension, causing values for c to be distributed and

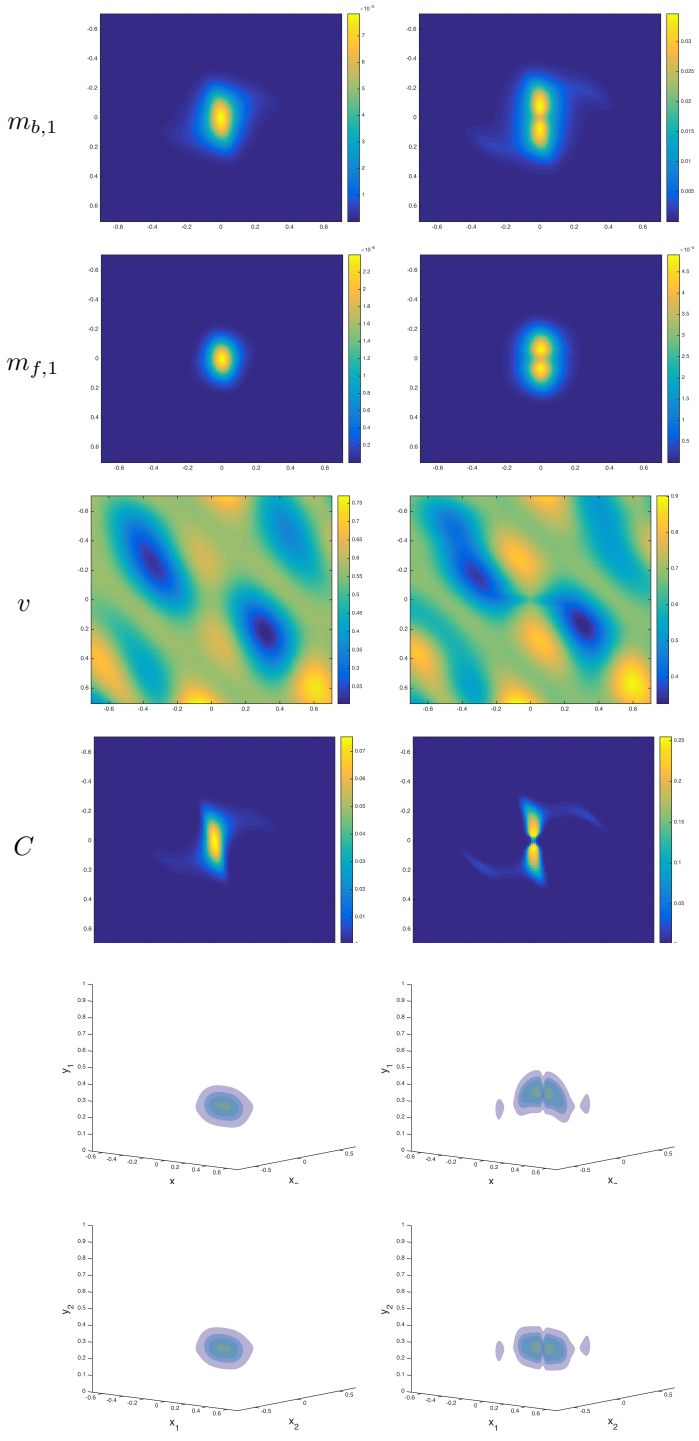

(a) t=3 (b) t=9

Figure 2.7: Numerical 2D-spatial 2D-structural results for (2.3) for heterogeneous ECM, plotted at times $t \in \{3, 9\}$: $m_{b,1}$ *(row 1)*, $m_{f,1}$ *(row 2)*, v *(row 3)*, C *(row 4)*, $\int_{[0,1]} c\, dy_2$ *(row 5)* and $\int_{[0,1]} c\, dy_1$ *(row 6)* as isosurfaces on the 2D x-plane.

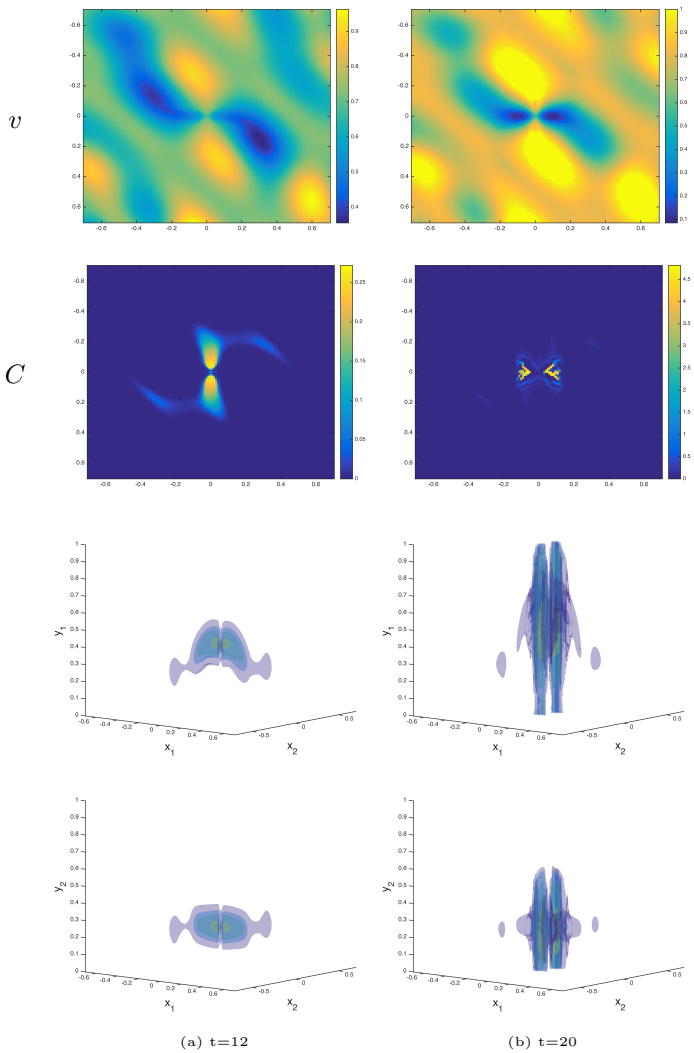

(a) t=12 (b) t=20

Figure 2.8: Numerical 2D-spatial 2D-structural results for (2.3) for heterogeneous ECM, plotted at times $t \in \{12, 20\}$: v *(row 1)*, C *(row 2)*, $\int_{[0,1]} c\, dy_2$ *(row 3)* and $\int_{[0,1]} c\, dy_1$ *(row 4)* as isosurfaces on the 2D x-plane.

for C to be reduced. Overall, these solution were in line with the 1D-spatial test-systems but not indicative of natural cancer behaviour.

Once we endow the cancer species with its natural habitat (the heterogeneous ECM) one observes behaviours absolutely characteristic of the biological system. These behaviours included the volume filling properties for the inside of the

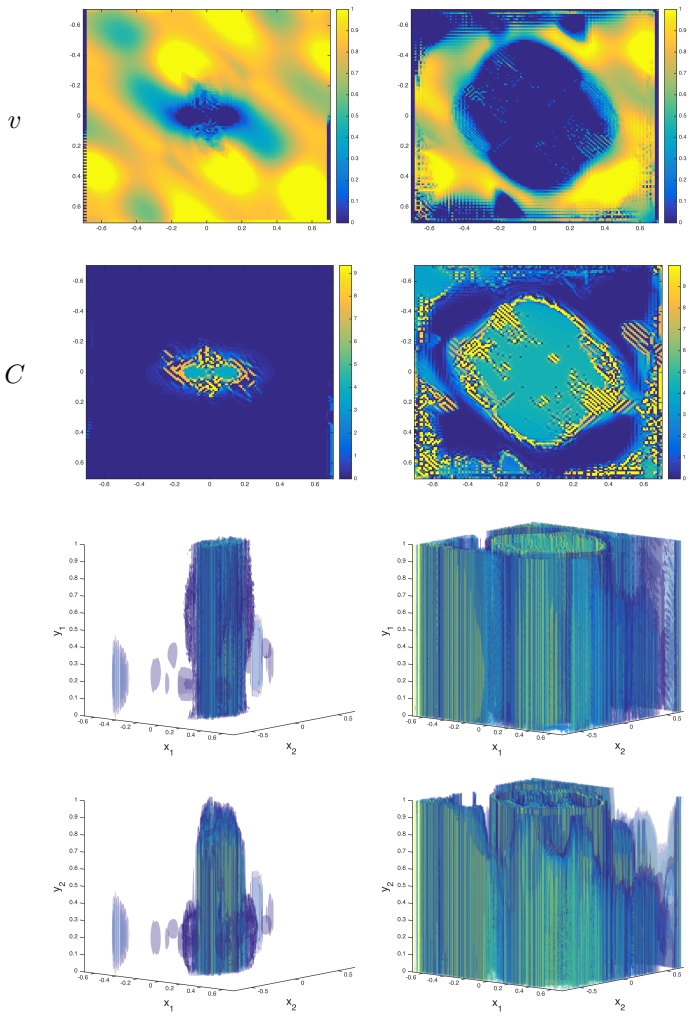

(a) t=25 (b) t=35

Figure 2.9: Numerical 2D-spatial 2D-structural results for (2.3) for heterogeneous ECM, plotted at times $t \in \{25, 35\}$: v (*row 1*), C (*row 2*), $\int_{[0,1]} c\, dy_2$ (*row 3*) and $\int_{[0,1]} c\, dy_1$ (*row 4*) as isosurfaces on the 2D x-plane.

tumour; the aggressive behaviour of the cancer's perimeter; and the primary invasion into areas of lower tissue density. It is not clear whether or not the initial splitting of the cancer into two subpopulations is characteristic of nature but certainly is of the model, which is again likely a consequence of the initial conditions.

It can also be directly observed that the numerical solution is stable in its spatial dynamics but unstable in structural dynamics, which can be seen from the total permeation of $\mathcal{P}$ on the boundary of c whilst the spatially considered cancer population, C, does not exhibit uncontrolled migration in $\mathcal{D}$. The areas of higher values for C (Fig. 2.6) can be attributed to the fact that y-waves continue to exist within the body of the tumour and behave as in the 1D-spatial model.

The largest errors arise from the structural differentiation in the second term of the equation for $\frac{\partial c}{\partial t}$, where we incur second order errors as a result of the symmetric difference quotient approximation. This method is commonly used and there are no clear contenders to be used in its place since reaching a higher order approximation is far more difficult than incurring computational and processing penalties as a result of increasing the number of required arithmetic calculations.

We then have a third order error that results from the trapezoidal approximation on the local integral. This could, potentially, be improved by, for example, taking a higher order approximation, such as Simpson's rule polynomial approximation, but one necessarily has a trade off between accuracy and computational intensity.

On the whole, these errors tend to be small so long as δ_x and δ_y are kept sufficiently small, $\delta_x, \delta_y \leq 10^{-2}$.

The result of stability analysis was to confirm the conclusions of the numerical simulations that, notwithstanding ones ability to compensate for the errors produced, the system is unstable in y. Any perturbation induced with non-zero y-component will result in the exponential growth of the perturbation through the structure space.

This simply implies that for fine perturbations in x, one must have sufficiently low migration in y so as to allow the profile to remain stable. This is particularly interesting when taken in combination with the numerical solutions which revealed explosive instabilities upon rapid migration to the y boundary, or the boundary of $\bar{\mathcal{P}}$, $\partial\bar{\mathcal{P}}$.

Given that, for stability, one considers the magnitude (or absolute values) of the parameters involved, one has that **m** is unstable under all conditions and for small perturbation around any hypothetical stable solution. We also find that v is stable at the cancer-ECM equilibrium such that, since we are interested in the cancer growth and destruction of its local environment, the system is stable, notwithstanding the instability in **m**.

Numerical results show interesting behaviours, particularly with the introduction of y-waves, resulting from the structural considerations in c. One sees the expected characteristics of the aggressive cancer species considered, with smooth degradation of the ECM and concurrent advancement of the cancer species to encroach on the healthy tissue. One shows how various considerations as to how one could amend the system result in more reasonable and expected behaviours in the cancer species but how, ultimately, the results that most closely correlate with the biological paradigm require a rethink of the underlying assumptions for the system, as a whole.

The numerical results for the system may elucidate an interesting propensity of the biological cancer system to utilise unconventional mechanisms of invasion, under the influence of chemical inhibitors. Inhibiting the uPA system appears, in some way, to impede the uniform invasion of the stroma by this aggressive cancer species, whilst allowing the ECM to remain intact by reducing the cancer's ability to degrade collagen has allowed the cancer to more readily utilise haptotactic behaviours. Therefore, what one observes in the inhibitor system, in comparison to its counterpart, is a more sporadic distribution of cancer cells who invade but do not degrade the ECM (growing in areas where competition for space is reduced.

This gives rise to important biological decisions about how one treats and prevents the spread of these cells, since inhibition may cause greater clinical issues. The inhibitors fail to inhibit the initial devastation of the ECM by uPA but leave the ECM open to exploitation. This may be a survival mechanism utilised by cancer and may have been evolutionarily beneficial to it propensity to

arise in the human body, rather than acting to the detriment of its progression.

Chapter 3

Novel Approaches to Modelling Drug Resistance in Melanoma

3.1 Introduction to Drug Resistance in Melanoma as a Multi-Scale, Spatio-Temporal Process

Although novel targeted therapies have significantly improved the overall survival of patients with advanced melanoma [200], understanding and combatting drug resistance remains a major clinical challenge. This is mainly due to the propensity of advanced melanoma to rapidly develop resistance to targeted therapies, such as BRAF inhibitors (BRAFi) or MEKi, or, indeed, to general immune-enhancing therapies, such as ipilimumab. We find that increasing our ability to deal with this problem on multiple scales, with spatial invasion on a macro-scale and metabolic interactions occurring on a micro-scale, allows the mathematical formulation of the problem to more closely model the biological reality of the situation.

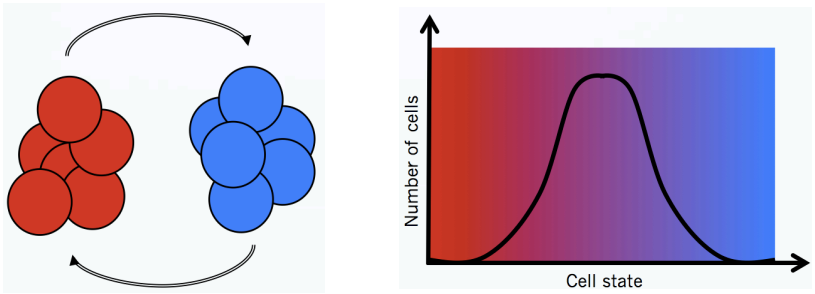

(a) (b)

Figure 3.1: Diagrams indicative of (a) a discrete paradigm, wherein a cell undergoes instantaneous and complete transitions between healthy and resistant states, and (b) a continuous paradigm, in which a cell undergoes a continuous alteration between two extreme healthy and resistant states and is capable of inhabiting all points between these two extremes.

Current mathematical abstractions of the biological paradigm for drug resistance characterise the biological system as existing in a series of discrete states; perhaps susceptible cells; cells with resistance to drug 1; cells with resistance to drug 2; and cells with resistance to both drugs. This discrete interpretation (Fig. 3.1a), however, is not born out in experimentation since the observation of cells under the influence of any given drug will demonstrate a spectrum of response patterns. The common assumption that cells instantaneously realign themselves to a 'resistant' phenotype also appears to presuppose the eventual survival of such cells. Moreover, gene expression levels of a given cell population submitted to treatment do not appear to exhibit strong qualitative differentiation and are more accurately described as a continuum.

Therefore, we take an alternative approach to modelling wherein we consider the cellular population as a single population which is continuously variable through some structural dimension (Fig. 3.1b). The structural dimension can be understood as a set of variables characterising the cell state at a molecular and/or phenotypic level. Within the cell population, subgroups are differentially sensitive to drugs and may exhibit differing proliferative and migratory behaviours, more generally. This gives us extended scope to model the more nuanced aspects of the heterogeneous cellular pathways towards resistance and invasion of the surrounding tissue in cancer.

Uniquely, this allows us to deal with the question of resistance to targeted and general cancer therapies by treating the tumour – and surrounding tissue – as a single bio-mathematical entity; accounting for resistance phenomena in terms of the modern notion of spatio-structural heterogeneity [321, 44, 234, 233]. In this view of the tumour, cancer cells evolve, through time and in the context of their local spatial environment [22], into individuated entities which will exhibit differential responses to the cancer treatment, on the basis of their phenotype [321]. Rather, then, of developing drugs to defeat 'cancer' it is necessary to think of the tumour as heterogeneous and treat the qualities of these individuated subpopulations appropriately for their personal survival stratagem. Moreover, these subpopulations may interact with one another, as well as the drug, either cooperatively, competitively, or separately in accordance with their phenotypes [234]. We attempt to account for each and all of these behaviours through modelling techniques that allow us to represent and continuously evolving and related tumour and its altered behaviours when faced with a drug challenge.

In the proceeding sections, we will explore both a theoretical and a data-driven approach to the modelling of drug resistance; each with its own advantages and disadvantages. The theoretical approach, utilised in Section 3.2, allows for a simple and elegant demonstration of the problem and the underlying mechanics which give rise to resistance but provides only a theoretical, or hypothetical, solution to the problem. The data-driven approach, employed in Section 3.3 on the other hand, poses a difficult series of propositions with which we must mathematically characterise the microscopic problem but allows us to generate immediately testable hypotheses with instantly recognisable consequences for clinical practice and scientific investigation. The verity of each of these approaches shall require extensive scrutiny, validation, and comparison with experimental observation.

3.2 Spatio-Genetic and Phenotypic Modelling Elucidates Resistance and Re-Sensitisation to Treatment in Heterogeneous Melanoma

3.2.1 Mathematical Background

The vast majority of existing, quantitative models of drug resistance are based on discrete stochastic mechanisms of evolution, which fail to take into account the intermediary stages and continuous nature of phenotypic development [172, 122, 42, 189].

Of the continuous models, several provide insights into the dynamics of evolutionary processes but are often restricted to single cell or non-spatial population models [213, 212], necessarily containing space averaging assumptions (well-stirred reactor hypothesis). Of these models, few take into account the prominent theory of PE [103] or have the depth to explain its significance in the context of drug resistance. Herein, we present a continuous spatio-structuro-temporal model to describe both the dynamics of the population of evolving tumour cells as a whole and how targeted therapy can produce resistant strains. We further use the model to recommend future strategies for prevention of this process. One recent study has further looked at the effect of diffusion-based drug gradients on the effective outcome of population diversity and heterogeneity [332].

A new addition to the variety of available bio-mathematical modelling frameworks has been spatio-structuro-temporal modelling, introduced by Domschke *et al.* [97] and later subjected to higher-dimensional simulation and numerical analysis [158]. This allows one to represent not only the spatial aspects of a population but also, simultaneously, some underlying aspect of its structure, giving one more insight into the co-evolution of these characteristics. This model has since been extended further [161] but has not yet been used to look at intrinsic properties of tumours, with respect to their systematic resistance to targeted

therapies.

In the proceeding section (Section 3.2.2), we present a general mathematical approach to modelling biological cancer systems whose spatial and structural dynamics are coupled and introduce the various terms within this system. Moving forward we provide a possible application for this model in the study of systems who develop resistance through the sequential mutation of particular oncogenes and the effects of BRAF inhibitors and immunotherapies on this development (Section 3.2.3). The results for this mutational model are then studied in detail, with particular interest given to the effects of the order and methodology of treatment and heterogeneity in the tumour environment (Section 3.2.4). Next, we provide a second possible application for this model in the study of systems whose metabolism of certain nutrients, particularly the metabolism of glucose through glycolysis or oxidative phosphorylation, shapes their response to drugs, resulting in a plastically resistant system (Section 3.2.5). We then explore results coming from this metabolically plastic system with a specific view to understanding the effect of treatment of spatial and metabolic heterogeneity and the resulting responses to treatment (Section 3.2.6). Finally we discuss the results from both of these systems in the wider context and the ramifications of this current study (Section 3.2.7).

3.2.2 Presentation of the General Model

Herein, we present a mathematical model that contains

(1) One cell species function, denoted $c(t, x, y)$, depending on time t, space x, and structure y, representing a continuous distribution of mutational or metabolic phenotypes of cancerous cells:

(1a) The structure variables y describe either mutational or metabolic status of the cell. In general, cells will be able to move in either a positive or negative mutational or metabolic direction, depending on the paradigm in question and possibly based on environmental

factors.

(1b) The mutational or metabolic alterations taking place within this cellular species will fundamentally alter its behaviour and the nature of its interaction with the micro- and macro-environments,

(2) A function representing the extracellular nutritional environment (ECNE), denoted $v(t,x)$; including the collagen matrix, distributed fibronectin, and vasculature, assumed to be proportional to one another as explored in the mathematical model of Gatenby [117],

(3) A vector valued function representing the concentrations of diffusible molecular species, denoted $\bar{m}(t,x)$, including metabolites, metallo-proteases, chemo-attractants or chemo-repellents, which will have the ability to mediate the interactions among the variables $c(t,x,y)$, and ECNE, $v(t,x)$,

(4) A vector valued function representing the concentrations of some medicines, denoted $\bar{p}(t,x)$, of detriment to the growth of certain of the cancerous species.

In the following, we describe the main steps for building the model:

Mathematically, we employ a multi-dimensional framework which allows for the coupling of spatial dynamics, in x, with other biological or biochemical dynamics in the cells themselves, which we call structural dynamics and denote by y. Then we can use an existing mathematical framework [97, 161] to deduce that the change in cell density $c(t,x,y)$ is given by the continuity equation

$$\frac{\partial}{\partial t}c(t,x,y) = \nabla_x \cdot \underbrace{F(c,v,\bar{m})}_{\text{Spatial Flux}} + \nabla_y \cdot \underbrace{G(y,c,v,\bar{m},\bar{p})}_{\text{Structural Flux}} + \underbrace{S(y,c,v,\bar{m},\bar{p})}_{\text{Source}}, \qquad (3.1)$$

where $\bar{a} \cdot \bar{b}$ stands for the dot product of vectors $\bar{a}$ and $\bar{b}$.

Through this, we recognise that the function $F(c,v,\bar{m})$ describes the movement of the cellular population in space, whilst $G(y,c,v,\bar{m},\bar{p})$ describes the structural change in the cellular population, and $S(y,c,v,\bar{m},\bar{p})$ describes the

overall change in the population or the number of cells entering or leaving the system through mitosis or apoptosis/necrosis, respectively.

Spatial flux of the cellular population

Begin by denoting ρ the collective spatial volume of the cellular and ECNE populations, defined as

$$\rho(c, v) := \int_{\mathcal{P}} c(t, x, y)\, dy + v(t, x)\,. \tag{3.2}$$

where $\mathcal{P}$ is the structural domain. This $\rho(c, v)$ then represents a measure of the total volume occupied by the cellular and ECNE population, together, and will allow us to model the unoccupied volume into which the cells and ECNE may grow. Further, we assume that the cell spatial dynamics are given by diffusion, chemo- and haptotactic directed transport, as in Chaplain *et al.* [56]. Diffusive dynamics correspond to autonomous stochastic motility in spatial cellular dynamics whilst chemo- and haptotaxis correspond to directed motion evoked through attraction to biochemicals or substrate components, respectively. The diffusion, chemotactic, and haptotactic rate constants are then given by D_c, $\bar{\chi}_m$, and χ_v, respectively. This may be mathematically represented as the following term:

$$F(c, v, \bar{m}) = D_c \nabla_x c + c(1 - \rho(c, v))\left(\nabla_x(\bar{\chi}_m \cdot \bar{m}) + \nabla_x \chi_v v\right)\,. \tag{3.3}$$

As in [56], the chemo- and haptotactic fluxes are volume constrained and vanish when the collective spatial volume reaches a maximum capacity that, without loss of generality, is considered equal to one. A simple way to take this constraint into account is to consider that these two fluxes are proportional to $1 - \rho$, where $\rho(c, v)$ is defined as in (3.2).

Structural flux of the cellular population

The structural flux is the sum of two terms, an advection flux and a structural diffusion flux, corresponding to biased and unbiased evolution in the structure space, respectively.

In order to define the advection flux we introduce the function $\Psi(y, \bar{m}, \bar{p})$, representing the normalized structural velocity, who is dependent upon the population's structural distribution, the local nutrient concentration and the local concentration of drugs. Given some maximal rate for the population's velocity through the structural dimension, r_μ, the structural velocity shall be given by $r_\mu \Psi(y, \bar{m}, \bar{p})$, where the normalized structural velocity satisfies $|\Psi(y, \bar{m}, \bar{p})| \leq 1$. The structural advection flux term is the product of the structural velocity and the cell distribution density and reads

$$G_a(y, c, v, \bar{m}, \bar{p}) = r_\mu \Psi(y, \bar{m}, \bar{p}) c \,. \tag{3.4}$$

In this paper, we shall consider one cellular system in which behaviour is adapted through the accumulation of consecutive mutation (Section 3.2.3) and one in which a cell may plastically evolve its behavioural phenotype through metabolic reprogramming dynamics (Section 3.2.5). For each of these scenarios, it will be necessary to define a distinct and biologically relevant form for the function $\Psi(y, \bar{m}, \bar{p})$.

Diffusion in structural space can occur as the result of a stress, following a change of environmental conditions. In order to adapt to the environment, the population tends to diversify its behaviour which leads to an increase in spread of the y-space cell distribution. This diversification of behaviour can be phenomenologically described by a structural diffusion matrix $\Sigma(y, \bar{m}, \bar{p})$. The structural diffusion flux is supposed to satisfy Fick's law and reads

$$G_d(y, c, v, \bar{m}, \bar{p}) = -\Sigma(y, \bar{m}, \bar{p}) \nabla_y c \,. \tag{3.5}$$

Although structural diffusion is possible both in a mutational and a metabolic

context, in this paper we will consider it only in relation to metabolic remodelling.

The total structural flux is the sum of the structural advection and structural diffusion terms and reads

$$G(y, c, v, \bar{m}, \bar{p}) = G_a(y, c, v, \bar{m}, \bar{p}) + G_d(y, c, v, \bar{m}, \bar{p})\,. \tag{3.6}$$

Source/Sink terms for the cellular population

The growth of any given cell will be dependent on an assortment of intracellular and environmental factors, including its structural state, y; the availability of nutrients, $\bar{m}$; and the volume surrounding the cell which has not yet been filled, $\rho(c, v)$. Therefore, we write the growth rate of the population generically as $\Phi(y, \bar{m}, c, v)$ such that we may define its particular dynamics for the considered scenario. It is important to remember that this term accounts only for growth of the cell population and not the negative growth caused by the introduction of drugs.

It is clear that, since drugs are typically designed to exploit a particular behaviour or dependence of a given cancerous population, its effectiveness will be dependent upon the current structural state of the cell, y. We account for the effect of drugs on the cellular population, then, by taking the product of the cellular apoptosis rate, the drugs' effectiveness functions, and the respective local drug concentrations $\delta_c \bar{p}(t, x)\bar{f}(y)$. Multiplying this by the cellular concentration, itself, will yield the degradative sink. As such, the entire source/sink term may be written mathematically as

$$S(y, c, v, \bar{m}, \bar{p}) = \Phi_c(y, \bar{m}, c, v)c - \delta_c \bar{f}(y) \cdot \bar{p}c\,. \tag{3.7}$$

Since, in this particular study, we are interested in the effects of structural heterogeneity on the success of a given cancer population the normalized structural velocity, $\Psi(y, \bar{m}, \bar{p})$; structurally-dependent growth function, $\Phi_c(y, \bar{m}, c, v)$; and the structurally-dependent drug effectiveness function, $\bar{\mathfrak{f}}(y)$, are of most in-

terest. Their dependence on structural considerations makes them of particular relevance to the particular situation in which they are applied and so all 3 terms will be specifically defined for the mutational (Section 3.2.3) or phenotypic (Section 3.2.5) considerations, respectively.

Dynamics in the ECNE, molecular, and drug species

The dynamics of the ECNE, $v(t,x)$, will be described simply, without spatial dynamics, as growth given by the ECNE remodelling function $\Phi_v(c,v)$ and the degradation of the ECNE by chemical species. The degradation constant vector will then be given by $\bar{\delta}_v = [\delta_{v,m_1}, \delta_{v,m_2}, \dots]^T$ and will have the same number of components as there are chemical species. For any i^{th} chemical species that does not degrade the ECNE, the degradation constant $\delta_{v,m_i} = 0$. Our PDE for the ECNE dynamics is then given by

$$\frac{\partial v}{\partial t} = \Phi_v(c,v)v - \bar{\delta}_v \cdot \bar{m}v \,. \tag{3.8}$$

Spatial dynamics of the molecular species vector, $\bar{m}(t,x)$, are given simply by diffusion with its rate vector $\bar{D}_m$. Chemical species are then produced either by the ECNE, and connected network of capillaries, $v(t,x)$, or the cellular species, $c(t,x,y)$, with rates dependent on y such that its general expression may be given by the function $\bar{\Phi}_m(y,\bar{m},c,v)$. We then assume that environmental factors, which are not directly accounted for, shall contribute to the degradation of molecular species with respective degradation rates of $\bar{\delta}_m$. Dynamics for the molecular species are then collectively written as

$$\frac{\partial \bar{m}}{\partial t} = \nabla_x \cdot \text{diag}(\bar{D}_m)\nabla_x \bar{m} + \int_{\mathcal{P}} \bar{\Phi}_m(y,\bar{m},c,v)\, dy - \text{diag}(\bar{\delta}_m)\bar{m} \,. \tag{3.9}$$

Finally, spatial dynamics for the drug species vector, $\bar{p}(t,x)$, are also given by diffusive dynamics, with a rate vector $\bar{D}_p$. We then represent the input of drug species to the population as a vectorial function, $\bar{\theta}(t,x)$, which is to define the drug regimen used by the clinician/scientist in treating the tumour.

This will normally be given by a sum of Dirac delta functions centred at the time of injection of the drug but may be given by other forms and will be particular to the experiment that the model attempts to replicate. Finally, we assume that the drug's effect on the cellular system requires the drug to be taken in by cells and systematically degraded during apoptosis. Therefore, given a drug degradation vector, $\bar{\delta}_p$, this degradation shall be committed by the non-structured cellular population, written as the integral $\int_{\mathcal{P}} c\,dy$. The complete equation for drug dynamics is then given by

$$\frac{\partial \bar{p}}{\partial t} = \nabla_x \cdot \mathrm{diag}(\bar{D}_p)\nabla_x \bar{p} + \bar{\theta}(t,x) - \mathrm{diag}(\bar{\delta}_p)\bar{p}\int_{\mathcal{P}} c\,dy\,. \tag{3.10}$$

Summary of the General Mathematical Model

We then write the system of PDEs as

$$\begin{cases} \dfrac{\partial c}{\partial t} = \underbrace{\nabla_x \cdot \left[D_c \nabla_x c + c(1-\rho(c,v))\left(\nabla_x(\bar{\chi}_m \cdot \bar{m}) + \nabla_x \chi_v v\right)\right]}_{\text{Spatial Flux}} \\ \qquad + \underbrace{\nabla_y \cdot \Sigma(y,\bar{m},\bar{p})\nabla_y c - r_\mu \nabla_y \cdot \Psi(y,\bar{m},\bar{p})c}_{\text{Structural Flux}} + \underbrace{\Phi_c(y,\bar{m},c,v)c}_{\text{Growth}} - \underbrace{\delta_c \bar{\mathfrak{f}}(y)\cdot \bar{p}c}_{\text{Drug Influence}} \\ \dfrac{\partial v}{\partial t} = \underbrace{\Phi_v(c,v)v}_{\text{ECNE Remodelling}} - \underbrace{\bar{\delta}_v \cdot \bar{m}v}_{\text{MMP Degradation}} \\ \dfrac{\partial \bar{m}}{\partial t} = \underbrace{\nabla_x \cdot \mathrm{diag}(\bar{D}_m)\nabla_x \bar{m}}_{\text{Spatial Diffusion}} + \underbrace{\int_{\mathcal{P}} \bar{\Phi}_m(y,\bar{m},c,v)\,dy}_{\text{Chemical Synthesis}} - \underbrace{\mathrm{diag}(\bar{\delta}_m)\bar{m}}_{\text{Natural Degradation}} \\ \dfrac{\partial \bar{p}}{\partial t} = \underbrace{\nabla_x \cdot \mathrm{diag}(\bar{D}_p)\nabla_x \bar{p}}_{\text{Spatial Diffusion}} + \underbrace{\bar{\theta}(t,x)}_{\text{Drug Input}} \underbrace{- \mathrm{diag}(\bar{\delta}_p)\bar{p}\int_{\mathcal{P}} c\,dy}_{\text{Drug Degradation}}\,. \end{cases} \tag{3.11}$$

This system of equations (3.11) is considered together with no-flux boundary conditions in c, m, and $\bar{p}$. In the case of c we consider zero spatial fluxes, and zero structural fluxes on the boundaries of the spatial and structural domains, respectively.

In the following sections, we present an intuitive explanation for the origin of the equations and relations used for two particularisations of this general mathematical system, along with a thorough description of the biological evidence for such phenomena.

Discussion and justification of the mathematical model

Current modelling approaches consider the cell as a discretely changing variable who exists in an explicitly sensitive or resistant state. We wish, here, to conceive of the cell as a continuously changing and finely tunable evolutionary population. Different cancer cells have similar, if not identical, origins and are not innately differentiable but have rather gained different characteristics. Therefore, we introduce a novel modelling framework in order to reconceive the mathematical representation of the cell, from this more nuanced perspective.

Cells do, however, function differently. Within these categories, then, there must be a wealth of diversity to reflect the reality of the structural differences between cells. In order to reflect this, we incorporate a term that operates similarly to those structural models previously employed [213, 212], whilst building on the solid mathematical derivation given by existing spatio-structuro-temporal models [97, 161]. Letting $\mathcal{I} := [0, T] \subset \mathbb{R}_+$ be the time interval over which the experiment is conducted; $\mathcal{D} := [0, 1]^2 \subset \mathbb{R}_+^2$ be the spatial domain; and $\mathcal{P} := [0, 1] \subset \mathbb{R}_+$ define the continuous domain over which the mutational or metabolic changes may occur, we couple these dynamics using a simple conservation of mass assumption. If $V \times W \subseteq \mathcal{D} \times \mathcal{P}$ is an arbitrary volume of the spatio-structural domain with piecewise smooth boundaries ∂V and ∂W respectively, then we can write that the total population of cells in this volume is given by

$$c(t)_{V\times W} = \int_W \int_V c(t, x, y)\, dx\, dy\,. \tag{3.12}$$

Then we can use an existing mathematical framework [97, 161] to deduce that

the change in cell density $c(t,x,y)$ is given by the partial differential equation

$$\frac{\partial}{\partial t}c(t,x,y) = \nabla_x \cdot \underbrace{F(c,v,\bar{m})}_{\text{Spatial Flux}} + \nabla_y \underbrace{G(y,c,v,\bar{m},\bar{p})}_{\text{Structural Flux}} + \underbrace{S(y,c,v,\bar{m},\bar{p})}_{\text{Source}} . \tag{3.13}$$

Let $\Psi(y,\bar{m},\bar{p}) : \mathcal{I}\times\mathcal{D}\times\mathcal{P} \to \mathbb{R}$ be the normalized structural velocity for the cellular population. During a time interval of small length Δt, those cells having the mutational or metabolic state y initially at t, will evolve to a state $y + r_\mu \Psi(y,\bar{m},\bar{p})\Delta t$ at $t+\Delta t$, where r_μ is the mean mutation rate. Moreover, let $\Sigma(y,\bar{m},\bar{p}) : \mathcal{I}\times\mathcal{D}\times\mathcal{P}$ be the structural diffusion matrix for the cellular population. Hence, the structural flux reads

$$\begin{aligned} G(y,c,v,\bar{m},\bar{p}) =& G_a(y,c,v,\bar{m},\bar{p}) + G_d(y,c,v,\bar{m},\bar{p}) , \\ G_a(y,c,v,\bar{m},\bar{p}) =& r_\mu \Psi(y,\bar{m},\bar{p}) c(t,x,y) , \\ G_d(y,c,v,\bar{m},\bar{p}) =& -\Sigma(y,\bar{m},\bar{p})\nabla_y c(t,x,y) . \end{aligned} \tag{3.14}$$

With this concept of a continuum of phenotypic progression, we then recognise that pharmaceuticals are generally targeted at specific metabolic pathways (related to selected cancer-related phenotypes and their respectively triggered mechanisms). Therefore, we employ a description of a phenotypic 'spectrum' wherein cells may inhabit any point on that available spectrum in y. These drugs may then target specific regions on this spectrum which employ the molecular pathways inhibited by these drugs. For this we form an effectiveness vector $\bar{\mathfrak{f}}(y) \in \mathcal{Y}^P$ which describes the bandwidth in the mutational dimension $\mathcal{P}$ on which the drug is effective at diminishing the population of cells, for each given drug, p_j, $j \in \{0,...,P\}$.

3.2.3 Mutational Evolution and the Establishment of Drug Resistance

Resistance to BRAF inhibitors (BRAFi) and antibody therapies in melanoma

Melanoma is one of the most common cancers of the skin and approximately 50% of melanomas contain a mutation in an oncogene known as BRAF, often appearing at codon 600 [178]. Therefore, BRAF inhibitors (BRAFi) have been the major drug of choice in treating advanced melanoma tumours and their various subtypes. The application of BRAFi as an anti-oncogenic, however, has had mixed results due to the frequent presence of BRAFi resistant phenotypes existing as subspecies within the overall melanoma species [37, 257, 256, 286, 300]. The resistance mechanism could involve activation of collateral signalling pathways when the main signaling is inhibited [231]. For this reason, simultaneous inhibition of several pathways is often proposed as a possible strategy against resistance [231].

Moreover, recent studies suggest that intravenously injected, water-soluble MAPK activator can overcome, to some extent, the resistance to BRAFi [134]. This, in turn, suggests that the penetration to the inner domain of the tumour is a critical component of the destruction of the resistant cancer cells. Moreover, BRAFi is often used in combination with MEKi in order to target several mechanisms of activation within the MAPK pathway.

In animal models, as well as in patients, relapse occurs systematically several months after treatment with BRAFi [267]. Studies have shown that the adaptations and resistance to BRAFi happen early in the treatment process [328, 296], which may suggest that cancer cells have acquired a resistant state before application of BRAFi.

The order in which drugs are supplied to the tumour may also have a significant effect on the clinical outcome. Progression-free survival rates were higher among those receiving immunotherapy prior to BRAFi than vice versa [2] whereas one particular study looking at treatment with immunotherapy and

BRAFi found that preceding BRAFi with immunotherapy does not alter the effectiveness of the drug. Treatment with immunotherapy post-BRAFi, however, gives the patient a particularly poor clinical outcome [3].

One strategy for drug application on the premature tumour has been shown to apparently forestall the resistance to BRAFi. This methodology involved applying the drug to the tumour, for a period of time appearing to demonstrate a reduction in the tumour volume, before removing the drug and repeating the process, again. This method showed mixed results although a significant number of the resistant tumours did not survive the treatment [77].

Tumours that have been shown to have innate BRAFi resistance have further been shown to have increased incidence of mutations in genes known as NRAS [244, 10] and PTEN [299], respectively.

In human liver cells, those cells with an induced PTEN knockdown have been shown to increase the rates of Akt phosphorylation and, importantly, to inhibit Foxo1 signalling [182]. Foxo1, in return, is a transcription factor responsible for mediating the T-cell response to healthy cells [254]. In $CD8^+$ T-cells, Foxo1 has been shown to have an intrinsic role in establishing long-lived memory programs that are essential for developing cells capable of immune reactivation during secondary responses to infection [186, 154].

On the other hand, the gene encoding for phosphatidylinositol 3-kinase (PI3K), whose oncogenic pathway is inhibited by PTEN expression, has been shown to reduce the cytokine expression in cells [135], thereby reducing the inflammatory response of the surrounding tissue and limiting T-cell recruitment to the site. Cells with a PTEN deletion might then be protected from immune response through mediation of cytokines and the local apoptosis induced through PI3K/Akt signalling, which may subsequently be overcome by the induction of T-cell hyperactivity induced by ipilimumab – a melanoma-specific immune enhancer therapy.

Therefore, it is possible that melanoma cells undergo sequential genetic alterations in BRAF and PTEN, respectively, and that the pattern in which these mutations occur, along with considerations with respect to competition for nu-

trients, could explain the build up of resistance to the combined effects of BRAFi and ipilimumab anti-oncogenic treatments.

It may also be that BRAF mutated cells, as a result of causal genomic instability, acquire NRAS mutations which confer resistance. This change, for example, was observed within ovarian cell lines and was predicted to have formed as a result of exon 11 BRAF mutations being insufficient to satisfactorily activate the MAPK pathway, requiring additional NRAS activity [79]. Furthermore, BRAF V600E cells have sufficient MAPK activity such that they do not necessitate supplementary mutation and, as such, display a more positive response to therapy [59], which is supported in the majority of cases of melanoma with a native BRAF mutation [126]. Yet, despite the fact that BRAF and NRAS mutations are described commonly as "mutually exclusive", NRAS mutations appear in increased numbers of BRAFi resistant tumours [10].

In our model, we interpret the primary and consequent mutation to be that in BRAF and assume, further, that the cell will acquire some further mutation capable of conferring resistance to BRAF inhibitors.

Interpreting the structural dimension for a mutational system

In order to understand how this system of sequential mutations contributes to the cancer cell population's success at avoiding targeted and immune-enhancement therapies, we must first interpret the structural-, y-, dimension. So, letting the cellular population be given by a function $c(t, x, y)$ and the ECNE concentrations be given by the function $v(t, x)$, with $\bar{m}(t, x)$ and $\bar{p}(t, x)$ giving the molecular and drug species, respectively, we observe the bio-mathematical dynamics of such a system in the structure space, $\mathcal{P}$.

We also assume, that the cellular species will migrate unidirectionally through the structure space, which is to say that mutations are irreversible. Let the structural mutation variable and space, then, be given by the interval $y \in \mathcal{P} = [0, 1]$, such that $y = 0$ and $y = 1$ give the extreme states of primary tumour (or as yet without a mutation) and resistant, respectively. For ease, let us

also define that $y = 1/2$ defines a BRAF mutation and the state at which the cellular species is most sensitive to BRAFi. Realistically, the ipilimumab immune-enhancer drug will be effective across the entire spectrum of mutations but we assume it to be most effective posterior to BRAF mutation and prior to complete consolidation of resistant features at $y = 1$.

Growth, ECNE remodeling and drug dosing in a mutational system

Let $\rho(t, x)$ be defined as in 3.2 such that the growth of the cellular species, $c(t, x, y)$, shall be dependent upon the unoccupied local volume, $1 - \rho(t, x)$ and is also dependent upon the nutritional species, $m_2(t, x)$, being above a given threshold, θ_{m_2}. The cellular growth rate, with an overall rate parameter ϕ_c, is then written as

$$\Phi_c(y, \bar{m}, c, v) \quad = \quad \phi_c(m_2 - \theta_{m_2})(1 - \rho(c, v)) \,, \tag{3.15}$$

where we consider that growth, in this case, is not dependent upon the mutational status of the cells y.

Again, the ECNE remodelling takes place within the unoccupied portion of the local available volume, $1 - \rho(t, x)$, and with a rate constant ϕ_v, such that

$$\Phi_v(c, v) \quad = \quad \phi_v(1 - \rho(c, v)) \,. \tag{3.16}$$

Although we assume here that ECNE remodelling is only dependent on the unoccupied volume, we recognise that more realistically this could depend on fibroblast cells and ultimately on the cell phenotype represented by y.Therefore, future iterations of this modelling approach could incorporate more complex remodelling through a redefinition of the Φ_v term.

We then endow the system with two molecular species. m_1 is a species that is secreted by the cell species and will act to degrade the ECNE. This can be thought of as a matrix metalloproteinase (MMP) which acts to break-down the ECNE. m_2 is a species which is secreted by the ECNE and acts to the benefit

of the cellular species. This chemical species can be thought of as a nutrient or growth factor, the presence of which aids the growth of cellular species.

We further assume that more mutated and aggressive cellular populations will produce MMP molecules at a greater rate, such that their production is proportional to y, and that the overall rate constant is given by ϕ_{m_1}. We write this as

$$\Phi_{m_1}(y, \bar{m}, c, v) \quad = \quad \phi_{m_1}(1 - m_1)yc\,. \tag{3.17}$$

Nutrient, or nutritional species, are produced by the ECNE and with a rate of ϕ_{m_2}, such that

$$\Phi_{m_2}(y, \bar{m}, c, v) \quad = \quad \phi_{m_2}(1 - m_2)v\,. \tag{3.18}$$

We assume an instantaneous introduction of drug species through the vasculature, which we assume to be proportional to ECNE concentration. The instantaneous nature of this drug introduction mean that we may write this as a Dirac delta function $\breve{\delta}(t - \tau)$ centered at some time τ, whilst its introduction through the vasculature of the ECNE is represented by proportionality to $v(t, x)$. Then, given that the number of doses of some j^{th} drug species, $p_j(t, x)$, is a natural number, $N_{p_j} \in \mathbb{N}$, we write that the doses are given at the ordered set of time points $\{\tau_{j,1}, \tau_{j,2}, \ldots, \tau_{j,N_{p_j}}\}$, $\tau_{j,1} < \tau_{j,2} < \cdots < \tau_{j,N_{p_j}}$. Then the mathematical expression for drug dosing is given by

$$\theta_j(t) \quad = \quad v(t, x) \sum_{k=1}^{N_{p_j}} \breve{\delta}(t - \tau_{j,k})\,. \tag{3.19}$$

Mutational dynamics in melanoma: Phyletic gradualism or punctuated equilibria?

Patterns in genetic evolution can generally be categorised by the theory of punctuated equilibrium (PE) or phyletic gradualism (PG). PG originates in the theory of Darwinian evolution by natural selection and seeks to explain the variety of species by continuous gradual change [75, 81]. PE, on the other hand, is a currently prominent theory in evolutionary biology that seeks to explain the

nature of evolution by natural selection through the prism of large scale genetic and environmental changes, rather than a gradual process [232, 103]. Recent papers in the field of evolutionary biology advance the PE framework as a superior explanation of microbiological, paleontological, and phylogenetic evidence available today [208].

Starting with pioneering contributions of Knudson [191], Cairns [48] and Nowell [250], theory of evolution and population genetics ideas were applied to explain cancer progression. These theories added chromosome instabilities and selection processes to the older idea that cancer results from an accumulation of somatic mutations [19]. Furthermore, the gradual accumulation of mutations over time has been challenged by recent evidence that tumours evolve by a few catastrophic events that generate large scale genome[305] or chromosome lesions[240, 295]. These findings suggest that cancer genomes evolve by PE, being thus able to acquire quickly new capacities such as invasiveness and drug resistance [68, 290, 249]. This PE can be explained on a more microscopic level by assuming that the intermediary stages of mutation, although significant, happen more quickly and to greater effect under certain optimal conditions. Conflictingly, gradualism would convey a sense of regular and linear progression within the phyletic tree of the cancer species with little or no change in the rate of mutation.

Single-cell genetic analysis reveals clonal frequencies and phylogeny patterns of evolving tumours [28, 236, 234, 80]. Various clones have heterogeneous survival properties in the presence of drugs; as a result of this selection pressure, drug resistant clones can become predominant. For instance, mutations of the genes BRAF and NRAS are well known to be driver mutations for melanoma [162, 44, 78, 294]. The wealth of literature on melanomal branching evolution has identified BRAF as the major trunk driver mutation and NRAS or MEK1 as the major branch driver mutations [325, 334]. It has also been recognised that the targeted treatment of genetically evolved melanoma results in a reduction of their heterogeneity [78], as only drug resistant genetic variants survive, but not in their eradication.

For the sake of simplicity, in our model we consider that only two mutations can occur, and that their occurrence is sequential.

A structural flux function in a mutational system

To clarify the mathematical evolution of our cancer cell population, we must more clearly define how the population changes in structure, through the normalized structural velocity $\Psi(y, \bar{m}, \bar{p})$ (further discussion in 3.2.3). This function is intended to represent the velocity of any given cell in the y-direction (in other words, the mutation rate), for given current structural state (y-coordinate) and local nutritional condition, $m_2(t, x)$. We shall define a separate normalized structural velocity for both a PG and a PE assumption.

In the case of PG, we wish for the evolution of this population to be steady and regular throughout the domain, such that the mutation rate must fundamentally be constant throughout the domain. Then, in order to ensure that our population does not migrate beyond the boundaries of the domain, $y = 0$ or $y = 1$, we set the values of the normalized structural velocity to 0 at these locations, yielding no mutation at these biological positions (Fig. 3.2a).

In the PE case, we require for the mutation rate to be significantly greater in periods between mutational realisation that at those positions themselves. Therefore, we represent the normalized structural velocity as a bimodal function with velocity maxima positioned between the mutational states. Likewise with the PG function, however, we require for the PE paradigm to yield a 0, non-mutational behaviour at the boundaries of the domain (Fig. 3.2b). Remember, given that these function represent the rate of mutation, a higher value of $\Psi(y, \bar{m}, \bar{p})$ will convey a faster rate of mutation whilst a lower value will convey a more quiescent state, where change is somewhat slower.

For the sake of simplicity, we do not consider genetic diversification and structural diffusion in this context.

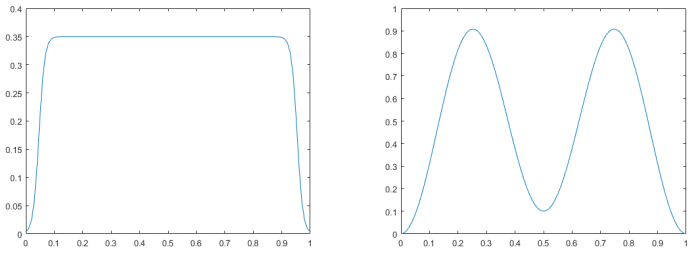

(a) (b)

Figure 3.2: Normalized structural velocity, $\Psi(y, \bar{m}, \bar{p})$ for the (a) phyletic gradualism (PG) and (b) punctuated equilibrium (PE) assumptions.

On mutationally evolving systems

The choice of mutational rate of change function would have to accurately represent the most sensible possible case for PG and PE, respectively. From (3.14) it is clear that the no-flux boundary condition is fulfilled automatically if the structural veolocity satisfies

$$\Psi(\tilde{y}, \bar{m}, \bar{p}) = 0, \quad \forall \tilde{y} \in \partial\mathcal{P},$$

where $\partial\mathcal{P}$ is the boundary of the structural domain $\mathcal{P}$.

The structural velocity for PG is considered to be constant, except for a small region at the boundary. In order to construct such a function, we start with

$$\hat{\Psi}_g(y, \bar{m}, \bar{p}) := 1 - \sum_{i=0}^{1} \left(1 + \exp\left[-\beta_g \left((2y-1)i - y + \frac{5}{\beta_g}\right)\right]\right)^{-1}, \qquad (3.20)$$

where β_g is chosen sufficiently large such that the function $\hat{\Psi}_g(y, \bar{m}, \bar{p})$ is close to one everywhere except at narrow neighborhoods of $y = 0$ and of $y = 1$. The symmetry of the function $\hat{\Psi}_g$ implies that no-flux boundary conditions can be achieved by the imposition of

$$\Psi_g(y, \bar{m}, \bar{p}) := \psi_g\left(\hat{\Psi}_g(y, \bar{m}, \bar{p}) - c_g\right),$$

where the lower case ψ_g gives the mutation rate parameter and $c_g := \hat{\Psi}_g(0, \bar{m}, \bar{p}) = \hat{\Psi}_g(1, \bar{m}, \bar{p})$ (Fig. 3.2a).

For the PE function, one must consider several features. Beyond smoothness, that is needed for both technical and biological reasons, one must again satisfy the no-flux conditions and impose the further conditions

$$\begin{aligned} &\frac{\partial^2}{\partial y^2}\Psi_e(y, \bar{m}, \bar{p})\Big|_{y=\frac{1}{2}} > 0\,, \qquad \frac{\partial^2}{\partial y^2}\Psi_e(y, \bar{m}, \bar{p})\Big|_{y=\{\frac{1}{4},\frac{3}{4}\}} < 0\,, \\ &\frac{\partial}{\partial y}\Psi_e(y, \bar{m}, \bar{p})\Big|_{y=\{\frac{1}{4},\frac{1}{2},\frac{3}{4}\}} = 0 \end{aligned} \tag{3.21}$$

which is to say that maximal mutational velocity should occur between points of phyletic stability, "equilibria", and minimal velocity should occur at intermediate points of phyletic stability (where boundary conditions cover the cases of minimal and maximal phyletic deviance). Thus, one can choose a function of the form

$$\hat{\Psi}_e(y, \bar{m}, \bar{p}) := \frac{1}{2}\left(1 - \cos\left(2\pi\hat{N}_\psi y\right)\right) + \alpha_g \sum_{i=1}^{N_\psi - 1} \exp\left[-\beta_e\left(y - \frac{i}{N_\psi}\right)\right], \tag{3.22}$$

where $N_\psi = 3$ is the number of absolute mutational states in the considered paradigm (pre-mutated, BRAF mutated, & resistantly mutated); β_e is chosen such that distribution is increased smoothly; and the symmetry of this function in the domain implies that the no-flux boundary conditions can be satisfied by imposing

$$\Psi_e(y, \bar{m}, \bar{p}) := \psi_e\left(\hat{\Psi}_e(y, \bar{m}, \bar{p}) - c_e\right), \tag{3.23}$$

where ψ_e again gives the mutational rate and $c_e := \hat{\Psi}_e(0, \bar{m}, \bar{p}) = \hat{\Psi}_e(1, \bar{m}, \bar{p})$ (Fig. 3.2b).

Drug effectiveness functions in a mutational system

The drug effectiveness is given by a vector valued function $\bar{\mathfrak{f}}(y) := [\mathfrak{f}_1(y), \mathfrak{f}_2(y)]^T$, where $\mathfrak{f}_i(y)$ gives the effectiveness of its corresponding i^{th} drug, $p_i(t, x)$. For

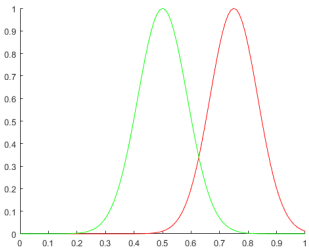

Figure 3.3: Distribution for the drug effectiveness functions $\mathfrak{f}_1(y)$ (*green*) and $\mathfrak{f}_2(y)$ (*red*).

simplicity, we assume that each of these functions is given by a Gaussian function centred at its point of greatest structural significance, or the structural location in y at which it is most effective against cancer cells.

Now, since $p_1(t, x)$ is define to be a BRAFi therapy and we have defined that the BRAF mutation is fully realised at the structural location $y = 1/2$, we assume that $\mathfrak{f}_1(y)$ attains its maximal value at $y = 1/2$ (Fig. 3.3 *green*). The considerations for ipilimumab are somewhat more numerous and difficult to entirely confirm but are, for our purposes, limited to the following. Firstly, we assume that immune cells should largely ignore healthy cells without a mutation such that there effectiveness at $y = 0$ should be negligible. Moreover, we know that cancer cells will eventually become resistant even to this immune-enhancer therapy and, as such, the value of effectiveness function must be sufficiently low in the neighbourhood of $y = 1$, so as to allow this resistance phenomenon to manifest. Likewise, immune cells require the expression of some protein on the surface of any given cell in order to identify its genetic properties; as such, we assume that only as the BRAF mutation becomes realised, near $y = 1/2$, shall the ipilimumab therapy begin to have a significant effect. Given these considerations, we place the maximum of $\mathfrak{f}_2$ at $y = 3/4$ (Fig. 3.3 *red*).

3.2.4 Results for the Mutational System

Primarily, in the application of this system to studying the death and regrowth models of tumour resistance in mice, we wished to know whether or not our *in*

silico model was able to recapitulate *in vivo* results. In the process of exploring this potential in the model, we attempt to asses the ability of either phyletic gradualistic or punctuated equilibrium assumptions, on the tumour's evolution, were more able to consistently capture this phenomenon (Section 3.2.4). Secondly, we wished to test whether, given knowledge of sequenced treatments' ability to succeed in the ablation of the tumour, we could draw conclusions about the sequencing of treatments and their relative success (Section 3.2.4). In line with this, we tested periodic treatments to understand what the heterogeneity in initial conditions of the tumour could teach us about the outcomes for treatments (Section 3.2.4) and, finally, what effect a heterogeneous environment would have on these above conclusions (Section 3.2.4); whether results would be conserved or altered in the presence of a heterogeneous spatial conditions.

In order to test these scenarios, the *in silico* experimental approach was primarily as so: We began by choosing a melanoma mouse model for which one could attempt to tune our parameters and, effectively, challenge the model. The model that we chose for this task was that of Perna *et al.* who explored the explosive regrowth of tumours after some post-treatment dormancy period [267], amongst other things. Once we had used this *in vivo* model to tune and test our mathematical *in silico* model, we would use other biological models in order to challenge the mathematical model with no further doctoring of the mathematical model or its parameters. For this challenge we chose, initially, that of Thakur *et al.* [77].

Thus, we obtain that these mutations occur at maximal probabilistic rates of approximately 1.9×10^{-2} genetic events per day. This corresponds to acquiring a genetic mutation every 40-50 days posterior to some precursor event, where we consider only 2 such events. This is supported by the fact that tumours planted in the mouse species show significant change in expression pattern after 25-45 days [88, 183], where below 40 days BRAFi was a largely successful treatment [38], and mouse models show significant behavioural change in the cancer cell dynamics after 100 days since inocculation [267].

Proliferative and degradative parameters were chosen to be in line with pre-

	c	v	m_1	m_2	p
D	1×10^{-5}		1×10^{-4}	1×10^{-4}	5×10^{-4}
ϕ	0.4	5×10^{-2}	0.1	0.1	
δ	2	10	0.1	5×10^{-2}	5×10^{-2}
χ		5×10^{-5}	1×10^{-3}	0	0

Table 3.1: List of parameters used for numerical simulations of the model. Parameters are defined within a non-dimensionalised system (excepting for time measured in days) and, as such, are defined in terms of units days^{-1}.

vious models and were fine-tuned for the mouse model considered, based on tumour growth rates observed in tuning experiments [267]. All of these values are summarised in Table 3.1.

Initial conditions were chosen to be consistent with previous models [28] and for consistency with the biological methodology, as regards the impregnation of mice with cancerous cells. The particular study, using animal models, with which we compare our results injected mice with approximately $5 \times 10^3 - 2 \times 10^5$ cells [150]. Therefore, our initial conditions reflect this with

$$c_0 = \exp\left[-50(x^2 + 8 \cdot (y - \eta)^2)\right] \quad \text{such that} \quad \iint_{\mathcal{D}} \int_{\mathcal{P}} c_0(t, x, y)\, dx\, dy \approx 1 \times 10^8\,, \tag{3.24}$$

where, since we know that the biological experiments were initiated with an approximate cell count of 2.5×10^4 cells, we assume that the cellular distribution is measured approximately in 10^3 cells unit_x^{-2}. Further, the default initial location in the phenotypic dimension is given by $\eta = \frac{1}{50}$. One should also clarify that this constitutes not an entirely pre-mutated cell population but an already heterogeneous mixture of cells with at least one precursor event that induces the early stages of the BRAF mutation process.

Other quantities for which it is imperative that one have measures include the gross spatial population, which is given by the cellular population taken over the entirety of the structure domain, $\mathcal{P}$, and is given by

$$C(t, x) := \int_{\mathcal{P}} c(t, x, y)\, dy\,. \tag{3.25}$$

To calculate the volume of their tumour from its 2-dimensional section, Perna *et al.* [267] measure the lengths of the major and minor axes of the visible tumour, given by a and b respectively, and use the formula of an ellipsoid to write

$$V = \frac{4\pi}{3}\frac{a}{2}\frac{b}{2}\frac{b}{2} = \frac{\pi}{6}abb \tag{3.26}$$

In order to avoid having to define the value of our function, $c(t, x, y)$, above which the tumour would constitute a visible tumour, which would otherwise be given by a threshold of visibility θ_v, we assume the proportionality of the tumour mass and the area of the section over which the tumour is visible, written as

$$\iint_{\mathcal{D}} \int_{\theta_y}^{1} c(t,x,y)\, dy\, dx \approx k(\theta_v) \iint_{\mathcal{D}} \mathbb{1}_{\left\{ \int_{\theta_y}^{1} c(t,x,y)\, dy \geq \theta_v \right\}} dx\,, \tag{3.27}$$

where the proportionality constant is dependent on the visibility threshold and is given by $k : \mathbb{R} \to \mathbb{R}$. To calculate the model's tumour volume, i.e. the volume of cells which have developed into cancerous subtypes, we then take the mass of the tumour at $y \geq \theta_y$ and invoke the calculation from the tuning model [267] such that

$$V_c := K \sqrt{\left(\iint_{\mathcal{D}} \int_{\theta_y}^{1} c(t,x,y)\, dx\, dy \right)^3}\,, \tag{3.28}$$

with the adaptation of the ellipsoidal volume equation to $V = \frac{\pi}{6}ab\sqrt{ab}$ and where we take that $\theta_y = 0.2$ and K is an arbitrary constant.

Then, in order to carry out our test experiment, we control the heterogeneity using the following formula for the initial condition

$$c_0 := \sum_{j=1}^{J} \exp\left[-\left(x^2 + (y - \eta_j)^2 \right) \right]\,, \qquad \eta_j \in (0, 0.5],\, \forall j \in \{1, ..., J\}$$

and also in line with the initial volume condition (3.24), and where J is in some sense a measure of the initial heterogeneity. We then apply the drug dosage periodically in time intervals given by $[0, 20] \cup [40, 60] \cup [80, 100] \cup [120, 140]$. For

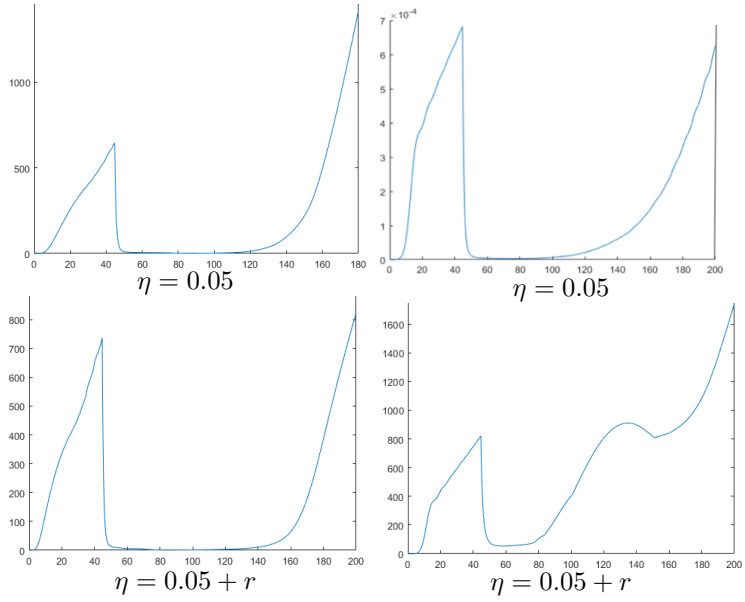

(a) Punctuated Equilibrium (PE) (b) Phyletic Gradualism (PG)

Figure 3.4: **Punctuated evolution is more consistent with biological results than gradual evolution.** Tumour volume graphs for (a) punctuated equilibrium (PE) and (b) phyletic gradualism (PG) assumptions under a simply BRAFi therapy option applied at $t = 40$ for initial conditions of $\eta = 0.05$ or $\eta = 0.05 + r$, where η represents the initial mean location of the tumour cells along the phenotypic dimension, and $r = 0.1$ represents a perturbation.

the simulations given in this current study, we use the range $J \in \{1, \ldots, 5\}$ to establish example data.

Punctuated equilibrium (PE) assumptions are more consistent with *in vivo* experimental results than phyletic gradualism (PG) assumptions

Given certain initial conditions for the cellular population, namely an initial structural distribution centred at $\eta = 1/20$, both PE and PG assumptions can give rise to the characteristic death and regrowth curves, albeit with differing characteristics (Fig. 3.4). In both cases, one observes an initial growth phase which is quickly stunted and violently reversed by the introduction of the drug species at $t = 45$. This is followed by a period of dormancy or 'tolerance' before the characteristic resistant growth (or regrowth) phase, which is of particular

interest to our current study. Observe, initially that the regrowth phase manifests a an earlier time point and with a faster growth rate under PE assumptions than with PG assumptions.

Now, observe that inducing a significant (200%) perturbation in only the position of the initial conditions, we evoke dramatically differing behaviours from our two *in silico* tumours (Fig. 3.4). For the case of PE, the rate at which our tumour regrows to its pre-treatment volume is much slower but the death and prolonged dormancy phases are conserved between these two experiments (Fig. 3.4a). Under the assumptions of PG, however, one observes at all time points a tumour volume with a significant positive minimum value (Fig. 3.4b). This shift in the volumes of tolerant tumours to be visible for all time points is not consistent with the results of comparative *in vivo* experiments [267] and, thusly, the initial conditions of a PG model would have to be strictly constrained to some smaller subset of possible conditions in order to maintain its relevance.

In biological, and especially in the case of *in vivo*, experimentation, however, the initial conditions of a given tumour or its new environment may never be strictly limited. This would suggest, due to its robustness to fluctuations in initial conditions, that the PE modelling assumption is most consistent with the results of murine experimentation, since the characteristic death and regrowth curve is conserved.

Sequencing and order of treatments are vital to their success

In order to test the importance of the order of drug treatments on the resistance phenomenon we have first used homogeneous initial conditions for the ECNE. These conditions also preserves the spherical symmetry of the tumour when drugs are applied uniformly on the periphery. Heterogeneous initial conditions leading to non-spherically symmetric tumours will be tested in Section 3.2.4.

With that understood, in all cases and treatment scenarios the tumours initially respond to treatment, exhibiting a significant period of apoptotic degradation (Fig. 3.5). Experiments wherein only one treatment was used (Fig. 3.5a &

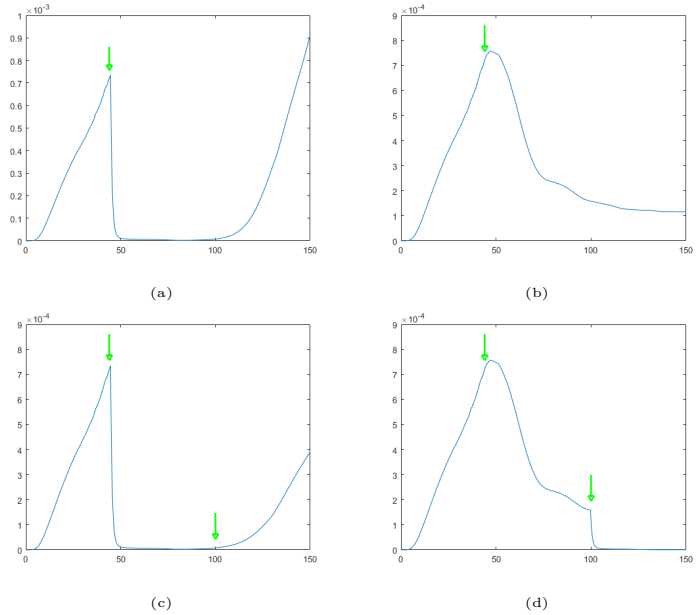

Figure 3.5: **The sequencing of treatments is crucial to success.** Overall tumour volume over time, calculated using (3.28), with the drug strategies (a) BRAFi, (b) ipilimumab, (c) BRAFi followed by ipilimumab, and (d) ipilimumab followed by BRAFi; where the drugs are applied constantly after some $t = 45$ (1^{st} *green arrow*) and then $t = 100$ (2^{nd} *green arrow*) when applicable

3.5b) show dramatically differing clinical treatment profiles. BRAFi treatment shows an extremely promising tumour response with almost complete erradication occuring within days of treatment but followed by an exaggerated regrowth (Fig. 3.5a), as seen in murine experiments. Ipilimumab therapy does not show as successful an eradication pattern at earlier time points but is more consistent in quelling its resistance and resulting regrowth (Fig. 3.5b), although ultimately unsuccessful in eradicating the tumour.

Observing the therapeutic strategy of utilising a BRAFi treatment followed by an ipilimumab post-treatment is ineffective at destroying the tumour (Fig. 3.5d). Although the ipilimumab post-treatment is slowing the growth of the now aggressive tumour, it may already be resistant to immunological therapies. The ipilimumab treatment followed by BRAFi post-treatment, however, appears to be extremely effective (Fig. 3.5d), with a negative growth rate for the tumour volume maintained as of $t = 1000$ (Results not shown). This counter-

intuitive result may be explained as follows: Firstly, BRAFi appears extremely effective at depleting the tumour volume but is incapable of preventing the resistant escape of subpopulations to higher values of y (Fig. 3.5a). On the other hand, ipilimumab's effectiveness function is centred at a greater value of y than BRAFi's, making ipilumumab appear less effective but allowing ipilimumab to effectively confine surviving tumour cells at lower values of y, where BRAFi remains effective. Therefore, these results would suggest that BRAFi should be used to destroy the tumour once its tendency towards resistance has been stemmed through ipilimumab's immunological mechanisms.

Oscillatory tumour volumes as a result of periodic treatments do not necessarily imply re-sensitisation

Our second experimental approach was to attempt the experiment of Thakur *et al.* [77] who implemented a periodic treatment regimen for their *in vivo* tumours. This periodic treatments managed to eradicate the death and rapid regrowth phases of those previous experiments and instead resulted in oscillatory dynamics in the tumour volume. Across several cycles of these treatments, some tumours managed to outgrow the drugs and became resistant, although more slowly, whilst others appeared to reduce their volume even over far longer time-periods. The research team explained this by suggesting that the application of less severe treatment regimes may delay the resistance to treatment in solid tumours by failing to encourage the development of such resistance.

Likewise, in our experiments we observed an oscillatory dynamics resulting from the periodic application of smaller dosages to the tumour and subsequent removal of the dose. We found that as we increased the number of independent starting y positions in the initial conditions for our cancer cell population, our results gave a greater qualitative agreement with those of Thakur *et al.* [77]. Moreover, we found that there was a strong correlation between the average y-position of the initial condition and the final tumour volume at $t = 160$.

These results allowed us to reinterpret this oscillatory behaviour. In our *in*

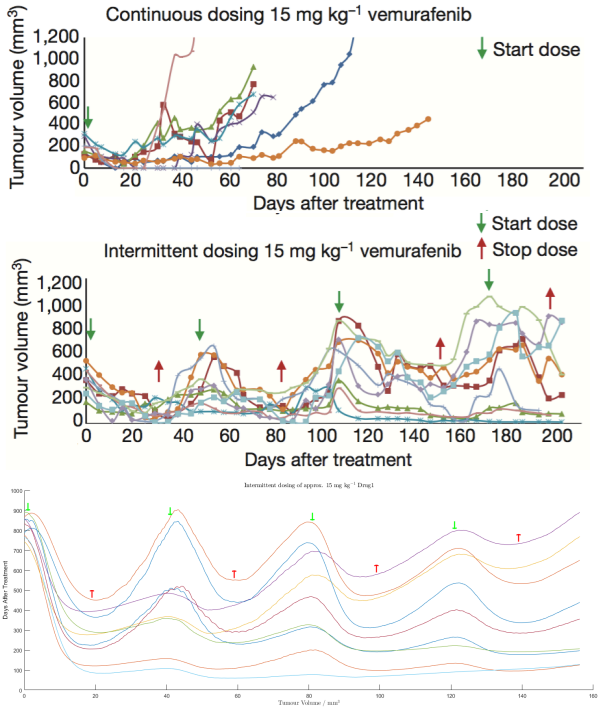

Figure 3.6: **Oscillatory tumour volumes can emerge in the absence of re-sensitisation.** The *top* and *middle* panels are figures from Das Thakur *et al.* [77] for *in vivo* melanoma tumours under an intermittent dosing strategy and the *bottom* panel gives the *in silico* results of the same experiments run using the mutational mathematical model. (Licenses applied for from Nature Publishing Ltd.)

silico model, the acquisition of resistance is certainly not delayed because cells are progressing irreversibly in the y direction. In fact, what may be occurring is that in a situation where some number of cells are resistant whilst other are not, these two heterogeneous subpopulations will have to compete for available nutrients in the environment. Not only this but, together, they will consume more nutrients, leaving fewer such nutrients for the resistant subpopulation and leaving a greater subpopulation sensitive to existing treatment options. A dynamical state will be reached where the two sub-populations are oscillating while keeping their volumes bounded.

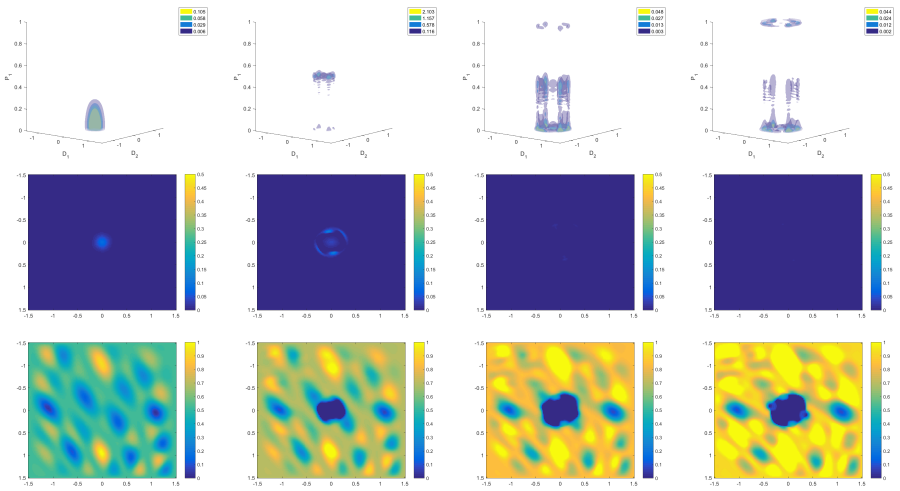

(a) t=5 (b) t=40 (c) t=80 (d) t=120

Figure 3.7: **Spatial heterogeneity eradicates treatment success.** Panels displaying (*top*) the structured cellular population with space across the lower plane and mutational state given along the vertical axis; (*middle*) the spatial cellular distribution; and (*bottom*) the ECNE density, where ipilimumab treatment is given at $t = 40$ and BRAFi treatment is given at $t = 100$, for time points $t \in \{5, 40, 80, 120\}$ are shown.

Drug success rates decay under heterogeneous spatio-environmental assumptions

In order to examine the effect that spatial heterogeneity of the ECNE concentrations and, thusly, the resulting cancer cell population on the longer term effectiveness of targeted and immunological treatments, we considered only that treatment protocol which proved effective in the homogeneous case; namely that of an ipilimumab treatment followed by BRAFi post-treatment. The introduction of spatial heterogeneity whilst maintaining all other factors, in their entirety, was sufficient to cause the degeneration of treatment success into the characteristic death and regrowth curves seen previously (Results not shown, although they may be inferred from figures 3.7 & 3.8 *middle*).

Notice, firstly, that the spatial cancer cell population (Fig. 3.7 & 3.8 *middle*) initially spreads to the nearby regions of elevated ECNE concentration, prior to treatment. As the treatment is applied, and the regions of highest cell population coincide with the regions of highest ipilimumab concentration, the cell

population is reduced to invisibility for some times $40 < t < 200$. It should be understood, here, that under a great evolutionary selective pressure only very few cells survive these initial waves of treatment but those cells which do survive will be completely resistant to both treatments. At this time, and with almost the entirety of the surviving cellular population being resistant to both BRAFi and ipilimumab, the cellular population begins to regrow at regions of highest nutritional content, or ECNE.

One may observe this dynamic in the spatio-structural cellular population, progressively over the entire time domain. Consistently with the punctuated equilibrium assumptions within the model, one notices a pulsatile movement of the cellular subpopulations between $y = 0$ and $y = 1/2$, and again towards $y = 1$ (Fig. 3.7 & 3.8 *top*). In particular, however, the first time at which the cancer cell population has been visibly eradicated (Fig. 3.7c), the visible coincidence of those areas of low ECNE concentration with those cancer cell clusters at the most elevated value of y. In other words, the difference in the heterogeneous case, as compared with the homogeneous case, is that the cancer cell population is able to preferentially avoid drug-induced apoptosis by remaining in regions of low ECNE and drug concentrations, which allows the cellular population to become resistant before migrating to regions of high nutrition and increasing their collective proliferation rate.

This demonstrates that particular prudence must be paid during consideration of spatial factors in the study of drug resistance and strategy. One should also notice the clinically difficult tumour that results from this method of treatment (Fig. 3.8d *middle*) and the nature of the underlying environmental infrastructure, or ECNE. The tumour is viable although sparsely populated which raises significant questions about the ability to remove such a tumour, surgically. The approach to treating such a patient would classically be to use chemical means, which have now been exhausted and given rise to a uniformly resistant tumour.

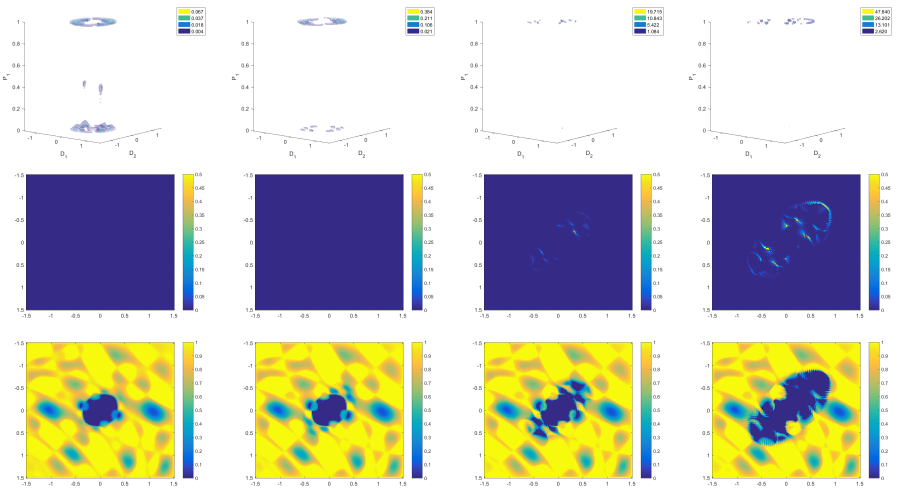

(a) t=160 (b) t=200 (c) t=240 (d) t=280

Figure 3.8: **Spatial heterogeneity eradicates treatment success.** Panels displaying (*top*) the structured cellular population with space across the lower plane and mutational state given along the vertical axis; (*middle*) the spatial cellular distribution; and (*bottom*) the ECNE density, where ipilimumab treatment is given at $t = 40$ and BRAFi treatment is given at $t = 100$, for time points $t \in \{160, 200, 240, 280\}$ are shown.

3.2.5 Metabolic Remodeling and the Re-Establishment of Drug Sensitivity

Recent studies have looked at the effect of BRAFi on the human melanoma PDX lines implanted in the immunodeficient mouse and found that this drug is largely ineffective, implicating a role for the immune system in its functioning. This result is contrasted with the effectiveness at eradicating the tumour with BRAFi+MEKi, again with the characteristic relapse curve [278].

These same studies have suggested that after a primary phase of treatment, and subsequent washing of the drug species from the tumour, the cancerous cells may regain their sensitivity [278]. This is illustrated in the cells' recapitulation to later phases of treatment and suggests that some metabolic, or other, plasticity may lead to the observed resistance to BRAFi and MEKi. This plastic response may be reversed upon the removal of the drug and is believed to be as a direct result of stress on the cells themselves.

Beyond these conclusions of the study, the observation is made that the

system remains the genetic equal of the precursor tumour at every stage during this adaptive process. This suggests that a population-wise phenotypic switch occurs from populations that are composed 1% of epigenetically resistant cells, prior to treatment, to being comprised 70% of this cell type, post-treatment and post relapse [278]. Little is known about the phenotypic status of the tumour immediately prior to the secondary round of BRAFi+MEKi dosing.

Moreover, cutaneous tissue is naturally and significantly heterogeneous in its composition and, being the tissue furthest from the major vasculature, is greatly dependent on the arterial supply of oxygen and other nutritional components of the cellular system. In areas with the lowest such supplies of oxygen, cells switch their metabolism from mostly oxidative phosphorylation (oxphos) to glycolysis. Using, then, BRAFi and MEKi in order to inhibit the glycolytic pathway [259, 41] induces an excessive stress regimen within the cell. It has been suggested that, under such powerful metabolic stresses, the cell will diversify its metabolic behaviour in order to attempt an increase in efficiency. This switching between glycolytic and oxphos modes of metabolism may, therefore, be instrumental in facilitating the avoidance of targeted inhibition within cancer cells; cancer cells may use oxphos metabolism to avoid the targeted inhibition of glycolysis [145].

This, however, implies that we are now existing within a different paradigm with respect to the evolution of the cells in response to drug application or, perhaps, in general. To begin with, we recall that $p_1(t, x)$ is given by the spatio-temporal concentration of BRAFi and we, now, redefine that $p_2(t, x)$ should be given by the spatio-temporal concentration of MEKi, a second metabolic inhibitor of glycolysis.

Re-interpreting the structural dimension for a metabolic system

In order to capture the re-sensitisation phenomenon, we must reinterpret the structural y variable to take into account the newfound plasticity of the cellular population. We assume that the effect of the drugs and the variability in the cellular population may be adequately illustrated through the cellular pathways

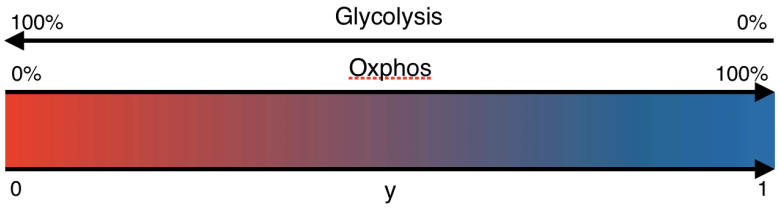

Figure 3.9: Visual reinterpretation of the structural y variable to account for the metabolism of glucose molecules proportionally and competitively through glycolytic and oxphos pathways, respectively.

involved in the metabolism of glucose; namely those of glycolysis and of oxphos. Given that a given glucose molecule, may be metabolised through the utilisation of either one of these pathways, but not both, we may represent the structure of the cell as the proportion of glucose sent to glycolytic pathways as opposed to oxphos pathways; such that $y = 0$ represents 100% of glucose being metabolised through glycolysis, and 0% by oxphos, whilst $y = 1$ represents 0% of glucose being metabolised through glycolysis, and 100% by oxphos (Fig. 3.9).

A cellular growth function in a metabolic system

Likewise with our previous paradigm, we assume that proliferation requires the presence of nutrients, $m_2(t, x)$, above a certain threshold, θ_{m_2}. As was recognised by Warburg in 1956 [338], and was subsequently termed the Warburg effect, highly proliferative cancer cells appear to preferentially utilise glycolytic pathways to synthesise membrane lipids and other essential components from glucose. Therefore, we assume that there exists some underlying proliferation rate, $\phi_{c,1}$, which is common amongst all cells and a further 'Warburg' proliferation rate, $\phi_{c,2}$, which is contributed dependent upon the degree to which the cell utilises glycolysis; as the cell utilises the glycolytic pathways to a greater extent, its proliferation rate shall increase concurrently. Moreover, since we are particularly interested in the cell's ability to absorb and utilise available nutrients in the environment, we modify our competition assumptions so that the cellular population's proliferation will not be inhibited by the presence of the ECNE but will rather simply increase the pressure on the ECNE itself. Thusly,

we replace the unoccupied volume term by $1 - \int_{\mathcal{P}} c\, dy$ and write the full growth term as

$$\phi_M(y, c, \bar{m}) := c \left(1 - \int_{\mathcal{P}} c\, dy\right) \Big(m_2 - \theta_{m_2}\Big)\Big(\phi_{c,1} + \phi_{c,2}(1-y)\Big). \tag{3.29}$$

A structural flux function in a metabolic system

The cell is biologically engineered to complete its cell cycle and evolution has selected for cellular populations who are particularly efficient at achieving this goal. Therefore, given that a cell requires nutrition and the ability to freely adapt in order to achieve this objective, if the cell is deprived of its essential environment then it will take extreme measures in order to continue to proliferate. We here define stress, or 'stressed conditions', as those conditions which are not conducive to cellular metabolism and proliferation. In particular, those scenarios which would lead the cell to feel 'stressed' are given explicitly by nutritional deprivation or targeted inhibition of metabolically essential genes, such as BRAF or MEK. Therefore, we define the weighted stress term as $\psi_{p_1} p_1 + \psi_{p_2} p_2 - \psi_{m_2} m_2$, where ψ_{p_1}, ψ_{p_2}, ψ_{m_2}, are positive weights such that $\psi_{p_1} + \psi_{p_2} + \psi_{m_2} = 1$. Under stress, the cell shall randomly diversify its behaviour; each cell becoming stochastically more or less oriented towards glycolytic metabolism such that the population, as a whole, becomes more metabolically diverse. Therefore, we may represent this at the population level by a structurally diffusive behaviour. The structural diffusion coefficient $\Sigma(y, \bar{m}, \bar{p})$ is proportional to the weighted stress, therefore

$$\Sigma(y, \bar{m}, \bar{p}) = \sigma_c \left(\psi_{p_1} p_1 + \psi_{p_2} p_2 - \psi_{m_2} m_2\right), \tag{3.30}$$

where σ_c is a positive constant.

In the absence of stress, the cell population relaxes by advection to the preferential metabolic state $y = \omega_c$. The relaxation rate is proportional to the weighed non-stressed factor defined as $1 - \psi_{p_1} p_1 - \psi_{p_2} p_2$. Thus, the normalized

structural velocity reads

$$\Psi_M(y, \bar{m}, \bar{p}) = \bar{\sigma}_c \left(\omega_c - y\right) \left(1 - \psi_{p_1} p_1 - \psi_{p_2} p_2\right) , \tag{3.31}$$

where $\bar{\sigma}_c$ is a positive constant.

On phenotypically evolving systems

Thusly, we describe the metabolic change function, $\Psi : \mathcal{D} \times \mathcal{P} \to \mathbb{R}$, in terms of the phenotypic stress on the cell. We assume, firstly, that under a condition in which the influence of stressors is minimised, the cell has a preferred phenotypic state at $y = \omega_c$, which corresponds to a given utilisation of each pathway. We also assume that the primary stressors for the cell are malnutrition, which will be a function of m_2, the presence of BRAFi, p_1, and that of MEKi, p_2, which act to deplete the cells ability to proliferate effectively.

Then the non-stressed term in the function must be given such that phenotypic advection is positive below this preferential state and negative above this state such that it will depend upon the relation $1 - \omega_c$ for a non-dimensionalised system. The non-stressed condition must then be given by the opposing probability to that of stress such that $\Psi_{\bar{\sigma}} := 1 - \psi_{p_1} p_1 - \psi_{p_2} p_2$, with parameters chosen such that $\Psi_{\bar{\sigma}} \geq 0$, $\forall (t, x) \in \mathcal{I} \times \mathcal{D}$.

Stressed conditions for the cell are then quantified by the gradient of the cellular concentration in the region, giving a measurement of the collectivity of the behaviours of local cells. This choice of function for stressed conditions gives rise to diffusion under cellular stress, the rationale for which can be given by the intuitive understanding that cells diversify their behaviours in the presence of stressors. The magnitude of this stress is then determined by the concentrations of BRAFi, p_1, and MEKi, p_2, and is linearly diminished with the concentration of nutrient species, m_2. All of these factors act as stressors to the cell and have their relative effects quantified by the weights ψ_{p_1}, ψ_{p_2}, $\psi_{m_2} \geq 0$, respectively.

Then, the structural flux has diffusion and advection terms as follows

$$\begin{aligned}\Psi_M(y,\bar{m},\bar{p}) := &-\sigma_c\left(\psi_{p_1}p_1+\psi_{p_2}p_2-\psi_{m_2}m_2\right)\nabla_y c(t,x,y)\\ &+\bar{\sigma}_c\left(\omega_c-y\right)\left(1-\psi_{p_1}p_1-\psi_{p_2}p_2\right)c(t,x,y)\,,\end{aligned} \tag{3.32}$$

with the introduction of the stress, σ_c, and non-stress, $\bar{\sigma}_c$, parameters determining the weightings of the diffusion and advection terms with respect to one another.

Now, one must consider the nature and form of the effectiveness functions for the drug species, BRAFi (p_1) and MEKi (p_2), on the cellular population, in terms of their effect on the glycolytic or oxphos pathways. Firstly, we begin by writing the vector

$$\mathfrak{f}(y) := [\mathfrak{f}_1(y), \mathfrak{f}_2(y)]^T\,,$$

to represent functions $\mathfrak{f}_1(y)$ and $\mathfrak{f}_2(y)$ in compact notation and begin by noticing that both of these drugs target genes essential to glycolysis. The transcription factors HIF1α, c-Myc, and Mondo A have been found to be downstream upregulators of glycolytic behaviours in BRAF^{v600} cells [259, 146]. Moreover, BRAFi has been shown to prevent the hyperswitching of mutant melanoma cells to pyruvate based metabolism [84] – the primary product of glycolysis.

Withal, MEKi is responsible for targeting this same pathway, in melanoma cells. It has also been found that the PI3K pathway, activated by MEK, is responsible for glucose transport, and glycolytic metabolism, and can be inhibited by inhibition of MEK [315, 229].

The biological literature points to a link between melanoma associated genes, including BRAF and MEK, and the glycolytic pathway for glucose metabolism. Therefore, we write that the standard forms of the effectiveness functions will be Gaussian functions, with low values for variance, or high values for $\beta_{\mathfrak{f}_1}$ and $\beta_{\mathfrak{f}_2}$, such that

$$\begin{cases}\mathfrak{f}_1(y) := \exp[-\beta_{\mathfrak{f}_1}(y-\alpha_{\mathfrak{f}_1})^2]\\ \mathfrak{f}_2(y) := \exp[-\beta_{\mathfrak{f}_2}(y-\alpha_{\mathfrak{f}_2})^2]\,.\end{cases} \tag{3.33}$$

The values around which these functions are centred, $\alpha_{\mathfrak{f}_1} < \frac{1}{2}$ and $\alpha_{\mathfrak{f}_2} < \frac{1}{2}$, are chosen to align with the peak effect of the drug on the glycolytic and oxphos pathways.

Finally, we choose the proliferation function, $\phi_M : \mathcal{I}\times\mathcal{D}\times\mathcal{P} \to \mathbb{R}$, such that it is space-wise logistic in $c(t, x, y)$. Moreover, we assume that the cellular population requires nutrient in order to achieve positive proliferation and choose some arbitrary threshold value θ_{m_2} in order that, below such a value, the cellular population is depleted due to malnutrition. It is then imposed upon the system that there are two concurrent modes of proliferation: glycolytic and non-glycolytic. The non-glycolytic mode is not dependent upon the phenotypic state of the cell, y, and is rather an underlying process of all cells, whereas the glycolytic pathway is linearly enhanced by the percentage of glycolytic metabolism utilised (such that it is maximal at $y = 0$). This is justified on account of the excess lipids produced through utilisation of glycolytic pathways. Therefore, we write

$$\phi_M(y, c, \bar{m}) := c\left(1 - \int_{\mathcal{P}} c(t, x, y)\, dy\right)\Big(m_2 - \theta_{m_2}\Big)\Big(\phi_{c,1} + \phi_{c,2}[1 - y]\Big), \tag{3.34}$$

where $\phi_{c,1}$ and $\phi_{c,2}$ give the rates of non-glycolytic and glycolytic metabolism, respectively.

Due to the nature of the structural flux (3.32), it is necessary to develop a set of zero-flux boundary conditions which prevent, for example, diffusion in y from causing cells to exit the domain, $\mathcal{P}$. Although (3.32) has both advection and diffusion terms, the metabolic change function is defined such that $\Psi_{\bar{\sigma}}(y) = 0$, $y \in \partial\mathcal{P}$, meaning that advection fluxes are identically zero on the boundary. Therefore, we simply implement zero-Neumann boundary conditions on structural diffusion fluxes, namely $\nabla_y c(t, x, y) = 0$, $y \in \partial\mathcal{P}$.

To begin treatment, one gradual dosage was given between $t = 80$ and $t = 100$, linearly in time, t. The drug was then washed from the tumour, in a step-wise fashion, at $t = 210$, as this is the point at which the tumour volume had regrown to $\sim$20% of its previous maximum, and the tumour was allowed to

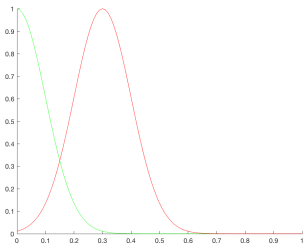

Figure 3.10: Distributions for the drug effectiveness functions $\mathfrak{f}_1(y)$ (*green*) and $\mathfrak{f}_2(y)$ (*red*).

regrow, unencumbered by glycolytic inhibitors for 30 days. A second gradual dosage was then given between $t = 240$ and $t = 260$, whereafter no further interventions were made.

Further, we define the unique structured population profile by the cellular population over the entirety of the spatial domain, $\mathcal{D}$, given by

$$k(t, y) := \iint_{\mathcal{D}} c(t, x, y)\, d\mathbf{x}\,. \tag{3.35}$$

This can be used to describe the metabolic or structural profile of the tumour at a given time, t.

Drug effectiveness functions in a metabolic system

The drug effectiveness functions for BRAFi and MEKi, $p_1(t, x)$ and $p_2(t, x)$ respectively (further discussion in 3.2.5), are given simply by Gaussian functions centred at $\alpha_{\mathfrak{f}_1} = 0$ and $\alpha_{\mathfrak{f}_2} = 3/10$ respectively. We write these mathematically

$$\begin{cases} \mathfrak{f}_1(y) := \exp[-\beta_{\mathfrak{f}_1}(y - \alpha_{\mathfrak{f}_1})^2] \\ \mathfrak{f}_2(y) := \exp[-\beta_{\mathfrak{f}_2}(y - \alpha_{\mathfrak{f}_2})^2]\,. \end{cases} \tag{3.36}$$

whilst the widths of these Gaussian functions are uniform with $\beta_{\mathfrak{f}_1} = \beta_{\mathfrak{f}_2} = 50$ (Fig. 3.10), in order to replicate results from the murine models from [278].

3.2.6 Results for the Metabolic System

Again, our primary motivating factor for these metabolically plastic systems was to understand whether these mathematical models were capable of recreating or predicting the complex dynamics underlying *in vivo* results (Section 3.2.6). Beyond this, we wished to try to understand the spatio-metabolic dynamics of the tumour which are allowing resistance to develop (Section 3.2.6). Finally, given the complexity of the plastic model, we wished to know what the dynamics of the cellular population, under the influence of drugs, might tell us about the reaction of this population to treatments and the clinical significance of this reaction (Section 3.2.6).

In order to test this *in silico* model, we attempted to recreate the conditions in the experiments run by Rambow *et al.* [278]. In these experiments, mice were given a PDX melanoma and the tumour was allowed to grow for some initial period without treatment. Tumours were then treated with BRAFi+MEKi combination therapy at a time point which corresponded to 80 days of growth ($t = 80$) in our *in silico* tumours. As the tumour developed resistance to the treatment, the dose was released at the time point corresponding to the volume of tumour increasing to approximately 50% of its volume prior to treatment, which we selected as $t = 210$ in our tumours. A final dose was given after approximately 30 days of unimpeded growth, at $t = 240$.

Resistance and re-sensitisation dynamics are captured by plastic, metabolic *in silico* modelling

As is the case with the *in vivo* experiments, we observe the death, tolerance, and regrowth pattern within the tumour (Fig. 3.11). This is then followed by a period of rapid, unimpeded growth due to the removal of drugs from the tumour. It is important to notice that upon the second wave of treatment, the tumour is again eradicated entirely for some brief period before becoming resistant more rapidly on this second occasion (Fig. 3.11). This correlates qualitatively with the *in vivo* results but may not be explained by a mutational model since those

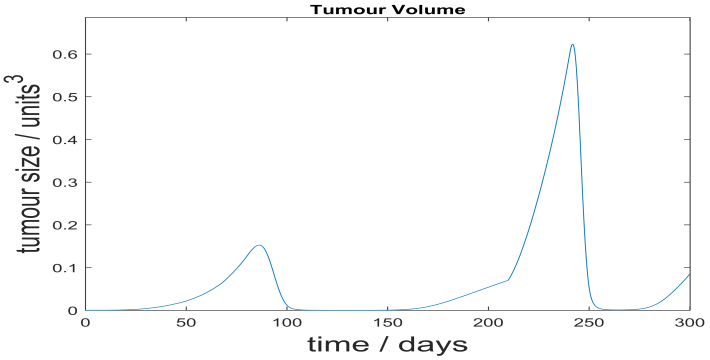

Figure 3.11: **Resistance and re-sensitisation dynamics are captured by *in silico* modelling.** Graph displaying the tumour volume of the metabolic tumour model over the duration of the *in silico* experiment, with continuous doses given from $t \in \{80, 240\}$ and a drug holiday initiated at $t = 210$

resistant cells would not reestablish their sensitivity to treatment. This effect is termed 're-sensitisation' and may be biologically and clinically significant.

In order to more accurately capture the results of the biological, experimental approach we use a lower dosing rate in this model. Also, the dose was applied uniformly in time between the start and the end of the treatment, instead of instantaneously (we used Heaviside functions instead of Dirac functions for the drug temporal profiles). This ensured a more gradual switch from the initial growth stage in the tumour to a drug-sensitive apoptotic phase, prior to tolerance (Fig. 3.11). Moreover, the primary regrowth stage appears to be damped in comparison to the mutational model under BRAFi treatment, alone, but this could be explained by the supplementary dosing of the tumour with MEKi, stunting regrowth to a greater extent.

Temporary oxphos metabolism may allow cancers to evade targeted treatments

Recall that lower values in y are associated with more glycolytic modes of metabolism, where higher values of y are associated with more oxphos modes of metabolism and that each of these structural y-coordinates is associated with a 2D spatial x-coordinate. Moreover, a *green* encircled 1 in the upper right-hand

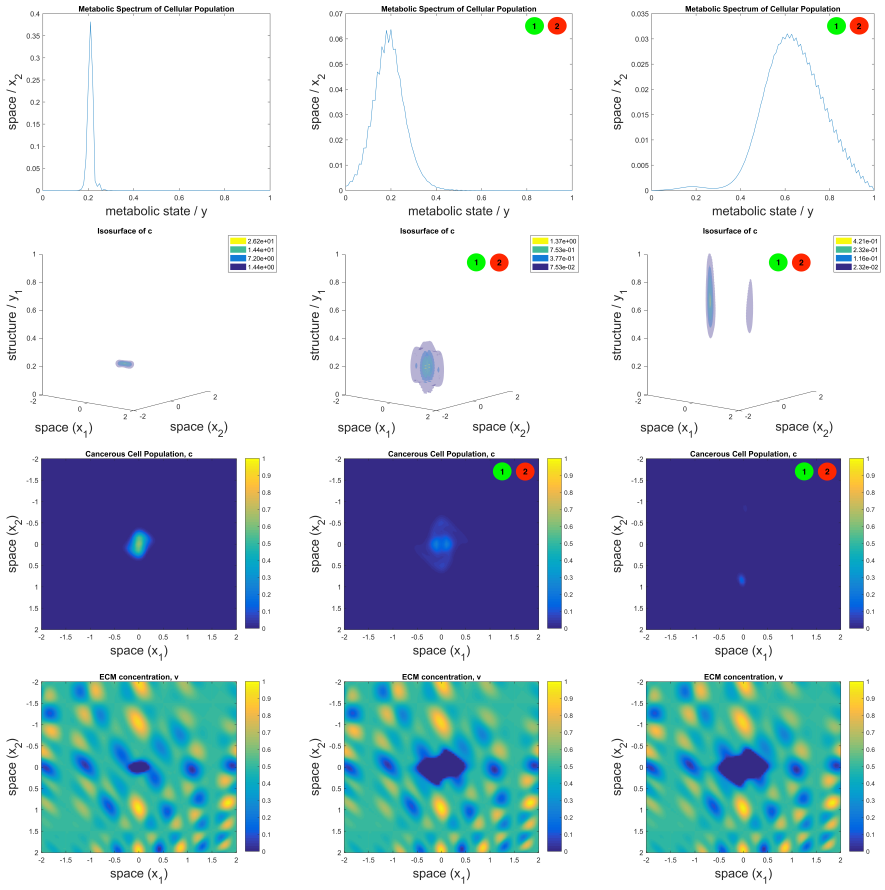

(a) t=50 (b) t=100 (c) t=150

Figure 3.12: **Tumours use oxphos metabolic pathways to resist targeted inhibition of glycolytic pathways by BRAFi and MEKi therapies.** Shown are the phenotypic distribution (1^{st} *row*); the spatio-phenotypic surface distributions (2^{nd} *row*); and spatial distribution (3^{rd} *row*) of the cellular population. The spatial distribution of the ECNE, with colour-bar, is also shown (4^{th} *row*), for completeness and in order that one can place the tumour within its environmental context. All figures are given at times $t \in \{50, 100, 150\}$ within subfigures (a), (b), and (c) respectively. Within the surface plots, the colours represent surfaces of approximately equal concentrations within the spatio-phenotypic context of the cell gradiated from lowest to highest concentration as purple, blue, green, then yellow.

corner of a graphic shall signify that the tumour is under BRAFi treatment, where a *red* encircled 2 in the upper right-hand corner of a graphic shall signify that the tumour is under MEKi treatment (Fig. 3.12–3.15).

Observe, then, that in the initial growth phase (Fig. 3.12a) the cell population is tightly associated with a glycolytic metabolic state and that its spatial composition is compact, whilst during the sensitivity phase (Fig. 3.12b) the cell

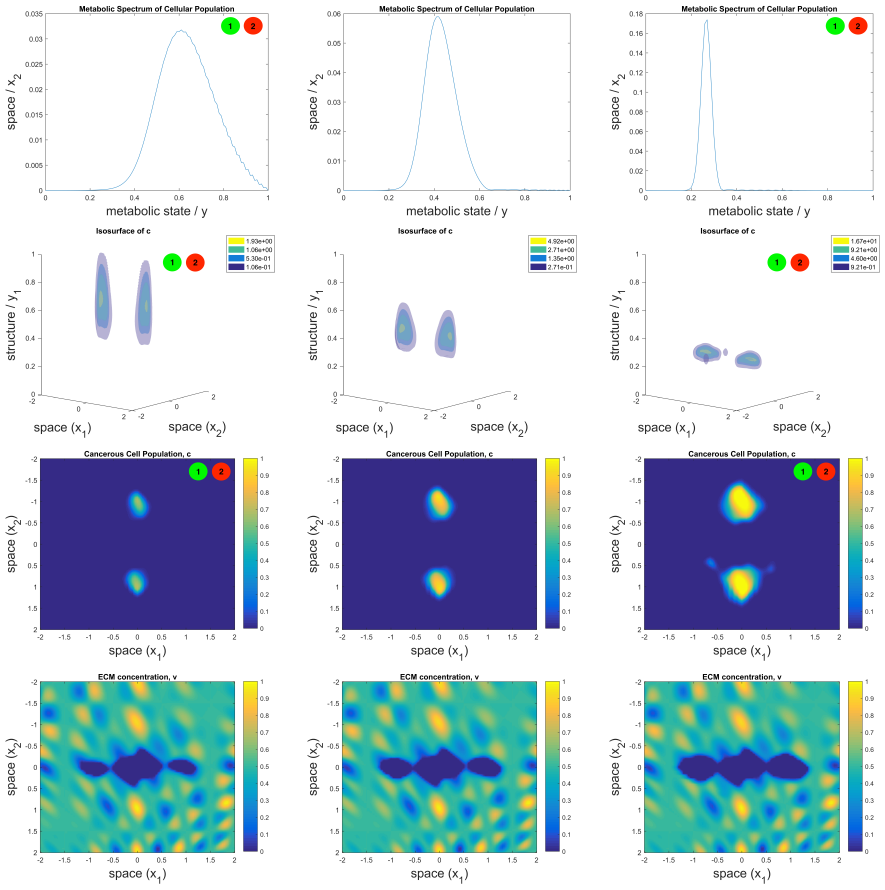

(a) t=200 (b) t=220 (c) t=240

Figure 3.13: **Tumours use oxphos metabolic pathways to resist targeted inhibition of glycolytic pathways by BRAFi and MEKi therapies.** Shown are the phenotypic distribution (1^{st} *row*); the spatio-phenotypic surface distributions (2^{nd} *row*); and spatial distribution (3^{rd} *row*) of the cellular population. The spatial distribution of the ECNE, with colour-bar, is also shown (4^{th} *row*), for completeness and in order that one can place the tumour within its environmental context. All figures are given at times $t \in \{200, 220, 240\}$ within subfigures (a), (b), and (c) respectively. Within the surface plots, the colours represent surfaces of approximately equal concentrations within the spatio-phenotypic context of the cell gradiated from lowest to highest concentration as purple, blue, green, then yellow.

population begins to diverge from this behaviour and cells may be spatially observed further afield. Moreover, and throughout this phase, one can observe the degeneration of the narrow peak, during the initial growth phase (Fig. 3.12a, 1^{st} *row*), into a larger metabolic distribution centred at the same position as this initial peak (Fig. 3.12b, 1^{st} *row*). The increase in variance of the metabolic distribution is as a result of the diversification of metabolism under stressed

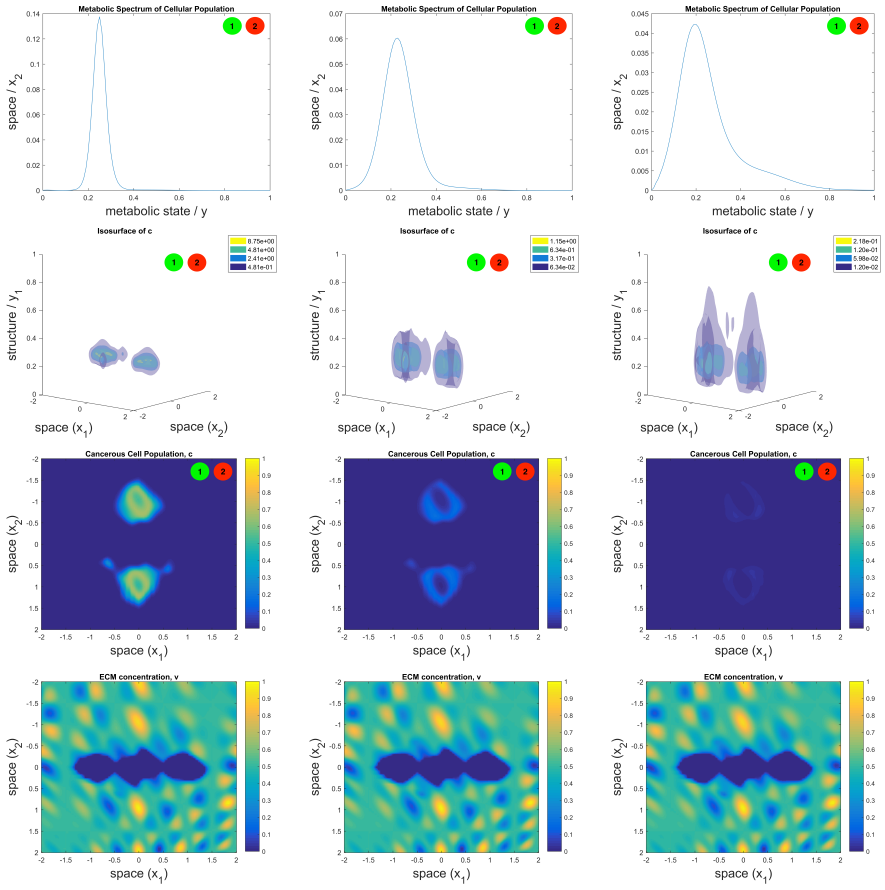

(a) t=245 (b) t=250 (c) t=255

Figure 3.14: **Tumours use oxphos metabolic pathways to resist targeted inhibition of glycolytic pathways by BRAFi and MEKi therapies.** Shown are the phenotypic distribution (1^{st} *row*); the spatio-phenotypic surface distributions (2^{nd} *row*); and spatial distribution (3^{rd} *row*) of the cellular population. The spatial distribution of the ECNE, with colour-bar, is also shown (4^{th} *row*), for completeness and in order that one can place the tumour within its environmental context. All figures are given at times $t \in \{245, 250, 255\}$ within subfigures (a), (b), and (c) respectively. Within the surface plots, the colours represent surfaces of approximately equal concentrations within the spatio-phenotypic context of the cell gradiated from lowest to highest concentration as purple, blue, green, then yellow.

conditions, whereas the displacement of the mean towards a resistant oxphos population (Fig. 3.12c, 1^{st} *row*) is as a result of selective pressure.

During the resistance phase, the newly oxphos population continues to proliferate (Fig. 3.13a), whilst any glycolytic cells are induced to apoptosis. When the drugs are washed from the tumour, however, at $t = 210$ one observes the cellular population beginning to migrate monotonically towards its preferred metabolic

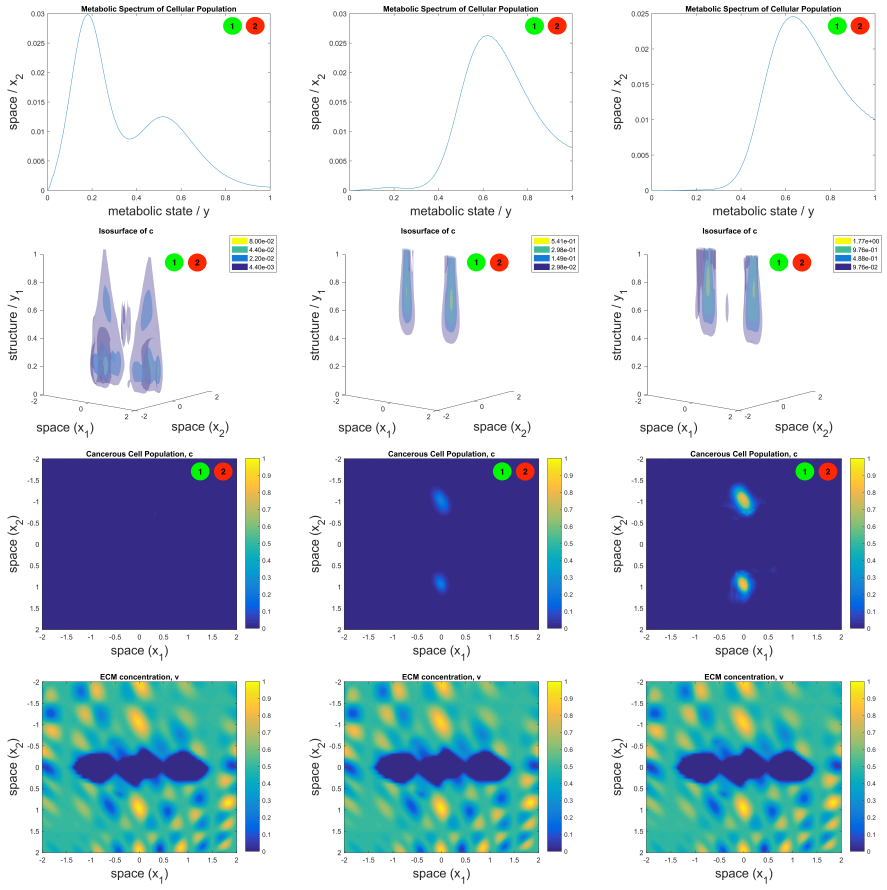

(a) t=260 (b) t=280 (c) t=300

Figure 3.15: **Tumours use oxphos metabolic pathways to resist targeted inhibition of glycolytic pathways by BRAFi and MEKi therapies.** Shown are the phenotypic distribution (1^{st} *row*); the spatio-phenotypic surface distributions (2^{nd} *row*); and spatial distribution (3^{rd} *row*) of the cellular population. The spatial distribution of the ECNE, with colour-bar, is also shown (4^{th} *row*), for completeness and in order that one can place the tumour within its environmental context. All figures are given at times $t \in \{260, 280, 300\}$ within subfigures (a), (b), and (c) respectively. Within the surface plots, the colours represent surfaces of approximately equal concentrations within the spatio-phenotypic context of the cell gradiated from lowest to highest concentration as purple, blue, green, then yellow.

state (Fig. 3.13b, 1^{st} *&* 2^{nd} *rows*), ω_c as observed at earlier time points (Fig. 3.12a, 1^{st} *row*), before reestablishing its glycolytic phenotype $y \approx \omega_c = 0.2$ at $t = 240$ (Fig. 3.13c). This whole process is then repeated during the second wave of treatment (Fig. 3.13c, 3.14 & 3.15), with the tumour being visibly eradicated during a process of metabolic diversification and upheaval (Fig. 3.14b, 3.14c & 3.15a) before regrowing as an oxphos oriented tumour (Fig. 3.15b &

3.15c).

In this model, one may far more clearly see that the regrowth in the tumour is spatially correlated with the regions of highest ECNE concentrations (Fig. 3.12c, 3^{rd} *&* 4^{th} *rows*) and those regions where the cellular species will necessarily have the greatest access to nutrients. Interestingly, this will also be the spatial subregion in which the selective pressure is most elevated due to the presence of high concentrations of BRAFi+MEKi leading to the apoptosis of glycolytic cells and selecting for a more oxphos-dependent population of cells (Fig. 3.12c & 3.13a, 2^{nd} *row*).

To sum the above analysis of these results, the tumour exhibits an initially glycolytic mode of metabolism which, through stress-induced diversification, decays into a less defined mode of glucose metabolism. By spatially correlating with regions of heightened nutritional content, these resistant oxphos cells are able to outgrow their drug-induced apoptotic rate and proliferate. By removing the drug from the tumour, and the stressor of the cell, the cellular population attempts to reconsolidate its glycolytic state and increases its proliferative rate, ultimately allowing the second wave of treatment to visibly eradicate the remaining population of cells. Nevertheless, these cells are able to regain their metabolic advantage and return to an oxphos state, in order to once again become resistant to treatment.

More rapid secondary resistance wave may be explained by residual oxphos populations

One feature of the growth, which is of great clinical significance, is that of the increased rapidity to resistance upon the second wave of treatment (Fig. 3.11). In order to understand this, notice the pattern of metabolic migration in the cancer cell population, towards the preferred glycolytic state, during the drug holiday (Fig. 3.13). The tail on the right-hand side of the oxphos cell distribution (Fig. 3.13a & 3.13b, 1^{st} *row*) are not entirely consolidated during their backwards migration but, rather, remain as a residual oxphos cell population (Fig. 3.13b,

1^{st} *row*), which begin to appear upon selective degradation of glycolytic populations (Fig. 3.14b, 1^{st} *row*). Although these cells will migrate gradually towards their preferred metabolic state, ω_c, it could be that their lower local nutritional value is allowing them to retain their oxphos state to a greater extent than the remainder of the population. Under the selective pressure applied by the drug, the glycolytic subpopulation is degraded, as it again attempts to diversify its metabolic status, whilst the oxphos population is free to grow (Fig. 3.14b, 3.14c, & 3.15, $1st$ *&* 2^{nd} *rows*), eventually replacing the glycolytic population as the dominant population within the tumour (Fig. 3.15b & 3.15c).

One may also clearly observe the difference in the spatio-structural distributions 20 days posterior to the first wave of treatment (Fig. 3.12b, 2^{nd} *row*) in comparison to 20 days posterior to the second (Fig. 3.15a, 2^{nd} *row*). After the first wave of treatment, the tumour having never been exposed to stress prior to this event, the metabolic profile of the tumour is neatly distributed around its preferred glycolytic state. After the second wave of treatment, however, the metabolic profile is bimodal, with a distinct oxphos as well as a glycolytic population. This appears to be due to the fact that not all of the cells from the resistant oxphos population have migrated fully back to their preferred glycolytic state and are, thus, able to repopulate the new resistant population far more rapidly since they are not subject to the same selective pressures as their glycolytic counterparts.

3.2.7 Discussion

We have introduced a general modelling framework for evolution of heterogeneity in solid tumours submitted to multiple drug therapy, wherein the definition of an appropriate normalized structural velocity, $\Psi(y, \bar{m}, \bar{p})$; structural diffusion matrix, $\Sigma(y, \bar{m}, \bar{p})$; growth function, $\Phi_c(y, \bar{m}, c, v)$; and vector valued drug effectiveness function, $\bar{\mathfrak{f}}(y)$, may give rise to importantly nuanced patterns of behaviour. Using this framework, we then introduced two primary models for considering different dynamics within a tumour population. Firstly, the mu-

tational model considered population level dynamics for a system in which an individual cell will sequentially undergo a BRAF mutation, followed by subsequent mutations which confer resistance to BRAFi and ipilimumab therapies. Secondly, we considered a plastic model of drug resistance, in which the switching of cellular dependence on glycolytic and oxphos pathways for the metabolism of glucose may confer a survival advantage when faced with glycolysis inhibiting BRAFi+MEKi treatments.

Using our mutational model to consider paradigms of punctuated equilibrium and phyletic gradualism in the evolution of the cellular genome, we found that punctuated equilibrium assumptions were more consistent with biological data. This shows good consistency with the modern cancer genomic literature, in asserting that short term catastrophes, rather than the gradual accumulation of mutations, is more likely to contribute to the mutational state of tumours [305, 240, 295]. We also predicted that using ipilimumab, immune cell-enhancers, in advance of a BRAFi is more effective at reducing the tumour population over the long term. This model prediction is confirmed by studies which used both ipilimumab and BRAFi [3].

Performing experiments for which drug was applied periodically in time we were able to qualitatively recapitulate the results of Thakur *et al.* [77]. We have suggested a mechanism for the apparently counterintuitive result of this experiment, that consists in keeping the tumour under control without completely eliminating the resistant subpopulation. We suggest that relative success of this therapy protocol in some tumours may imply their lesser mutated states at the initiation of the experiment, where the irregularity of the oscillations appears to depend on the number of different clones within or the clonal heterogeneity of the sample. This hypothesis may, presumably, be tested biologically in order to confirm this prediction from our model. The decay of the success of varying treatment strategies within a heterogeneous ECNE is consistent with the *in vivo* failure of treatments to adequately deal with tumours on the long term, and our experiments still predicted the preservation of the characteristic death and growth curves [267] under heterogeneous initial conditions.

Turning to the plastic metabolic model for the development of resistance to targeted therapies, we proposed and conformed the ability of such a model to predict re-sensitisation *in silico*. This model may then provide a clinical opportunity to model the success of therapy against such tumours on the basis of their respective environments (i.e. for tumours in differing tissue elasticities or densities). Moreover, our model illustrates the metabolic switching of the tumour as a continually heterogeneous spatio-structural population, allowing one to understand how spatial effects may influence structural resistance manoeuvres. The evolution of the glycolytic tumour to a metabolically oxphos cell populations, in combination with the coincidence of strongly selected cell populations and nutrient populations, may allow for the resistant proliferation of these subpopulations. These metabolically resistant populations will then preferentially re-sensitise themselves through metabolic remodelling, allowing for the effective second wave of treatment.

Moreover, our model provides an opportunity to understand the underlying dynamics of such metabolically plastic tumours and also the mechanisms of resistance and re-sensitisation, showing strong agreement with *in vivo* PDX tumour experiments. For both waves of treatment, our model shows a characteristic death, tolerance, and regrowth pattern, but with a quicker relapse occurring with the second wave of treatment. Experiments conducted by Rambow *et al.* [278] also show this pattern of death and growth, with faster regrowth posterior to the second wave of treatment, such that our model may provide an explanation of this phenomenon. Residual, metabolically resistant cells from the first wave of treatment may provide a basis for a resistant population to grow back more quickly upon the second wave of treatment. Implicitly, our model would predict that reducing treatment to as great an extent as is possible, whilst still eradicating the tumour, would reduce the opportunity for the tumour to establish this residual population and resist future waves of treatment.

3.3 Higher-Dimensional, Data-Driven Modelling of Drug Resistance in Melanoma

3.3.1 Introduction

In an important advancement to the paradigm of cancer investigation, Rambow *et al.* [278] used single-cell RNA-sequencing to anlyse whole melanoma tumours from patient-derived xenografted (PDX) mice who had been treated with BRAF and MEK targeted inhibitory therapies. Using principle component analysis (PCA) followed by t-distributed stochastic neighbour embedding (tSNE) techniques, subpopulations of cells exhibiting several phenotypes significant to cancer prognosis and progression were identified, alongside their development in time. In this particular case, although this also holds more generally, the treated tumour development cycle was separated into 4 major stages (pre-treatment; sensitivity, exhibiting extensive cell death; tolerance, exhibiting neither death nor growth of cells; and resistance, exhibiting growth even with the continued presence of the treatment), while measurements were taken from several mice during each of these stages. This yielded significant insights about the fundamental nature of cancer cells, including a detailed and temporally quantitative demonstration of the, at least, inter-generational plasticity of cancer cells and their propensity to give rise to resistant strains that were absent before treatment.

In order to deal with this paradigm, we employ those multi-dimensional models that we had used previously, for the modelling of phenotypic resistance to treatment in melanoma, and utilise this same framework (3.11) once more. The method by which we establish the nature of the functions within this framework, however, must entirely differ since we had, previously, the dynamics of our structural dimensions, *a priori*, and had simply to place these within a spatial context. On this occasion, the functions describing the structural dynamics of the system are not pre-determined. Therefore, the function to be placed within these dynamical equations shall be determined through a meta-heuristic

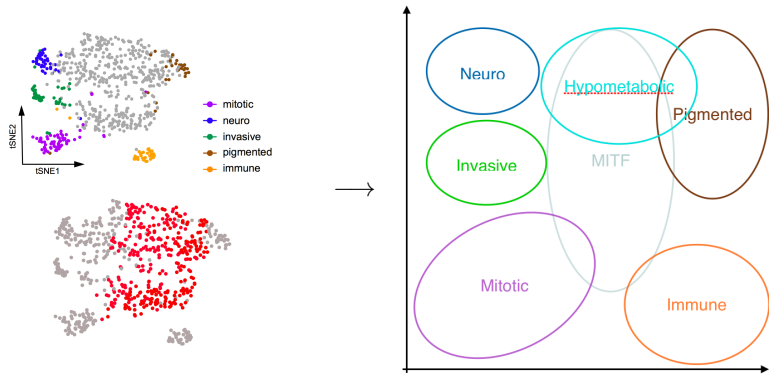

Figure 3.16: tNSE data becomes principal axis map (PrAM).

analysis of the data, rather than through a theoretical approach; producing a system which is significantly more difficult to interpret. This is also likely due to the difficult nature of interpreting the tSNE data itself, since these represent more abstract natural constructs rather than pure properties. Finally, we must reïnterpret the structural variable, y, in order that it is able to account for the biological context in which we wish to place our model.

3.3.2 Spatio-Structuro-Temporal Modelling of Single-Cell RNA-seq Data

Firstly, we note the biological context in which we place this model: The mapping of the metabolic profile, drawn through the use of principal component analysis on single cell RNA-seq data [278], has managed to describe the vast array of biological, or metabolic, heterogeneity within PDX melanomas under treatment, using only two principal axes. As such, we call this map the principal axis map (PrAM) and define our metabolic variable $\bar{y}$ correspondingly with those principal axes (Fig. 3.16). Therefore, y_1 becomes the 'east-west' variable and y_2 becomes the 'north-south' variable where, for example, to move metabolically north is only to move through positive values on the secondary metabolic principal axis, or y_2. As in traditional cartography, the difficulty and ramifications of moving in a given direction are dependent on the context provided with

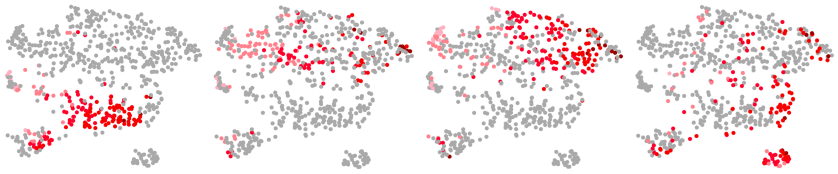

(a) Phase t_0 (b) Phase t_1 (c) Phase t_2 (d) Phase t_3

Figure 3.17: Time resolved tNSE scatter plots for Phases $t_0 - t_3$.

the initial position $(\xi_0, \nu_0) \in \mathcal{P}$.

Our PrAM then characterises all of the significant RNA-dependent states available to the tumour, without biological motivation for its form. It is an important factor of this diagram, however, that, within the paradigm of metabolic reorganisation or adaptation, sufficient research has not yet been conducted in order to establish the nature of the dynamics between any two states on this PrAM. Therefore, it is the task of the modeller to infer these dynamics from the data provided and confirm them through the validation of predictions.

To begin, using the tNSE data, we then identify and delineate the same 5 overriding subpopulations explored in Ranbow *et al.* [278]:

s1. 'Mitotic' :- exhibiting high rates of cellular proliferation and appearing in the south-west corner of the PrAM;

s2. 'Invasive' :- exhibiting high levels of activation within the subset of invasion-related genes and appearing on the western border;

s3. 'Neuro' :- exhibiting high expression levels of neural markers and appearing in the north-west corner;

s4. 'Pigmented' :- exhibiting heightened levels of pigmentation, lower levels of MITF-pathway utilisation, and appearing in the north-east corner; and

s5. 'Immune' :- exhibiting higher activation levels of IFN-inducible, immune-related genes and appearing in the south-east corner.

Proliferation

Unsupervised clustering of gene expression in single cells showed a distinct subset of cells utilising high transcriptional rates in genes known to be linked to

mitosis, within the cell. This subset of cells the researchers named 'mitotic' and reside within the south-west corner region of the PrAM. Moreover, one can locate a band-region running from north to south down the centre of the map, wherein cells are utilising MITF-related metabolic pathways (with more northern cells exhibiting hypometabolic attributes) (Fig. 3.17). Cells transcribing high levels of MITF-related genes are known to exhibit greater rates of mitosis than those transcribing lower such levels [58]. Likewise, hypometabolic cells, or those exhibiting very low levels of MITF-related genetic transcription, exhibit extremely low levels of cell-cycle progression and mitosis.

Accepting these observations, we make the following assumptions on the behaviours of our mathematical system:

- $\Phi 1$. Mitotic cells are those cells with the highest mitotic rates of the entire population;
- $\Phi 2$. MITF high cells have elevated mitotic rates, with respect to the average non-mitotic cell;
- $\Phi 3$. hypo-metabolic cells are incapable of exhibiting mitotic behaviours; and
- $\Phi 4$. all cells, consistent with the above assumptions, exhibit some basic mitotic rate, ϕ_0.

Degradation

Since the targeted therapies, BRAFi and MEKi, are known to target cells utilising glycolytic pathways [259, 41] and that the glycolytic pathways, themselves, constitute a related subgrouping to MITF pathways [17, 107], we need then make only one major assumption on the system, with regards to drug-motivated degradation:

- $\Delta 1$ Drugs BRAFi and MEKi primarily target genes involved in characterising the mitotic and MITFhigh states.

Metabolic Adaptation

The metabolic adaptation of cancer cells, since it constitutes a set of dynamic parameters of the system (affecting the way that the system behaves rather than through direct augmentation or diminution), involves a set of far more complicated considerations. In order to attempt to extract these dynamics from only sparsely collected still representations of specific phasic phenotypes, in the absence of intermediate measurements, we must couple dynamic observations with our *a priori* knowledge and assumptions on cancer-drug interactions. We also commit to making the simplest possible assumptions which are capable of explaining the data with which we are faced; in line with this, diffusion is considered a simpler assumption than advection since it does not assume directionality. (The addition of any assumptions beyond the necessary may lead to the addition of scientific bias in the spatio-structuro-temporal results and is, hence, avoided.)

Firstly, notice that cells in the north-westerly corner of the graphic (in the t_1 phase) are replaced by cells more skewed towards the north-easterly quadrant, through time, and that this takes place mostly in the absence of drug-mediated death, since neural stem cells are not particularly susceptible to BRAFi or MEKi. Couple this with the observation that diffusive, or random, processes should not result in a shift in the mean position in the PrAM and we arrive at our first observation over the model mechanics. A similar observation may be made concerning cells in the south-easterly quadrant, since these give rise to cells within the mid-section of the PrAM, at later time points in spite of degradation acting to achieve the opposite dynamic.

Starting with either northerly or southerly biased cell distributions seems to result in an interchange between these distributions, so that each sub-grouping will feed the population of the other. This appears to be especially true at the easterly and westerly edges of the PrAM, where cells are frequently seen switching between northerly and southerly states, between phases. Likewise, cells in the northerly region of the PrAM appear far more dynamic than those in

southerly regions and, therefore, an increasing assumption that this is conveyed by convective processes must be accompanied by an equal commitment that random processes govern this interchange.

Thusly, we arrive at the following set of dynamical assumptions:

A1 Northern cells are characterised by a fondness for migration towards a pigmented state;

A2 southern cells are characterised by a slow rate of migration towards a mitotic cell state;

A1.5 the metabolic point of attraction for cells between north and south is giverned by a linear relationship between these two foci;

A3 western and eastern cells exhibit high levels of north-south cellular interchange (or metabolic diffusion), decreasing with centrality;

A4 east-west diffusion increases with proximity to the northern border; and

AX The metabolic dynamics of cancer cells are otherwise net-neutral.

Full System

In order to build the following model, we have employed a multi-dimensional approach capable of embracing the fullest complexity of this model [161] and which we have previously utilised in modelling similar dynamics in tumour drug resistance [160]. This method uses partial differential equations (PDEs) to couple 2-dimensional spatial dynamics to the 2-dimensional dynamics of the PrAM given above. Given the continuous nature of PDEs, however, this places some major constraints upon the dynamics of the model, itself.

To cope with these constraints, one large implicit assumption of the model is that cells may only enter adjacent points in the diagram and that their are no discrete jumps between locations in tSNE space. That is to assume that the values measured in the single cell RNA-seq experiments in fact measure changes in RNA states which exist on a continuum, which is accurately represented by

the tSNE diagram, and that these states may only be reached by incremental movements towards any given location from the current; paths between points are themselves continuous. This necessarily means that proliferation is metabolically local and that metabolic evolution is achieved through advective and diffusive processes.

Using the above set of assumptions, we can then write the full mathematical system as

$$
\begin{aligned}
\frac{\partial c}{\partial t} = \; & \nabla_x \cdot \left[D_c \nabla_x c + c \left(1 - \int_{\mathcal{P}} c \, dy \right) \left(\nabla_x \sum_{k=1}^{q} \chi_k m_k + \nabla_x \chi_v v \right) \right] \\
& + \nabla_y \cdot \operatorname{diag} \left(\begin{bmatrix} D_1 y_2 \\ 4 D_2 \left(y_1 - \frac{1}{2} \right)^2 \end{bmatrix} \right) \nabla_y c \\
& + r_\mu \frac{\partial}{\partial y_1} \left[\left(y_1 - \frac{\xi_{\phi_{\max}} - \xi_{\phi_{\text{hyp}}}}{\nu_{\phi_{\max}} - \nu_{\phi_{\text{hyp}}}} (y_2 - \nu_{\phi_{\text{hyp}}}) - \xi_{\phi_{\text{hyp}}} \right) \left((y_2 - r_{\min}) + r_{\min} \right) \right] c \\
& + \Phi_c \begin{pmatrix} \phi_0 \\ \phi_{\text{up}} \\ \phi_{\max} \end{pmatrix} \cdot \begin{pmatrix} 1 \\ \exp \left[- \left(\operatorname{diag} \begin{pmatrix} w_{\phi_{\text{up}},\xi} \\ w_{\phi_{\text{up}},\xi} \end{pmatrix} \left[y - \begin{pmatrix} \xi_{\phi_{\text{up}}} \\ \nu_{\phi_{\text{up}}} \end{pmatrix} \right] \right)^2 \right] \\ \exp \left[- w_{\phi_{\max}} \left[y - \begin{pmatrix} \xi_{\phi_{\max}} \\ \nu_{\phi_{\max}} \end{pmatrix} \right]^2 \right] \end{pmatrix} \\
& \qquad \cdot \left(1 + \exp \left[- \alpha_{\phi_{\text{hyp}}} \left(\left[y - \begin{pmatrix} \xi_{\phi_{\text{hyp}}} \\ \nu_{\phi_{\text{hyp}}} \end{pmatrix} \right]^2 - w_{\text{hyp}}^2 \right) \right] \right)^{-1} \\
& - \bar{\bar{\delta}}_c \cdot \bar{p} \exp \left(- \begin{bmatrix} 1 \\ 1 \end{bmatrix}^T \left(\left\{ \bar{y} - \begin{bmatrix} \frac{\xi_{\phi_{\max}} + \xi_{\phi_{\text{up}}}}{2} \\ \frac{\nu_{\phi_{\max}} + \nu_{\phi_{\text{up}}}}{2} \end{bmatrix} \right\}^2 \begin{bmatrix} \alpha_{\delta_\xi} & 0 \\ \kappa & \alpha_{\delta_\nu} \end{bmatrix} \right) \begin{bmatrix} 1 \\ \frac{\kappa}{\kappa + \alpha_{\delta_\nu}} \end{bmatrix} \right) c
\end{aligned}
$$

$$\begin{aligned}
\frac{\partial v}{\partial t} &= \phi_v(1-v)v - \bar{\delta}_v \bar{m} v \\
\frac{\partial \bar{m}}{\partial t} &= \nabla_x \cdot \nabla_x \mathrm{diag}(\bar{D}_m)m + \mathrm{diag}\left(\begin{bmatrix} \phi_{m_1}(1-m_1)\int_{\mathcal{P}} c\,dy \\ \phi_{m_2}(1-m_2)v \end{bmatrix}\right)\cdot \bar{m} - \mathrm{diag}(\bar{\delta}_m)\bar{m} \\
\frac{\partial \bar{p}}{\partial t} &= \nabla_x \cdot \nabla_x \mathrm{diag}(\bar{D}_p)\bar{p} + \bar{\Theta}_p(t) - \mathrm{diag}(\bar{\delta}_p)\bar{p}\int_{\mathcal{P}} c\,dy\,,
\end{aligned} \tag{3.37}$$

where

$$\kappa := \frac{1}{2}\left(\alpha_{\delta_{\xi\nu}} - 2b - a \pm \sqrt{(a-\alpha_{\delta_{\xi\nu}})^2 + 4ab}\right)\,. \tag{3.38}$$

3.3.3 Results

Initial conditions for the tumour are given by a normal, or Gaussian, joint distribution in $(x_1, x_2, y_1, y_2) \in \mathcal{D}\times\mathcal{P}$ centred at $(\frac{1}{2}, \frac{1}{2}, \frac{1}{5}, \frac{1}{5})$, such that the tumour is centred in its spatial domain and mitotic in metabolism. The initial conditions for the extra cellular nutritional environment (ECNE) are given by a spatially heterogeneous distribution generated as in (2.50) (Fig. 3.18a) Although spatial and metabolic dynamics are simulated as codependent in a joint distribution, we have chosen to represent the resultant data separately, due to the high dimensional nature of the data and in order to avoid confusion: Spatial data is represented by a 2-dimensional heat map in x_1 and x_2, where 'yellow' regions represent regions of high cancer cell density and 'blue' regions represent those of low density. Likewise, representative metabolic t-SNE data is represented by a 2-dimensional heat map in y_1 and y_2, where 'yellow' regions represent regions of high cancer cell density and 'blue' regions represent those of low density. The metabolic heat maps are a direct representation of those produced by Rambow *et al.* [278], where cellular subpopulation identified are represented by analogous subregions within our own plots.

In our *in silico* experiment, we allow the tumour to grow for some arbitrary time before treating continuously from $t = 0$. The first thing to notice about

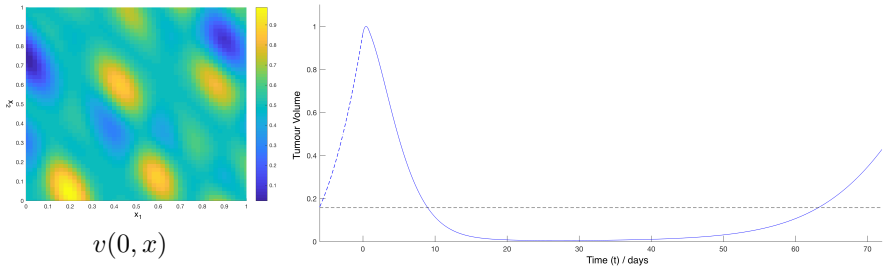

$v(0, x)$

(a) (b)

Figure 3.18: Numerical simulations of (a) the initial conditions for the heterogeneous ECNE system and (b) tumour volume over time, normalized with respect to its maximal volume. On the tumour volume plot, we have indicated the tumour volume (*black* - - -) below which the tumour is no longer clinically visible.

the results from simulation is that we are able to fully recover the 4 stage death and regrowth cycle for the tumour under treatment with BRAFi and MEKi. This implies that, on the lowest possible resolution representation of the *in vivo* tumour, we have a hypothetically sound model with which to explore the dynamics of this tumour. Since the purpose of this model was not to make any prediction as to the evolution of the metabolic data but simply to reproduce this data, all of the parameters for this model were chosen in order to accurately recreate the metabolic dynamics measured in the *in vivo* single-cell RNA-seq experiment.

During the tumour growth, pre-treatment period the initially mitotic tumour remains mitotic and hyper-metabolic (Fig. 3.19, $t \in [-8, 10)$), exhibiting an exponential growth rate (Fig. 3.18b). Upon treatment, the vascularised tumour retreats from its hyper-metabolic status and a new invasive, neural stem cell-like and hypo-metabolic generation is born in the north-west of the PrAM (Fig. 3.19, $t \in (0, 20)$). (The reason that we refer to this tumour as vascularised may not be immediately obvious but is because the ECNE is dense within the tumour and the tissue's vascular density is assumed to be proportional to the density of the ECNE.) This is followed by a further degeneration of the tumour volume and consolidation of the hypo-metabolic subpopulation through the tolerance phase (Fig. 3.19, $t \in (10, 30]$), inducing the emergence of a pigmented cell subpopulation (Fig. 3.20, $t \in [30, 40)$) which are themselves hypo-metabolic.

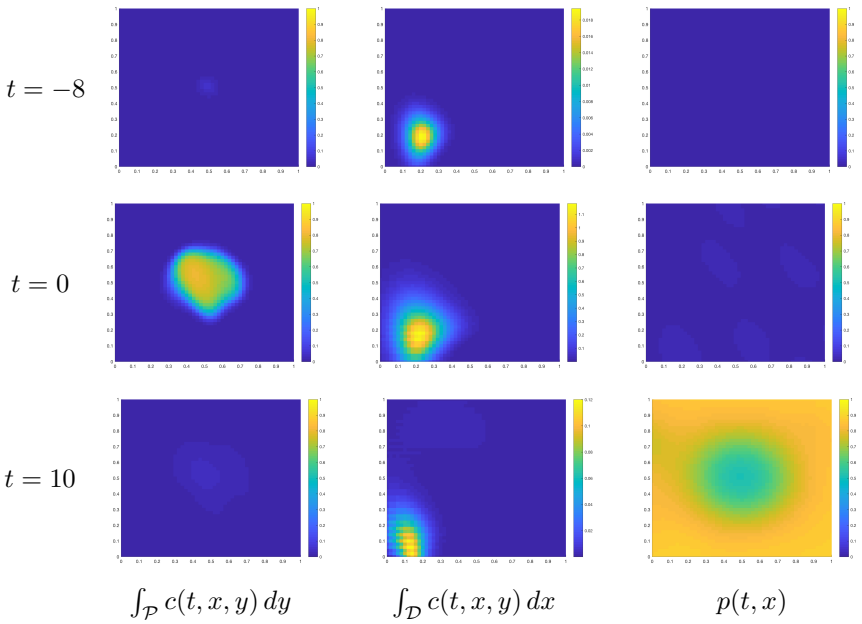

Figure 3.19: Numerical simulations of tumour growth and drug particle dynamics prior to and during treatment for $t \in \{-8, 0, 10\}$, where $t = 0$ indicates the time at which treatment began. Given are the 2-dimensional spatial cancer population, $\int_{\mathcal{P}} c(t, x, y)\, dy$, in (x_1, x_2); structural cancer population, $\int_{\mathcal{P}} c(t, x, y)\, dy$, in (y_1, y_2); and the drug particle population, $p(t, x)$, in (x_1, x_2), respectively for each time point.

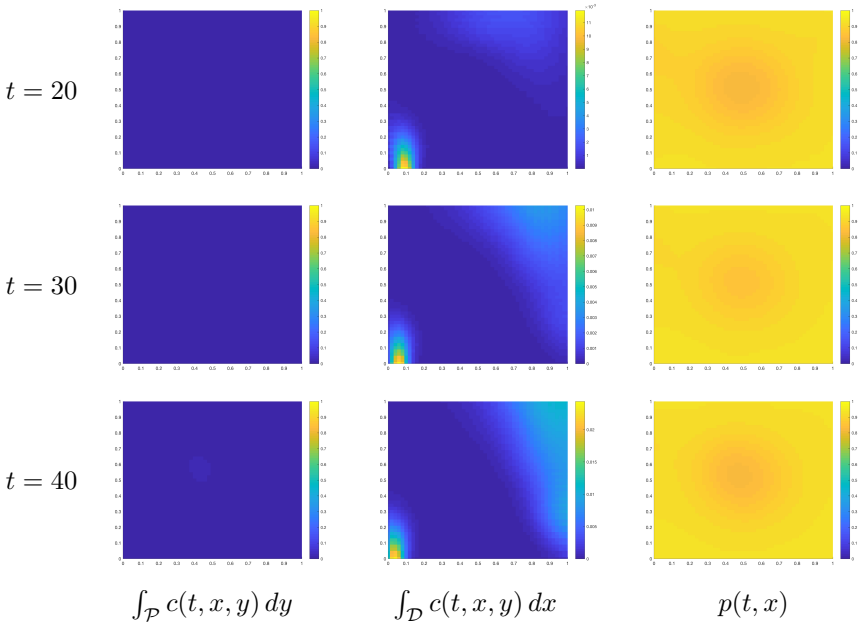

Figure 3.20: Numerical simulations of tumour growth and drug particle dynamics during treatment for $t \in \{20, 30, 40\}$, where $t = 0$ indicates the time at which treatment began. Given are the 2-dimensional spatial cancer population, $\int_{\mathcal{P}} c(t, x, y)\, dy$, in (x_1, x_2); structural cancer population, $\int_{\mathcal{P}} c(t, x, y)\, dy$, in (y_1, y_2); and the drug particle population, $p(t, x)$, in (x_1, x_2), respectively for each time point.

Since the numbers of cells, within the tumour during the tolerance phase, becomes infinitesimal, although measurable, the primary signature of the tumour entering resistance phase and beginning to regrow is the recession of drugs from a certain location in space, indicating the local regrowth of cells in the region. The metabolic resistance of tumour is then mainly characterised by the spawning of immune-reactive cells (Fig. 3.20, $t \in (30, 60]$) who are simultaneously resistant to treatment, as may be inferred from the data [278], and hyper-metabolic in comparison to their pigmented neighbours in the PrAM. Throughout this resistance phase the immune-reactive subpopulation continues to grow with respect to the, also resistant, pigmented cell subpopulation but one should also notice the increased growth of the mitotic cell subpopulation (Fig. 3.20, $t \in [40, 60]$) who, until resistance, had been subdued with respect to their absolute numbers.

As an overall trend, one will notice that, at least qualitatively, the metabolic results from the *in silico* simulated experiment (Fig. 3.19 & 3.20) well capture those of the *in vivo* experiment (Fig. 3.17). The spatial dynamics of the tumour are also similar to those expounded through previous modelling using this framework [160], with drugs diffusing towards the centre of the tumour and with highest density where tumour cell density is lowest. It is worth noting that, as with the *in vivo* PDX tumour, the mitotic cell population remains throughout the simulation, although it is diminished relatively and absolutely.

For the final act in this experiment, we attempt to make a prediction which may be verified by experiment, by accounting for the limitations of experimental technique. To do this, we simulate the taking of a sample from the resistant tumour ($t = 70$) simultaneously at regions of high tumour density and low drug concentration (Fig. 3.22, *red*) and of low tumour density and high drug concentration (Fig. 3.22, *green*); the former occurring on the interior of the tumour and the latter on the exterior. In the region of highest tumour density and lowest drug concentration, one observes that the metabolic state of the cell is described by a preponderance of mitotic cells (sensitive to treatment) alongside some significant numbers of immune-reactive and pigmented cells. In the case where the tumour density is at its lowest and drug concentration at its highest,

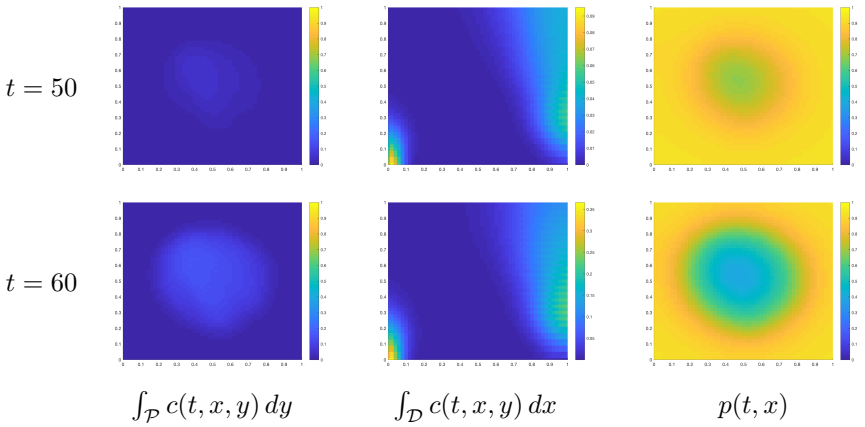

Figure 3.21: Numerical simulations of tumour growth and drug particle dynamics during treatment for $t \in \{50, 60\}$, where $t = 0$ indicates the time at which treatment began. Given are the 2-dimensional spatial cancer population, $\int_{\mathcal{P}} c(t, x, y)\, dy$, in (x_1, x_2); structural cancer population, $\int_{\mathcal{P}} c(t, x, y)\, dy$, in (y_1, y_2); and the drug particle population, $p(t, x)$, in (x_1, x_2), respectively for each time point.

however, one observes that the bulk of the cells are immune-reactive (resistant to treatment) and that the remainder of the cells of hypo-metabolic or pigmented. This predicts, therefore, that despite the heterogeneous nature of the biological results, this heterogeneity is in fact compartmentalised in the tumour, where the resistant exterior of the tumour provides an absorptive barrier to the penetration of the treatment to internal regions. This means that sensitive but highly mitotic cells are able to continue to proliferate on the interior of the tumour where drug concentrations are sufficiently low as to allow it.

3.3.4 Discussion

In comparison with previous, theoretically derived mutli-dimensional models [157] (Section 3.2–3.2.7), however, both the simplicity of interpretation and mechanism of action are lost in the data-driven approach. The reasons for this are two-fold: Firstly, the data-driven approach itself constrains the theoretician to using only those mathematical constructs which will given rise the to the data before them; using the data as an *a priori* structure to guide the model rather than for the purposes of *post hoc* verification. Secondly, in reality these

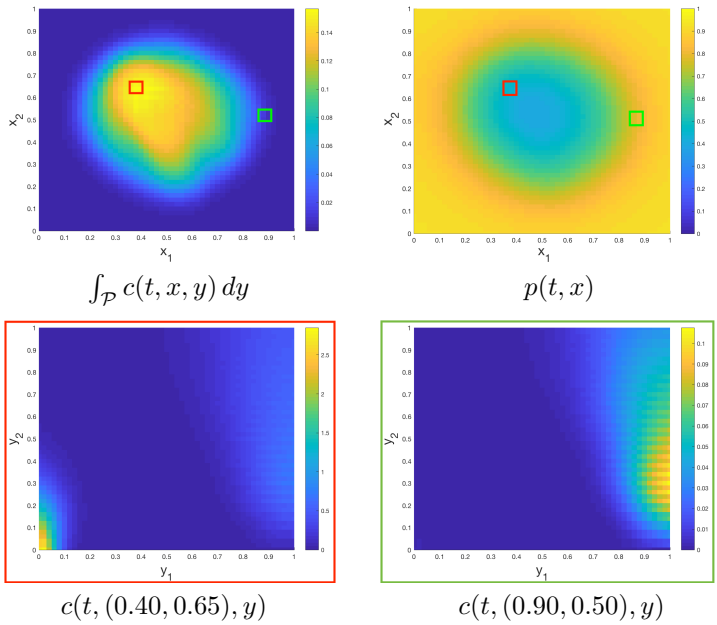

Figure 3.22: Simulation of *in silico* sample collection for the tumour at regions of high cancer cell density and low drug particle concentration, and *vice versa*, at the final time point after treatment. Above are given the regions from which samples were taken, indicated on the spatial maps of the cancer population and drug particle population as *red* and *green* squares, respectively, whilst below are given the structural distribution in the cancer population at the sample points.

phenotypic changes to the cancer cell population are multi-faceted and would more aptly be described using a far greater number of dimensions, each of which with its own dynamics, in order to approach and fully describe the true transcriptional landscape of the cells.

Although the data-driven model presented herein may not exhibit the same level of theoretical parsimony as previous similar models [157], it does have the major advantage of being completely derived from, and explanatory of, a set of empirical *in vivo* data. This advantage, alone, allows it the potential of deriving new hypotheses about the nature of reality from existing knowledge. In this particular case, we have been able to hypothesise, on the basis of *in vivo* PDX single cell RNA-seq data [278], that the spatio-phenotypic heterogeneity of the tumour is driving both the resistance of the tumour and its ability to grow rapidly in its post-resitsance state.

Chapter 4

Modelling Ligand-Activated Signalling Processes Applied to Interferon

4.1 Introduction to Inter-cellular Signalling and Interferon

The field of immunology is of increasing interest to oncologists, due to the increased interest in oncolytic viral therapies – which induce a local infection within cancerous cells, leading to their eventual lysis – and the increasing realisation that the tumour interacts dynamically with the immune environment – decreasing the avidity of T-cells for tumour cells. Therefore, we have chosen to investigate some of the fundamental problems within the field of immunology, which directly impact the fields of cancer therapy.

The interferon (IFN) system, in particular, is of crucial importance to the success of oncolytic viral therapies; since it is often the IFN activated pathway which leads to the suppression of viral proliferation and the resulting lysis of

infected cells. It is also of fundamental interest, therefore and in advance of interfering with such a system, to understand why, in a system with extremely high-affinity ligands, humans and other mammals have such a diverse range of genetically-encoded affinities of IFN. The first of our investigations, therefore, sought to tackle precisely this problem and introduce a higher-dimensional modelling approach for the IFN binding system, and subsequent metabolic reaction. We found that low affinity IFNs could evade capture by surrounding cells and, thusly, propagate through a system, across far more vast distance than high affinity ligands, who mainly maintain this signal on a more local scale.

Using this result, we embarked on a secondary path of discovery and asked what precisely is the role of this IFN propagation and maintenance pathway when interacting with a local viral infection. Coupling our higher-dimensional system with a viral population; increasing the number of IFN subspecies represented within the model; and more realistically characterising the biological, *in vivo* situation, we asked what the potential consequences were for the infection itself. We found that systems with low affinity ligands, as opposed to those missing only the very lowest affinity ligands, reduced the viral load by up to 23% over their counterpart systems, constituting a major evolutionary survival advantage.

4.1.1 Ligand-Activated Sensing and Reciprocating Systems

In order for biological systems to initiate changes in behaviour at the scale of a group of cells or of a tissue in response to a localized event, it is necessary for small signals to be transformed into large signals and sequentially communicated to other cells. This is no more apparent than in the human immune response where T-cells are actively recruited to the site of infection through the amplification and dispersion of the precursor signal [222]. The intermediate signal must be received and amplified, in order that distant cells may receive the signal with sufficient veracity as to respond.

In the case of the immune system, the cell-to-cell communication can be at

least partially orchestrated by dynamic changes of the cell membrane receptors and by secretion of communication proteins such as chemokines [222] and cytokines [255]. Other cell-to-cell communication and amplification mechanisms are used by bacteria in a phenomenon known as "quorum sensing" [247] and by yeast to optimize mating efficiency [25]. In order to synchronise the phenotypes expressed by a local group of cells, bacteria and yeast posses internal feedback loops that amplify incoming diffusible chemical signals. Similar examples where local behavior spreads by cell-to-cell communication can be found in animal development, when blocks of tissues can be developed from sheets of cells by a phenomenon called "community effect" [136] or when cell fate is specified by "sequential patterning" such as in the spatial regulation of Delta-Notch signalling [165, 152]. Collective synchronous behaviour of cells is also needed in insulin secretion by pancreatic islets but, in this case, the possible cell-to-cell communication mechanisms are still under debate [263]. We call such systems sensing and reciprocating systems (SARs), on the basis that the initial chemical signals are replicated and amplified, which is similar to the concept of secrete and sensing cells [228, 252].

SARs are ubiquitous in biology and some mathematical models dealing with properties of such systems exist. The versatility of collective properties of secrete and sensing cells was studied using phenomenological, compartment based models and ordinary differential equations (ODEs) [344]. The same type of formalism was used for metabolic synchronisation of insulin secretion in islets [263] and for studying cell-to-cell communication in the immune system [112]. ODE based models allow rather detailed descriptions of intracellular signalling and metabolic dynamics but do not cope accurately with cell proliferation, migration, and cell-to-cell interactions.

Although not yet used for SARs, frameworks based on partial differential equations (PDEs) could integrate many of these processes and explain aspects related to spatial heterogeneity such as the role played of spatial arrangement of cells in determining the conveyance of these signals [255]. However, in PDE models, non-spatial heterogeneity, resulting from the fact that cells in close

spatial proximity do not necessarily respond synchronously to stimuli, is lost by averaging. This "structural heterogeneity" can be an essential part of a complex cell dynamics, in which cell sub-populations behave differently to the average, and may be essential to understanding the complicated dynamics of biological systems. As an example, such models have predicted that below a certain threshold value, interferon (IFN) signalling allows the activity of the cellular population to decay entirely [149].

A paradigm which seems appropriate to exploring the possible structural dimensions of biological problems, in a mathematical context, is that of the continuous structural approach [29, 213, 212]. This approach encompasses the genetic or epigenetic state of a cell, under temporal conditions which are consistent with the continuous nature of dynamic biological problems by employing the application of PDEs in structure, rather than in spatial position. On the other hand, these approaches neglect the spatial dimensions associated with chemical communication between cells and, thusly, do not provide the descriptive breadth necessary to analyse these situations.

One recent "spatio-structural-temporal" (SST) framework, which demonstrates the potential to represent greater details of dynamical processes in dimensions of both structure and space, was developed in order to model the urokinase plasminogen activator system in breast cancer [97, 318]. Herein, we present a similar derivation in order to augment the generality of this framework and present a modelling form capable of capturing the intricacies, and important heterogeneous features of SARs. Compared to [97, 318] we introduce new metabolic structural variables and conjugated advection fluxes that are derived from the continuity equation and Liouville's theorem. These variables are needed for modelling stimulated amplification in SARs. The use of Liouville theorem is a major advance in the SST framework as it can relate any single cell ODE dynamics to population dynamics in structure space.

4.1.2 An Example of a SAR System: Cellular Interferon (IFN) System

We look, here, specifically at a detailed model for the IFN binding process of a given cell and the concurrent metabolic processes that result from this binding process. This SAR shall serve as an exemplar biological system on which to base models that will explore the efficacy of the framework to be proposed.

There are 13 forms of IFNα and 1 of IFNβ, which we subcategorise as low and high affinity and denote as IFNα and IFNβ respectively. Their ability to activate a cell's internal infrastructure is dependent on their ability to concurrently bind the IFN-α/β receptors 1 (IFNAR1) and 2 (IFNAR2) on the surface of the cell. The association rate of IFN with IFNAR2 is approximately $10\times$ that of IFNAR1, therefore the primary interaction is with the jak1 signalling complex of IFNAR2 [119, 118]. It is also essential, however, that IFN bind the lower affinity IFNAR1 and so IFNAR1 is recruited to the location of the bound IFN/IFNAR2 complex [119, 118]. These tyk2 and jak1 protein phosphorylate one another to initiate what is known as the Jak-Stat pathway [304].

The Jak-Stat pathway is predicated on the fact that the phosphorylated Jak1-tyk2 complex is capable of phosphorylating the transcription factors Stat1 and Stat2. These two factors are then able to bind the IFN regulatory (transcription) factor (IRF)-9 in order to form the IFN stimulated gene factor (ISGF)-3 complex [304, 288], which is capable of entering the nucleus [209]. Having achieved this step, this complex can bind to the promoter region of IFN stimulated genes (**ISG**s) and effectively initiate their transcription [304, 288].

One particularly significant ISG is the IRF-7 protein who is capable of the downstream binding of and IRF-3. This IRF-7-3 complex is directly responsible for the promotion of **IFN-**α and **IFN-**β genes [142]. Another effect of transcribing ISGs is the transcription of USP18, which will compete with jak1 for binding of the intracellular domain of IFNAR2 [111]. IFNAR2s bound by USP18 have also been shown to be ineffective at affecting the transcription of IRF-7 [279, 341, 18].

Therefore, this system can be looked at through the simplified lens of two major and important processes:

(a) the binding of IFN to the surface of the cell, and

(b) the activation of the metabolic pathway which eventually leads to the creation of new IFN molecules.

We use the phrase 'metabolic activation' in order to characterise the state of the cell in terms of the chemical activity levels of those proteins involved in the Jak/Stat pathway and, ultimately, the transcription of the genes necessary for the synthesis of IFN. Thus, when one describes the metabolic activation of the cell, with regards to the IFN pathway, one is actually describing, in some way, the spatially differentiated presence of IRF-7-3 within the cell (Figure 4.2).

Moreover, one review of experimental data plotted the relationship over time between the activation of genes within the cell and the fractional levels of bound and unbound surface receptors, for both IFNα2 and IFNβ [292]. This graph importantly showed that, for low levels of IFNα2, as the number of surface receptors decreased, the metabolic activation level rose concurrently. Further, as genetic activation levels decreased, one could observe a corresponding normalisation of the fractional surface receptor levels [202]. Comparably, for high levels of IFNβ, one finds that the cells genetic mechanism is activated in a locally irreversible process and that the fraction of IFNAR1 receptors is maintained at approximately 40% [292].

In order to demonstrate the descriptive power within the existing modelling frameworks, we choose the biological IFN system in T-cells as an illustrative example of such a system of SARs. This will serve as a comparative case for the development of a framework, which is capable of significantly improving upon one's existing capacity.

4.2 Signal Propagation in Sensing and Reciprocating Cellular Systems with Spatial and Structural Heterogeneity

4.2.1 A Simple Spatio-Temporal Model of SARs

If one were to create the simplest possible system of SARs, one would begin with only the population of SARs, themselves, and the molecular population of SAR diffusing ligands. In reality, however, these systems are rarely as simplistic as this and often require consideration of spatially intermediate cells which may mediate the levels of the SAR ligands, by consuming these proteins without reciprocally producing them. This is the case in the biological IFN system and, as such, we call such intermediate cells 'consumers' and the SAR cells as 'producers', within a system that considers only such a responsive protein.

Therefore, begin by defining a temporal domain, given by $\mathcal{I} = [0, T]$ with $t \in \mathcal{I}$, and a two-dimensional spatial domain, given by $\mathcal{D} \subseteq \mathbb{R}^2$ with $x \in \mathcal{D}$. We then write cellular population functions such that $c_1 : \mathcal{I} \times \mathcal{D} \to \mathbb{R}$ gives the population of IFN producing cells and $c_2 : \mathcal{I} \times \mathcal{D} \to \mathbb{R}$ gives the global population of consumer cells, whilst $m : \mathcal{I} \times \mathcal{D} \to \mathbb{R}$ gives the non-dimensionalised concentration of IFN molecules.

In order to write as simple a model as is possible, we begin by ignoring all dynamics in the cellular populations are given simply by $c_1(t, x) := c_1(0, x)$ and $c_2(t, x) := 1$, respectively. This is so that one might analyse only the communicative capabilities of the IFN itself.

We then write the dynamics of the system as a whole as a spatio-temporal partial differential equation (PDE) in $m(t, x)$, such that the spatial dynamics are given entirely by the diffusion of this molecule in the solution. Interferon is then systematically consumed by c_2, at a rate λ, and is autoreplicated within c_1 cells, at a rate ϕ_2, and where this autoreplication is further stabilized by

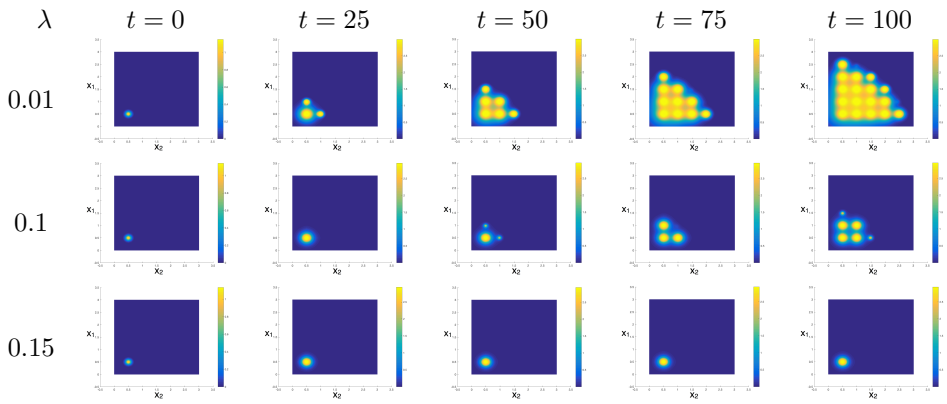

Figure 4.1: Multi-cluster results in the concentration of molecular species $m(t, x)$ from simulation of the simple model (4.1) for varying affinities, $\lambda \in \{0.01, 0.1, 0.15\}$, and for $t \in \{0, 25, 50, 75, 100\}$ respectively.

negative self-regulation, with the rate constant ϕ_3. Therefore, we have that

$$\frac{\partial m}{\partial t} = D_m \nabla_x^2 m - \lambda m c_2 + (\phi_2 m^2 - \phi_3 m^3) c_1 \tag{4.1}$$

where D_m is the coefficient for diffusion of IFN.

Simulations were performed for this system using a 4^{th} order Runge-Kutta predictor and MacCormack corrector, with a central difference formula used for the calculation of diffusion terms. Initial conditions for the producer cells are given by

$$c_1(0, x) = \sum_{j=1}^{5} \sum_{i=1}^{5} \exp\left[-(x_1 - \frac{1}{2}i)^2 - (x_2 - \frac{1}{2}j)^2\right],$$

and for the IFN concentration is given by the Gaussian distribution

$$m_0 := m(0, x) = \exp\left[-(x_1 - \frac{1}{2})^2 - (x_2 - \frac{1}{2})^2\right],$$

with the rate constants given by $D_m = 10^{-3}$, $\phi_2 = \frac{3}{4}$, and $\phi_3 = \frac{1}{8}$ and λ being variable between simulations. Moreover, zero-Neumann boundary conditions are used in order to conserve the molecular population.

The results for the simulation of system (4.1) show, most simply, that communicative capability increases with decreasing values for affinity of IFN for its

consumer cells (Fig. 4.1). The approximate threshold value for which this is true falls in the interval $\lambda \in (0.1, 0.15)$ (Fig. 4.1), given the values chosen for $\mathcal{D}_m$, λ, ϕ_2, ϕ_3.

This may, to some extent, give a mathematical explanation for why it may be biologically advantageous to maximise the utilisation of lower affinity IFN in a system where one wishes to stop the spread of the infection. It could be that cells employ this methodology in order to spread a panic signal upon the initial detection of a virus and initialisation of a local IFN signal.

The explanation given by this simple model, however, does not explain the nature of the interaction between molecules and cells that allows this system to proffer communicative capabilities as it does. For example, we artificially introduce the notion that increasing the affinity of IFN molecules will increase their consumption but must still question what effect this alteration should have on the interaction with producer cells. It is difficult to intuit, also, how this increase in affinity should change the interactions that impact the metabolism of IFN within the cell. One might expect that affinity would increase production but would it also increase feedback sufficiently to dampen that response? Alterations to equation 4.1, however, require suppositions on the desired final behaviour of the system, rather than *a priori* biological assumptions.

Therefore, in response to this fundamental issue, we aim to create a more biologically descriptive model that will serve to quantify dynamics in the cell-surface receptors; the binding of these receptors by free molecules; and the consequential alterations in metabolism in a spatial context. We will also realise the interactions between these various dynamical behaviours, in order that one might better understand how the biological reality is affected by changing individual characteristics.

4.2.2 General SAR Model Within the Spatio-Structuro-Temporal Framework

We introduce here a general SST model for SAR systems. Various instances of

this model can serve to study different biological problems.

In this framework we consider that cells of the same type can differ in their states. The cell state is described by three variables $\xi \in \Upsilon \subset \mathbb{R}^{\upsilon}$, $y \in \mathcal{P} \subset \mathbb{R}^{p}$ and $\alpha \in \Gamma \subset \mathbb{R}^{\gamma}$, where ξ, y, α represent the total density of receptors on the cell membrane; the part of receptors that have bound ligands; and the metabolic variables, respectively. We consider that there are q different diffusible ligands of concentrations $m_l(t,x), 1 \leq l \leq q$. As a simplifying assumption we consider that ligands m_k bind with no competition to their cognate receptors ξ_i, $1 \leq i \leq \upsilon$. Competition could be easily introduced by considering that the same receptor can bind several ligands, but in this case the y space has to be supplemented with extra dimensions corresponding to the simple and double charge of the receptors. The binding event can trigger the signalling and activation of metabolic variables $\alpha_k, 1 \leq k \leq \gamma$ that are responsible of the production of the ligands $m_j, 1 \leq j \leq q$.

A spatially and structurally heterogenous cell population is described by a structured cell density, namely by a positive, integrable function $\hat{c}(t,x,\xi,y,\alpha)$, with $t \in (0,T]$, $x \in \mathcal{D} \subset \mathbb{R}^d$, $\xi \in \Upsilon$, $y \in \mathcal{P}$, and $\alpha \in \Gamma$.

The spatial cell density $c(t,x)$ can be obtained as the marginal distribution of the structured cell density

$$c(t,x) = \int\limits_{\Upsilon \times \mathcal{P} \times \Gamma} \hat{c}(t,x,\xi,y,\alpha) d\xi \, dy \, d\alpha. \tag{4.2}$$

The dynamics of the structured cell density is described by

$$\begin{aligned} \tfrac{\partial}{\partial t}\hat{c}(t,x,\xi,y,\alpha) &= \hat{S}(t,x,\xi,y,\alpha) - \nabla_x \cdot \hat{F}(t,x,\xi,y,\alpha) - \nabla_\xi \cdot \hat{G}(t,x,\xi,y,\alpha) \\ &\quad -\nabla_y \cdot \hat{H}(t,x,\xi,y,\alpha) - \nabla_\alpha \cdot \hat{K}(t,x,\xi,y,\alpha) \end{aligned} \tag{4.3}$$

whose full derivation is based upon work by Domschke *et al.*[97] and is given in 1.2, along with a novel derivation of a structural source term, where $\hat{S}$ is a source term and where $\hat{F}, \hat{G}, \hat{H}, \hat{K}$ are space-structure fluxes conjugated to the variables x, ξ, y, α, respectively.

We then proceed to more clearly define each of the flux terms in (4.3) as

follows.

Spatial flux

The general form of the spatial flux equation is commonly obtained from Fick's law and is given by

$$\begin{aligned}\hat{F}(t,x,\xi,y,\alpha) &= -D_c\nabla_x\hat{c}(t,x,\xi,y,\alpha) \\ &\quad +\hat{c}(t,x,\xi,y,\alpha)\chi_v\nabla_x v(t,x) \\ &\quad +\hat{c}(t,x,\xi,y,\alpha)\sum_{i=1}^{q}\chi_i(y)\nabla_x m_i(t,x),\end{aligned} \tag{4.4}$$

where the first term represents the spatial undirected diffusion of cells, the second term and third terms correspond to directed haptotactic and chemotactic cell migration, respectively.

Dynamics in receptoro-binding space

Notice that each ligand binds to the available cognate receptors. Thus, the binding rate depends on the free receptor amount $\xi_i - y_i$ and is proportional to the ligand concentration m_i

$$b_i(\xi,y,m) = \beta_i\vartheta(\xi_i - y_i)m_i, \tag{4.5}$$

where ϑ is a function allowing to cope with the situation when binding is thresholded in the concentration of free receptors. The unbinding rate is simply proportional to the fraction of the carrying capacity of bound receptors

$$u_i(y) = \eta_i y_i. \tag{4.6}$$

Bound receptors are internalised with a rate

$$\iota_i(y) = k_i y_i. \tag{4.7}$$

A subset of these internalised receptors are recycled. The timescale ζ_i^{-1} of this process results from complex interactions between receptors and scaffolds inside the endosome [133] and depends nonlinearly on y. Therefore, the recycling rate reads

$$r_i(y) = \zeta_i(y) y_i, \quad 0 \leq \zeta_i(y) \leq k_i. \tag{4.8}$$

Receptors are synthesised by the cell with a rate $p_i(\alpha, \xi)$ that depends on the metabolic variables α and also on actual concentration of receptors ξ and are lost by various mechanisms with a rate proportional to ξ

$$d_i(\xi) = d_i \xi_i. \tag{4.9}$$

In summary, the receptoro-binding variables of a single cell follow the differential equations

$$\frac{d\xi}{dt} = \Psi_\xi(\xi, y, \alpha) = \mathcal{P}(\alpha, \xi) - \mathcal{D}\xi + (\mathcal{R}(y) - \mathcal{I})y \tag{4.10}$$

$$\frac{dy}{dt} = \Psi_y(\xi, y) = \beta \mathcal{B}(\xi - y)m - (\mathcal{U} + \mathcal{I})y, \tag{4.11}$$

where $\mathcal{P}$, $\mathcal{D}$, $\mathcal{R}$, $\mathcal{I}$,β, $\mathcal{B}$, $\mathcal{U}$ are diagonal matrices with diagonal entries p_i, d_i, ζ_i, k_i, β_i, $\vartheta(\xi_i - y_i)$, η_i, respectively.

It follows that the advection fluxes in receptor and binding spaces are

$$\hat{G}(t, x, \xi, y, \alpha) = \hat{c}(t, x, \xi, y, \alpha)[\mathcal{P}(\alpha, \xi) - \mathcal{D}\xi + (\mathcal{R}(y) - \mathcal{I})y] \tag{4.12}$$

$$\hat{H}(t, x, \xi, y, \alpha) = \hat{c}(t, x, \xi, y, \alpha)[\beta \mathcal{B}(\xi - y)m - (\mathcal{U} + \mathcal{I})y]. \tag{4.13}$$

Dynamics in metabolic space

The part of internalisation flux that is not recycled and that escapes lysosome degradation triggers signaling and induces changes of the metabolic variables α. We use a flux-based description of these variables that considers that there

are γ irreversible metabolic fluxes each one producing a different molecule. The reversible case can be simply obtained by doubling the number of variables for each reversible flux. To each one of these fluxes we associate a scalar variable $0 \leq \alpha_i \leq 1$, meaning no production activity and maximum production activity for $\alpha_i = 0$ and $\alpha_i = 1$, respectively. In order to represent competition between fluxes we impose the condition $\sum_{i=1}^{r} \alpha_i \leq 1$. Thus $\alpha \in \Gamma$, where $\Gamma = \{(\alpha_1, \ldots, \alpha_r) \mid 0 \leq \alpha_i \leq 1, \sum_{i=1}^{r} \alpha_i \leq 1\}$ is a simplex. This description is equivalent to the space of admissible fluxes in stoichiometric and flux balance analysis of metabolic networks where α_i, $1 \leq i \leq r$ represent activities of extreme pathways or currents [62, 291]. The dynamics in the metabolic space is described phenomenologically imposing the invariance of the simplex Γ as fundamental property. A possible such choice is

$$\frac{d\alpha_i}{dt} = \Psi_{\alpha_i}(y, \alpha) = f_i(y)(1 - \alpha_i) - \mu_i \alpha_i \,, \tag{4.14}$$

where $\mu_i \geq \mu_0 > 0$, $f_i \leq f_0$, $f_0 > 0$, $rf_0 < (f_0+1)$. The corresponding advection flux in the metabolic structure space is $\hat{K} = (K_1, \ldots, K_\gamma)$ with the components

$$K_i = \hat{c}[f_i(y)(1 - \alpha_i) - \mu_i \alpha_i] \,. \tag{4.15}$$

Spatial dynamics of diffusible ligands

Begin by denoting $\bar{m} := [m_1, \ldots, m_p, m_{p+1}, \ldots, m_q]^T$, with $m_j := m_j(t, x)$, as the total vector of molecular species, where there exist q molecular species of which the first $p \leq q$ species are binding ligands.

Then, the spatial dynamics of all molecular species are defined by a diffusive process, and with a species specific diffusion coefficient D_{m_j} for $m_j(t, x)$. The binding ligands, within the molecular species, are removed from the population of free molecules through binding. All molecules are produced by the cellular population, in a metabolic-activity-dependent manner, and are either

contributed to or detracted from by a situation specific sink or source function $\bar{\Theta}(t,x)$. Therefore, denoting the q-dimensional vectors of parameters $\bar{\cdot} := [\cdot_1,\ldots,\cdot_q]^T$, we obtain the relations for molecular species as

$$\begin{aligned}\frac{\partial \bar{m}}{\partial t} =& \nabla_x \cdot \mathrm{diag}(D_{\bar{m}})\nabla_x \bar{m} - \varepsilon \int_{\Gamma}\int_{\mathcal{P}}\int_{\Upsilon} (\mathrm{diag}(\bar{\beta}\vartheta(\xi - y))\bar{m} - \mathrm{diag}(\bar{\eta})\bar{y})\hat{c}\, d\xi\, dy\, d\alpha \\ &+ \int_{\Gamma}\int_{\mathcal{P}}\int_{\Upsilon} \bar{\phi}_\alpha(\alpha)(1-\bar{m})\hat{c}\, d\xi\, dy\, d\alpha + \bar{\Theta}(t,x)\,,\end{aligned} \tag{4.16}$$

with $\bar{\phi}_\alpha(\cdot) : \Upsilon \to \mathbb{R}^q$ defining a vector of production values for each molecular species given the cellular metabolic activity level, α; $\bar{\beta} = [\beta_1,\ldots,\beta_p,0,\ldots,0]^T$; and $\bar{\eta} = [\eta_1,\ldots,\eta_p,0,\ldots,0]^T$; ε is a constant converting surface to volume binding/unbinding rates.

Summary of the derived modelling framework

The modelling framework derived above has been given in its most general form to allow applicability to most any problem in cell-cell communication. The major contribution of this model is its completeness, in relation to other such models. The spatial partial derivative form allow the description of cell migration, including directional motility resulting from chemotactic and haptotactic interactions. The Liouville equation form in structure variables can cope with distribution dynamics of heterogeneous cellular populations. The dynamics of the cellular population in space and structure is described by major flux functions given by

$\hat{S}(t,x,\xi,y,\alpha)$– who can be used to specify the precise nature of the mitotic process within the cellular population (for which a suggestion for cell-cycle based mitosis is given in Sections 1.3);

$\hat{F}(t,x,\xi,y,\alpha)$– who specifies the spatial movements and interactions of the cellular populations within its micro- and macro-environment, such as diffusive, hapto- or chemotactic dynamics;

$\hat{G}(t, x, \xi, y, \alpha)$– who particularises the dynamic mechanisms through which the cell alters its receptor expression pattern and who may depend on spatial, binding, or metabolic considerations;

$\hat{H}(t, x, \xi, y, \alpha)$– who intimates the binding dynamics of the particular molecular species to the cellular population in question and who, in previous treatments [97, 161], has been used to describe even binding-contingent inhibitory dynamics;

$\hat{K}(t, x, \xi, y, \alpha)$– who describes the metabolic dynamics of the cellular population in response to binding or other dynamics.

Together, these flux functions allow one to describe the dynamics of cellular populations in oncological, immunological, and many other scenarios.

The totality of the above propositions are summarised as the system of

equations

$$
\begin{cases}
\dfrac{\partial c}{\partial t} = \hat{S}(t,x,\xi,y,\alpha) \\
\qquad - \nabla_x \cdot \underbrace{\left[- D_c \nabla_x + \chi_v \nabla_x v(t,x) + \sum_{i=1}^{q} \chi_i(y) \nabla_x m_i(t,x) \right] \hat{c}(t,x,\xi,y,\alpha)}_{\hat{F}} \\
\qquad - \nabla_\xi \cdot \underbrace{\left[\mathcal{P}(\alpha,\xi) - \mathcal{D}\xi + (\mathcal{R}(y) - \mathcal{I}) y \right] \hat{c}(t,x,\xi,y,\alpha)}_{\hat{G}} \\
\qquad - \nabla_y \cdot \underbrace{\left[\beta \mathcal{B}(\xi - y) m - (\mathcal{U} + \mathcal{I}) y \right] \hat{c}(t,x,\xi,y,\alpha)}_{\hat{H}} \\
\qquad - \nabla_\alpha \cdot \underbrace{\left[f_i(y)(1-\alpha_i) - \mu_i \alpha_i \right] \hat{c}(t,x,\xi,y,\alpha)}_{\hat{K}} \\
\dfrac{\partial \bar{m}}{\partial t} = \nabla_x \cdot \mathrm{diag}(D_{\bar{m}}) \nabla_x \bar{m} \\
\qquad - \varepsilon \int_\Gamma \int_{\mathcal{P}} \int_\Upsilon (\mathrm{diag}(\bar{\beta}\vartheta(\xi - y))\bar{m} - \mathrm{diag}(\bar{\eta})\bar{y}) \hat{c}(t,x,\xi,y,\alpha)\, d\xi\, dy\, d\alpha \\
\qquad + \int_\Gamma \int_{\mathcal{P}} \int_\Upsilon \bar{\phi}_\alpha(\alpha)(1 - \bar{m}) \hat{c}(t,x,\xi,y,\alpha)\, d\xi\, dy\, d\alpha + \bar{\Theta}(t,x)\,,
\end{cases}
\tag{4.17}
$$

and shall be used as the basis of the particular models used throughout the remainder of this paper.

4.2.3 Particularised IFN-Based Model

It is necessary to first have a discussion about the context into which we shall place this model, with respect to the generalised SST framework for SARs. First of all, and for simplicity, we neglect the receptor space and source terms in the IFN case. This is due to the fact that we do not consider the creation of IFN SARs, but rather their behaviour and spatial recruitment, and the change in binding in the IFN case appears to be related to affinity rather than flux of the binding proteins themselves.

It should be clear, that a main concern in modelling the IFN system is the

numerical simplification involved in the reduction of the number of necessary dimensions under consideration. This has succeeding consequences in terms of our ability to intuit the results of the system and better understand both the SST framework, and the internal processes for communicative SARs. For this reason, we also neglect, initially, the spatial dynamics of the SAR cells and concentrate first on cell-cell communication mediated by the diffusible ligand.

Now, we contextually define the binding variable, $y \in \mathcal{P}$ with $v = p = 1$, $0 \leq y \leq \xi = 1$, such that increasing values of y correspond to the increasing concentration of bound IFN-IFNAR1-IFNAR2 complexes for some given $(t, x, \alpha) \in \mathcal{I} \times \mathcal{D} \times \Gamma$.

The metabolic variable, $\alpha \in \Gamma$, is somewhat more complicated in biological terms since we wish to encapsulate a state of the cell under which a certain reaction is more likely to take place. In the particular case of IFN, for example, we understand the metabolic variable as describing a state of the cell wherein ISGs implicated in the production of or response to IFN (such as IRF-7, implicated in production, or USP18, a key regulator of the cellular response to IFN) are more frequently transcribed. Therefore, begin by describing $\alpha = 0$ as a state in which ISGs are not transcribed and $\alpha = 1$ as some state where ISGs are transcribed at their physiologically maximal rates. Then we understand α, itself, as encapsulating the propensity for the cell to proactively transcribe ISGs through the activity of the Jak-Stat pathway.

Within this paradigm, then, these two variables will interact in the following way. Begin by considering a scenario in which one cluster of IFN SARs are stimulated by a single initial dosage of IFN. The cell will bind these IFN molecules and increase in binding state of the cell, y, will form the IFN-IFNAR1-IFNAR2 complex and initiate the reactions of the Jak-Stat pathway. This will subsequently increase the cells metabolic state, α, of the cell and cause the increased production of IFN. The increase in transcription of ISGs, specifically USP18, will also cause a decrease in the efficacy of the ternary complex (IFNAR1-IFN-IFNAR2) assembly [341] or maximal effective binding, y. This, in turn, will subsequently lead to a decrease the physiological concentration of the Jak-Stat

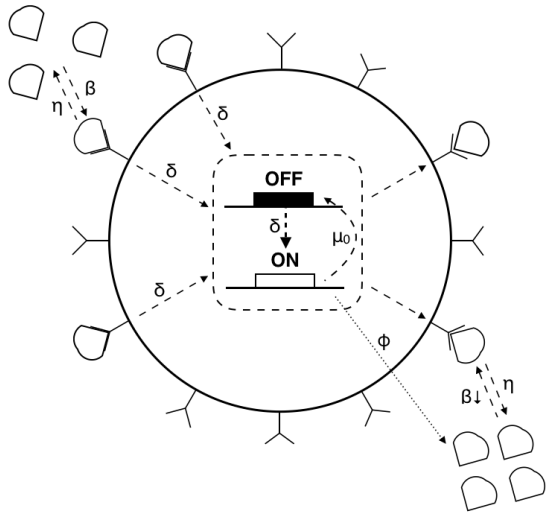

Figure 4.2: Diagram describing the simplified IFN cell-regulatory system. Unbound IFN (*top left*) will attempt to bind unbound receptors (*'Y's*) on the surface of the cell (*circle*), in accordance with its affinity for these receptors, with binding rate β. Likewise, these bound IFN-receptor complexes unbind with some rate η. The other way in which the proportion of surface bound molecules may decrease in through the internalisation of IFN receptor complexes with rate δ. The internalisation of IFN, through a complicated biological pathway, leads to a metabolic switching of the IFN-producing cell infrastructure from the default state of dormant (OFF) to active (ON), in which state the cell produces greater levels of IFN with rate ϕ (*centre*). The cell infrastructure attempts to return to the default (OFF) state with a constant rate μ_0. In the active (ON) state the conformation of receptors, in the presence of IFN, is reduced which can be modelled through the reduction of the ability of IFN molecules to bind their receptors (i.e. $\beta\downarrow$, *bottom right*).

reactions and reduce the metabolic state, α, of the cell.

Unthresholded binding model

Throughout this model, we assume a homogeneous and constant concentration of biological pathogen, such that IFN response is consistently encouraged. We have chosen illustrative values for the binding rates, consistently with previous models [97, 318], but with the difference that we consider here the negative feedback loop of the IFN system between the metabolic state of the cell and the binding of molecular species to the surface. In this respect, we consider binding to be non-dimensionalised and that feedback causes the maximal binding rate to decrease linearly with the metabolic state of the cell such that the range of values of y for which positive binding exists is given by $y < 1 - \alpha$. Thus, we consider that the binding dynamics of molecular species to the surface, b :

$\mathcal{I} \times \mathcal{D} \times \mathcal{P} \times \Gamma \to \mathbb{R}$, can be given by

$$b(m, y, \alpha) := \beta(1 - y - \alpha)m$$

where β is the binding rate constant for IFN.

When we say 'binding' in this context, we actually make a generalisation of the concept of 'meaningful binding' which is to say that binding is sufficient to allow for recruitment of the secondary complex (IFNAR2) and subsequent co-phosphorylation of their protein tails.

The rate of removal of bound molecular species from the surface of the cell has a first component corresponding to unbinding and a second component corresponding to internalisation and degradation of bound receptors. Therefore, we consider that the removal of species from the cell surface, $d : \mathcal{P} \to \mathbb{R}$, can be given by

$$d(y) := (\eta + \delta)y\,,$$

where η gives the unbinding rate of molecules from the surface of $c_1(t, x, y, \alpha)$ and δ gives the rate of cellular degradation of bound IFN.

Further, we make the assumption that the gene responsible for regulating the production of IFN has a default transcriptional state of 'off', such that the gene is not transcribed unless appropriately upregulated. Therefore we arrive at a relation for the advective rate for change in metabolic profile, $\mu : \mathcal{P} \times \Gamma \to \mathbb{R}$, of the cells which is given by

$$\mu(y, \alpha) := \delta y(1 - \alpha) - \mu_0\alpha$$

where δy is the internalisation-degradation rate (as above) and μ_0 is the intrinsic metabolic restoration rate, the purpose of which is to restore the default metabolic position of the cell $\alpha = 0$. The term $(1 - \alpha)$ is chosen such that the metabolic state of the cell might never exceeds a maximum value normalized to one.

Production of m with respect to the metabolic state of the cell is given by

the production rate function $\phi : \Gamma \to \mathbb{R}$ and is assumed to be of the form

$$\phi(\alpha) := \phi_\alpha \alpha(\alpha - \theta_\alpha)\,,$$

where ϕ_α is the rate constant for metabolic production of m and θ_α is some thresholding value above which the cell become metabolically active with respect to the production of IFN, m.

For reasons that will become clear in the following subsection we call this model the *unthresholded binding* model, which is then written

$$\begin{cases} \frac{\partial c_1}{\partial t} &= -\nabla_y \cdot [\beta(1-y-\alpha)m - (\eta+\delta)y]\, c_1 - \nabla_\alpha \cdot [\delta(1-\alpha)y - \mu_0\alpha]\, c_1 \\ \frac{\partial c_2}{\partial t} &= 0 \\ \frac{\partial m}{\partial t} &= \nabla_x \cdot D_m \nabla_x m - \int\limits_\Gamma \int\limits_{\mathcal{P}} (\beta(1-y-\alpha)m - \eta y)\varepsilon c_1(t,x,y,\alpha)\, dy\, d\alpha \\ & \quad \int\limits_{\mathcal{P}} \int\limits_\Gamma \phi_\alpha \alpha(\alpha-\theta_\alpha)(1-m)c_1(t,x,y,\alpha)\, d\alpha\, dy - \lambda m c_2\,. \end{cases} \tag{4.18}$$

Thresholded binding model

There are several alternative interpretations of potency of a ligand for meaningful binding and signaling triggering [184]. One interpretation associate this potency to the product between concentration and affinity of the ligand, suggests that ligands are detected irrespective to their quality as long as their concentration is above a threshold. Thresholds in the number of triggered receptors have been observed for immune T cells [329]. The second interpretation is based on kinetic proof-reading and suggests that a minimal binding time is needed for a given ligand to trigger signaling [112]. The correlation between binding time characteristics and immune cell activation is confirmed by several studies [184, 116]. Furthermore, recent dynamical studies demonstrated the phosphorylation of STAT2 to follow the formation of the complex (which is more or less instantaneous, < 1 second) by approximately 8 seconds [211] for complete

activation. All these studies suggest the intrinsic assumption that meaningful binding requires that receptor-ligand complex to be bound for at least a minimal time $\tau_{\min}$. In general, depending on the comparison between the timescales of meaningful complex formation and dissolution and those of activation of the signaling processes it is possible that both concentration and temporal thresholds apply to the ligand recognition. We do not aim to resolve this issue here. Because our model does not account for binding time heterogeneity, we simply replace the temporal threshold by a concentration one, considering that there is a function $\tau_b(m)$ relating the concentration of ligands to the binding time. Then, for some concentration $m(t,x) = \theta_m$ we have that

$$\tau_b(\theta_m) = \tau_{\min}$$

such that θ_m gives the concentration of m sufficient for effective binding of the IFNAR2 protein and IFNAR1-IFNAR2 complex. In order to cope with this threshold effect, we rewrite the binding flux term as

$$b(y,\alpha,m) := \beta(1-y-\alpha)(m-\theta_m).$$

Substituting this new relation back into our model, we obtain the *thresholded binding model*

$$\begin{cases} \frac{\partial c_1}{\partial t} &= -\nabla_y\cdot[\beta(1-y-\alpha)(m-\theta_m)-(\eta+\delta)y]\,c_1 - \nabla_\alpha\cdot[\delta(1-\alpha)y-\mu_0\alpha]\,c_1 \\ \frac{\partial c_2}{\partial t} &= 0 \\ \frac{\partial m}{\partial t} &= \nabla_x\cdot D_m\nabla_x m - \int\limits_\Gamma\int\limits_{\mathcal{P}}(\beta(1-y-\alpha)m-\eta y)\varepsilon c_1(t,x,y,\alpha)\,dy\,d\alpha \\ & \quad \int\limits_{\mathcal{P}}\int\limits_\Gamma \phi_\alpha\alpha(\alpha-\theta_\alpha)(1-m)c_1(t,x,y,\alpha)\,d\alpha\,dy - \lambda m c_2\,. \end{cases} \tag{4.19}$$

Spatially dynamic, thresholded binding model

Finally, we consider a spatially dynamic system wherein cells are able to move through the spatial domain. We choose to endow this system with 2 primary functions of migration:

(i) diffusion, by virtue of immune cells' natural inclination to motility, and

(ii) chemotaxis, by virtue of immune cells' ability to actively respond to an immune-response signal as a recruitment signal.

In stating this, we therefore assume that the immune cell will interpret the presence of IFN as a response to, for example, a viral threat to the body and respond to this signal by migrating towards its origin. We further assume that even in the absence of an IFN gradient, cell Brownian motion will generate spatial fluxes leaving regions of highest cell concentration.

We thusly rewrite the system as

$$\begin{cases} \frac{\partial c_1}{\partial t} &= \nabla_x \cdot D_{c_1} \nabla_x c_1 - \nabla_y \cdot \left[\beta(1-y-\alpha)(m-\theta_m) - (\eta+\delta)y\right] c_1 \\ & \quad -\chi_m \nabla_x \cdot c_1 \nabla_x m - \nabla_\alpha \cdot \left[\breve{\mu}_+(1-\alpha)y - \mu_-\right] c_1 \\ \frac{\partial c_2}{\partial t} &= 0 \\ \frac{\partial m}{\partial t} &= \nabla_x \cdot D_m \nabla_x m - \int\limits_{\Upsilon}\int\limits_{\mathcal{P}} (\beta(1-y-\alpha) - (\eta+\nu_r\delta)y)\varepsilon c_1(t,x,y,\alpha)\, dy\, d\alpha \\ & \quad \int\limits_{\mathcal{P}}\int\limits_{\Upsilon} \phi_\alpha \alpha(\alpha-\theta_\alpha)(1-m)c_1(t,x,y,\alpha)\, d\alpha\, dy - \lambda m c_2\,, \end{cases} \tag{4.20}$$

4.2.4 Numerical methods

We use the 4^{th} order Runge-Kutta predictor for this system, given by

$$\bar{c}_1^{\tau+1} := c_1^\tau + \frac{d\tau}{6}\left(F(k^\tau_{c_1,1}) + 2F(k^\tau_{c_1,2}) + 2F(k^\tau_{c_1,3}) + F(k^\tau_{c_1,4})\right)\,,$$

with

$$k^{\tau}_{c_1,1} := c^{\tau}_1, \quad k^{\tau}_{c_1,2} := c^{\tau}_1 + \frac{h}{2} k^{\tau}_{c_1,1},$$
$$k^{\tau}_{c_1,3} := c^{\tau}_1 + \frac{h}{2} k^{\tau}_{c_1,2}, \quad k^{\tau}_{c_1,4} := c^{\tau}_1 + d\tau k^{\tau}_{c_1,3}\,,$$

where $F(c^{\tau}_1) := F(c^{\tau}_1, m^{\tau})$ are given by the local central difference approximation of the spatio-structural dynamics for $c^{\tau}_1 := c_1(t^{\tau}, x, y, \alpha)$ at the given time point t^{τ}. We then use a MacCormack corrector, of the form

$$\hat{c}^{\tau+1}_1 := \frac{c^{\tau}_1 + \bar{c}^{\tau+1}_1}{2} + \frac{d\tau}{2} F(\bar{c}^{\tau+1}_1)\,.$$

Likewise, these formulae are used for the calculation of the solution for the IFN molecular species, $m(t, x)$.

We further apply the population-based constraint

$$c^{\tau+1}_1 := \hat{c}^{\tau+1}_1 \frac{\int_{\mathcal{P}} \int_{\Gamma} c^0_1 \, d\alpha \, dy}{\int_{\mathcal{P}} \int_{\Gamma} \hat{c}^{\tau+1}_1 \, d\alpha \, dy}\,, \tag{4.21}$$

in order to constrain growth in the population due to the advective term under condition $c(t, x, \xi, y, \alpha) \geq 0$. We can write this in the particular case give since $S(t, x, \xi, y, \alpha) = 0$ and therefore we have that there is no overall change in population. Otherwise, however, this can be achieved by stepwise accumulation and conformity.

In order to compute accurate solutions to the multi-cluster distribution arrays, we denote one individual cluster as $c_{1,i}(t, x, y)$ for any $i \in \{1, \ldots, k\}$, where k is the total number of clusters or initial distributions. Then we have that the entire cellular population distribution is defined as

$$c_1(t, x, y, \alpha) := \sum_{i=1}^{k} c_{1,i}(t, x, y, \alpha).$$

Observe that from the fundamental theorem of calculus we, therefore, have

$$\begin{aligned}\nabla_x \cdot c_1(t,x,y,\alpha)\nabla_x m &= \nabla_x \cdot \left(\sum_{i=1}^{k} c_{1,i}(t,x,y,\alpha)\right)\nabla_x m \\ &= \sum_{i=1}^{k} \nabla_x \cdot c_{1,i}(t,x,y,\alpha)\nabla_x m\end{aligned} \tag{4.22}$$

Since we have that the overall population does not change with respect to changes time ($S(t,x,y,\alpha) = 0$), we can use that (4.21) and (4.22) imply that the population constraint holds on each individual cluster of IFN producer cells

$$c_{1,i}^{\tau+1} := \hat{c}_{1,i}^{\tau+1} \frac{\int_{\mathcal{P}}\int_{\Gamma} c_{1,i}^{0}\, d\alpha\, dy}{\int_{\mathcal{P}}\int_{\Gamma} \hat{c}_{1,i}^{\tau+1}\, d\alpha\, dy}, \qquad \forall i. \tag{4.23}$$

and then the total population changes with

$$c_{1}^{\tau+1} := \hat{c}_{1}^{\tau+1} \frac{\int_{\mathcal{P}}\int_{\Gamma} \sum_{i=1}^{k} c_{1,i}^{0}\, d\alpha\, dy}{\int_{\mathcal{P}}\int_{\Gamma} \hat{c}_{1}^{\tau+1}\, d\alpha\, dy}, \qquad \forall i. \tag{4.24}$$

These constraints should either leave the population $c(t,x,y,\alpha)$ unaltered or correct for any small instabilities arising from the long-term cumulation of $\mathcal{O}(\delta^2)$ spatial advective errors, which are not adequately dealt with by the predictor-corrector methodology.

We also introduce the notations

$$c_\alpha := \int_{\mathcal{P}} c(t,x,y,\alpha)\, dy \quad \text{and} \quad c_y := \int_{\Gamma} c(t,x,y,\alpha)\, d\alpha$$

as quantifying the spatio-metabolic and spatio-binding distributions, respectively, and

$$\breve{c} := \iint_{\mathcal{D}} c(t,x,y,\alpha)\, dx$$

as quantifying the non-spatial metabolo-binding distribution of the cellular population $c(t,x,y,\alpha)$.

Parameters

Here we give the table of parameters for the complete, SST system:

dependent variable	independent variable	parameters		
$\hat{c}$	x	$D_c = 10^{-5}$	$\chi_m = 10^{-4}$	
	y	$\beta = 2\lambda$	$\upsilon = 10^{-1}$	$\theta_m = 10^{-1}$
	α	$d = \frac{1}{4}\beta$	$\mu_0 = 10^{-1}$	
m	x	$D_m = 4\times 10^{-3}$		
		$\varepsilon = 10^{-2}$	$\theta_\alpha = 10^{-1}$	$\phi = 1$

Table 4.1: Table of parameters

4.2.5 Results from Numerical Simulations

Spatially static, single-cluster results were generated by simulating (4.18), whilst multi-cluster results generate by simulating (4.19) with Neumann zero boundary conditions in spatial variables and Neumann zero boundary conditions in structural variables. Spatially-dynamics results were generated by simulating (4.20). A full description of numerical parameters used for simulating this system of equations is given in 4.2, where parameters were used as appropriate for the simulated model.

dependent variable	independent variable	parameters		
$\hat{c}$	x	$D_c = 10^{-5}$	$\chi_m = 10^{-4}$	
	y	$\beta = 2\lambda$	$\upsilon = 10^{-1}$	$\theta_m = 10^{-1}$
	α	$d = \frac{1}{4}\beta$	$\mu_0 = 10^{-1}$	
m	x	$D_m = 4\times 10^{-3}$		
		$\varepsilon = 10^{-2}$	$\theta_\alpha = 10^{-1}$	$\phi = 1$

Table 4.2: Table of parameters for a model SAR system

In the following we will refer to two types of numerical simulations that differ by the type of initial condition. Single cluster simulations start with a localized cell distribution having a single maximum. Multiple cluster simulations start

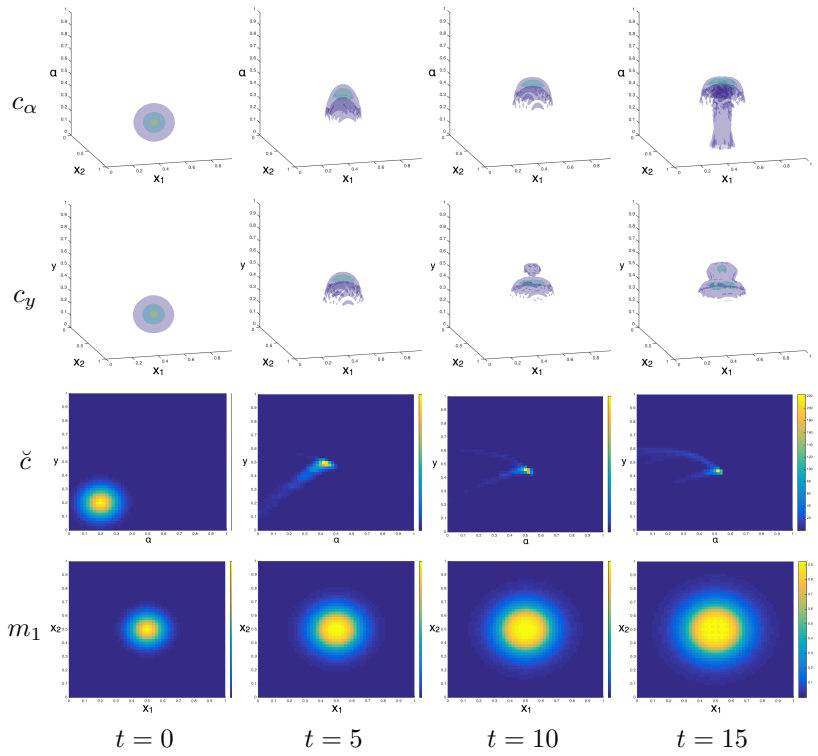

Figure 4.3: Single-cluster results from simulation of model (4.18) for low affinity ($\lambda = 0.1$) are given for $c(t, x, y, \alpha)$ in the spatio-metabolic domain (1^{st} *row*, c_α), with x on the horizontal plane and α on the vertical axis; in the spatio-binding domain (2^{nd} *row*, c_y), with x on the horizontal plane and y on the vertical axis; in the metabolo-binding domain (3^{rd} *row*, $\breve{c}$), with α on the horizontal axis and y on the vertical axis; and for $m(t, x)$ in space (4^{th} *row*), for $t \in \{0, 5, 10, 15\}$ respectively.

with an initial cell distribution having several maxima periodically positioned in space.

Spatially-static, single-cluster simulations

Single-cluster results (Fig. 4.3 & 4.4) demonstrate an initial rise in average binding position, c_y, of the cellular population with a concurrent rise in average metabolic position, c_α. In $\breve{c}$ we also observe the rise in metabolo-binding state with a focus developing at approximately $(y, \alpha) \approx (0.45, 0.55)$, with a negatively graduated non-linear ridge, and a tail between the focus and $(y, \alpha) = (0, 0)$.

Beyond $t = 20$, the average distribution in the binding space remains largely static, whilst the population continues to redistribute itself into a teardrop ge-

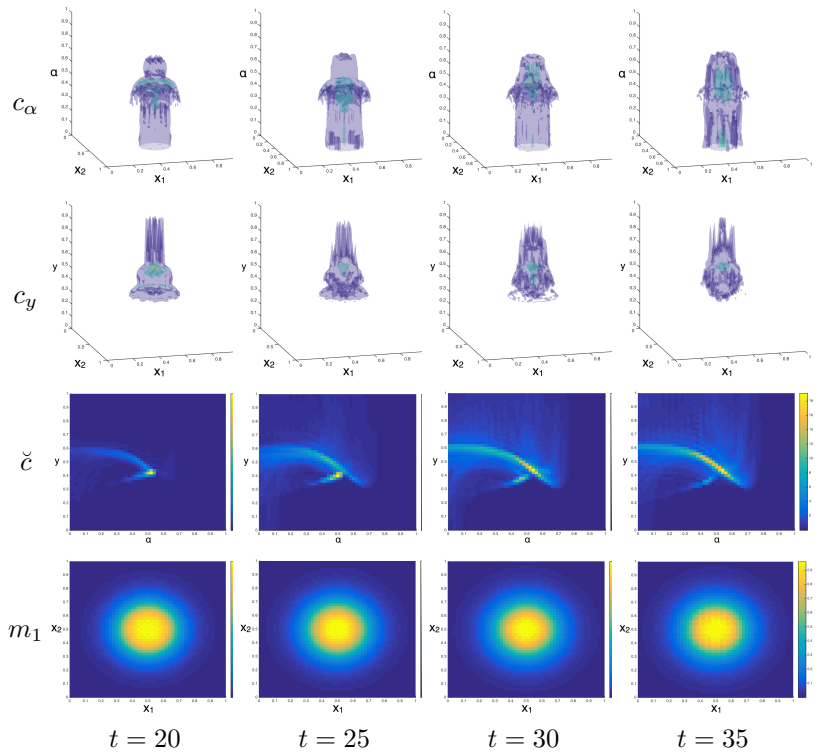

Figure 4.4: Single-cluster results from simulation of model (4.18) for low affinity ($\lambda = 0.1$) are given for $c(t, x, y, \alpha)$ in the spatio-metabolic domain (1^{st} *row*, c_α), with x on the horizontal plane and α on the vertical axis; in the spatio-binding domain (2^{nd} *row*, c_y), with x on the horizontal plane and y on the vertical axis; in the metabolo-binding domain (3^{rd} *row*, $\breve{c}$), with α on the horizontal axis and y on the vertical axis; and for $m(t, x)$ in space (4^{th} *row*), for $t \in \{20, 25, 30, 35\}$ respectively.

ometry, around the average position. This indicates, firstly, that the cell is capable of sustaining its own binding state, through production, upon initial stimulation with IFN. The formation of this geometry could be as a result of the maximal concentration of producer cells being central, and thusly producing greater levels of IFN which can be bound by the population, itself.

The distribution in the metabolic space exhibits oscillation, around its average position, for all time points $t \geq 15$ (Fig. 4.4 c_α). This oscillation is both transverse and longitudinal, and is likely to occur as a result of the SAR-cycling between the metabolic and binding states of these cells. This demonstrates the importance of the establishment of heterogeneity within the cellular population as it acts to regulate the IFN output of the system, whilst concurrently

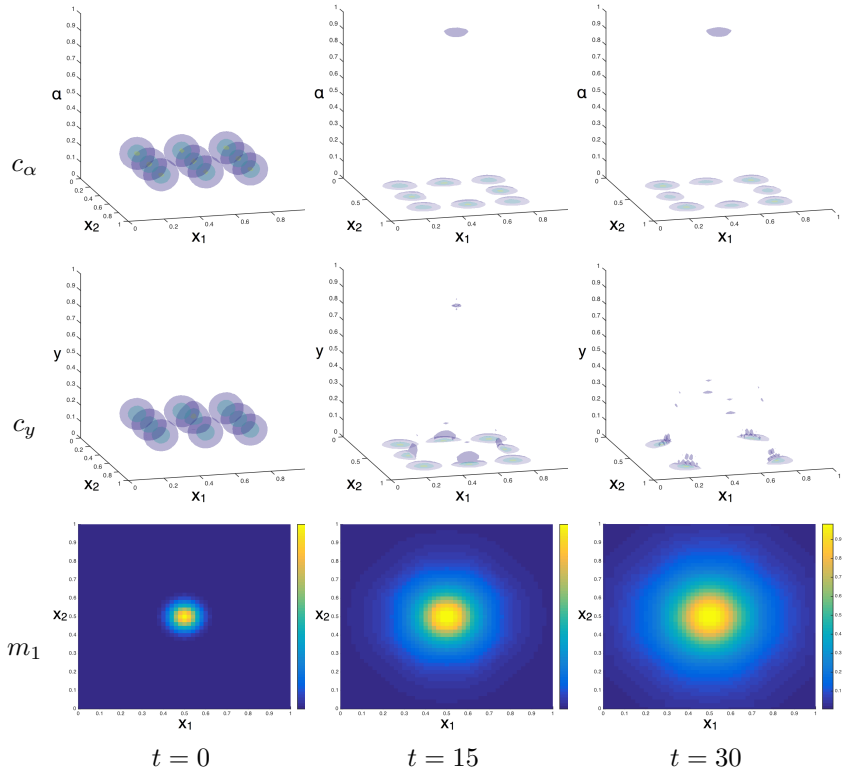

Figure 4.5: Multi-cluster results from simulation of model (4.19) for low affinity ($\lambda = 0.01$) are given for $c(t, x, y, \alpha)$ in the spatio-metabolic domain (1^{st} *row*, c_α), with x on the horizontal plane and α on the vertical axis; in the spatio-binding domain (2^{nd} *row*, c_y), with x on the horizontal plane and y on the vertical axis; and for $m(t, x)$ in space (3^{rd} *row*), for $t \in \{0, 15, 30\}$ respectively.

maximising metabolic expedition from the available and bound IFN supplies. Interferon producer cells do not act in unison and, indeed, use heterogeneity to co-regulate cells within such a cluster.

The final observation that one wishes to make in the results for the single-cluster case is the visible SAR-cycle displayed within the metabolo-binding space (Fig. 4.3 & 4.4 č). Regions of the solution for the cellular population appear to increase their binding state of IFN; before concurrently increasing their metabolic state and slightly decreasing their binding state; subsequently decreasing their metabolic and binding states, together; and beginning this cycle, once more. Whilst the majority of the population maintains its position within the bulk of this distribution, there exist cells (or subpopulations of the cellular

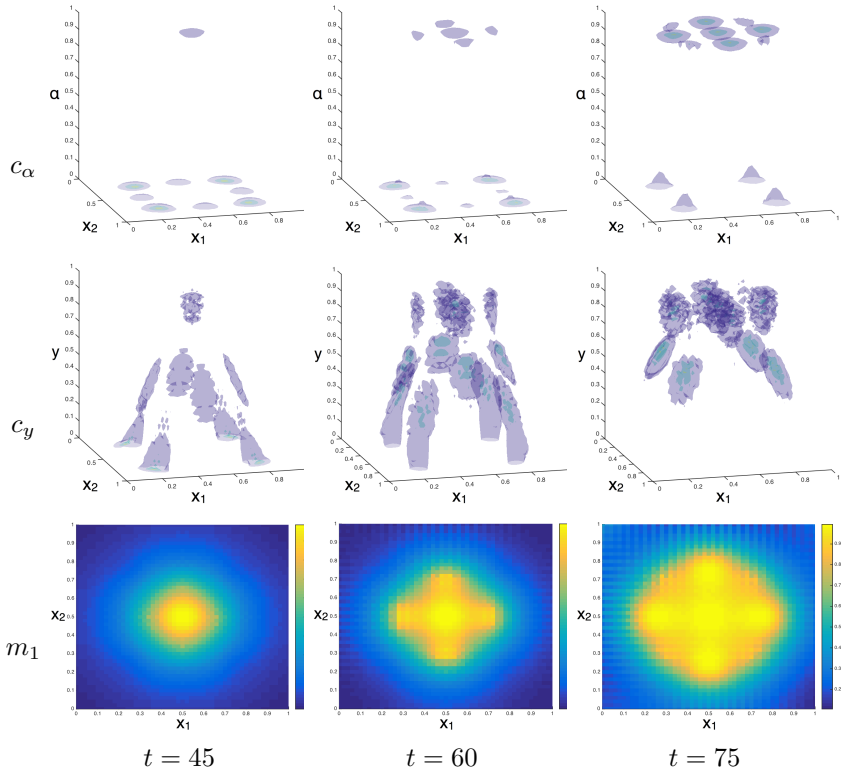

Figure 4.6: Multi-cluster results from simulation of model (4.19) for low affinity ($\lambda = 0.01$) are given for $c(t, x, y, \alpha)$ in the spatio-metabolic domain (1^{st} *row*, c_α), with x on the horizontal plane and α on the vertical axis; in the spatio-binding domain (2^{nd} *row*, c_y), with x on the horizontal plane and y on the vertical axis; and for $m(t, x)$ in space (3^{rd} *row*), for $t \in \{45, 60, 75\}$ respectively.

population) that are affected by this feedback cycle.

Spatially-static, multi-cluster simulations

In the multi-cluster results (Fig. 4.5–4.8) we observe a significant difference in the behaviour of the metabolic and binding spaces, in comparison to those of the single cluster. One observes the appearance of stable regions within the metabolic space, at high values for α; a phenomenon that we term 'metabolic trapping'. In the low affinity case, where the focal point for metabolo-binding dynamics would be lower in value, this effect is likely due to the feeding back of IFN proteins between clusters that lead the internal feedback mechanism to be ineffective at downregulating the metabolic state of the cell. In the high

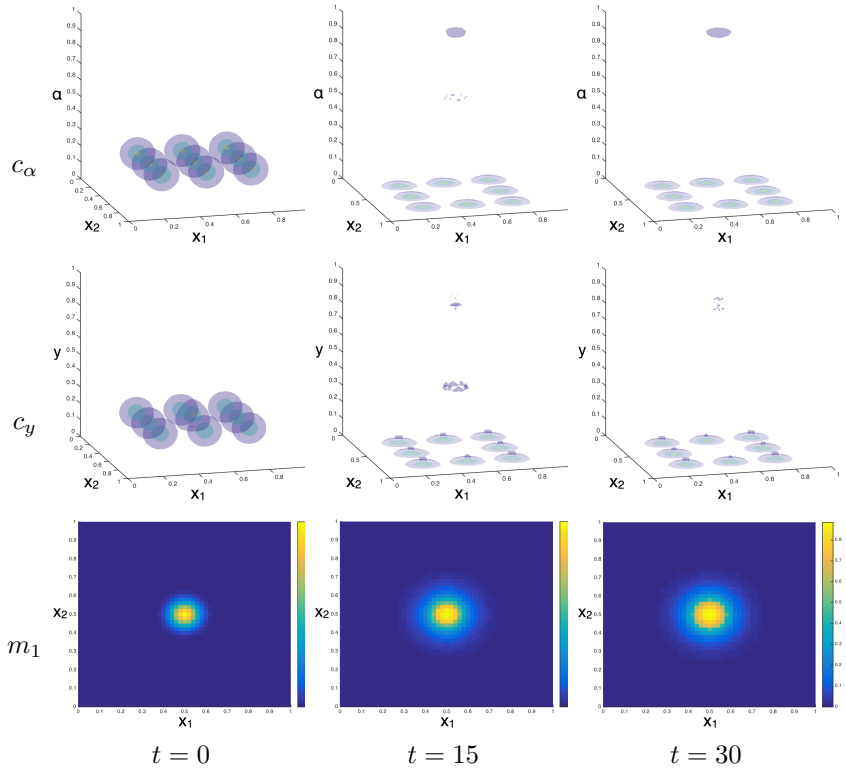

Figure 4.7: Multi-cluster results from simulation of model (4.19) for high affinity ($\lambda = 0.5$) are given for $c(t, x, y, \alpha)$ in the spatio-metabolic domain (1^{st} *row*, c_α), with x on the horizontal plane and α on the vertical axis; in the spatio-binding domain (2^{nd} *row*, c_y), with x on the horizontal plane and y on the vertical axis; and for $m(t, x)$ in space (3^{rd} *row*), for $t \in \{0, 15, 30\}$ respectively.

affinity case, this is likely to be due to the high binding and retention rates, in comparison to the unbinding rate, which causes the internalisation rate to remain high.

The binding state (Fig. 4.5–4.8 c_y), on the other hand, demonstrate oscillatory dynamics which were before characteristic of the metabolic state. Upon the establishment of stable metabolic dynamics, at high values for α, one expects that the conflict between the high rates of binding (caused by high rates of production and subsequent values for free chemical concentrations) and the feedback mechanism of the metabolic gene circuitry would cause such a behaviour. Cells will attempt to bind the high levels of IFN whilst the feedback mechanism continually acts to diminish the affinity of producer cells for IFN.

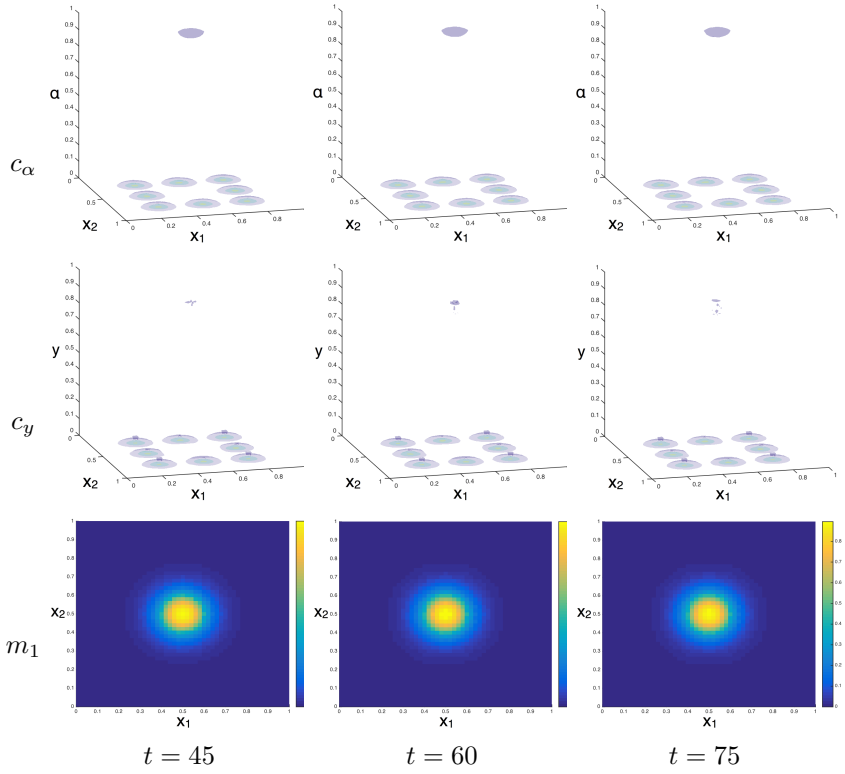

Figure 4.8: Multi-cluster results from simulation of model (4.19) for high affinity ($\lambda = 0.5$) are given for $c(t, x, y, \alpha)$ in the spatio-metabolic domain (1^{st} *row*, c_α), with x on the horizontal plane and α on the vertical axis; in the spatio-binding domain (2^{nd} *row*, c_y), with x on the horizontal plane and y on the vertical axis; and for $m(t, x)$ in space (3^{rd} *row*), for $t \in \{45, 60, 75\}$ respectively.

One should also notice that in the low affinity case (Fig. 4.5 & 4.6), as opposed to the high affinity case (Fig. 4.7 & 4.8), one observes that the signal is conveyed to the neighbouring cells. This can only be achieved through the implementation of a threshold in the binding dynamics for $c(t, x, y, \alpha)$ and this same threshold mediates the distance at which the signal can be conveyed.

Moreover, a simple comparative between the high affinity multi-cluster (Fig. 4.7 & 4.8), low affinity multi-cluster (Fig. 4.5 & 4.6), and single-cluster (Fig. 4.3 & 4.4) results will show that the concentrations of IFN produced by the low affinity multi-cluster system were far in excess of those in the other two cases. This is likely as a result of the cumulative production but also as a result of the production of the two, or more, clusters feeding back the IFN to one another,

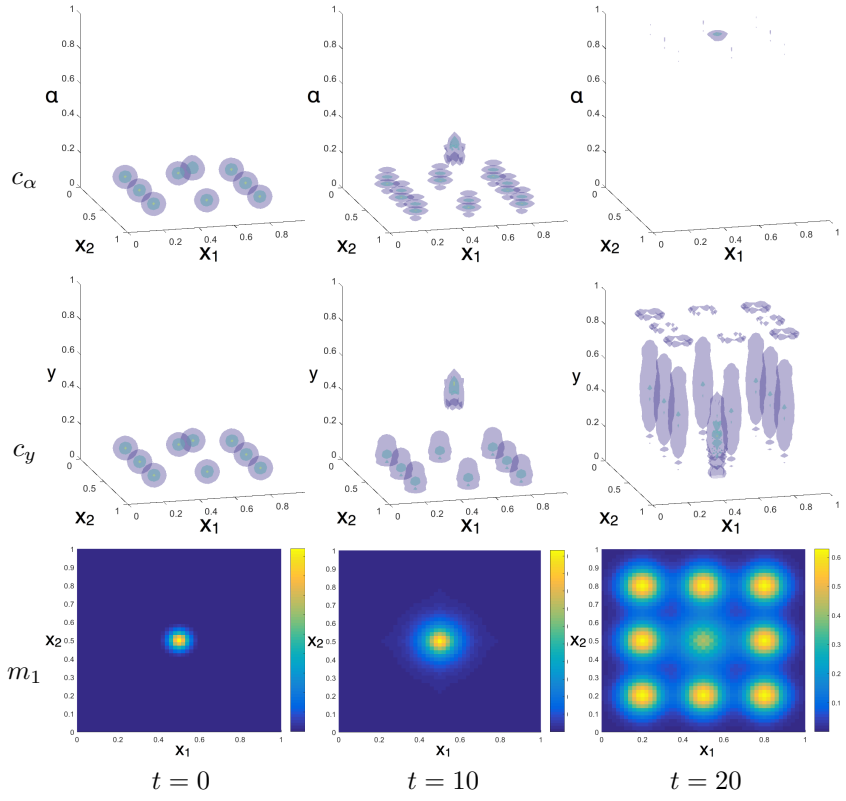

Figure 4.9: Multi-cluster results from simulation of model (4.20) for high affinity ($\lambda = 0.5$) are given for $c(t, x, y, \alpha)$ in the spatio-metabolic domain (1^{st} *row*, c_α), with x on the horizontal plane and α on the vertical axis; in the spatio-binding domain (2^{nd} *row*, c_y), with x on the horizontal plane and y on the vertical axis; and for $m(t, x)$ in space (3^{rd} *row*), for $t \in \{0, 10, 20\}$ respectively.

causing a metabolic trapping effect. This metabolic trapping is manifest as an emergence of the population at the upper boundary of the metabolic space and retention of this position. This effect is opposed to that of the metabolo-binding SAR-cycling that one observes in the single cluster case and is as a direct result of inter-cluster heterogeneity, where the promotion of the primed state in one cluster will facilitate the priming of the second, and so on.

Spatially-dynamic, multi-cluster simulations

Consider, now, the numerically generated results for the system (4.20), with parameters given as in above sections (Table 4.2). We give the simulated solu-

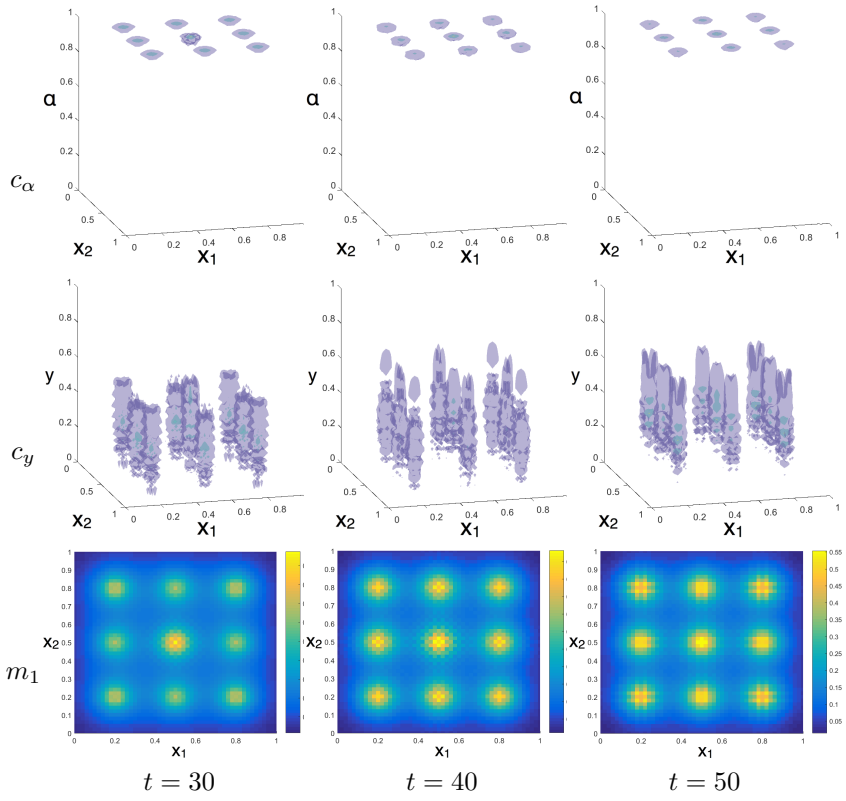

Figure 4.10: Multi-cluster results from simulation of model (4.20) for high affinity ($\lambda = 0.5$) are given for $c(t, x, y, \alpha)$ in the spatio-metabolic domain (1^{st} *row*, c_α), with x on the horizontal plane and α on the vertical axis; in the spatio-binding domain (2^{nd} *row*, c_y), with x on the horizontal plane and y on the vertical axis; and for $m(t, x)$ in space (3^{rd} *row*), for $t \in \{30, 40, 50\}$ respectively.

tions for the high-affinity, multi-cluster IFN case (Fig. 4.9 & 4.10), only, as the spatio-metabolo-binding dynamics are similar at both high and low affinities. One immediately observes the dissolution of the discrepancy between the two species in terms of their communicative capability. The high affinity SARs are able to communicate with one another under a spatially-dynamic, chemotactic regime.

In order to best understand these dynamics, one must observe them in the passage of time. The chosen initial conditions impose a stimulus on the central cluster of cells, whilst peripheral clusters are in a state of metabolic relaxation (Fig. 4.9). The spatial dynamics of the central cluster, at early

time-points, will be mainly balanced between diffusive processes and chemotactic auto-aggregation. In the peripheral clusters, however, the absence of IFN means that the spatial dynamics are mainly dictated by diffusive processes.

This diffusion in the cellular population allows some small subpopulation of cells to migrate sufficiently towards the central cluster so as to overcome the thresholding in the metabolic dynamics. Coupling this subpopulation with high affinity molecules, one achieves a fast dynamics in the binding and metabolic spaces on the perimeter of the peripheral clusters (Fig. 4.9, $t = 20$). Once these peripheral subpopulations have been potentiated to the point where they are capable of producing high affinity IFN, the cluster attains an intra-cluster supply and is capable of maintaining its own levels of IFN (Fig. 4.9, $m(20, x)$), resulting in initially peaked levels of IFN concentration at peripheral sites.

In the chemotactic simulations, one can more clearly see the elements of inter-cluster oscillation as an illustration of similar intra-cluster events. One observes an initially raised production dynamics in the central clusters (Fig. 4.9, $t = 10$); followed by fast metabolic dynamics within, and a concurrent raising of the local concentrations around, the peripheral clusters (Fig. 4.9, $t = 20$); a subsequent response from the central cluster as the peripheral clusters feedback IFN to elevate binding rates (Fig. 4.10, $t = 30$); and the resolution of this oscillatory behaviour in the establishment of a quasi-equilibrium (Fig. 4.10, $t \geq 40$), where intra-cluster dynamics prevail but result in little macroscopic change. The initial inter-cluster heterogeneity is a necessary precursive state for the establishment of this uniformity in behavioural dynamics.

Moreover, the establishment of this synchronicity between the clusters leads to another effect stemming from the chemotactic dynamic. Not only are cells capable of communicating in the chemotactic paradigm but they also self-attenuate their diffusion and auto-aggregate upon the establishment of intra-cluster activation. This may have profound implications for immunity: If, as one might intuitively predict, cells who are inclined to utilise chemotactic dynamics were attracted to the first cluster, and activated at some gradualistic pace, then the infection of the organism by a pathogen would result in the ac-

cumulation of IFN excreting cells. The decay of the spatial diversity in the cells would then lead the body to become more vulnerable to infection at novel sites, as there would no longer be IFN SARs present. If, however and as predicted by our model, we have a slight diffusive process which allows the signal to be passed but followed by auto-aggregation, then the cells would remain mostly *in situ* and would propogate the signal without compromising their position in the event of a further wave of infection.

4.2.6 Discussion

The model and framework that we have herein developed is sufficiently general so as to be useful in cases that extend beyond the IFN system and even beyond the more general category of SARs. Generality is achieved through the biologically global forms of the binding and unbinding functions as well as the particularly general form chosen for the metabolic flow function, which describes a whole metabolic pathway in a reasoned but condensed single ODE form.

The single-cluster model demonstrates a qualitative biological SAR-cycling between binding and metabolic dynamics of a SAR (Fig. 4.3 & 4.4). More basic, or simplistic, models may be capable of producing quantitatively similar results but could not capture the mechanistic heterogeneity within biological systems which cause them to function as they do. Alone, this illustrates the potential for SST systems to differentially mimic biological systems to a far greater accuracy than can current modelling techniques.

In terms of the biology, this model makes two important realisations: That low affinity molecules may be necessary, for the functioning of the system, in order that the concentrations of such molecules, at long range, are sufficiently high so as to activate distant clusters of producer cells. In other words, low affinity molecules allow cell-cell communication, at a distance. Also, the biological system actually has two important functions of heterogeneity internally, in order to self regulate clusters and maintain sensible levels of IFN, and externally between clusters, so as to convey the activation signal of one cluster by firstly

priming an initially excited cluster at a distance.

The internal heterogeneity established by clusters informs one that the ability for a cluster of SARs (specifically those for IFN) to maintain optimal levels of metabolism and reciprocal output, it is necessary for some subpopulation of cells to sacrificially reduce their levels of binding. This appears to be as a consequence of the feedback between metabolism, α, and binding, y, such that as one subpopulation rapidly increases its metabolism it will feel and subsequent inhibition of its ability to bind and will sacrifice itself such that another subpopulations may rapidly increase its binding and metabolism, due to the increased availability of local IFN. This is an important effect of intra-popular heterogeneity which we term 'subpopular quiescence', and may explain several of the inter-cellular, intra-popular oscillatory events in biology.

The latter of these two realisations recognises the importance of heterogeneity to the biological system. We demonstrate that in order that a primary cluster be primed, upon excitation, it must be allowed to be internally heterogeneous such that more active cells serve to activate less active cells whilst down regulating their own activity. This is essential for maintenance of activity levels and eventually for switching the system off. We further show that this ability for one cluster to self-activate and autoregulate is essential to maintain the long range signal and activate further clusters, at a distance. This nuancing is not possible within the simple spatial model (4.1).

One phenomenon, observed within the multi-dimensional model, which cannot be recreated within more simple mathematical models is that of 'metabolic trapping', and therefore, production in the presence of inter-cluster cooperativity. In the simple models, one has a mechanism of feedback wherein a cluster will create IFN in the presence of IFN, amplifying a given local signal. This return, however, always achieves a maximal concentration and the rate is dependent only on local IFN concentration. In the SST context, one observes that the inter-cluster supply of IFN protein between clusters actually increases the metabolic state of all involved clusters causing the productions rates to increase,

concurrently. This is a qualitative result which makes a qualitative difference to the final resting state of IFN concentration.

We recognise, also, that the conveyance of the signal in the low affinity cases (Fig. 4.5 & 4.6) is dependent on some thresholding parameter in the binding space, and can be justified through the biological realisation that sufficiently low quantities of chemical are insufficient to bind the receptor for long enough durations so as to cause co-phosphorylation of the internal proteins. This is a further major difference between this and previous modelling techniques, since previous modelling techniques make no comment on this phenomenon. A demonstrable advantage of this modelling framework is the ability to flag up novel biological problems, not necessarily perceptible to simpler state-variable frameworks.

Spatially dynamic results demonstrated a breakdown in the different abilities of high and low affinity IFN to affect inter-cluster cell communication. This demonstrates that communication can be achieved either by means of reducing the barriers to the travelling molecule (affinity to consumer cells) or by cellular migration, reducing the distance between SARs themselves. In biology these dynamics may occur in environments which have more freedom for the cells to migrate and may not be achievable in many instances. In cases where migration is not possible it may be advantageous to increase production of lower affinity IFN, where high affinity IFN may be advantageous otherwise, due to the resultant increase in dynamic rate.

The biological significance of these processes are underscored by the intricate intra- and inter-cluster spatial and metabolo-binding dynamics. The major features are an intra-cluster oscillatory dynamic and a intra-cluster, post-potentiation auto-aggregation which may be immunologically advantageous (depending on the paradigm considered). In the paradigm where cells are capable of migration, however, one will immediately notice that any given signal is much harder to contain or confine to a local spatial domain. This may be important in organs, such as he brain, where the body wishes to localise inflammatory response and antiviral behaviour as far as is possible. Therefore, local biological

considerations may effect the evolutionary choice of method for communication chosen.

Finally, this framework is far more approachable for the biological community, in terms of understanding. The internal and inter-cluster heterogeneity described by the SST framework is relatable to biologists in a way that is conducive to dialogue. In line with this a further explanation proffered to the thresholding problem, however, could be that there are two such IFN molecules involved in this process; one of high and one of low affinity. The high affinity molecules may serve to perpetuate the activation of the considered cell, or cluster, whilst the low affinity molecule may serve to convey this signal to other producer cells. This is a theme that the authors intend to explore in a further publication.

4.3 Human Multi-Affinity Interferon System is Necessary for an Effective Antiviral Response

4.3.1 Further Biological Details of the Interferon (IFN) System

(In this subsection, we briefly recap many of the biological details of the IFN system that have not yet been covered, in order to inform the latter biological discussion of the presented results.)

Cytokine signalling is the primary mechanism by which immune cells communicate and may play a major role in the spatial suppression of viral infections. Systems biological investigations have significantly contributed to the current understanding of cytokine communication [12, 106], and other such systems with the ability to detect and amplify biochemical signals [344, 280]. The spatial aspects and characteristics of cytokine communication have been given much attention and play a significant part in determining the outcomes of infection, defining the efficiency by which such communication may take place

[110, 108, 6, 261, 190, 303]. Novel modelling techniques provide an opportunity to intertwine mechanistic biochemical models with spatial models to determine interactions between, and the relative contributions of, these two aspects in the biological immune machinery [161].

One cytokine of particular interest, due to its prevalence throughout the mammalian body and its function in antiviral defences, is the type I interferon (IFN) family[40]. Several human pathologies take root in the alteration of the molecular pathways leading to type I IFN production and responses[284]. In humans, the type I IFN family includes several molecules; among them the 13 IFN-α subtypes and the IFN-β represent the vast majority of the IFN produced in response to viral infection. All these type I IFNs act through the same cellular receptor composed by IFNAR1 and IFNAR2[324]. Their actions are critical for alleviating viral infections through direct antiviral function in non-infected cells and through indirect effects elsewhere; activating the humoural and cellular immune responses[314].

All human cells are capable of producing type I IFNs in response to viral infection, through a process which is tightly regulated. Three phases can be distinguished: (i) The recognition of pathogen-associated molecular patterns (PAMPs) by pattern recognition receptors (PRRs), leading to the phosphorylation of IRF3 which, in conjunction with NFκB, induces the secretion of IFN-β. (ii) This IFN-β then acts in autocrine and paracrine manners through IFNAR1 and IFNAR2 present on the infected and neighbouring cells. This activates the JAK/STAT signalling pathway and induces the IFN-stimulated genes (ISGs); among them, the transcription factor IRF7. (iii) In the continued presence of PAMPs, IRF7 is capable of inducing the transcription of the remaining type I IFN genes, mainly IFN-α genes, as well as IFN-β[205]. The production of the IFN-α is thus, first of all, dependent of the presence of IFN-β and also in the response of the cells to this IFN for the induction of IRF7. Since IRF7 is an ISG, its synthesis is repressed by pathways which negatively control IFNAR-associated signalling, such as USP18 – an ISG which decreases the efficacy of the IFN receptor complex assembly[340].

Such a tightly controlled process for a hierarchical type IFN subtypes production appears to be largely conserved in all mammalian orders. All possess at least one IFN-α and one IFN-β gene as defined at least by their different promoter structure[205, 148]. The biological relevance of the network architecture, however, is poorly understood. In humans, the IFN-β and the 13 IFN-αs can be distinguished by the kinetic parameters of their interaction with IFNAR1 and IFNAR2. These binding parameters determine the stability of the ternary IFN-receptor complexes and, consequently, the specific activity or biological potency of each IFN subtypes. The IFN-β is the higher affinity subtype and the IFN-α contains several less potent subtypes, particularly IFN-α1 and IFN-α13 – two subtypes strictly identical in their primary sequence but exhibiting > 100 lower specific activity compared to IFN-β[323, 324]. Interestingly, whereas some IFN-α subtypes accumulate nonsense mutations in the human population, suggesting that they are undergoing pseudogenization, the IFN-α13 is one of the type I IFN subtypes that have been subject to the strongest purifying selection[230].

In this paper, we employ a recently developed mathematical framework to describe the simultaneous binding process of several IFN populations, of differing affinities, and their relative effect on the levels of ISG transcription, including IRF-7 and USP18. We propose that the existence of multiple subtypes in the IFN system will bestow, upon the host of a given pathogen, an evolutionary advantage through the increased ability to alert neighbouring cells to the presence of a pathogen, through low-affinity IFN molecules, whilst retaining the ability to sustain this reaction, through high-affinity IFN molecules.

4.3.2 A Mathematical Model for IFN Dynamics

In order to perform a controlled study into the dynamics of multi-affinity ligand systems, we composed a mathematical model to describe this system.

Accordingly as in Hodgkinson *et al.*[161], begin by defining the temporal and spatial domains $\mathcal{I} = [0, T) \in \mathbb{R}$ and $\mathcal{D} \subset \mathbb{R}^d$, respectively, and their respective variables $t \in \mathcal{I}$ and $x \in \mathcal{D}$. Then allow that the binding dimensions $\mathcal{P} \subset \mathbb{R}^p$, with

$p \in \mathbb{N}$, and binding variable $y \in \mathcal{P}$ exist, such that they define the percentage of the cells' available surface receptors, at a given spatio-temporal location (t, x), which have formed one of p different complexes with ligands. Further, let $q \in \mathbb{N}$ be the total number of different ligands. Finally, allow that the metabolic dimensions $\Gamma \subset \mathbb{R}^\gamma$, with $\gamma \in \mathbb{N}$, and the binding variable $\alpha \in \Gamma$ exist, such that they define the metabolic state of the cells as a percentage of the carrying capacity of the cells metabolic activity in some i^{th} pathway, for $i \in \{1, \dots, \gamma\}$.

In the current case, where we focus on the system's ability to communicate, we focus primarily on the instance $d = 2$ or a system of 2 spatial dimensions. Further, we simplify the system to take into account 2 IFN proteins (high- and low-affinity), $q = 2$ such that $\bar{m}(\cdot, \cdot) : \mathcal{I} \times \mathcal{D} \to \mathbb{R}^q$, forming one binding complex, IFNAR-IFN such that $p = 1$. Further, we only comprehensively take into account 1 group of metabolic pathways (those producing IRF-7) such that $\gamma = 1$.

Consider, now, a cellular distribution in time, space, binding, and metabolism, $c_1 : \mathcal{I} \times \mathcal{D} \times \mathcal{P} \times \Gamma \to \mathbb{R}$. The spatial dynamics of this distribution are not considered. Gross binding is positive up to the carrying capacity of the receptors minus the square of the metabolic state, $1 - \alpha^2$, due to the negative feedback mechanism within the cell, and occurs with a rate vector $\bar{\beta}$. In physical terms, each of the elements of $\bar{\beta} := [\beta_{m_1}, \beta_{m_2}]$ define the rate-normalised affinity of IFNα1/13 and IFNβ for the IFNAR2 receptor, respectively. Unbinding is proportional to the quantity of bound protein, with a rate δ. The metabolic state of the cell is increased upon binding, up to the normalised maximum 1, with a rate μ_+ and decreases with a rate μ_-. Then we write

$$\begin{aligned} \frac{\partial c_1}{\partial t} = &- \nabla_y \cdot \left[\bar{\beta} \cdot \bar{m}(1 - y - \alpha^2) - \delta y\right] c_1(t, x, y, \alpha) \\ &- \nabla_\alpha \cdot \left[\mu_+(1 - \alpha)y - \mu_- \alpha\right] c_1(t, x, y, \alpha). \end{aligned} \tag{4.25}$$

For the first free molecular species, $m_1(t, x)$ or IFN-α1/13, we write that the dynamics are given primarily by diffusion, with a rate D_{m_1}, and degradation

by the consumer cell population, c_2, at a rate $\delta_{m_1}\beta_{m_1}$. Moreover, free IFN-α1/13 is removed from the system upon binding and replaced into the system upon unbinding, with a parameter, ε, responsible for scaling the rate of binding with the surface area of the cell. IFN-α1/13 is further produced by the cell population, c_1, in a metabolically dependent manner in the presence of viral protein, and up to the normalised capacity one, and at rate ϕ_α.

$$\begin{aligned}\frac{\partial m_1}{\partial t} =& \nabla_x \cdot D_{m_1}\nabla_x m_1 - \delta_{m_2}\beta_{m_1} m_1 c_2 \\ &- \int_\Gamma \int_{\mathcal{P}} (\beta_{m_1} m_1(1-y-\alpha) - \delta y)\varepsilon c_1(t,x,y,\alpha)\, dy\, d\alpha \\ &+ v \int_{\mathcal{P}} \int_\Gamma \phi_\alpha \alpha(\alpha-\theta_\alpha)(1-m_1)c_1(t,x,y,\alpha)\, d\alpha\, dy.\end{aligned} \tag{4.26}$$

The second free molecular species is, likewise, defined in terms of its diffusion and consumption, with rates D_{m_2} and $\delta_{m_2}\beta_{m_2}$ respectively. The species is further removed from its free state through binding and replaced in response to metabolic potentiation. We assume, in this model, that the rates of production due to the increase in IRF-7 is equal for both species (*i.e.* that the genes IFN-α1/13 and IFN-β will be transcribed with equal veracity). Thus, the metabolic production rate ϕ_α remains equal between the two species and

$$\begin{aligned}\frac{\partial m_2}{\partial t} =& \nabla_x \cdot D_{m_2}\nabla_x m_2 - \delta_{m_2}\beta_{m_2} m_2 c_2 \\ &- \int_\Gamma \int_{\mathcal{P}} (\beta_{m_2} m_2(1-y-\alpha) - \delta y)\varepsilon c_1(t,x,y,\alpha)\, dy\, d\alpha \\ &+ v \int_{\mathcal{P}} \int_\Gamma \phi_\alpha \alpha(\alpha-\theta_\alpha)(1-m_2)c_1(t,x,y,\alpha)\, d\alpha\, dy \\ &+ \phi_{m_2}(1-m_2)v \int_\Gamma \int_{\mathcal{P}} c_1(t,x,y,\alpha)\, dy\, d\alpha.\end{aligned} \tag{4.27}$$

Finally, we denote the virus $v(t,x)$, endowing it with diffusive spatial dynamics, with a rate D_v, and logistic growth in the presence of c_2, with a rate ϕ_v. We also assume that the virus is naturally degraded, with rate δ_v, or destroyed, with some immune dependent rate $\iota\delta_\iota$.

$$\frac{\partial v}{\partial t} = \nabla_x \cdot D_v \nabla_x v + \phi_v v(1-v)c_2 - \delta_\iota \iota v - \delta_v v. \tag{4.28}$$

Since the immune cell population, ι, in this case serves as a biological marker of the degradation of viral proteins, we consider that IFNβ is a proportional surrogate for produced cytokines such that immune cell recruitment is proportional to local IFNβ concentrations. The relation for recruitment is then given by a normalised logistic growth function, with rate ϕ_ι, such that

$$\frac{\partial \iota}{\partial t} = \phi_\iota m_2(1-\iota). \tag{4.29}$$

4.3.3 Numerical Methods

Simulations were run using a McCormack predictor-corrector scheme with a 4^{th} order Runge-Kutta time-step. Since we work within a normalised system, we need only ensure that the orders of magnitude of our parameters are accurate, with respect to one another. Therefore, we use the literature to gain this insight, and choose the values of our parameters to reflect their relative difference and to elucidate the mechanics of the process.

Studies have found that the diffusion coefficient of typeI IFN is $\sim 7.43\times 10^{-5}\, mm^2\, s^{-1}$ [275] whilst the diffusion coefficient of the influenza virus A, for example, is within the range $\sim 1.02 - 5.58\times 10^{-6}\, mm^2\, s^{-1}$, with a peak at $\sim 2.62\times 10^{-6}\, mm^2\, s^{-1}$ [260]. Therefore, we set the micron-scale diffusion coefficients of IFN molecules at $D_m = 7.4\times 10^{-3}$ and of the influenza A virus at $D_v = 2.6\times 10^{-4}$, as an exemplar.

We also have that IFNAR2 affinity is quantified by on-rates (or association constants) of $\sim$757 and 151 $\mathrm{M}^{-1}\,\mathrm{hr}^{-1}$ and off-rates (or dissociation constants) of $\sim 2.78\times 10^{-7}$ and 3.33×10^{-5} hr^{-1} for IFN-α1 and IFN-β [177], respec-

Variable	Parameters		
c_1	$\beta_1 = \lambda_{m_1}$ $\mu_+ = 2\times10^{-2}$	$\beta_2 = \lambda_{m_2}$ $\mu_- = 2\times10^{-2}$	$\delta = 2\times10^{-1}$
v	$D_v = 2.6\times10^{-4}$	$\phi_v = 10^{-1}$	$\delta_v = 10^{-2}$
m	$D_m = 7.4\times10^{-3}$	$\varepsilon = 10^{-3}$	$\phi_\alpha = 2.0$
m_1	$\delta_{m_1} = 6\times10^{-2}$	$\lambda_{m_1} = 5\times10^{-1}$	$\theta_{\alpha,1} = 2\times10^{-1}$
m_2	$\delta_{m_2} = 6\times10^{-2}$	$\lambda_{m_2} = 8$	$\theta_{\alpha,2} = 2\times10^{-1}$

Table 4.3: Parameters used in generating numerical results for the full IFN system described by (eq:4.25-4.29).

tively. Also, it has been found that control cells produced IFN-β at a rate of $\sim$ 12.5–17pg ml^{-1} hr^{-1} in macrophages [164] and fibroblast [65] cells; for which metabolic parameters are chosen, accordingly with appropriate binding and unbinding rates, to reflect this behaviour at $\mu_+ = 2\times10^{-2}$, $\mu_- = 5\times10^{-2}$, $\theta_{\alpha,1} = \theta_{\alpha,2} = 0.2$, and $\phi_\alpha = 2.0$. The remainder of the parameters – namely those quantifying degradation rates – are estimated. The parameters used in numerically simulating (eq:4.25-4.29) are then given in Table 4.3.

Initial conditions are given by $c_1^0 := c_1(0,x,y,\alpha)$, $c_2^0 := c_2(0,x)$, $m_1^0 := m_1(0,x)$, and $m_2^0 := m_2(0,x)$ with

$$c_1^0 = \sum_{i=0}^{2}\sum_{j=0}^{2} \exp\Bigg[-500\Bigg((x_1 - \frac{1}{5} - \frac{3i}{10})^2 + (x_2 - \frac{1}{5} - \frac{3j}{10})^2 + (y - \frac{1}{10})^2 + (\alpha - \frac{1}{10})^2 \Bigg)\Bigg], \qquad (4.30)$$

$$c_2^0 = 1\,, \quad v^0 = m_1^0 = m_2^0 = \frac{1}{2}\exp\Bigg[-500\Big(x_1^2 + x_2^2 \Big)\Bigg].$$

Furthermore, in order to simplify the analysis and illustration of non-temporal, spatio-metabolo-binding (4-dimensional), we use the notations

$$c_1^y = \int_{\Upsilon} c_1(t,x,y,\alpha)\,d\alpha \qquad \text{and} \qquad c_1^\alpha = \int_{\mathcal{P}} c_1(t,x,y,\alpha)\,dy \qquad (4.31)$$

to denote the spatio-binding and spatio-metabolic distributions, respectively.

A dual-affinity, sparsely distributed IFN model

To begin, we consider only one high-affinity IFN ligand in IFN-β and one low-affinity IFN ligand in IFN-α1. We take, as an illustrative example of viral dynamics, the model parameters of the influenza A virus. Using a relatively narrow gaussian distribution to represent a 'cluster' of hæmatopoietic, IFN producing cells, we arrange these clusters in a 3x3 square grid. This provides a spatially heterogeneous distribution of cells with spatially consistent clusters but with spatial separation between clusters, allowing one to observe differentiated communication patterns within and between clusters.

A humanoid IFN model

In order to study the human type I IFN system consisting of 1 high-affinity, 10 medium-affinity, and 2 low-affinity ligands, we insert an additional term, $m_3(t, x)$ to account for medium-affinity populations and augment our normalised system to account for the respective changes in carrying capacity. The carrying capacity for medium-affinity ligands becomes 10 whilst that of low-affinity ligands becomes 2. Moreover, in an attempt to more realistically capture the biologically relevant spatial distribution of cells, we assume that hæmatopoietic cells are continuously and homogeneously distributed across the considered spatial domain.

4.3.4 Results & Discussion

Henceforth, the use of the general term 'IFN' shall be used to refer to all of the members of the type I IFN family, simultaneously. IFN-β refers to itself, an IFN exhibiting high-affinity for its receptor and having the ability to be produced independently of IRF-7 activity. IFN-α refers to the IFN-α subtypes showing low-affinity for IFNAR2, such as IFN-α1 or IFN-α13 in humans.

Our model then characterises the interactions between 6 populations: the cellular population, c, who produce IFN upon infection; the surrounding consumer cell population, c_2 who is not dynamic; the IFN-α and IFN-β popu-

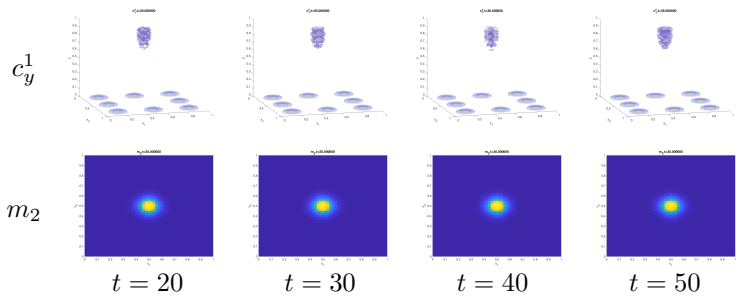

Figure 4.11: Time series showing the temporal dynamics of the interferon binding system upon mimesis of the artificial stimulation of a central cell cluster with IFNβ, in a High/Low IFN system where IFNα1/13 production is inhibited. Top: The cellular population is illustrated as a 3D iso-surface with space represented across the lower plane and the proportion of the cell surface bund to IFN along the vertical axis. Bottom: The IFNβ concentration is illustrated in terms of its spatial distribution (high: *yellow*, low: *blue*).

lations, m_1 and m_2 respectively; the population of virions, v; and a distant cellular population, ι, representing immune cells and who mount the immune response. The model then describes the proliferation of the virus within cells and the consequent production and release of IFN-β in response to the viral population. The cellular population will bind IFN-α or -β with their respective affinity-dependent binding rates and will concurrently remove those IFN proteins from the free molecular population. (Cells are also capable of unbinding these ligands.) In order to understand how the feedback between binding and metabolic processes influences the overall dynamics of the system, we model these processes through cell-specific y and α values respectively. The binding of IFN molecules will increase a given cell's y-value, or binding state, and lead to an increase in its ISG transcription state, or α-value. IFN-α is, further, only produced upon the elevation of this α state and strictly in the presence of the virus. Finally, the production and release of IFN-β will act as a proportional surrogate for cytokine release and lead to an increase in the local immune cell population who, in turn, will then locally degrade the viral population.

Parameters for the system are, as far as possible, taken from the available biological literature, where others are estimated in order to approach the behaviours described in the literature. Initial conditions of the cellular populations for simulations are given by a 3×3 grid of cellular Gaussian distributions, each

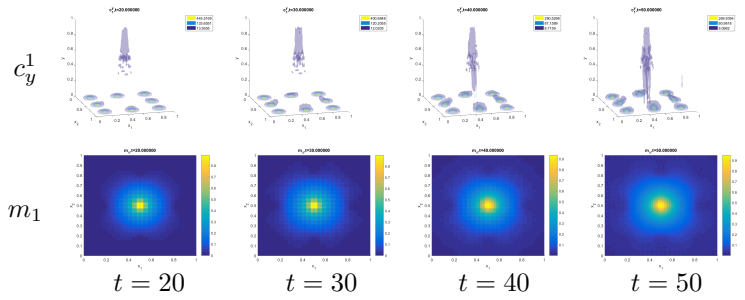

Figure 4.12: Time series showing the temporal dynamics of the interferon binding system upon mimesis of the artificial stimulation of a central cell cluster with IFNβ, in a High/Low IFN system. Top: The cellular population is illustrated as a 3D isosurface with space represented across the lower plane and the proportion of the cell surface bound to IFN along the vertical axis. Bottom: The IFNα concentration is illustrated in terms of its spatial distribution (high: *yellow*, low: *blue*).

of which we refer to as a 'cluster'. This choice facilitates the study of long-range communication of the signal and mimics particular experimental settings.

Results of numerical simulations using (eq:4.25-4.29) are displayed in two forms. The first represents a spatial distribution of quantities of IFN-α or IFN-β, as a colour-mapping on a 2-dimensional axis between dark blue representing low values (near 0) and yellow representing high values (near 1). The second one displays higher dimensional variables, such as the IFN producer cells, as a 3-dimensional isosurface where space is given along the lower plane and the binding (y) or transcriptional (α) value is given along the vertical axis, with each body separated in space representing a separate cluster of IFN producing cells. Yellow isosurfaces indicate regions of maximal values for the cellular population, whilst blue isosurfaces indicate regions of $(1/100)^{\text{th}}$ the maximal value, at any given time point.

High-affinity ligands sustain local activity whilst low-affinity ligands transmit local signals.

We simulate cells who were capable of producing only IFN-β by preventing the production of IFN-α within the population. Moreover, we realise the constraint that autocrine signalling should be sufficient to produce IFN by imposing a constant, spatially-homogeneous distribution of viral protein and the condition that ISG transcription should be necessary and sufficient. This is equivalent

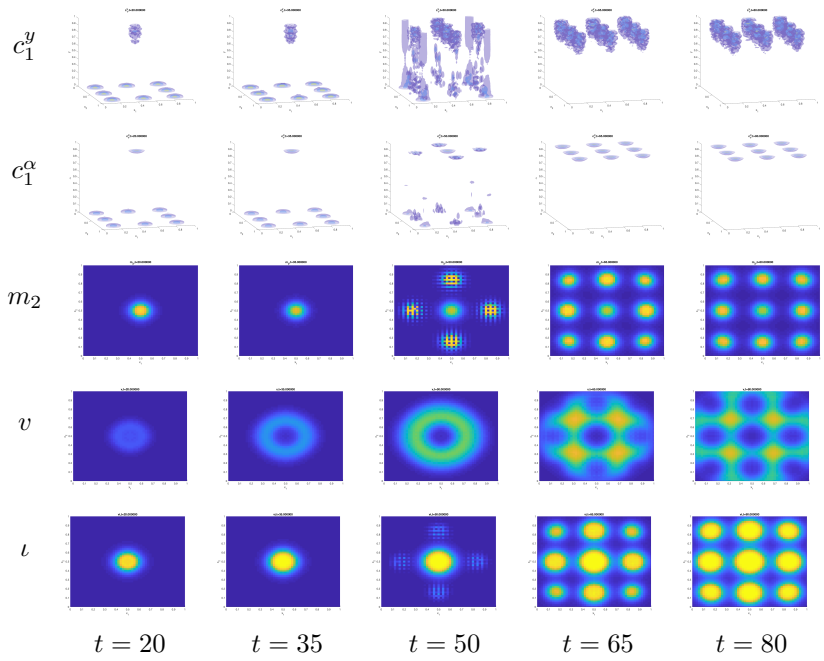

Figure 4.13: Time series showing the temporal dynamics of the interferon binding system upon mimesis of the artificial stimulation of a central cell cluster with IFNβ, in a High/Low IFN system where IFNα1/13 production is inhibited. 1$^{\text{st}}$ Row: The cellular population is illustrated as a 3D isosurface with space represented across the lower plane and the proportion of the cell surface bound to IFN along the vertical axis. 2$^{\text{nd}}$ Row: The cellular population is illustrated as a 3D isosurface with space represented across the lower plane and non-dimensionalised ISG activity along the vertical axis. 3$^{\text{rd}}$ Row: The IFNβ concentration is illustrated in terms of its spatial distribution. 4$^{\text{th}}$ Row: The virion concentration is illustrated in terms of its spatial distribution. 5$^{\text{th}}$ Row: The immune cell concentration is illustrated in terms of its spatial distribution (high: *yellow*, low: *blue*).

to demanding that increases in the transcriptional state, or α-value, of the cell permit the cell's increase in IFN-β production rate.

Upon stimulation of the central cluster with high-affinity IFN-β, we observe the cluster respond by producing its own IFNβ in response. This results in the augmentation the incoming signal and maintenance of the transcription of IRF-7/USP18 in the long term (Fig. 4.11). We also see, however, that the high rate of degradation by consumer cells, resulting from IFN-β's high-affinity for IFNAR2, causes a sharper decline of IFN-β concentrations from the central cluster. This, in turn, results in a highly localised distribution and prevents IFNβ from activating peripheral clusters. This demonstrates that IFN-β production is locally sustained through to the molecule's affinity for the producer cells, aug-

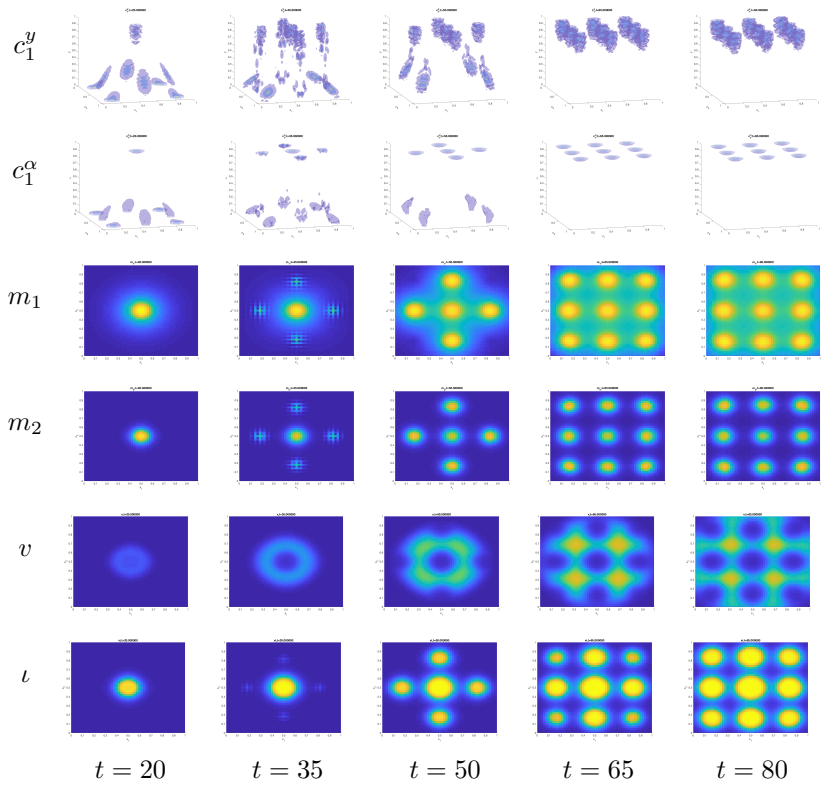

Figure 4.14: Time series showing the temporal dynamics of the interferon binding system upon mimesis of the artificial stimulation of a central cell cluster with IFNβ, in a High/Low IFN system. 1$^{\text{st}}$ Row: The cellular population is illustrated as a 3D isosurface with space represented across the lower plane and the proportion of the cell surface bound to IFN along the vertical axis. 2$^{\text{nd}}$ Row: The cellular population is illustrated as a 3D isosurface with space represented across the lower plane and non-dimensionalised ISG activity along the vertical axis. 3$^{\text{rd}}$ Row: The IFNα1/13 concentration is illustrated in terms of its spatial distribution. 4$^{\text{th}}$ Row: The IFNβ concentration is illustrated in terms of its spatial distribution. 5$^{\text{th}}$ Row: The virion concentration is illustrated in terms of its spatial distribution. 6$^{\text{th}}$ Row: The immune cell concentration is illustrated in terms of its spatial distribution (high: *yellow*, low: *blue*).

menting the intracellular production of IRF-7, and is spatially diminished due to its high-affinity for consumer cells.

We then, likewise, simulated cells who were capable of producing only IFN-α by preventing the local production of IFN-β by the cellular population. We also impose the autocrine signalling sufficient criterion, requiring transcriptional activation of IFN-α production. Since IFN-α is a low-affinity ligand, we stimulated the central cluster with a constant artificial stimulus of IFN-β at all times, in order to maintain local transcriptional activation and IFN-α production.

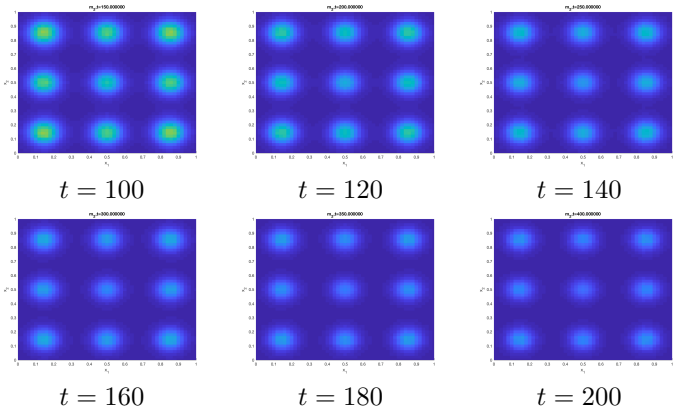

Figure 4.15: Time series showing the temporal dynamics of the interferon binding system after the mimesis of the artificial stimulation of a central cell cluster with IFNβ, in a High/Low IFN system. Shown are IFNα1/13 concentrations at time points $t \in \{100, 120, 140, 160, 180, 200\}$, showing the relaxation of the IFN signalling system.

In this case, results show a global inability of the system to communicate the IFN response (Fig. 4.12). One observes a local excitation of the central cluster, to significant transcriptional levels and due to the IFN-β stimulation, but with no such reciprocal response from distant neighbouring clusters. Concurrently with the decrease in central cluster activation, however, and compared with systems unable to produce IFN-α (Fig. 4.11), one notices a potentiation of peripheral clusters' binding states. Therefore, systems capable of producing only IFN-α are able to activate peripheral IRF-7 transcriptional states but not sufficiently to cause the production of IFN.

Together, these scenarios imply that although IFN-α appears capable of traversing greater distance than IFN-β, and thusly potentiating distant clusters, it is incapable of sustaining its own levels of production due to its low binding affinity and continual consumption by the ubiquitous non-producer cell population.

Systems with additional low affinity ligands elicit faster responses to advancing viral fronts.

We began by simulating cells capable of producing only IFN-β, by arresting the production of IFN-α, with the ability to recruit immune cells in the presence of a advancing viral wave front. We observed an immediate IFN response from the central cluster, leading to the recruitment of immune cells and depletion of the virus at this location. This produced an advancing viral front with a depleted central region, resulting in a ring-like viral distribution (Fig. 4.13, $t \in [35, 50]$) at intermediate time-points. As the virus reaches significant concentrations in the locality of peripheral clusters, IFN producer cells begin to produce and secrete IFN-β, in an IRF-3-3 or first-wave response. This production of high-affinity IFN-β is sufficient to increase local binding and transcriptional states, to the extent where second-wave IFN production may be established (Fig. 4.13, $t = 60$). Finally, we see a recruitment of immune cells to the peripheral regions of the domain and a local destruction of the viral pathogen (Fig. 4.13, $t \geq 65$).

We then simulated the full system (4.18) of cells capable of producing both IFN-α and IFN-β, with the ability to recruit immune cells in the presence of a viral wavefront. Again, one observes the local recruitment of immune cells (Fig. 4.14, ι) and formation of a ring-like front in the viral pathogen, at low times (Fig. 4.14, $t \approx 35$).

Also at low times, however, one observes a potentiation of the binding state and underlying transcriptional state of the peripheral cellular subpopulations as a result of the increased permeation of IFN-α (Fig. 4.14, $t = 20$). This means that as the viral pathogenic travelling front approaches the peripheries of the domain, the cellular population achieves an early onset second wave production process at lower concentrations of the virus (Fig. 4.14, $t = 35$). This means that, in comparison to those cells who can only produce IFN-β (Fig. 4.13), cells capable of producing both IFN-α and IFN-β reach their asymptotic production capacity at far earlier time points (Fig. 4.14, $t = 50$).

Moreover, in both cases, and upon the local depletion of the viral popula-

tion, one observes a gradual decrease in the local concentrations of IFN-β (Fig. 4.13 & 4.14, $t \geq 65$), particularly in the central cluster. The deactivation of intra-cellular IRF-3, as a direct result of the depletion of viral pathogen, may be sufficient to explain this phenomenon. This more rapid removal of the virus may confer an evolutionary advantage to the host as they suffer immunologically derived symptoms of infection for less time than those who are incapable of producing IFN-α, which may explain the abundance of low-affinity IFN in nature.

Over long time scales, and upon the degradation of the local viral population, one observes the dissipation of the local IFN-β signal (Fig. 4.15). The slow relaxation time of cytokine concentrations may explain, to some extent, the prolongation of the symptoms of the immune response beyond the time of infection whilst in some way validating the model.

The communicative relationship between the production and diffusion of IFN molecules, along with the affinity dependent consumption of these molecules, is reminiscent of results shown for experiments performed with IFN-β in IFNAR1$^{-/-}$ mice[1] and interleukin-2[255], another cytokine. Further, our results would support the differential antiviral effects of these molecules[245] and explain the finding that the blocking of IFN-β signalling would be sufficient to significantly reduce antiviral effects[246], through the observation that high-affinity IFN-β alone is capable of sustaining the IFN response.

As in previous biological[258, 227] and mathematical[253] studies, we observed differing STAT1/downstream ISG expression responses to varying affinities of IFN molecule. In contrast to previous studies focusing on the bistability of the STAT1 pathway and neglecting spatial effects[253], however, our explanation of the differential response is based on the spatial organisation of ligands diffusing in a biochemical system designed to sense and amplify an incoming signal.

Our results may thusly go some way to explaining the abundance of lower-affinity IFNs despite their inability to elicit a significant response, relative to high-affinity IFNs[177, 201], under normal conditions. Our model suggests that

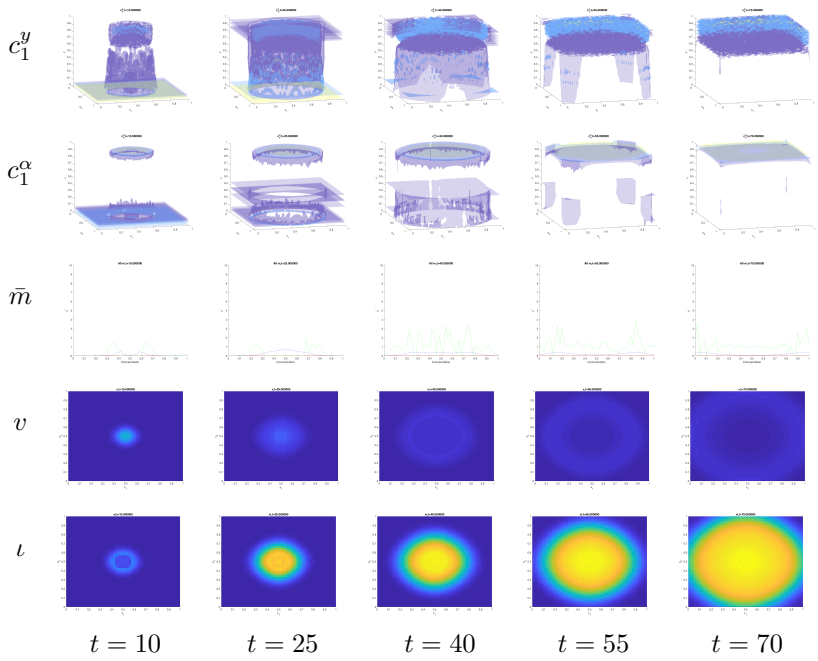

Figure 4.16: Time series showing the temporal dynamics of the interferon binding system upon mimesis of the stimulation of a central cell cluster with low diffusivity virions, in a High/Medium/Low IFN system where IFNα1/13 production is inhibited. 1$^{\text{st}}$ Row: The cellular population is illustrated as a 3D isosurface with space represented across the lower plane and the proportion of the cell surface bound to IFN along the vertical axis. 2$^{\text{nd}}$ Row: The cellular population is illustrated as a 3D isosurface with space represented across the lower plane and non-dimensionalised ISG activity along the vertical axis. 3$^{\text{rd}}$ Row: The summed IFN concentration is illustrated in terms of its spatial distribution. 5$^{\text{th}}$ Row: The virion concentration is illustrated in terms of its spatial distribution. 6$^{\text{th}}$ Row: The immune cell concentration is illustrated in terms of its spatial distribution (high: *yellow*, low: *blue*).

both high-and low-affinity IFN are necessary for a biological IFN-dependent immune system and that low-affinity interferon acts as a communicator whilst high-affinity interferon acts as a consolidator. Therefore, the greater the number of tiers of IFN affinity within a biological system, the more that system may maximise its response at differing distances from the source of infection.

This relationship is further supported by the independent evolution of human and murine type I IFN families[170], both of whom display a vast diversity of affinities[326, 177, 123]. These diverse affinities have been established to produce a diversity of activities and biological functions[155, 289] within the organism and in response to any given virus[123, 163]. It is also possible that other such biological systems operate using the same duality in order to sustain and

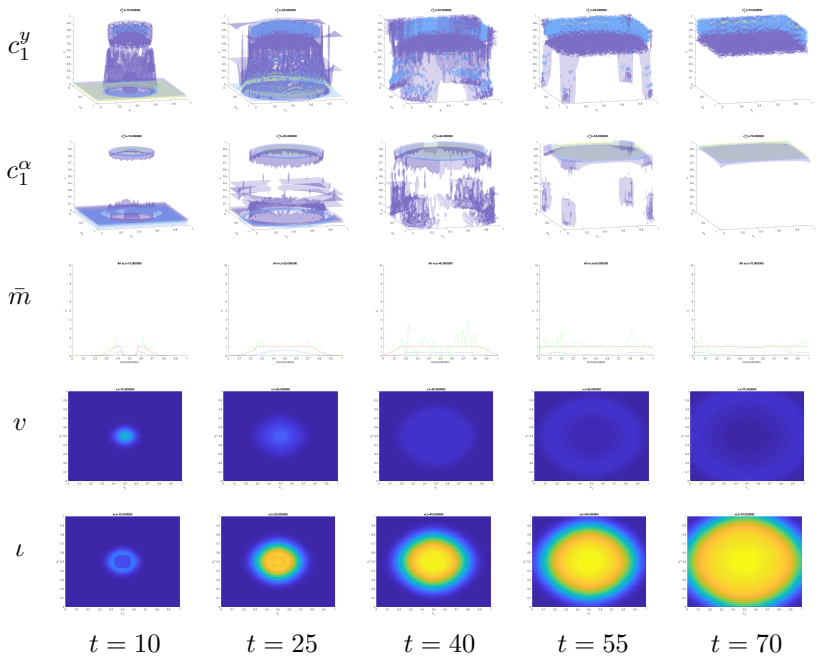

Figure 4.17: Time series showing the temporal dynamics of the interferon binding system upon mimesis of the stimulation of a central cell cluster with low diffusivity virions, in a High/Medium/Low IFN system. 1^{st} Row: The cellular population is illustrated as a 3D isosurface with space represented across the lower plane and the proportion of the cell surface bound to IFN along the vertical axis. 2^{nd} Row: The cellular population is illustrated as a 3D isosurface with space represented across the lower plane and non-dimensionalised ISG activity along the vertical axis. 3^{rd} Row: The summed IFN concentration is illustrated in terms of its spatial distribution. 5^{th} Row: The virion concentration is illustrated in terms of its spatial distribution. 6^{th} Row: The immune cell concentration is illustrated in terms of its spatial distribution (high: *yellow*, low: *blue*).

propagate local signalling.

Cells capable of producing multiple IFN subtypes elicit more diverse response to infection.

In order to demonstrate the effect on the immune system elicited by system of multiple IFN affinities, we simulated a system of 1 high-affinity IFN, 2 low-affinity IFNs, and 10 intermediate-affinity IFNs; as in the case of humans[177, 201]. We denote this medium-affinity population as m_3 – redefining the carrying capacities of the molecular species accordingly – and begin with a homogeneous spatial distribution of cells; closer to the *in situ* experiment. We assume, in line with the existing literature, that all of these IFN species are produced with

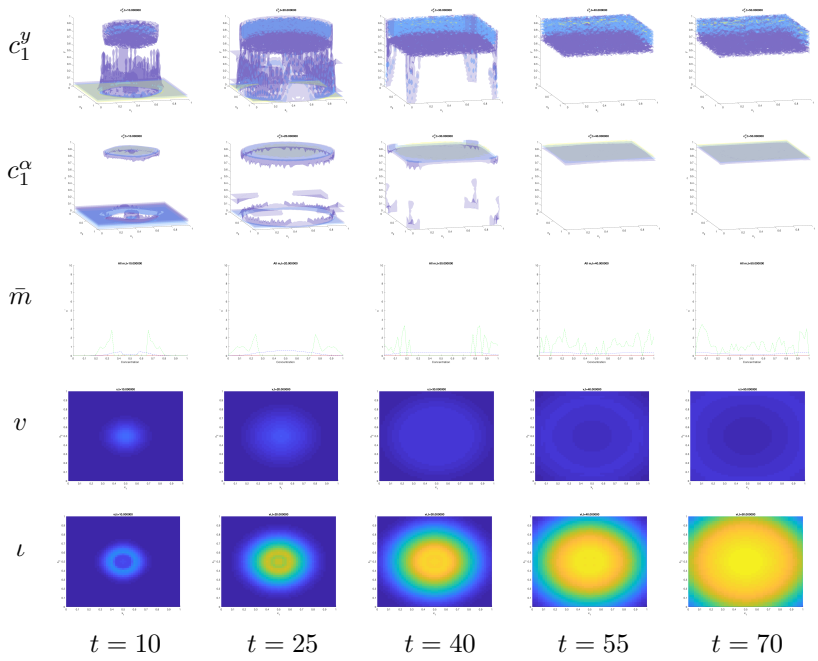

Figure 4.18: Time series showing the temporal dynamics of the interferon binding system upon mimesis of the stimulation of a central cell cluster with high diffusivity virions, in a High/Medium/Low IFN system where IFNα1/13 production is inhibited. 1$^{\text{st}}$ Row: The cellular population is illustrated as a 3D isosurface with space represented across the lower plane and the proportion of the cell surface bound to IFN along the vertical axis. 2$^{\text{nd}}$ Row: The cellular population is illustrated as a 3D isosurface with space represented across the lower plane and non-dimensionalised ISG activity along the vertical axis. 3$^{\text{rd}}$ Row: The summed IFN concentration is illustrated in terms of its spatial distribution. 4$^{\text{th}}$ Row: The virion concentration is illustrated in terms of its spatial distribution. 5$^{\text{th}}$ Row: The immune cell concentration is illustrated in terms of its spatial distribution (high: *yellow*, low: *blue*).

approximately equal rates[64, 351].

To test the hypothesis that these populations of low-affinity IFN molecules would become more biologically relevant in the presence of increasingly diffusive viral species, we tested the system's differential reaction across 10 differing viral diffusivities, ranging from 1×10^{-4} to 1×10^{-3}.

One observes, firstly, that the transition of distributions between unbound or inactive states and bound or active states appear smoother in systems producing IFNα molecules (Fig. 4.16 – 4.19, c_1^y & c_1^α). As high-affinity IFNs act more effectively at the site of infection, the medium-affinity IFNs become dominant immediately outside the range of high-affinity IFNs, and low-affinity IFN molecules are dominant at longer ranges. The medium-affinity molecular popu-

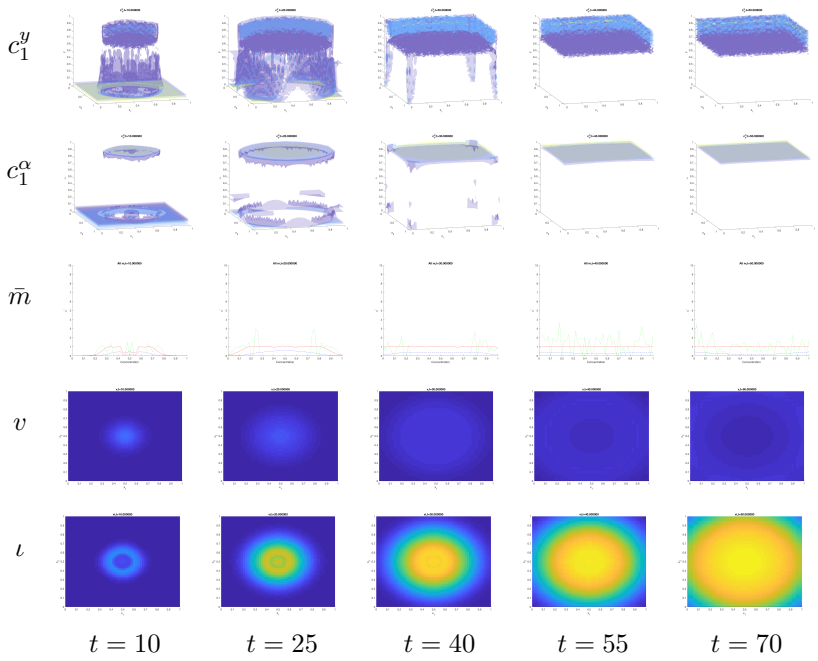

Figure 4.19: Time series showing the temporal dynamics of the interferon binding system upon mimesis of the stimulation of a central cell cluster with high diffusivity virions, in a High/Medium/Low IFN system. 1^{st} Row: The cellular population is illustrated as a 3D isosurface with space represented across the lower plane and the proportion of the cell surface bound to IFN along the vertical axis. 2^{nd} Row: The cellular population is illustrated as a 3D isosurface with space represented across the lower plane and non-dimensionalised ISG activity along the vertical axis. 3^{rd} Row: The summed IFN concentration is illustrated in terms of its spatial distribution. 4^{th} Row: The virion concentration is illustrated in terms of its spatial distribution. 5^{th} Row: The immune cell concentration is illustrated in terms of its spatial distribution (high: *yellow*, low: *blue*).

lation appears to be more acutely sensitive to heterogeneity within the cellular population, resulting in a less smooth and more sporadic distribution of these ligands (Fig. 4.16 – 4.19, $\bar{m}$).

One observes an ability of both low- and medium-affinity IFN molecules to diffuse and sustain an IFN distribution at a greater range than the maximal reach of the virion population (Fig. 4.16 & 4.17, $\bar{m}$ & v). Moreover, the virion population is dissipated to a slightly greater extent at its peak but its distribution is not significantly altered in the case involving low-affinity molecules (Fig. 4.16 & 4.17, v). This is likely due to low-affinity molecules remaining dominant at long ranges, where the virus progresses too slowly for this potentiation to be important to the system reactivity.

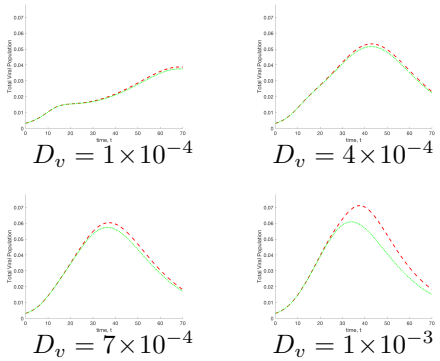

Figure 4.20: Total viral concentration over time for an infected system where IFNα1/13 production is inhibited (*red*) and for a fully functional system (*green*) for viruses with diffusion coefficients of 1×10^{-4}, 4×10^{-4}, 7×10^{-4}, and 10×10^{-4}, respectively.

Therefore, we simulated a system of viral infection for a 4-fold increase in viral diffusivity, to explore the effect of these longer-range IFN molecules in a system where virions approach peripheral regions at earlier time points. Again, one finds that the distribution of low-affinity IFNs extends further that that of the virus (Fig. 4.18 & 4.19, $\bar{m}$ & v) such that one observes peripheral transcriptional potentiation of cells. At higher time points ($t \in (40, 60)$) one can see an approximate 23% decrease in the overall virion population for high viral diffusion coefficients ($D_v = 1\times10-3$) as compared to a 4% decrease for low values ($D_v \in [1\times10^{-4}, 4\times10^{-4}]$, Fig. 4.20 & 4.21). Interestingly, in the case where IFNα1/13 production is suppressed, the system appears to attenuate for the lack of low-affintiy IFNs through the sufficient expression of medium-affinity IFNs (Fig. 4.18 & 4.19, $\bar{m}$) whereas, for viruses diffusing outside the range of the medium-affinity IFN, low-affinity IFNs appear to confer a significant advantage to the system.

It was recently found that *Rousettus aegyptiacus*, a species of bat, have a natural immunity to the Marburg virus; a virus which is deadly when contracted by humans and other primates. The authors explain this as deriving, for the most part, from a genetically diversified family of type I interferon molecules[262]. The major distinction in this species are the 22 IFN-ω subtypes, which may inhibit the proliferation of such a virus. Our results may explain this inhibition

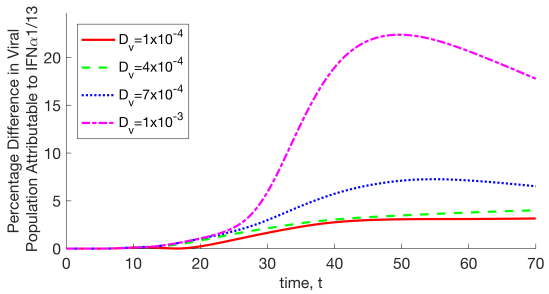

Figure 4.21: Percentage change in total viral concentration for a system without IFN-α1/13, as compared to one with, corresponding to the populations given in Figure 4.20 for all times t, and given for 4 different viral diffusion coefficients.

simply through the increased diversity of affinities in the type I IFNs allowing for cells to more efficiently activate the immune system at various ranges from the site of infection. This effect may allow *Rousettus aegyptiacus* to suppress the spatial advancement of the virus.

Furthermore, our model showed that the multiple IFN system is capable of activating the immune response at an earlier time than either the high- or high/medium-affinity systems. This conferred advantage may play a critical role in containing the virus and curtailing long-term symptoms in the organism. Moreover, this provides the first quantitative rationalisation for the evolutionary conservation of multi-ligand systems, since mutations which increase the number of affinities of IFN available to the organism will confer additional fitness in response to viral selective pressures.

Chapter 5

Multi-Dimensional Analysis of Theoretical Problems in Evolution

5.1 Introduction to Evolutionary Modelling as a Multi-Scale Process

Evolution is a process which takes place within an individual – as an interaction between their phenotype, extended phenotype, and environment – but whose effects only truly manifest themselves on the longest of imaginable time scales and across vast regions of space. Predation events, likewise, take place between individuals and within instants, depending on the identification and capture of the prey item by the predator. Moreover, the evolution of a tumour also has important dynamical consequences realised over the time-scale of a cell-cycle, where the evolutionary survival of the tumour is determined over the lifetime of the host. Therefore, evolution is truly a multi-scale process which requires a appreciation of population- and individual-scale adaptations.

To tackle this problem, we employ the higher-dimensional approach in the absence of spatial considerations (since concrete results for spatial interactions between predator and prey are difficult to fully characterise) to ask whether beauty, which we assume to be a trait worthy of sexual selection, will be conserved in a system where its manifestation in a phenotype is detrimental to survival of the individual. This is important to the context of cancer and IFN since, in order to know whether the existence of a trait owes its existence to survival advantage, we must know whether there are reasons outside survival for which a trait may be developed or conserved. We find that this is, indeed, the case and that beauty, even in the case where it is evolutionarily disadvantageous from a survival point of view, will be conserved so long as it is sexually desirable.

5.1.1 Current Evolutionary Theory & Modelling

Evolution by natural selection [75] has an extensive evidentiary backing but, even with the later Darwinian augmentation of sexual selection [76], still struggles to explain the aberration of natural male æsthetic elaboration. In general, females tend to be the selective sex whilst males are the ornamented sex [105]. Often, elaboration will provide direct or parallel benefits, for example looking threatening or dangerous to a potential predator [66, 306], and may also provide a camouflage or crypsis into one's environment [237, 124]. There are, however, elaborations which provide immediate and isolated impediments to survival.

It is, therefore, absolutely necessary that the following question be answered: In systems where trait inheritance is dependent upon offspring survival and where increasing beauty comes with increasing costs to survival, why is sexual selection for beautiful males preserved?

The earliest credible attempt to answer this question, theoretically was the handicap principle (HP) [346, 130], which states that males with expressed impedimentary traits are advertising to females that they can survive in spite of this evolutionary impediment. The honest signalling hypothesis (HSH) was an

extension of this principle and supposes that only those signals which honestly convey enhanced survival will be selected for [347, 348]. Both the HP and HSH have been supported by modelling [273, 130, 131, 274], which has come under recent criticism [310, 311]. Controversial experiments, designed to test these hypotheses [272], have also been criticised [311] for failing to critically scrutinise evolutionary honesty rather than temporally local honesty. It is clear that a new model is required to overcome these criticisms and transcend the current debate.

The biological case is demonstrated in the peacock, whose bright colouration and functionally irrelevant feathering may only increase the bird's vulnerability to predation, yet encourages the female to mate with him [76, 270]. Conflicting studies, observing peafowl mating habits, found that the ornate nature of the male train did [271, 270] and did not [312] positively influence a females preference to copulate with such a male. It is, therefore, clear that other, more obscure, factors also influence this selection process [72]. More palpably, female red-winged blackbird copulation correlated strongly with male epaulet redness [343]. The case for sexual selection is relatively strong but selection for garish males may also contribute to vulnerability.

Observations of remains from Sparrowhawk nests revealed that the plumage intensity of prey was the greatest factor in determining predation risk [171] and that colouration accounted for approximately 23% of measured vulnerability [242]. Studies in Denmark, however, found that predatory Sparrowhawks attacked colourful male chaffinches more often than inconspicuous female chaffinches [129] but inconspicuous flycatcher females more often than colourful males [128, 129]. Moreover, these orthogonal traits, or beneficial traits which are not directly related and yet arise within the same species, have been shown to be under current selection within species [241]. In certain of these cases, decorative impediments are accompanied by advantageous compensations such as increasing escape capabilities in conspicuous chameleons [69]; increased timidity towards dangerous environments in increasingly vocal crickets [151]; and amplified escape behaviours among other conspicuous lizard species [53].

Moreover, and in birds, an increase in vivaciousness of colouration between species, correlated with an increased exhibition of locomotive deterrence signalling in response to predator audition [181]. This has caused some to hypothesise that colouration is used to warn predators that preying upon them would be unproductive [23], through the unprofitable prey hypothesis (UPH), but this certainly does not hold true across all species [129]. Also, in contrast to the UPH, peacocks who displayed their tail feathers more frequently and had larger numbers of tail ocelli responded better to an immune challenge than their counterparts [218]. Likewise, the plumage yellowness of the blue tit has been found to be predictive of foraging ability [114], postulating an orthogonal advantage rather than a direct one.

We, herein, use mathematics to test a novel hypothesis: That, in a system where costly colouration evolves orthogonally with genes yielding sufficiently evolutionarily advantageous phenotypes, selection for brightly coloured males will select more highly for the orthogonal trait, yielding genetically advantaged offspring. For simplicity, we shall refer to this as the 'orthogonal disadvantage (OD) hypothesis', where the colourful disadvantage is playing the role of a selection pressure for the advantageous gene. We present a novel mathematical model capable of testing this hypothesis, which utilises structural evolution within a population to observe dynamics of the population as a whole, and validate this model by showing adherence to existing evolutionary literature.

5.2 Darwinian Beauty and Survival Traits are Evolutionarily Symbiotic

5.2.1 An Evolutionary Mathematical Model

Evolutionary theory has long provided a welcome nexus between the experimental work of ecology and the theoretical pursuit of modelling [20]. A significant gain for mathematical modelling was achieved when Grafen [130] used a genetic

model to successfully demonstrate the independence of the handicap principle in evolutionary biology. This result has been widely accepted, even by those who previously denigrated the handicap model, and brought welcome validation for the role of mathematical modelling in this difficult field. Since then, alternative hypotheses to account for these evolutionary dynamics have been suggested with the aid of modelling and simulation [353]. As a consequence of the complexity of biology, however, deterministic models are often disfavoured with the respect to modern trends towards game theoretic [143, 238, 147, 7] or stochastic [350, 167, 219] models, which are able to more accurately account for the nuanced realities implied by probability theory.

Recently, we and others have used higher-dimensional, partial differential equation (PDE)-based, mathematical modelling techniques to great effect in describing dynamic biological processes in oncology and beyond [96, 158, 161, 160]. Similar methods have already been employed for the exploration of spatially distributed evolutionary models [26]. Herein, we intend to use a novel approach where adaptive processes are not an intrinsic character of the system but rather occur randomly during the process of reproduction, where the population's source term gives rise to the variability in traits. Likewise, following the rich history of predator-prey modelling, originally derived by Lotka [215, 216, 217] and Volterra [330, 331], we adopt predator-prey dynamics to aid us in understanding the process of natural selection [75]. This approach has been used extensively and throughout the literature to demonstrate processes of speciation and environmental adaptation [39, 67, 281, 98, 297, 43].

Description of the theoretical paradigm

In order to understand how natural selection interacts with sexual selection we postulate the existence of two discrete species; namely a predator, $p(t)$, and a prey species. We then decompose the prey species into its female, $f(t, \mathbf{y}, z)$, and male, $m(t, \mathbf{y}, z)$, constituents, who are in turn decomposed into their distributions through some trait space described by $(\mathbf{y}, z) \in \Upsilon^2 \times \mathcal{Z}$. In *Drosophila*

serrata, a quantitative study found that male mate choice correlates extremely weakly with generational ornamentation, while female mate choice correlated very strongly with male ornamentation; producing female ornamentation as a secondary byproduct [127]. Therefore, since $\mathbf{y}$ is composed of the vector $\mathbf{y} := [y_1, y_2]^T$, we are implicitly assuming that there exists 3 sets of character traits important to this particular study: 'trait selectivity,' $y_1 \in \Upsilon$, which relates the extent to which females display an avidity to mate with males who present vibrant or patterned facades; 'trait elaboration,' $y_2 \in \Upsilon$, which relates the extent to which males posses or present vibrant or patterned facades; and 'trait survival,' $z \in \mathcal{Z}$, which relates an animal's particular ability to evade predation.

Of course, y_1 and y_2 will co-evolve dependently upon the other's character traits and we assume that fundamentally female traits, y_2, are passed to progeny through the female lineage whilst male traits, y_1, are passed exclusively through the male lineage. Moreover, we assume that androgynous traits, z, are otherwise undiscriminated for and that males and females with particular z traits will mate indiscriminately with those of differing z traits. The result of copulation between a male and female, randomly paired with traits $z^\dagger$ and $z^\ddagger$, is a progeny with an intermediate z state, $\frac{1}{2}(z^\dagger + z^\ddagger)$. The dynamics of the male and female populations will then depend upon their position in the trait space, whilst predators will have differential success in preying on male or female subgroups dependent upon their respective positions. A predator's predatory capacity is unaffected by the female selectivity, y_1, for attractive males, although females will preferentially mate with more attractive males as they increase in selectivity. As males increase their attractiveness, y_2, although they will receive a mating advantage from selective females, will also become more conspicuous to potential predators and will be preyed upon more often then their less attractive counterparts. Traits which advantage survival in a species, z, on the other hand, will evolve orthogonally with $\mathbf{y}$ traits and serve only to decrease the rate of predation. These relationships are described concisely within figure 5.1.

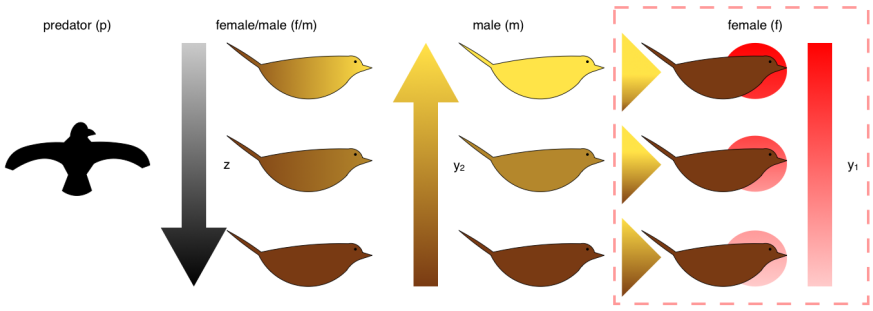

Figure 5.1: Diagram displaying the interactions between traits survival (z), beauty (y_2), and selectivity (y_1) within the prey population and between the prey and unstructured predator populations: As trait survival increases, the ability of the predator to catch prey decreases ($\downarrow$). As trait beauty increases in expressive males, the ability of the predator to catch male prey increases. As trait selectivity increases in expressive females, females more often choose to mate with males who are high in trait beauty.

Bio-mathematical description

We allow, to take the female population as exemplary of the male, that the dynamics of any given population is given by the difference between its reproductive capacity, $R(t, \mathbf{y}, z)$, and its degradative cost, $D(t, \mathbf{y}, z)$, imposed by predation, such that

$$\frac{\partial}{\partial t} f(t, \mathbf{y}, z) = R(t, \mathbf{y}, z) - D_f(t, \mathbf{y}, z)\,. \tag{5.1}$$

The reproductive terms for females and males are the same whereas the degradative terms will differ due to the influence of male plumage variation on predation, which does not affect females. Moreover; since females are considered not to display male attractiveness traits, while males are considered to mate without inhibition we respectively describe the unembellished female and indecisive male populations as

$$f^{\ddagger}(t, y_1, z) := \int_{\Upsilon} f(t, \mathbf{y}, z)\, dy_2 \tag{5.2}$$

and

$$m^{\dagger}(t, y_2, z) := \int_{\Upsilon} m(t, \mathbf{y}, z)\, dy_1\,, \tag{5.3}$$

where we shall refer to these populations as $f^{\ddagger} := f^{\ddagger}(t, y_1, z)$ and $m^{\dagger} := m^{\dagger}(t, y_2, z)$ for brevity.

The reproductive term gives rise to the dynamics of population growth, inheritance, and mutation, making it of particular importance to the current theoretical model. Therefore, we denote the choice kernel $\kappa : \Upsilon \to \mathbb{R}_+$, defined by

$$\kappa(\mathbf{y}) := \frac{y_2^{2y_1}}{\int\limits_{\Upsilon} y_2^{2y_1}\, dy_2}\,, \tag{5.4}$$

such that $\kappa([1, y_2]^T) = 3y_2^2$ and $\kappa([0, y_2]^T) = 1$, with a continuous transition between these two selective profiles with y_1. This is a formal statement that nonselective females, $y_1 = 0$, will mate with all males equally whilst hyper-selective females, $y_1 = 1$, will mate proportionally with the square of male trait beautifulness. Moreover, recall that both female and male traits which assist survival will be passed on to the offspring, resulting in an averagely successful child. This can be accounted for by introducing a non-dimensional variable $\zeta \in [0, 1]$, over which one may sum, such that as $2\zeta z$ increases for the female species, the result of copulation with her counterpart at structural location $(2 - 2\zeta)z$ will be an offspring with structural location z. The factor of 2 is accounting for the factor $\frac{1}{2}$ from the resultant averaging. We thusly arrive at the following expression for reproduction:

$$R'(t, \mathbf{y}, z) = \alpha \int\limits_{[0,1]} 2\zeta(1-\zeta)\kappa(\mathbf{y}) \int\limits_{\Upsilon} f(t, \mathbf{y}, 2\zeta z)\, dy_2 \int\limits_{\Upsilon} m(t, \mathbf{y}, (2-2\zeta)z)\, dy_1\, d\zeta\,, \tag{5.5}$$

whose full mathematical derivation and justification can be found within Section 1.3.1.

Furthermore, we assume that mutation may occur during reproduction, conferring some stochastic differentiation of the offspring's genes from those of the parents. The simplest assumption is that this genetic reproductive variation occurs, for a population at a given genetic location $(\mathbf{y}, z)$, across a normalised Gaussian distribution around that point. This is supported by evidence in fairy-wrens, for which distributions in male patterning were found to fit Brownian models of variation [179]. In order to describe this mathematically, we integrate

our reproductive term across a Gaussian kernel, called the 'mutation kernel' $\mu : \Upsilon^2 \times \mathcal{Z} \times \Upsilon^2 \times \mathcal{Z}$ and given by

$$\mu(\mathbf{y}, z, \mathbf{y}', z') := \frac{\exp(-\text{diag}(\nu_y)(\mathbf{y} - \mathbf{y}') \cdot (\mathbf{y} - \mathbf{y}') - \nu_z(z' - z)^2)}{\int\limits_{\mathcal{Z}} \iint\limits_{\Upsilon^2} \exp(-\text{diag}(\nu_y)(\mathbf{y} - \mathbf{y}') \cdot (\mathbf{y} - \mathbf{y}') - \nu_z(z' - z)^2)\, d\mathbf{y}\, dz}\,, \tag{5.6}$$

such that the population is slightly distributed across the structural space. The degree to which the population varies over time are parameters of the model, given by $\nu_y := [\nu_{y_1}, \nu_{y_2}]^T$ and ν_z. Reproduction of males and females, together, is also limited by some maximal sustainable carrying capacity, K. The reproductive term may then be given by

$$\begin{aligned} R(t, \mathbf{y}, z) = \alpha \Bigg(1 - \frac{1}{K} \iiint\limits_{\Upsilon^2 \times \mathcal{Z}} (f + m)\, d(\mathbf{y}, z) \Bigg) \\ \cdot \iiint\limits_{\Upsilon^2 \times \mathcal{Z}} \mu(\mathbf{y}, z, \mathbf{y}', z') R'(t, \mathbf{y}', z')\, d\zeta\, d(\mathbf{y}', z'), \end{aligned} \tag{5.7}$$

where α will be given respectively by α_f and α_m for females and males.

It is assumed that the degradation of a population of males or females is mediated entirely by predation. Survival is also augmented by increases in the structural z-location. The survival function, $s : \mathcal{Z} \to [0, 1]$, is then assumed to have an exponential decay on the interval $\mathcal{Z}$ such that it is given by $s(z) := \exp(z \ln \beta)$, where $\beta \in (0, 1]$ is the relative predation probability of a female at state $z = 1$ with respect to a female at $z = 0$. Given a constant of degradation, δ_f, we write the female degradative term as

$$D_f(t, \mathbf{y}, z) = \delta_f p(t) s(z) f(t, \mathbf{y}, z)\,. \tag{5.8}$$

For males, we require an supplementary term to account for the additional threat to survival resulting from colouration $r(y_2) := 1 + (q - 1)y_2$, where $q \in \mathbb{R}_+$ is the relative vulnerability of a male at $(y_2, z) = (1, 0)$ with respect to a male at $(y_2, z) = (0, 0)$. For values of $q < 1$, the colouration of an individual would be advantageous to their survival, while for values of $q > 1$, colouration would be

a detriment to survival, and $q = 1$ makes colouration a neutral transformation. Therefore, we write the degradative term for males as

$$D_m(t, \mathbf{y}, z) = \delta_m p(t) r(y_2) s(z) m(t, \mathbf{y}, z)\,. \tag{5.9}$$

Predators are assumed to have a carrying capacity, given by K_p, and a corresponding population growth rate, given by α_p, while their overall growth is logistic. Predatory success is proportional to their ability to prey on the male and female populations considered, taking into account the effects of the survival advantage and relative vulnerability functions, $s(z)$ and $r(y_2)$ respectively. Therefore, the predatory reproduction term is given by the logistic relationship

$$R_p(t) = \alpha_p p \left(1 - \frac{p}{K_p}\right) \iiint\limits_{\Upsilon^2 \times \mathcal{Z}} s(z)\big(f(t, \mathbf{y}, z) + r(y_2) m(t, \mathbf{y}, z)\big)\, d(\mathbf{y}, z)\,. \tag{5.10}$$

Meanwhile, popular predatory degradation is a naturally occurring process – assumed to be due to ageing, starvation, or intra-species conflict – with the rate constant δ_p. The whole term is written simply as

$$D_p(t) = \delta_p p(t)\,. \tag{5.11}$$

A system of equations for sexual and natural trait selection

By collating all of the relationships described above, we obtain the following system of partial integro-differential equations, which describe the dynamics of sexually and naturally selected populations of randomly evolving male and

female members of an arbitrary species:

$$\begin{aligned}\frac{\partial}{\partial t}f(t,\mathbf{y},z) =& -\delta_f p(t) s(z) f(t,\mathbf{y},z) + \alpha_f \left(1 - \frac{\iiint_{\Upsilon^2\times\mathcal{Z}} (f+m)\, d(\mathbf{y},z)}{K}\right) \\ & \cdot \iiint_{\Upsilon^2\times\mathcal{Z}} \mu(\mathbf{y},z,\mathbf{y}',z') \int_{[0,1]} \Big[2\zeta(1-\zeta)\kappa(\mathbf{y}) \\ & \cdot \int_{\Upsilon} f(t,\mathbf{y}',2\zeta z')\, dy_2 \int_{\Upsilon} m(t,\mathbf{y}',(2-2\zeta)z')\, dy_1 \Big]\, d\zeta\, d(\mathbf{y}',z')\end{aligned}$$

$$\begin{aligned}\frac{\partial}{\partial t}m(t,\mathbf{y},z) =& -\delta_m p(t) r(y_2) s(z) m(t,\mathbf{y},z) + \alpha_m \left(1 - \frac{\iiint_{\Upsilon^2\times\mathcal{Z}} (f+m)\, d(\mathbf{y},z)}{K}\right) \\ & \cdot \iiint_{\Upsilon^2\times\mathcal{Z}} \mu(\mathbf{y},z,\mathbf{y}',z') \int_{[0,1]} \Big[2\zeta(1-\zeta)\kappa(\mathbf{y}) \\ & \cdot \int_{\Upsilon} f(t,\mathbf{y}',2\zeta z')\, dy_2 \int_{\Upsilon} m(t,\mathbf{y}',(2-2\zeta)z')\, dy_1 \Big]\, d\zeta\, d(\mathbf{y}',z')\end{aligned}$$

$$\begin{aligned}\frac{d}{dt}p(t) =& \alpha_p p \left(1 - \frac{p}{K_p}\right) \iiint_{\Upsilon^2\times\mathcal{Z}} s(z)\big(f(t,\mathbf{y},z) + r(y_2) m(t,\mathbf{y},z)\big)\, d(\mathbf{y},z) \\ & - \delta_p p(t)\,.\end{aligned} \tag{5.12}$$

5.2.2 Equilibrium Analysis

For all of the algebraic analysis contained within this study, the integrals over ζ in the above system (5.12) are ignored, as are the asymmetries in contribution of the male and female population with regards to their traits' heritability. This should form the basis of a future study but was considered too challenging in the absence of the preliminary results that we present herein. As shall be expounded, even given these simplifications the analytic steady-state solutions to this model are challenging to come by and require much scrutiny to understand.

Nevertheless, we shall present 3 scenarios in which the populations differ, primarily in their structure, and extract equilibria for each. These populations

are (a) unstructured prey populations, for which particular values of $(\mathbf{y}, z)$ are assumed to be fixed parameters of the system; (b) discretely structured prey populations, for which we assume that the populations are distributed between two discrete states within the domain $\Upsilon^2 \times \mathcal{Z}$; and, finally, (b) continuously structured populations, for which we take discrete populations distributed across N points in the trait space and use this to generalise our solutions to the case of continuous distribution. We take each situation in turn:

Equilibria for Unstructured Populations (a)

For the unstructured populations we consider that our female and male equilibrium solutions are given respectively by

$$F^* := \lim_{t\to\infty} \iiint_{\Upsilon^2\times\mathcal{Z}} f(t, \mathbf{y}, z)\, d(\mathbf{y}, z), \qquad M^* := \lim_{t\to\infty} \iiint_{\Upsilon^2\times\mathcal{Z}} m(t, \mathbf{y}, z)\, d(\mathbf{y}, z), \quad (5.13)$$

and assume that these populations are both located at some point in $\Upsilon\times\mathcal{Z}$ which we generically term $(\mathbf{y}, z)$, as in the above system with the exception that this point is assumed to be discrete and fixed. Likewise, the predator population is defined by $p^* = \lim_{t\to\infty} p(t)$ and we may rewrite the full system of equations (5.12) at steady state as

$$\begin{cases} 0 = -\delta_f p^* s(z) F^* + \alpha_f \left(1 - \dfrac{F^* + M^*}{K}\right) \kappa(\mathbf{y}) F^* M^* \\ 0 = -\delta_m p^* r(y_2) s(z) M^* + \alpha_m \left(1 - \dfrac{F^* + M^*}{K}\right) \kappa(\mathbf{y}) F^* M^* \\ 0 = -\delta_p p^* + \alpha_p p^* \left(1 - \dfrac{p^*}{K_p}\right) s(z)(F^* + r(y_2) M^*)\,. \end{cases} \quad (5.14)$$

Let us first consider the case in which there exists no predator species at the steady state, such that $p^* = 0$ and our system simplifies to

$$\begin{cases} 0 = \alpha_f \left(1 - \dfrac{F^* + M^*}{K}\right) \kappa(\mathbf{y}) F^* M^* \\ 0 = \alpha_m \left(1 - \dfrac{F^* + M^*}{K}\right) \kappa(\mathbf{y}) F^* M^*\,, \end{cases} \quad (5.15)$$

yielding the trivial solutions for the unstable and stable steady states of our system, (F^*, M^*, p^*), given by $(0, 0, 0)$ and $(F^*, K - F^*, 0)$, $F^* \in [0, K]$, respectively. In the latter case, the steady state is dependent upon the initial conditions of the system and, therefore, does not contain a fixed point but, rather, a line in the solution space defined by all possible values of $(F^*, M^*) \in [0, K]^2$. This is also due to the fact that the female and male populations, $F(t)$ and $M(t)$, have a shared carrying capacity, K.

It is trivial to prove that the steady state given by $(F^*, M^*, p^*) = (0, 0, 0)$ is unstable, except in the case where solely the predator population is perturbed. For the slightly less trivial steady state, given by $(F^*, K - F^*, 0)$, we take the derivative with respect to the predator population, p^*, yielding

$$\begin{cases} 0 > -\delta_f s(z) F^*\,, & 0 > -\delta_m r(y_2) s(z)(K - F^*) \\ 0 > -\delta_p + \alpha_p s(z)(F^* + r(y_2)(K - F^*))\,, \end{cases} \tag{5.16}$$

which is trivially unstable with respect to the prey population, in the sense that small perturbation will yield long-term alterations in F^*, and stable in the the predator population, so long as $s(z) < \delta_p$ and assuming that we have $\alpha_p K \leq 1$.

Leaving this assumption, let us observe the more general case in which the predator population is non-zero, $p^* > 0$. Begin by observing that the differential equations (5.14) for $f(t, \mathbf{y}, z)$ and $m(t, \mathbf{y}, z)$ yield the following equalities for the equilibrium values of p^*,

$$\begin{cases} p^* = \dfrac{\alpha_f}{\delta_f s(z) F^*} \left(1 + \dfrac{F^* + M^*}{K}\right) \kappa(\mathbf{y}) F^* M^* \\ p^* = \dfrac{\alpha_m}{\delta_m r(y_2) s(z) M^*} \left(1 - \dfrac{F^* + M^*}{K}\right) \kappa(\mathbf{y}) F^* M^*\,. \end{cases} \tag{5.17}$$

Equating, these, we may then express the equilibrium value for the male population of prey animals as a fraction of the female population, as so

$$M^* = \frac{\alpha_m \delta_f}{\alpha_f \delta_m r(y_2)} F^*\,. \tag{5.18}$$

Next we substitute this (5.18) result into the steady state equation for the predator's growth (5.14),

$$\frac{\delta_p}{\alpha_p s(z)} = \left(1 - \frac{p^*}{K_p}\right)\left(F^* + r(y_2)M^*\right) , \tag{5.19}$$

in order to obtain an expression for p^* in terms of F^*, given by

$$p^* = K_p\left(1 - \frac{\delta_p}{\alpha_p s(z)}\left[F^*\left(1 + \frac{\alpha_m\delta_f}{\alpha_f\delta_m}\right)\right]^{-1}\right) . \tag{5.20}$$

Substituting both this result (5.20) and our previous result, for M^* (5.18), into our steady state equation for the female population (5.14), itself, we obtain

$$\begin{aligned}&\delta_f s(z)F^*K_p\left(1 - \frac{\delta_p}{\alpha_p s(z)}\left[F^*\left(1 + \frac{\alpha_m\delta_f}{\alpha_f\delta_m}\right)\right]^{-1}\right)\\ &= \alpha_f\left(1 - \frac{F^*}{K}\left(1 + \frac{\alpha_m\delta_f}{\alpha_f\delta_m r(y_2)}\right)\right)\kappa(\mathbf{y})F^*\frac{\alpha_m\delta_f}{\alpha_f\delta_m r(y_2)}F^* .\end{aligned} \tag{5.21}$$

Now, the equation (5.22) may be simply manipulated to yield a cubic in F^*, through an initial simplification

$$\begin{aligned}&s(z)K_p\left(F^* - \frac{\delta_p}{\alpha_p s(z)}\left(1 + \frac{\alpha_m\delta_f}{\alpha_f\delta_m}\right)^{-1}\right)\\ &= \frac{\alpha_m\kappa(\mathbf{y})}{K\delta_m r(y_2)}\left(K(F^*)^2 - (F^*)^3\left(1 + \frac{\alpha_m\delta_f}{\alpha_f\delta_m r(y_2)}\right)\right) .\end{aligned} \tag{5.22}$$

and using the simplifying substitutions

$$\Gamma = 1 + \frac{\alpha_m\delta_f}{\alpha_f\delta_m}, \qquad \hat{\Gamma} = 1 + \frac{\alpha_m\delta_f}{\alpha_f\delta_m r(y_2)}, \qquad \Omega = \frac{\delta_m K K_p r(y_2)}{\alpha_m\kappa(\mathbf{y})}, \tag{5.23}$$

we write our equation in standard form, as

$$\Gamma\hat{\Gamma}(F^*)^3 - K\Gamma(F^*)^2 - s(z)\Gamma\Omega F^* + \frac{\delta_p}{\alpha_p}\Gamma\Omega = 0. \tag{5.24}$$

Finally, our equilibrium solution for F^* is given by the cubic equation

$$\begin{aligned} F^* = \frac{K}{3\hat{\Gamma}} + \Bigg(& \frac{K^3}{3^3\hat{\Gamma}^3} + \frac{s(z)K\Omega}{6\hat{\Gamma}^2} - \frac{\delta_p\Omega}{2\alpha_p\hat{\Gamma}} \\ & + \left[\left(\frac{K^3}{3^3\hat{\Gamma}^3} + \frac{s(z)K\Omega}{6\hat{\Gamma}^2} - \frac{\delta_p\Omega}{2\alpha_p\hat{\Gamma}} \right)^2 + \left(-\frac{s(z)\Omega}{3\hat{\Gamma}} - \frac{K^2}{3^2\hat{\Gamma}^2} \right)^3 \right]^{\frac{1}{2}} \Bigg)^{\frac{1}{3}} \\ & + \Bigg(\frac{K^3}{3^3\hat{\Gamma}^3} + \frac{s(z)K\Omega}{6\hat{\Gamma}^2} - \frac{\delta_p\Omega}{2\alpha_p\hat{\Gamma}} \\ & + \left[\left(\frac{K^3}{3^3\hat{\Gamma}^3} + \frac{s(z)K\Omega}{6\hat{\Gamma}^2} - \frac{\delta_p\Omega}{2\alpha_p\hat{\Gamma}} \right)^2 + \left(-\frac{s(z)\Omega}{3\hat{\Gamma}} - \frac{K^2}{3^2\hat{\Gamma}^2} \right)^3 \right]^{\frac{1}{2}} \Bigg)^{\frac{1}{3}} \end{aligned} \tag{5.25}$$

Unfortunately, however, not only does this not yield a simple result for the steady state value of F^* but we are yet able to determine whether equilibrium solutions actually exist. In order to achieve this, we require that the discriminant of the above equation (5.24) is greater than or equal to zero, such that

$$\begin{aligned} 0 < & \underbrace{\frac{K^6}{3^6\hat{\Gamma}^6}}_{1^*} + \frac{s^2(z)K^2\Omega^2}{6^2\hat{\Gamma}^4} - \frac{\delta_p^2\Omega^2}{2^2\alpha_p^2\hat{\Gamma}^2} + \underbrace{2\frac{K^3}{3^3\hat{\Gamma}^3}\frac{s(z)K\Omega}{6\hat{\Gamma}^2}}_{2^*} - 2\frac{K^3}{3^3\hat{\Gamma}^3}\frac{\delta_p\Omega}{2\alpha_p\hat{\Gamma}} \\ & - 2\frac{s(z)K\Omega}{6\hat{\Gamma}^2}\frac{\delta_p\Omega}{2\alpha_p\hat{\Gamma}} - \frac{s^3(z)\Omega^3}{3^3\hat{\Gamma}^3} - \underbrace{\frac{K^6}{3^6\hat{\Gamma}^6}}_{1^*} - 3\frac{s^2(z)\Omega^2}{3^2\hat{\Gamma}^2}\frac{K^2}{3^2\hat{\Gamma}^2} - \underbrace{3\frac{s(z)\Omega}{3\hat{\Gamma}}\frac{K^4}{3^4\hat{\Gamma}^4}}_{2^*} \end{aligned} \tag{5.26}$$

By eliminating the denominators of this inequality, and simplifying significantly, we yield the discriminant function

$$\begin{aligned} \Delta(\Omega) := & -3\cdot 2^2 s^3(z)\hat{\Gamma}^2\alpha_p^2\Omega^3 + 3^2 s^2(z)K^2\hat{\Gamma}^5\alpha_p^2\Omega^2 - 2\cdot 3^3 s(z)K\hat{\Gamma}^2\alpha_p\delta_p\Omega^2 \\ & + 3^4\delta_p^2\hat{\Gamma}^3\Omega^2 - 2^3K^4\alpha_p^2 s(z)\Omega - 3\cdot 2^2K^3\hat{\Gamma}\alpha_p\delta_p\Omega - 2^2 s(z)K^4\alpha_p^2\Omega \end{aligned} \tag{5.27}$$

whilst retaining the inequality $\Delta(\Omega) := \Delta(\Omega) > 0$ for real roots. Given that this discriminant function is a quadratic in Ω, we choose to phrase it in terms of Ω. Now, given a certain parameter set, let us ask for what values of r we have real roots for our discriminant. By then taking the derivative of the discriminant function with respect to Ω, we may ask the behaviour of the discriminant, with

respect to the point $\Omega = 0$ as we change the variable y_2, for which Ω is a dependent:

$$\begin{aligned}\Delta^{(1)}(\Omega) := &- 3^2 \cdot 2^2 s^3(z)\hat{\Gamma}^2\alpha_p^2\Omega^2 + 2 \cdot 3^2 s^2(z)K^2\hat{\Gamma}^5\alpha_p^2\Omega - 2^2 \cdot 3^3 s(z)K\hat{\Gamma}^2\alpha_p\delta_p\Omega \\ &+ 2 \cdot 3^4\delta_p^2\hat{\Gamma}^3\Omega - 2^3K^4\alpha_p^2 s(z) - 3 \cdot 2^2K^3\hat{\Gamma}\alpha_p\delta_p - 2^2 s(z)K^4\alpha_p^2\end{aligned} \tag{5.28}$$

Likewise, and for completeness, we take the second derivative of the discriminant function $\Delta(\Omega)$, giving

$$\begin{aligned}\Delta^{(2)}(\Omega) := &- 3^2 \cdot 2^3 s^3(z)\hat{\Gamma}^2\alpha_p^2\Omega + 2 \cdot 3^2 s^2(z)K^2\hat{\Gamma}^5\alpha_p^2 - 2^2 \cdot 3^3 s(z)K\hat{\Gamma}^2\alpha_p\delta_p \\ &+ 2 \cdot 3^4\delta_p^2\hat{\Gamma}^3 \,.\end{aligned} \tag{5.29}$$

Reimposing an inequality which would guarantee that solutions do exist as $\Omega \to \infty$, we may rearrange this for Ω to find the fundamental constraint

$$\Omega < \frac{3^2\delta_p^2\hat{\Gamma} + s^2(z)K^2\hat{\Gamma}^3\alpha_p^2 - 3 \cdot 2s(z)K\alpha_p\delta_p}{2^2 s^3(z)\alpha_p^2} \,. \tag{5.30}$$

Observing the definition for Ω (5.23), we may realise that this is, in fact a constraint on the definition of the predator carrying capacity, K_p. The carrying capacity of the predator species, and its proliferation rate α_p, must be sufficiently low in order to maintain a real steady state within an ecosystem. This is an interesting observation on reality itself; as a predator grows too fast or to too great numbers the ecosystem will be at risk of exceeding its capacity to survive, without the introduction of a higher-order predator or new prey item.

Moving to the first derivative, we ask the associated discriminant is greater than 0, as follows

$$\begin{aligned}&(2 \cdot 3^2 s^2(z)K^2\hat{\Gamma}^5\alpha_p^2 - 2^2 \cdot 3^3 s(z)K\hat{\Gamma}^2\alpha_p\delta_p + 2 \cdot 3^4\delta_p^2\hat{\Gamma}^3)^2 \\ &> 3^2 \cdot 2^4 s^3(z)\hat{\Gamma}^2\alpha_p^2(2^3K^4\alpha_p^2 s(z) + 3 \cdot 2^2K^3\hat{\Gamma}\alpha_p\delta_p + 2^2 s(z)K^4\alpha_p^2) \,.\end{aligned} \tag{5.31}$$

One clear case where this inequality is satisfied is where the relative advantage to the male species, from elaboration, is exceptionally high so that predation

becomes 0. In this case $\hat{\Gamma} \to \infty$ and the steady states may disappear. This is true without regard to the condition on Ω given by (5.30). In nature, also, one might expect that near-invulnerability to predation may yield populations who oscillate around their carrying capacity (not obtaining it on the basis that a healthy female population is necessary for reproduction.

Another such case where this inequality is satisfied is when the predator reproduction constant is on the same scale as the reciprocal carrying capacity of the prey population, $\alpha_p K \leq 1$, which is realistic. Taking the case where $\alpha_p K = 1$, for example, we obtain

$$\begin{aligned}&(2 \cdot 3^2 s^2(z)\hat{\Gamma}^5 - 2^2 \cdot 3^3 s(z)\hat{\Gamma}^2\delta_p + 2 \cdot 3^4\delta_p^2\hat{\Gamma}^3)^2 \\ &> 3^2 \cdot 2^4 s^3(z)\hat{\Gamma}^2(3 \cdot 2^2 s(z) + 3 \cdot 2^2\hat{\Gamma}\delta_p)\,,\end{aligned} \tag{5.32}$$

which holds so long as $s(z) < 1$, since $RHS \to 0$ faster than $LHS \to 0$ in the case $s(z) \to 0$. let us evaluate the case at $s(z) = 1$, for clarity, which would give

$$\hat{\Gamma}^5 + 9\delta_p^2\hat{\Gamma}^3 > 6\hat{\Gamma}^2\delta_p + 4(\frac{1}{3}\hat{\Gamma}^2 + \frac{1}{3}\hat{\Gamma}^3\delta_p)^{\frac{1}{2}}\,. \tag{5.33}$$

In this case, we obtain the constraint that the relative disadvantage of the male species (q, y_2), implicit in $\hat{\Gamma}$, must not be too great in order to maintain real roots. As relative disadvantage increases, Γ moves from having a value of 2 to a value of 1, where the inequality eventually collapses. This constraint is decreasingly restrictive with the increasing advantage due to trait survival, $s(z)$.

Therefore, in the range of acceptable parameters, we have that there are no turning points in the discriminant (with respect to Ω) and that the double derivative is positive so that we have established that the gradient of the discriminant is positive. If we now establish that, for some value of $\Omega = \Omega_0$, the discriminant provides real roots, then we may say that real roots exist across all values of $\Omega \geq \Omega_0$. Let us then return to our discriminant function and reimpose

the inequality to yield

$$3 \cdot 2^2 s^3(z)\hat{\Gamma}^2\alpha_p^2\Omega_0^3 - 2 \cdot 3^3 s(z)K\hat{\Gamma}^2\alpha_p\delta_p\Omega_0^2 - 2^3K^4\alpha_p^2 s(z)\Omega_0 - 3 \cdot 2^2K^3\hat{\Gamma}\alpha_p\delta_p\Omega_0 - 2^2 s(z)K^4\alpha_p^2\Omega_0 \leq 3^2 s^2(z)K^2\hat{\Gamma}^5\alpha_p^2\Omega_0^2 + 3^4\delta_p^2\hat{\Gamma}^3\Omega_0^2\,. \tag{5.34}$$

Since we know that the above holds at least for $\Omega_0 = 0$, we may conclude that, notwithstanding the above stated constraints, our system of equations has real steady states given precisely by (F^*, M^*, p^*), as defined by (5.25), (5.18), and (5.20) respectively.

Equilibria for Discretely Structured Populations (b)

As in the above case, the discretely structured populations are assumed to have a collective populations which is distributed, not necessarily equally, at two discrete locations given by $(\mathbf{y}_i, z_i)$ and $(\mathbf{y}_j, z_j)$ so that our 4 prey populations are given by

$$\begin{aligned} F_i^* &:= \lim_{t\to\infty} f(t, \mathbf{y}_i, z_i)\,, \quad & F_j^* &:= \lim_{t\to\infty} f(t, \mathbf{y}_j, z_j)\,, \\ M_i^* &:= \lim_{t\to\infty} m(t, \mathbf{y}_i, z_i)\,, \quad & M_j^* &:= \lim_{t\to\infty} m(t, \mathbf{y}_j, z_j)\,. \end{aligned} \tag{5.35}$$

Additionally, we define that

$$\lim_{t\to\infty} \iiint_{\Upsilon^2\times\mathcal{Z}} f(t, \mathbf{y}, z)\, d(\mathbf{y}, z) = F_i^* + F_j^* \tag{5.36}$$

and likewise for $m(t, \mathbf{y}, z)$ so that the above quadruplet (5.35) defines the whole system at steady state.

Then our steady states for the full set of differential equations yields the

following system of nonlinear polynomial functions

$$\begin{cases} 0 = & -\delta_f p^* s_i F_i^* + \alpha_f \left(1 + \frac{F_i^*+F_j^*+M_i^*+M_j^*}{K}\right)(\mu_0 \kappa_i F_i^* M_i^* + \mu_1 \kappa_j F_j^* M_j^*) \\ 0 = & -\delta_m p^* s_i r_i M_i^* + \alpha_m \left(1 + \frac{F_i^*+F_j^*+M_i^*+M_j^*}{K}\right)(\mu_0 \kappa_i F_i^* M_i^* + \mu_1 \kappa_j F_j^* M_j^*) \\ 0 = & -\delta_p p^* + \alpha_p p^* \left(1 - \frac{p^*}{K_p}\right)(s_1 F_1^* + s_2 F_2^* + s_1 r_1 M_1^* + s_2 r_2 M_2^*), \\ & \qquad\qquad \forall i \in \{1, 2\}, \end{cases} \tag{5.37}$$

for which we must attempt to find solutions.

Equating the first two equations of this system (5.37) and analogously to the steps followed in the above example, (5.17) & (5.18), we may obtain an equation for the steady state of a given i^{th} male population M_i^* in terms of the structurally related female population, given by

$$M_i^* = \frac{\alpha_m \delta_f}{\alpha_f \delta_m r_i} F_i^* . \tag{5.38}$$

Then, using equation (5.38), we may substitute this into the predator equation in the full steady state system of equations (5.37) to yield

$$p^* = K_p \left(1 - \frac{\delta_p}{\alpha_p}\left[s_1 F_1^* \left(1 + \frac{\alpha_m \delta_f}{\alpha_f \delta_m}\right) + s_2 F_2^* \left(1 + \frac{\alpha_m \delta_f}{\alpha_f \delta_m}\right)\right]^{-1}\right) . \tag{5.39}$$

If we now rearrange the equation for any given i^{th} female population, in the steady-state system (5.37), for the predator term, we obtain a particular nonlinear equation,

$$\begin{aligned} p^* = & \frac{\alpha_f}{\delta_f s_i F_i^* K}\left(1 - F_i^*\left[1 + \frac{\alpha_m \delta_f}{\alpha_f \delta_m r_i}\right] + F_j^*\left[1 + \frac{\alpha_m \delta_f}{\alpha_f \delta_m r_j}\right]\right) \\ & \cdot \left(\mu_0 \kappa_i (F_i^*)^2 \frac{\alpha_m \delta_f}{\alpha_f \delta_m} + \mu_1 \kappa_j (F_j^*)^2 \frac{\alpha_m \delta_f}{\alpha_f \delta_m}\right) , \end{aligned} \tag{5.40}$$

belonging to that i^{th} female population. An analogous equation may be written for the j^{th} female population.

Equating these two relations, (5.40) and the analogy for the j^{th} population,

we obtain the following

$$s_i F_i^* \left(\frac{\mu_0 \kappa_j}{r_j} (F_j^*)^2 + \frac{\mu_1 \kappa_i}{r_i} (F_i^*)^2 \right) = s_j F_j^* \left(\frac{\mu_0 \kappa_i}{r_i} (F_i^*)^2 + \frac{\mu_1 \kappa_j}{r_j} (F_j^*)^2 \right) . \quad (5.41)$$

For convenience, we use the notation $\bar{F} = F_i^*/F_j^*$ and the like notations

$$\bar{s} = \frac{s_i}{s_j} \bar{r} = \frac{r_i}{r_j} \bar{\kappa} = \frac{\kappa_i}{\kappa_j} \bar{\mu} = \frac{\mu_0}{\mu_1} , \quad (5.42)$$

such that we may rewrite (5.41) as the cubic polynomial equation

$$\bar{s}\bar{\kappa}\bar{F}^3 - \bar{\mu}\bar{\kappa}\bar{F}^2 + \bar{s}\bar{\mu}\bar{r}\bar{F} - \bar{r} = 0 . \quad (5.43)$$

Using Cardano's formula for cubic polynomials [50], we find that the solution to this polynomial is given by

$$\begin{aligned} \bar{F} = & \left(\frac{\bar{\mu}^3}{3^3\bar{s}^3} - \frac{\bar{\mu}^2\bar{r}}{6\bar{s}\bar{\kappa}} + \frac{\bar{r}}{2\bar{s}\bar{\kappa}} + \left\{ \left[\frac{\bar{\mu}^3}{3^3\bar{s}^3} - \frac{\bar{\mu}^2\bar{r}}{6\bar{s}\bar{\kappa}} + \frac{\bar{r}}{2\bar{s}\bar{\kappa}} \right]^2 + \left[\frac{\bar{\mu}\bar{r}}{3\bar{\kappa}} - \frac{\bar{\mu}^2}{3^2\bar{s}^2} \right]^3 \right\}^{\frac{1}{2}} \right)^{\frac{1}{3}} \\ & + \left(\frac{\bar{\mu}^3}{3^3\bar{s}^3} - \frac{\bar{\mu}^2\bar{r}}{6\bar{s}\bar{\kappa}} + \frac{\bar{r}}{2\bar{s}\bar{\kappa}} - \left\{ \left[\frac{\bar{\mu}^3}{3^3\bar{s}^3} - \frac{\bar{\mu}^2\bar{r}}{6\bar{s}\bar{\kappa}} + \frac{\bar{r}}{2\bar{s}\bar{\kappa}} \right]^2 + \left[\frac{\bar{\mu}\bar{r}}{3\bar{\kappa}} - \frac{\bar{\mu}^2}{3^2\bar{s}^2} \right]^3 \right\}^{\frac{1}{2}} \right)^{\frac{1}{3}} \\ & + \frac{\bar{\mu}\bar{\kappa}}{3\bar{s}\bar{\kappa}} , \end{aligned} \quad (5.44)$$

where the discriminant of this cubic must be greater than 0, to guarantee real roots, and is clearly given by

$$\begin{aligned} & \underbrace{\frac{\bar{\mu}^6}{3^6\bar{s}^6}}_{1^*} + \underbrace{\frac{\bar{\mu}^4\bar{r}^2}{6^2\bar{s}^2\bar{\kappa}^2}}_{2^*} + \frac{\bar{r}^2}{2^2\bar{s}^2\bar{\kappa}^2} - 2\underbrace{\frac{\bar{\mu}^3}{3^3\bar{s}^3}\frac{\bar{\mu}^2\bar{r}}{6\bar{s}\bar{\kappa}}}_{3^*} + 2\frac{\bar{\mu}^3}{3^3\bar{s}^3}\frac{\bar{r}}{2\bar{s}\bar{\kappa}} + 2\frac{\bar{\mu}^2\bar{r}}{6\bar{s}\bar{\kappa}}\frac{\bar{r}}{2\bar{s}\bar{\kappa}} \\ & \qquad + \frac{\bar{\mu}^3\bar{r}^3}{3^3\bar{\kappa}^3} - 3\underbrace{\frac{\bar{\mu}^2\bar{r}^2}{3^2\bar{\kappa}^2}\frac{\bar{\mu}^2}{3^2\bar{s}^2}}_{2^*} + 3\underbrace{\frac{\bar{\mu}\bar{r}}{3\bar{\kappa}}\frac{\bar{\mu}^4}{3^4\bar{s}^4}}_{3^*} - \underbrace{\frac{\bar{\mu}^6}{3^6\bar{s}^6}}_{1^*} \geq 0 . \end{aligned} \quad (5.45)$$

Several terms of the discriminant (5.45) have been denoted 1^*, 2^*, or 3^* on the basis that the parameter combinations, and respective orders, match in those

marked with the synonymous label. Cancelling these terms, we arrive at

$$\frac{\bar{r}^2}{2^2\bar{s}^2\bar{\kappa}^2} + \frac{\bar{\mu}^3\bar{r}}{3^3\bar{s}^4\bar{\kappa}} + \frac{\bar{\mu}^2\bar{r}^2}{6\bar{s}^2\bar{\kappa}^2} + \frac{\bar{\mu}^3\bar{r}^3}{3^3\bar{\kappa}^3} - \frac{\bar{\mu}^4\bar{r}^2}{12\bar{s}^2\bar{\kappa}^2} \geq 0\,, \tag{5.46}$$

which may be simplified by eliminating the denominators and dividing through to remove extraneous terms of the function. This yields

$$2^2\bar{\mu}^3\bar{\kappa}^2 + 2^2\bar{\mu}^3\bar{r}^2\bar{s}^4 + 3^2(3 + 6\bar{\mu}^2 - \bar{\mu}^4)\bar{s}^2\bar{r}\bar{\kappa} \geq 0\,, \tag{5.47}$$

where the factorisation has been done strategically to display the primacy of $\bar{\mu}$ in determining the existence of roots to this system. If $\bar{\mu}$ is large then certain parameter values may not be allowed, particularly in consideration of the fact that $(\bar{\kappa}, \bar{s}, \bar{r}) \in [0, \infty)^4$. On the other hand, $\bar{\mu} \in (1, \infty)$ since $\mu_0 > \mu_1$ by definition of our particular system and this parameter provides a measure of the distance between our two populations, F_i^* and F_j^*. As our two population diverge, in proximity, $\bar{\mu}$ increases and we lose our guarantee of steady state solutions to our system. If, however, our two populations remain closely related in structure then we maintain our equilibria solutions – as given in (5.38), (5.39), & (5.49) – for all other parameter values.

This may be explained simply, by the observation that for a steady state to exist, each of these populations must maintain one another through mutational contribution to one another's numbers. The probability of contributing to another population, μ, given one's own trait state necessarily decreases with the extent of the mutation necessary for such a contribution (or a given population's relative trait distance from another). If two populations are sufficiently far from one another that contribution of one population to the other, and *vice versa*, becomes too low, then the steady state will not be maintained and, therefore, may not exist. Notice, also, that the other parameters remaining within this inequality are the survival advantage from contributory traits; relative disadvantage from æsthetic augmentation; and the reproductive choice kernel of females for æsthetically augmented males, which all contribute positively to this

explanation.

Moving on to establish the steady-state for either of the two female populations – so that we may recover the steady states for the system, in general – for notational convenience we turn our attention to the steady-state equation for the j^{th} female population (5.37) and substitute in the steady state solutions for M_i^* and p^*, (5.38) & (5.39), to give

$$\begin{aligned}\delta_f s_j F_j^* K_p \left(1 - \frac{\delta_p}{\alpha_p}\left[s_i F_i^*\left(1+\frac{\alpha_m\delta_f}{\alpha_f\delta_m}\right) + s_j F_j^*\left(1+\frac{\alpha_m\delta_f}{\alpha_f\delta_m}\right)\right]^{-1}\right) \\ = \alpha_f\left(1 - F_i^*\left(1+\frac{\alpha_m\delta_f}{\alpha_f\delta_m r_i}\right) - F_j^*\left(1+\frac{\alpha_m\delta_f}{\alpha_f\delta_m r_j}\right)\right) \\ \cdot\left(\mu_0\kappa_j (F_j^*)^2\frac{\alpha_m\delta_f}{\alpha_f\delta_m r_j} + \mu_1\kappa_i (F_i^*)^2\frac{\alpha_m\delta_f}{\alpha_f\delta_m r_i}\right).\end{aligned} \tag{5.48}$$

Then, noicing that we have, by definition

$$F_i^* = \bar{F}F_j^*\,, \tag{5.49}$$

we may substitute this value into the above equation (5.48) and rearrange this to yield

$$\begin{aligned}\frac{\alpha_m}{\delta_m}\left(\frac{\mu_0\kappa_j}{r_j} + \frac{\mu_1\kappa_i}{r_i}\bar{F}^2\right)\left(1 + \frac{\alpha_m\delta_f}{\alpha_f\delta_m r_j} + \bar{F}\left[1+\frac{\alpha_m\delta_f}{\alpha_f\delta_m r_i}\right]\right)(F_j^*)^3 \\ -\frac{\alpha_m}{\delta_m}\left(\frac{\mu_0\kappa_j}{r_j} + \frac{\mu_1\kappa_i}{r_i}\bar{F}^2\right)(F_j^*)^2 + s_j K_p F_j^* \\ -s_j K_p\frac{\alpha_p}{\delta_p}\left(1+\frac{\alpha_m\delta_f}{\alpha_f\delta_m}\right)^{-1}\left(s_i\bar{F}+s_j\right)^{-1} = 0\,,\end{aligned} \tag{5.50}$$

which is a simple polynomial in F_j^*. Also notice, in passing, that we have recovered the trivial steady-state through this conversion.

Next, for notational brevity we use the following substitutions, for parameter

values which remain constant in time,

$$\gamma = \frac{\alpha_m}{\delta_m}\left(\frac{\mu_0\kappa_j}{r_j} + \frac{\mu_1\kappa_i}{r_i}\bar{F}^2\right), \qquad \omega = \frac{\alpha_p}{\delta_p}\left(1 + \frac{\alpha_m\delta_f}{\alpha_f\delta_m}\right)\left(s_i\bar{F} + s_j\right), \\ \xi = \left(1 + \frac{\alpha_m\delta_f}{\alpha_f\delta_m r_j} + \bar{F}\left[1 + \frac{\alpha_m\delta_f}{\alpha_f\delta_m r_i}\right]\right), \tag{5.51}$$

to rewrite the polynomial (5.50) as

$$\xi\gamma(F_j^*)^3 - \gamma(F_j^*)^2 + s_jK_pF_j^* - \frac{s_jK_p}{\omega} = 0\,. \tag{5.52}$$

This cubic polynomial gives the steady-state solution for our system, so long as the discriminant inequality is satisfied. This gives us our full system of steady-state solutions for all 5 populations, given individually by (5.38), (5.39), (5.49), & (5.52).

The discriminant inequality for the cubic polynomial solution to (5.52) is given by

$$\left(\frac{\gamma^3}{3^3\xi^3\gamma^3} - \frac{\gamma s_jK_p}{6\xi^2\gamma^2} + \frac{s_jK_p}{2\omega\xi\gamma}\right)^2 + \left(\frac{s_jK_p}{3\xi\gamma} - \frac{\gamma^2}{9\xi^2\gamma^2}\right)^3 \geq 0\,. \tag{5.53}$$

Then, factorising this inequality and eliminating denominators, we arrive at

$$0 \leq \underbrace{2^2\gamma^3\omega^2}_{4^*} + 3^6s_j^2K_p^2\xi^4\gamma - \underbrace{3^22^2s_jK_p\xi\gamma^2\omega^2}_{5^*} + 2^23^3s_jK_p\xi^2\gamma^2\omega - 3^52s_jK_p^2\xi^3\gamma\omega \\ + 2^23^3s_j^3K_p^3\xi^3\omega^2 - \underbrace{2^2\gamma^3\omega^2}_{4^*} - 3^32^2s_j^2K_p^2\xi^2\omega^2\gamma + \underbrace{3^22^2s_jK_p\xi\gamma^2\omega^2}_{5^*}\,. \tag{5.54}$$

The terms denoted 4^* and 5^* cancel one another to simplify the above relation, whilst the remainder of terms may be factorised again;

$$0 \leq 3^3s_jK_p\xi^2\left(3^3s_jK_p\xi^2\gamma + 2^2\gamma^2\omega - 3^22K_p\xi\gamma\omega + 2^2s_j^2K_p^2\xi\omega^2 - 2^2s_jK_p\omega^2\gamma\right)\,, \tag{5.55}$$

which we may phrase in terms of a quadratic in the predatory carrying capacity

of our ecosystem, K_p:

$$2^2 s_j^2 \omega^2 K_p^2 + (3^3 \xi^2 s_j \gamma + 2^2 \gamma^2 \omega - 3^2 2 \xi \gamma \omega - 2^2 \omega^2 s_j \gamma) K_p + 2^2 \gamma^2 \omega \geq 0 \,. \quad (5.56)$$

Finally, we know that as $K_p \to \infty$ this inequality is satisfied (which may also be confirmed by checking that the second derivative of this quadratic is positive) and, therefore, we know that the greater root of this quadratic gives the root above which this equation remains positive for all values. Using quadratic equation, then, we may guarantee that solutions exist for our steady states so long as

$$K_p \geq \begin{cases} \dfrac{\sqrt{B^2 - 4AC} - B}{2A} & \text{if } B^2 \geq 4AC \\ 0 & \text{otherwise.} \end{cases} \quad (5.57)$$

where

$$A = 2^2 s_j^2 \omega^2 \,, \qquad B = 3^3 \xi^2 s_j \gamma + 2^2 \gamma^2 \omega - 3^2 2 \xi \gamma \omega - 2^2 \omega^2 s_j \gamma \,, \qquad C = 2^2 \gamma^2 \omega \,.$$

Due to the complicated nature of each of these terms, it is difficult to say under which conditions this is satisfied although, in any given particular situation, the bounds for K_p are well defined, given the solutions for $\bar{F}$. The solutions for $\bar{F}$ are independent on K_p. It is worth observing that each of our parameters in this quadratic does seem to have a particular role, given that γ depends upon our reproductive parameter values; ω is dependent upon our predation parameter values; and ξ is dependent upon the relative disadvantage to the male prey population due to æsthetic augmentations. It is too difficult to say, however, which factor is of greatest influence in any given situation and this must be evaluated for each system independently.

Equilibria for Continuously Structured Populations (c)

Allow that the population of female prey has a solution which is given by the discrete sum across step functions, along a linear path through the domain

$\Upsilon^2 \times \mathcal{Z}$, such that

$$F^* = \sum_{\ell=1}^{N} F_\ell^*, \qquad F_\ell^* := \lim_{t\to\infty} f(t, \mathbf{y}_\ell, z_\ell) \tag{5.58}$$

and likewise for the male prey population. Let us also assume that each of these points in $\Upsilon^2 \times \mathcal{Z}$ is equally distant from the next and the last and that they are distributed across the entire domain, such that $d((\mathbf{y}_{i-1}, z_{i-1}), (\mathbf{y}_i, z_i)) = d((\mathbf{y}_i, z_i), (\mathbf{y}_{i+1}, z_{i+1})) = N^{-1}, \forall i \in \{2, \ldots, N-1\}$. Then the steady-state system of equations becomes

$$\begin{cases} 0 = & -\delta_f p^* s_i F_i^* + \alpha_f \left(1 + \dfrac{1}{KN} \displaystyle\sum_{\ell=1}^{N} [F_\ell^* + M_\ell^*]\right) \\ & \quad \cdot \dfrac{1}{N} \left(\displaystyle\sum_{\ell^\dagger=0}^{N-i} \mu_{\ell^\dagger} \kappa_{i+\ell^\dagger} F_{i+\ell^\dagger}^* M_{i+\ell^\dagger}^* + \sum_{\ell^\ddagger=1}^{i-1} \mu_{\ell^\ddagger} \kappa_{i-\ell^\ddagger} F_{i-\ell^\ddagger}^* M_{i-\ell^\ddagger}^* \right) \\ 0 = & -\delta_m p^* s_i r_i M_i^* + \alpha_m \left(1 + \dfrac{1}{KN} \displaystyle\sum_{\ell=1}^{N} [F_\ell^* + M_\ell^*]\right) \\ & \quad \cdot \dfrac{1}{N} \left(\displaystyle\sum_{\ell^\dagger=0}^{N-i} \mu_{\ell^\dagger} \kappa_{i+\ell^\dagger} F_{i+\ell^\dagger}^* M_{i+\ell^\dagger}^* + \sum_{\ell^\ddagger=1}^{i-1} \mu_{\ell^\ddagger} \kappa_{i-\ell^\ddagger} F_{i-\ell^\ddagger}^* M_{i-\ell^\ddagger}^* \right) \\ 0 = & -\delta_p p^* + \dfrac{\alpha_p}{N} p^* \left(1 - \dfrac{p^*}{K_p}\right) \displaystyle\sum_{\ell=1}^{N} (s_\ell F_\ell^* + s_\ell r_\ell M_\ell^*), \qquad \forall i \in \{1, \ldots, N\}. \end{cases} \tag{5.59}$$

As in the previous examples, we have that the solutions for M_i^* are a function of the solutions for F_i^* given by (5.38). Moreover, solving the steady-state relations for the first ($i = 1$) and second ($i = 2$) female prey populations for p^* and equating these, we obtain

$$\begin{aligned} & s_1 F_1^* \left(\frac{\mu_1 \kappa_1}{r_1} (F_1^*)^2 + \frac{\mu_0 \kappa_2}{r_2} (F_2^*)^2 + \sum_{\ell=1}^{N-2} \frac{\mu_\ell \kappa_{\ell+2}}{r_{\ell+2}} (F_{\ell+2}^*)^2 \right) \\ & = s_2 F_2^* \left(\frac{\mu_0 \kappa_1}{r_1} (F_1^*)^2 + \frac{\mu_1 \kappa_2}{r_2} (F_2^*)^2 + \sum_{\ell=2}^{N-1} \frac{\mu_\ell \kappa_{\ell+1}}{r_{\ell+1}} (F_{\ell+1}^*)^2 \right). \end{aligned} \tag{5.60}$$

Dividing this equation through by the primary female prey population and

defining $\bar{F}_{i,j} := F_j^*/F_i^*$, we may rewrite the above equation (5.60) as

$$\begin{aligned} &s_1\frac{\mu_1\kappa_1}{r_1} + s_1\frac{\mu_0\kappa_2}{r_2}\bar{F}_{1,2}^2 + s_1\sum_{\ell=1}^{N-2}\frac{\mu_\ell\kappa_{\ell+2}}{r_{\ell+2}}\bar{F}_{1,\ell+2}^2 \\ &= s_2\frac{\mu_0\kappa_1}{r_1}\bar{F}_{1,2} + s_2\frac{\mu_1\kappa_2}{r_2}\bar{F}_{1,2}^3 + s_2\sum_{\ell=2}^{N-1}\frac{\mu_\ell\kappa_{\ell+1}}{r_{\ell+1}}\bar{F}_{1,\ell+1}^2\bar{F}_{1,2} \end{aligned} \tag{5.61}$$

and this may finally be written as a cubic equation in $\bar{F}_{1,2}$, given by

$$\begin{aligned} s_2\frac{\mu_1\kappa_2}{r_2}\bar{F}_{1,2}^3 + s_1\frac{\mu_0\kappa_2}{r_2}\bar{F}_{1,2}^2 + \left(s_2\frac{\mu_0\kappa_1}{r_1} + s_2\sum_{\ell=2}^{N-1}\frac{\mu_\ell\kappa_{\ell+1}}{r_{\ell+1}}\bar{F}_{1,\ell+1}^2\right)\bar{F}_{1,2}^2 \\ +s_1\frac{\mu_1\kappa_1}{r_1} + s_1\sum_{\ell=1}^{N-2}\frac{\mu_\ell\kappa_{\ell+2}}{r_{\ell+2}}(F_{\ell+2}^*)^2 = 0 \end{aligned} \tag{5.62}$$

and solved so that $\bar{F}_{1,2} = \mathcal{F}_{1,2}(\bar{F}_{1,3},\ldots,\bar{F}_{1,N})$. Therefore, we have written the ratio between the first ($i=1$) and second ($i=2$) structural populations in the female prey population as a function of the remaining ratios.

Let us continue in this direction by equating the relations for the first ($i=1$) and third ($i=3$) female populations, such that

$$\begin{aligned} &s_1F_1^*\left(\frac{\mu_2\kappa_1}{r_1}(F_1^*)^2 + \frac{\mu_1\kappa_2}{r_2}(F_2^*)^2 + \frac{\mu_0\kappa_3}{r_3}(F_3^*)^2 + \sum_{\ell=1}^{N-3}\frac{\mu_\ell\kappa_{\ell+3}}{r_{\ell+3}}(F_{\ell+3}^*)^2\right) \\ &= s_3F_3^*\left(\frac{\mu_0\kappa_1}{r_1}(F_1^*)^2 + \frac{\mu_1\kappa_2}{r_2}(F_2^*)^2 + \frac{\mu_2\kappa_3}{r_3}(F_3^*)^2 + \sum_{\ell=3}^{N-1}\frac{\mu_\ell\kappa_{\ell+1}}{r_{\ell+1}}(F_{\ell+1}^*)^2\right) \end{aligned} \tag{5.63}$$

and substituting the solution to (5.62) in order to further reduce this system of

equation to

$$\begin{aligned} s_1\frac{\mu_2\kappa_1}{r_1} + s_1\frac{\mu_1\kappa_2}{r_2}\mathcal{F}^2_{1,2}(\bar{F}_{1,3},\dots,\bar{F}_{1,N}) + s_1\frac{\mu_0\kappa_3}{r_3}\bar{F}^2_{1,3} + s_1\sum_{\ell=1}^{N-3}\frac{\mu_\ell\kappa_{\ell+3}}{r_{\ell+3}}\bar{F}^2_{1,\ell+3} \\ = s_3\frac{\mu_0\kappa_1}{r_1}\bar{F}_{1,3} + s_3\frac{\mu_1\kappa_2}{r_2}\mathcal{F}^2_{1,2}(\bar{F}_{1,3},\dots,\bar{F}_{1,N})\bar{F}_{1,3} \\ + s_3\frac{\mu_2\kappa_3}{r_3}\bar{F}^3_{1,3} + s_3\sum_{\ell=3}^{N-1}\frac{\mu_\ell\kappa_{\ell+1}}{r_{\ell+1}}\bar{F}^2_{1,\ell+1}\,. \end{aligned} \tag{5.64}$$

One may observe that we now have a polynomial regression where, by solving iterative pairs of equations, we come converge towards a solution for $\bar{F}_{1,N}$ which depends only upon the fundamental parameters of this system. Then, any other ratio may be obtained using the following substitution

$$\begin{aligned} \bar{F}_{i,j} =& \mathcal{F}_{i,j}(\bar{F}_{i,j+1},\dots,\bar{F}_{i,N}) \\ =& \mathcal{F}_{i,j}(\mathcal{F}_{i,j+1}(\mathcal{F}_{i,j+2}(\dots),\mathcal{F}_{i,j+3}(\dots),\dots),\dots,\mathcal{F}_{i,N-1}(\bar{F}_N),\bar{F}_N) \\ =& : \bar{\mathcal{F}}_{i,j}(\bar{F}_N), \qquad\qquad \forall i \in \{1,\dots,N-1\}\,. \end{aligned} \tag{5.65}$$

Solving the equation for the predator population, within the full system (5.59), we obtain

$$p^* = K_p\left(1 - \frac{N\delta_p}{\alpha_p}\left[\sum_{\ell=1}^{N}(s_\ell F^*_\ell + s_\ell r_\ell M^*_\ell)\right]^{-1}\right)\,, \tag{5.66}$$

which may be substituted into the steady-state equation for the first ($i = 1$) female population to arrive at

$$\begin{aligned} &\delta_f K_p\left(1 - \frac{N\delta_p}{\alpha_p}\left[\sum_{\ell=1}^{N} s_\ell F^*_\ell\left(1 + \frac{\alpha_m\delta_f}{\alpha_f\delta_m}\right)\right]^{-1}\right)s_1F^*_1 \\ &= \frac{\alpha_f}{N}\left(1 + \frac{1}{KN}\sum_{\ell=1}^{N}F^*_\ell\left[1 + \frac{\alpha_m\delta_f}{\alpha_f\delta_m r_\ell}\right]\right)\cdot\sum_{\ell^\dagger=0}^{N-1}\frac{\mu_{\ell^\dagger}\kappa_{\ell^\dagger+1}}{r_{\ell^\dagger+1}}(F^*_{\ell^\dagger+1})^2\frac{\alpha_m\delta_f}{\alpha_f\delta_m}\,, \end{aligned} \tag{5.67}$$

where we have also substituted in the solutions for the male prey populations (5.38). Finally, we may substitute in the definitional relations for F^*_i with

respect to F_1^* (5.49), for which all terms have now been evaluated, and factorise this relation to yield

$$\begin{aligned} & K_p\left(1-\frac{N\delta_p}{\alpha_p F_1^*}\left(1+\frac{\alpha_m\delta_f}{\alpha_f\delta_m}\right)^{-1}\left[s_1+\sum_{\ell=2}^{N}s_\ell\bar{F}_{1,\ell}\right]^{-1}\right)s_1F_1^* \\ & =\frac{\alpha_m}{\delta_m N}\left(1+\frac{F_1^*}{KN}\left[\left(1+\frac{\alpha_m\delta_f}{\alpha_f\delta_m r_1}\right)+\sum_{\ell=2}^{N}\bar{F}_\ell\left(1+\frac{\alpha_m\delta_f}{\alpha_f\delta_m r_\ell}\right)\right]\right) \\ & \cdot\left(\frac{\mu_0\kappa_1}{r_1}+\sum_{\ell^\dagger=1}^{N-1}\frac{\mu_{\ell^\dagger}\kappa_{\ell^\dagger+1}}{r_{\ell^\dagger+1}}\bar{F}_{\ell^\dagger+1}^2\right)(F_1^*)^2\,, \end{aligned} \tag{5.68}$$

which is a cubic equation of the form

$$\begin{aligned} & \tfrac{\alpha_m}{\delta_m K}\left[\left(1+\tfrac{\alpha_m\delta_f}{\alpha_f\delta_m r_1}\right)+\sum_{\ell=2}^{N}\bar{F}_\ell\left(1+\tfrac{\alpha_m\delta_f}{\alpha_f\delta_m r_\ell}\right)\right]\left(\tfrac{\mu_0\kappa_1}{r_1}+\sum_{\ell^\dagger=1}^{N-1}\tfrac{\mu_{\ell^\dagger}\kappa_{\ell^\dagger+1}}{r_{\ell^\dagger+1}}\bar{F}_{\ell^\dagger+1}^2\right)(F_1^*)^3 \\ & +N\tfrac{\alpha_m}{\delta_m}\left(\tfrac{\mu_0\kappa_1}{r_1}+\sum_{\ell^\dagger=1}^{N-1}\tfrac{\mu_{\ell^\dagger}\kappa_{\ell^\dagger+1}}{r_{\ell^\dagger+1}}\bar{F}_{\ell^\dagger+1}^2\right)(F_1^*)^2 \\ & -K_p s_1 N^2 F_1^* + K_p s_1\tfrac{N^3\delta_p}{\alpha_p F_1^*}\left(1+\tfrac{\alpha_m\delta_f}{\alpha_f\delta_m}\right)^{-1}\left[s_1+\sum_{\ell=2}^{N}s_\ell\bar{F}_{1,\ell}\right]^{-1}=0\,. \end{aligned} \tag{5.69}$$

In order to avoid tedium, we shall not venture to solve this equation or, even, look for its discriminant but leave it to the reader to decide upon the necessity of such a task. It is, however, worth pointing out that such a general solution holds for all or any number of such step functions and, as such, may be easily extrapolated to the continuous case as $N\to\infty$. Therefore, despite the fact that this is a discrete handling of the model, we call this the continuous solution to the model on the basis that it provides a direct route to the semi-analytic solution for continuous distributions. In fact, while F_1^*, here, provides an absolute steady-state solution at some discrete point in the structure space, $\Upsilon^2\times\mathcal{Z}$, as $N\to\infty$ we obtain a continuous distribution, relative to F_1^*, as the system of points

$$\lim_{N\to\infty}\left\{1,\bigcup_{\ell=1}^{N}\{\bar{F}_{1,\ell}\}\right\}\,, \tag{5.70}$$

where $\bar{F}_{1,1}=1$. Likewise, for an n-dimensional system of points, this same

method may be used to obtain analytic solutions as the union of infinitesimally narrow step-functions on the domain. This is true since we have maintained the generality of the path across which the 1-dimensional distribution is observed across the domain and, therefore, we maintain the generality of all sub-distributions and functions across it.

(It is also worth noting the fairness of the term distribution here since – in the case where either $\kappa_i \neq \kappa_j$, $s_i \neq s_j$, or $r_i \neq r_j$ for any $(i,j) \in \{1,\ldots,N\}^2$, $i \neq j$ – uniform distribution across the domain is not permitted. The functions $\kappa(\mathbf{y})$, $s(z)$, and $r(y_2)$ feature heavily in the characteristic polynomials for $\bar{F}_i$ and will thusly shape the distribution of the solutions across the domain. It is also worth noting that, in this particular case, the functions $f^*(\mathbf{y},z)$ and $m^*(\mathbf{y},z)$ will necessarily have the same distribution, on the basis that we have assumed away the asymmetries in their reproductive terms, in order to simplify the analysis. This discrepancy would be expected to show up in the numerical solutions, since the numerical system will conserve these asymmetries and the distributions will not align precisely.)

We have shown here, firstly that steady state solutions for all three scenarios; unstructured, discrete, and continuous. For the unstructured population, we have been able to go further by providing a tangible constraint on the predator and prey carrying capacities, K_p and K, for which steady states will be guaranteed so long as $\alpha_p K \leq 1$ and $s(z) \leq 1$. Since these values occur in nature, these constraints provide a welcome validation of the model with respect to its realism; as does the suggestion that predator numbers must be controlled for an ecosystem to persist (5.30). Secondly, we go on to provide methods for obtaining these solutions, which in the case of unstructured populations is somewhat trivial. In the case of the discrete structured and continuous we provide non-trivial, implicit, analytic solutions and these methods constitute a substantial contribution to analytic methods in integro-differential mathematics.

5.2.3 Numerical Methods

Numerical schemes were implemented in MatLab, where, to attempt to increase the stability and accuracy of numerical solutions, we implemented a McCormack predictor-corrector system. All integrals were evaluated using the standard, numerical trapezoidal rule, while integrands, under the integrals over ζ in particular, were linearly interpolated from existing results, since to choose an interpolation spline would be to assume a form for the solutions.

The constants chosen with which to simulate this system of equations (Table 5.1) was designed to explore the dynamics of the mathematical, or theoretical, system rather than of a specific species or set of species. This will not allow one to draw any specific conclusion about the dynamics of a particular species but, rather, allows one to understand the logical and necessary conclusions of the simple and few assumptions made in order to give rise to such a model.

In order to assess how the mass of the populations of females and males evolve over time, we define the female mass, $f_M : \mathcal{I} \to \mathbb{R}_+$, and the male mass, $m_M : \mathcal{I} \to \mathbb{R}_+$, as being given by the quantities

$$f_M(t) = \iiint\limits_{\Upsilon^2 \times \mathcal{Z}} f(t, \mathbf{y}, z)\, d(\mathbf{y}, z), \quad \text{and} \quad m_M(t) = \iiint\limits_{\Upsilon^2 \times \mathcal{Z}} m(t, \mathbf{y}, z)\, d(\mathbf{y}, z)\,. \tag{5.71}$$

Likewise, in order to present a more absolute quantitative measure of the female or male populations at any given time, we would like to know the average position of each population in a given trait. This is achieved by evaluating the centre of mass (COM) of the population in the quantities y_1, y_2, or z respectively

variable	constants		
f, m	$\nu_{y_1} = 50$	$\nu_{y_2} = 50$	$\nu_z = 20$
	$q \in [0, 4]$	$\beta \in (0, 1)$	
f	$\alpha_f = 3.2\times10^{-2}$	$\delta_f = 0.2$	$K = 2\times10^3$
m	$\alpha_m = 3.2\times10^{-2}$	$\delta_m = 0.2$	”
p	$\alpha_p = 1.5\times10^{-3}$	$\delta_p = 0.5$	$K_p = 2\times10^2$

Table 5.1: **Table of constants for the evolutionary sexual selection model.** All constants stated above and utilised within the simulation of the theoretical model are given along with their corresponding variable.

with

$$f_{C_y}(t) = \frac{\iiint\limits_{\Upsilon^2\times\mathcal{Z}} y_1 f(t,\mathbf{y},z)\,d(\mathbf{y},z)}{\iiint\limits_{\Upsilon^2\times\mathcal{Z}} f(t,\mathbf{y},z)\,d(\mathbf{y},z)}, \qquad f_{C_z}(t) = \frac{\iiint\limits_{\Upsilon^2\times\mathcal{Z}} z f(t,\mathbf{y},z)\,d(\mathbf{y},z)}{\iiint\limits_{\Upsilon^2\times\mathcal{Z}} f(t,\mathbf{y},z)\,d(\mathbf{y},z)}$$

and

$$m_{C_y}(t) = \frac{\iiint\limits_{\Upsilon^2\times\mathcal{Z}} y_1 m(t,\mathbf{y},z)\,d(\mathbf{y},z)}{\iiint\limits_{\Upsilon^2\times\mathcal{Z}} f(t,\mathbf{y},z)\,d(\mathbf{y},z)}, \qquad m_{C_z}(t) = \frac{\iiint\limits_{\Upsilon^2\times\mathcal{Z}} z m(t,\mathbf{y},z)\,d(\mathbf{y},z)}{\iiint\limits_{\Upsilon^2\times\mathcal{Z}} f(t,\mathbf{y},z)\,d(\mathbf{y},z)}, \tag{5.72}$$

where female populations are evaluated solely for their COM in y_1 and likewise for males in y_2, since these are the expressed traits of each sex.

5.2.4 Results

The theoretical model used throughout this paper explores the dynamics between a predatory species, $p(t)$, and female, $f(t,\mathbf{y},z)$, and male, $m(t,\mathbf{y},z)$, cohorts within some arbitrary prey species. These populations may change through selectivity-elaboration, $\mathbf{y} := [y_1, y_2]^T$, and trait survival, z, dimensions which together we refer to as the trait space. Whilst we assume, for the most part, that trait elaboration brings a natural disadvantage to male prey who express this trait; trait selectivity does not bring any survival disadvantage but increases the probability that females will mate with more elaborate males; and trait survival evolves orthogonally to these traits whilst always endowing the host to a survival advantage, with regard to predation. Offspring receive traits dependent upon those of the parents, whilst mutations are acquired through reproduction alone.

Results are presented in 3 major forms:

1) Mass-time plots present the temporal distribution in the overall population of each subpopulation of females, males, and predators as $f_M(t)$, $m_M(t)$, and $p(t)$ (Fig. 5.2), where $f_M(t)$ and $m_M(t)$ are defined as in (5.71). Each of these quantities is plotted with time in the x-dimension. Likewise, centre of

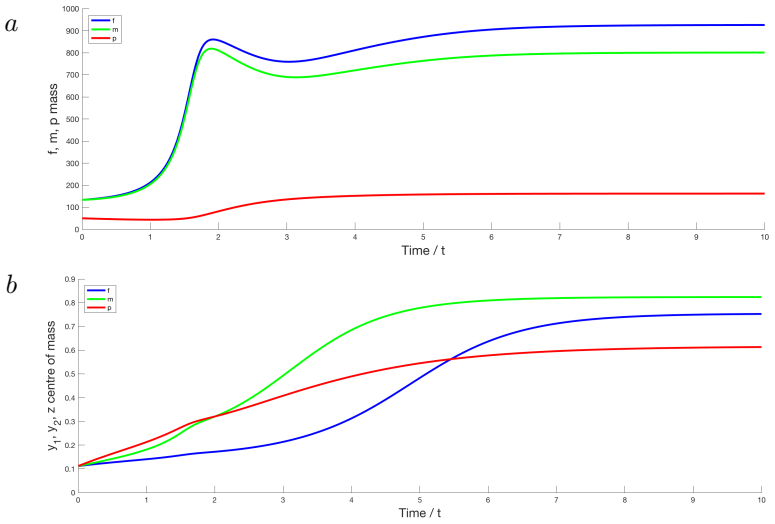

Figure 5.2: Population dynamics for a system with advantage parameters $q = 1.6$ and $\beta = 0.4$, presented as (a) mass-time plots illustrating the absolute population masses for $f_M(t)$ (*blue*), $m_M(t)$ (*green*), and $p(t)$ (*red*) and (b) centre of mass (COM)-time plots illustrating the COMs in y_1 (*blue*), y_2 (*green*), and z (*red*) respectively for females, males, and both during the interval $t \in \mathcal{I}$.

mass (COM)-time plots give the COM, or the average position, of the distribution in y_1, y_2, and z appropriately (Fig. 5.2, 5.5 & 5.9) as f_{C_y}, f_{C_z}, m_{C_y}, and m_{C_z} are defined in (5.72).

2) Time series, or final states, may be given as a series of 2-dimensional colour-maps (along with their respective colour-bars) to illustrate the relative distributions of $f(t, \mathbf{y}, z)$ and $m(t, \mathbf{y}, z)$ across the (y_i, z)-plane, for a given time point t and where $i = 1$ for females and $i = 2$ for males (Fig. 5.3, 5.4, 5.6, & 5.8). Thusly, female distributions are illustrated in their active (y_1, z)-plane and males are illustrated in their active (y_2, z)-plane.

3) Finally, parameter-COM colour-maps (along with their respective colour-bars) describe the final COM for a given distribution, at $t = 10$, as a colour plotted on axes defined by the value of two given parameters, where all other parameters have remained fixed (Fig. 5.7).

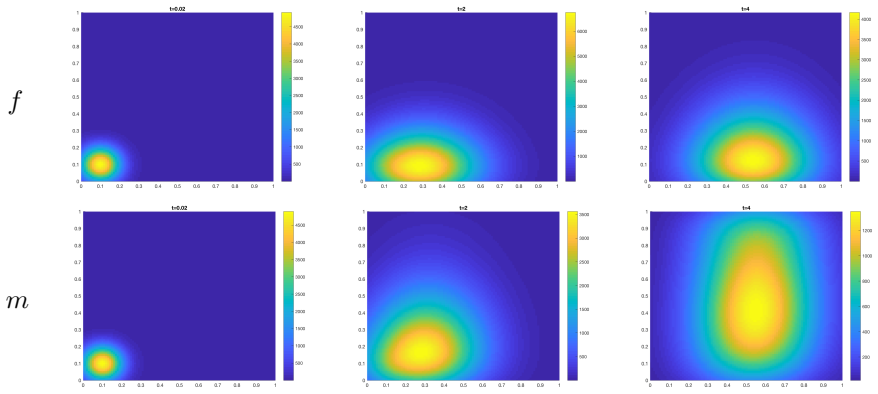

Figure 5.3: Time series colour-maps representing 2-dimensional distribution of population concentrations on the (y_1, z)-plane, for females, and the (y_2, z)-plane, for males, at time points $t \in \{0, 2, 4\}$.

Female sexual selection drives male elaboration

Observe, for example, the evolution of a predator-prey system given the relative trait elaboration disadvantage of 110%, $q = 1.1$, and the relative trait survival advantage of 20%, $\beta = 0.2$, (Fig. 5.2 – 5.4). Firstly, one should notice that the opening phases of the development of both the female and male populations are characterised by a broadening of the distribution in trat selectivity, trait elaboration, and trait survival, although to a comparatively greater extent in trait survival (Fig. 5.3). This dynamic is mediated by the mutation of the species in both elaboration and through the orthogonally advantageous trait survival, described by z. Further, these opening moments are characterised, to a great extent, by predation and result in the diminution of the female and male populations (Fig. 5.2).

The secondary phase of this process is characterised by a dynamic shift of the male population from a well defined inconspicuous population, low y_2, to a more genetically dispersed population, in terms of elaboration (Fig. 5.3). This shift is furthered by a subsequent consolidation of the population's genetic configuration, at high values of trait elaboration, and a subsequent dispersal in the selectivity of females. As males become less elaborate, then, females

may become more selective and this is observed through the fast dispersal and consolidation of females in more selective traits (Fig. 5.4) since those females who are less selective will be more likely to mate with unsuccessful males. This is a symbiotic relationship wherein selective females allow elaborate males to proliferate and survive whilst male elaboration allows females to become yet more selective. Throughout this process, the orthogonally advantageous trait propagates ever more steadily towards higher values of trait survival, increasing the population's average survival rate when considering only this trait (Fig. 5.3 & 5.4).

To be clear, this model does not allow for the population to organically shift, in the absence of growth or destruction, but rather it is the selective pressures of random mutation and natural selection by predation which are causing the shifts in trait survival. In the case of traits selectivity and elaboration, however, the case is more complicated. As the male population increases its standing in trait elaboration it will become more vulnerable to predation and, as a result, should die more frequently than its more elaborate counterparts. This would cause the population to remain at low values of elaboration. Given, on the other hand, the propensity of females to become concurrently more selective about which males they choose to mate with, the population of highly elaborate males will become more attractive mates and will copulate more often than their inconspicuous sexual rivals. This causes the growth in highly elaborate males to become sufficiently higher than less elaborate males and allows them to outgrow this inconspicuous population. This is a theoretical illustration of the process known as sexual selection.

To confirm the effect of sexual selection, we ran two almost identical experiments; one (i) wherein females would genetically diversify whilst, in the second (ii), females would remain non-selective at all times (Fig. 5.5). All other parameters affecting the experiment were kept constant throughout. In experiment (i) one observes a gradual increase in male trait elaboration and, although mean female trait selectivity is monotonically increasing, a retarded increase in female selectivity (Fig. 5.5, —). This increase in selectivity is, as in

previous experiments, triggered by male diversity in elaboration and the presentation of reasonable choice to female populations. In experiment (ii), however, one observes the regression of the female population monotonically towards a non-selective phenotype, despite initial conditions being identical (Fig. 5.5, - - -). This results in male populations initially exhibiting some, female selectivity-driven, increase in elaboration before a subsidence in trend and regression to a state of low elaboration, which is still maintained by the small selective female population maintained in the narrow distribution across trait selectivity. In this particular case, the success of orthogonal survival traits, z, is unaffected by changes in female or male distributions across selectivity and elaboration.

Advantageous elaboration gives rise to augmented male success

In order to test, and validate, the model further, we checked to confirm that defining the elaboration on males to be advantageous against predators, for example to serve as a warning or deterrence to predators, would result in strong selection for this trait. To do this, we set the relative disadvantage $q < 1$. Choosing an arbitrary value $q = 0.8$, satisfying $q < 1$, we ran the experiment as previously, with $\beta = 0.2$. We found that, in this case, male populations

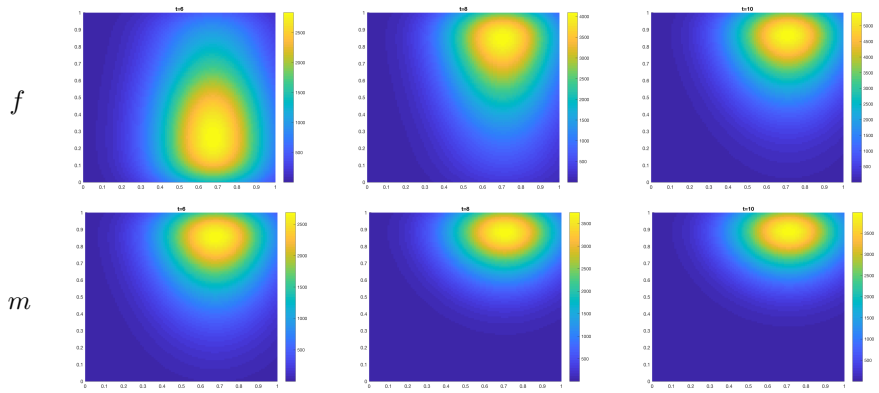

Figure 5.4: Time series colour-maps representing 2-dimensional distribution of population concentrations on the (y_1, z)-plane, for females, and the (y_2, z)-plane, for males, at time points $t \in \{6, 8, 10\}$.

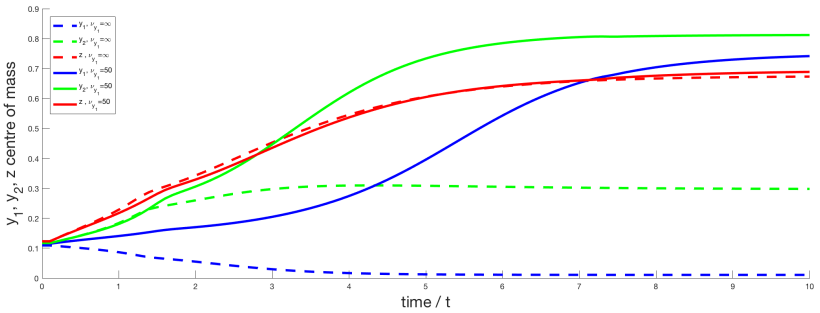

Figure 5.5: **Female sexual selection drives male elaboration.** Centre of mass (COM)-time plots for solutions to equations with mutation in the y_1-dimension, $\nu_{y_1} = 50$ (- - -), and without mutation in the y_1-dimension, $\nu_{y_1} = \infty$ (—). Temporal distributions are given for female selectivity, y_1 (*blue*); male elaboration, y_2 (*green*); and overall orthogonal survival traits, z (*red*), across the time interval $t \in \mathcal{I}$.

dominated female populations (Fig. 5.6A), by merit of their selective advantage. This also gave rise to strongly elaborate males and selective females (Fig. 5.6B), whose traits were more well defined than with previous populations (Fig. 5.5) but whose mass distributions across the trait space (Fig. 5.6) were not significantly altered with respect to previous experiments (Fig. 5.4).

Meanwhile, a parameter sweep across values of $q < 1$ and $\beta \in (0, 1)$ found that a strongly elaborate phenotype was achieved homogeneously across parameter space and that male populations consistently existed in greater numbers than female populations; a trend that increased inversely with q. This demonstrates that, no matter the advantage presented by orthogonal traits, advantageous elaboration always gives rise to a final population of highly elaborate males and a population with more males than females.

Theoretical models support the orthogonal disadvantage (OD) hypothesis, sometimes

In order to test the validity of the OD hypothesis, one must find those scenarios wherein trait elaboration is expressed and compare to those wherein trait elaboration is not selected for. To achieve this, a parameter sweep was performed across the elaboration disadvantage and survival advantage space, (q, β)-plane, to observe the dynamics of respective populations under differing systems of

pressure. Completing this, one observes extremely well defined phenotypes, high-y and low-y, in the elaboration and selectivity trait spaces, whilst a less well defined transitionary dynamic is observed for survival traits (Fig. 5.7). Above certain values in elaborative disadvantage, and depending on survival advantage, there exists a steep transition between elaborate, selective and inconspicuous, non-selective populations. Nevertheless, the correlation between this behaviour and that in trait survival is strong and statistically relevant.

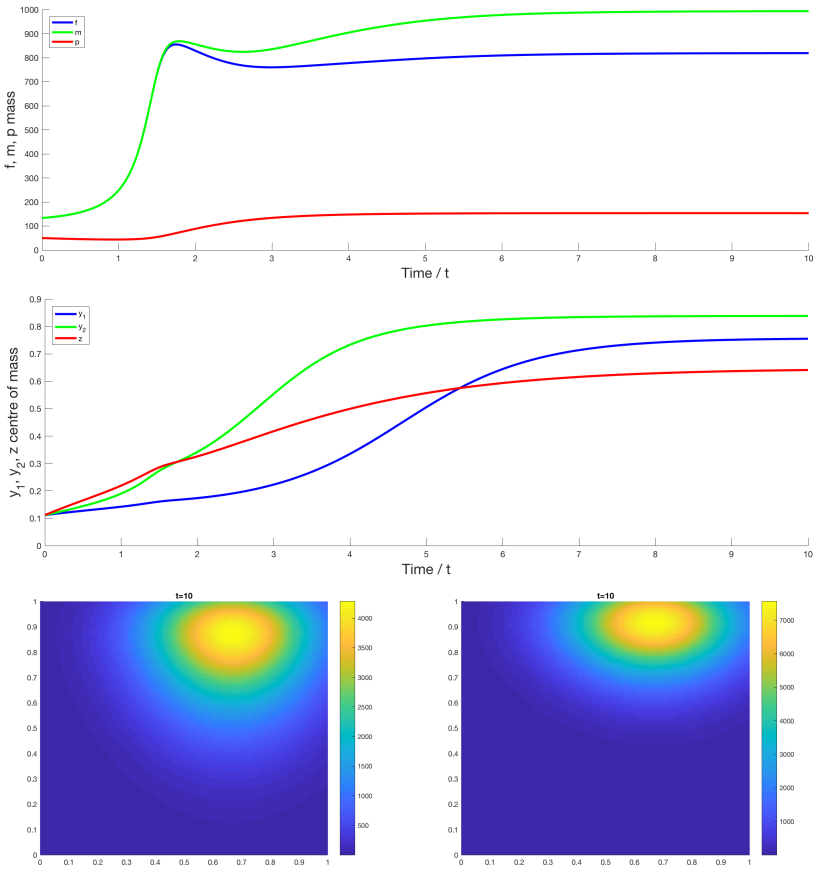

Figure 5.6: **Advantageous elaboration gives rise to augmented male success.** Population dynamics for a system with advantageous growth parameters $q = 0.8$ and $\beta =$, presented as (A) mass-time plots illustrating the absolute population masses for $f_M(t)$ (*blue*), $m_M(t)$ (*green*), and $p(t)$ (*red*) and (B) centre of mass (COM)-time plots illustrating the COMs in y_1 (*blue*), y_2 (*green*), and z (*red*) respectively for females, males, and both during the interval $t \in \mathcal{I}$. (C & D) Final state colour-maps representing 2-dimensional distribution of population concentrations on the (y_1, z)-plane, for females, and the (y_2, z)-plane, for males.

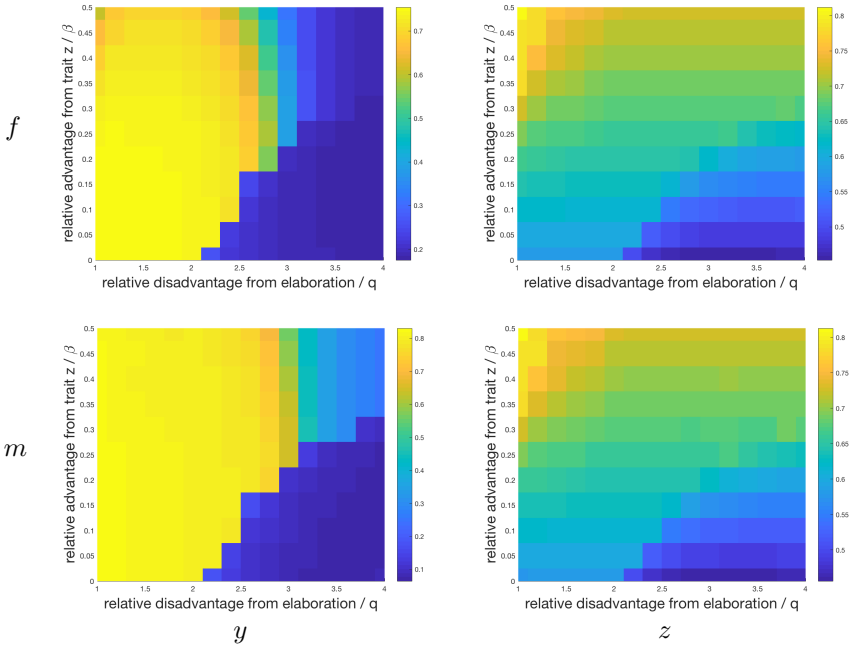

Figure 5.7: **Modelling predicts a steep drop-off in elaboration as costs exceed orthogonal compensations.** Final population states with varying trait advantage, presented as parameter-COM colour-maps for female and male final states in y_1/y_2 and z, where colour-bars indicate magnitude.

Moreover, one can clearly see that the significant decrease in y_2 value, or elaboration in males, resulting from the raised evolutionary cost of this trait correlates strongly with a decrease in both male and female z position, inflicting a clear penalty on any resultant female offspring. Although one may argue that this increase in trait survival, z, is only compensating for trait elaboration, y_2, in males, no such disadvantage is felt by female populations through the augmentation of trait selectivity or elaboration – since the model assumes that elaborate phenotypes are not expressed in females. Therefore, females are receiving a selective advantage from male elaboration, in that this causes a greater selection for higher trait survival in male populations and this is passed down to inconspicuous female offspring.

On the other hand, one should not fail to notice that this effect is only seen so long as the disadvantage of trait elaboration is not too great so as to

negate early compensatory dynamics for male populations; resisting the expression of elaborate phenotypes which allows for female selectivity to develop. In these cases, male elaboration is finally low and, although the residual benefit of augmented trait survival is not felt by female offspring, trait survival is still maintained to a relatively high degree, $\sim 63\%$.

Beauty is an evolutionary end in itself, when the cost is low

Observe that, in earlier experiments (Fig. 5.2), although trait survival and trait elaboration appear to co-evolve with one another, trait survival also leads the evolution of elaboration at early time points; that is, z increases ahead of y_2. Combining this observation with the OD hypothesis, therefore, implies that populations may be using an increase in trait survival to compensate for evolutionary or survival deficits incurred due to an increase in disadvantageous

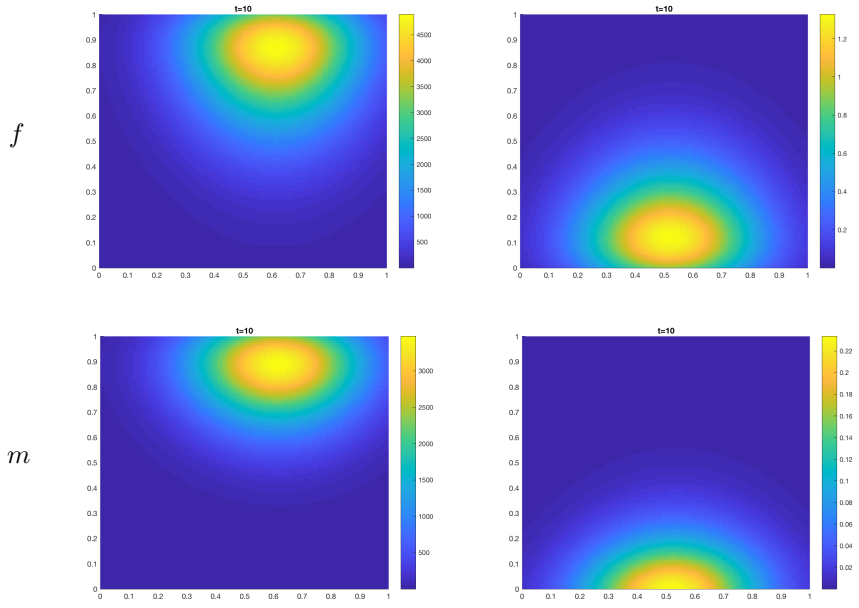

Figure 5.8: **Shifting elaboration costs causes elaborate-selective and inconspicuous-non-selective phenotypic selection.** Population states for a system with advantage parameters as indicated, presented as final state colour-maps representing 2-dimensional distribution of population concentrations on the (y_1, z)-plane, for females, and the (y_2, z)-plane, for males.

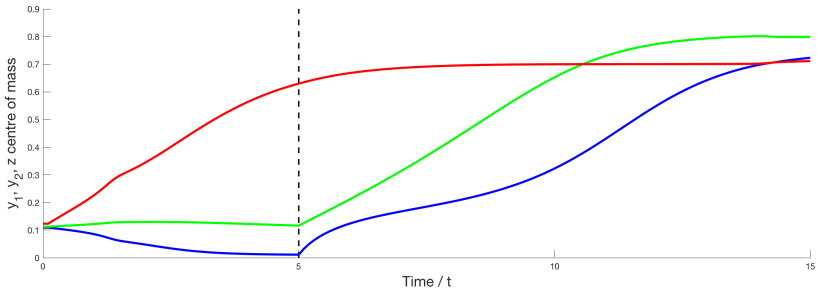

Figure 5.9: **Beauty is an evolutionary end in itself.** Centre of mass (COM)-time plots illustrating the COMs in y_1 (*blue*), y_2 (*green*), and z (*red*) respectively for females, males, and both during the interval $t \in \mathcal{I}$, where for $t < 5$ mutation in female trait selectivity and male trait elaboration is stemmed. At $t = 5$ (*black*, - - -) mutation in female trait selectivity, y_1, and male trait elaboration, y_2, are reinstated and maintained through $t \geq 5$.

elaboration. This would mean that beauty was an evolutionary end, in itself, that survival advantage was used to achieve in certain circumstances.

In order to test this hypothesis, we designed an experiment wherein the evolution of traits selectivity, y_1, and elaboration, y_2, would be stemmed during some initial period $t \in [0, 5)$ before the mutation through these trait spaces would be reinstated. During the initial period, trait survival increases monotonically whilst traits selectivity are greatly diminished (Fig. 5.9) when compared to fully mutational experiments (Fig. 5.2). Upon reinstatement of the full mutational dynamic, inclusive of traits selectivity and elaboration, to the female and male populations, one observes an increase in both traits without any significant augmentation in trait survival.

This suggests that, despite no survival advantage to the population, trait elaboration is sexually selected for by females purely through allowing trait selectivity to persist and freely mutate. In this case, the sexual urge to reproduce with attractive males will overcome the tendency of more naturally adept survivors to outnumber less successful survivors. Sexual selection for beauty is equally as strong a force as natural selection for survival. What one should also observe in these results is that the growth in trait elaboration COM is preceded by a fast increase in trait selectivity COM. This indicates that, although male trait elaboration leads females selectivity, female trait selectivity is necessary for the initial survival and diversification of elaborate males.

5.2.5 Discussion

To verify that our theoretical model is ecologically and evolutionarily relevant, we performed experiments which verified the origin of conserved disadvantageous traits were in female sexual selection, fittingly with the canon of evolutionary theory. We also found that imposing that this elaborative mutation was advantageous gave males an evolutionary advantage, which was conserved, and promoted female selectivity. These are precisely the results that one would expect to see in a functionally relevant theoretical model of evolution by natural and sexual selection [130]. Moreover, this modelling framework overcomes the criticisms [174, 121, 195, 310, 311] of previous models [273, 130, 131, 274] by acknowledging intra-species diversity, whilst allowing for the speciation mechanisms identified in others [188, 337] – for example by imagining a greater selective disadvantage in some autonomous spatial region, as compared to another. Likewise, we find support in statistical observations in dichromatic species [94, 337, 345], where our model supports the increasing turnover rate in these species whilst providing a mechanism for their local extinction. Our model also suggests, however, that speciation may not occur through sexual selection in a local environment where all pressures are equal.

Existing theoretical answers and approaches for this problem tend to involve the employment of deterministic ordinary or partial differential based modelling [130, 121, 195, 188, 293, 266] or game-, rule-, based systems [327, 174]. Our approach allows for the modelling of diverse distributions of populations across a well-defined trait space, resulting in a more nuanced solution and more natural interpretation for the results. Moreover, recent comparisons of vertebrate datasets to stochastic models found that evolution tends to happen in a pulsatile manner, through periods of rapid change [197]. Evolution of population distributions, in our model, follows periods of relatively small evolutionary change, which may be described as evolution by stasis [173], followed by periods of rapid upheaval and large phenotypic shifts in male and female populations, reconciling existing observations.

These results also provide strong basis for support of the HP [346, 130], although not the HSH. The HSH supposes that elaborative signalling, which is evolutionarily conserved, must be honest in order that it provides advantage to future generations and allows them to survive [347, 348, 273]. Our results have shown, however, that even when elaboration is purely disadvantageous, and does not provide any secondary advantage to male or female offspring, these elaboration will sometimes be conserved, so long as they are not too costly. Moreover, evolutionary advantage and elaboration are either directly related, in which case selection for elaboration may be explained solely through natural selection, or they are unrelated (orthogonal), in which case there is no mechanism to conserve honesty within a stochastic evolutionary system. This is in agreement with much of the modern literature [121, 310, 311]. To make mention of the UPH; this is actually covered within the trivial case of advantageous elaboration, in males, causing a male domination and evolutionary advantage to specifically male offspring.

The fact that female selectivity phenotypes begin to subside, upon decreasing advantages arising from trait survival, indicates that there must exist some significant compensatory mechanism in order for intra-species elaboration to be achieved. Likewise, as this advantage decreases, one observes a stronger expression of the trait; at once suggesting that disadvantageous sexual selection encourages selection for the orthogonal trait and that natural selective mechanisms will punish and compensate for this decreasing advantage. This supports the OD hypothesis and concurs with existing models for sexual and natural selective dynamics [346, 130, 174, 266] and recent natural observations [345]. The OD hypothesis is, however and in actual fact, a more formal sub-hypothesis stemming from the larger HP and the support that we lend for the OD hypothesis should be construed as a support for the HP itself.

This model may also suggest something quite unfamiliar to the scientific convention; that survival may not be the only end of evolution. This theoretical framework suggests that, at least, females are willing to assume the burden to their male offspring from mating with a disadvantaged male in order to fulfil

their genetically favoured æsthetic desires to mate with an attractive male, even when no survival gains are to be had.

Chapter 6

Further Methods in Multi-Scale Modelling of Cancer Invasion

6.1 Introduction to Pseudo-Spectral and Cellular Automata in Multi-Scale Cancer Problems

During the development and exposition of these higher-dimensional applications, a few limitations became clear in its scope. Although these methods remain extremely useful, when conceived in the appropriate settings, finite difference numerical strategies require a large computational memory capacity in order to implement – often in excess of that available. To overcome this, we attempted to implement a pseudo-spectral Chebyshev polynomial-based methodology for the estimation of solutions to yet higher dimensional problems and applied this to solving the problem of drug resistance (Section 6.2), covered in Section 3.2. The purpose of this was primarily to provide a comparison between

the justified results produced by finite difference and the estimations produced by the pseudo-spectral method – allowing us to estimate the reliability of the method.

In other cases, a continuous representation of space, where specific instances require dynamics to be considered at an individual cellular scale, are simply not capable of displaying the complex finite dynamics of individual cells and, instead, represent these dynamics as a probability distribution. This, occasionally, lacks the ability to align itself with the data which is often demanded of a model, if it is to be considered convincing. In order to rectify this, we implement an agent-based cellular automata model with the ability to simulate intra-cellular, cell-membrane, and population-level dynamics of a prearranged tumour. Herein (Section 6.3), we directly and explicitly tackle the problem of a proliferative cell population whose phenotypic behaviour alters in the presence of an invasive species of cancer cell, resulting in co-invasion of the proliferative cells. We also apply this method, for verification purposes, to additional problems in cellular invasion.

6.1.1 Brief Recap of Multi-Scale Drug Resistance

Drug resistance is a complex phenomenon which formed the primary focus of Chapter 3, wherein we discussed the major dynamics involved in the development of resistance to targeted therapies in melanoma. In the system which developed plastic resistance to therapy, by means of their metabolism, we make the following assumptions:

The cancer population, c exhibits diffusive, chemotactic, and haptotactic mechanics in space, representing random motion; attraction to environmental chemicals; and attraction to the extra-cellular matrix, respectively. In the structural or metabolic dimension, the cancer cells exhibit random motion in the presence of drugs and in the absence of nutrition – altering their metabolism without direction with Σ – and convection towards a genetically favourable metabolic state, ω, in the absence of drugs – as defined by Ψ. Cells are assumed

– in Φ_c – to grow logistically in the presence of nutrition, whilst – as with $\bar{\mathfrak{f}}$ – being degraded by targeted drug species appropriately with the targeted metabolic state space, in y.

The extra cellular nutritional environment (ECNE) population, v, is remodelled, using a logistic growth function, as in the function Φ_v, and is degraded linearly with the abundance of cancer cell produced matrix-metalloproteinases (MMPs). Molecular species, $\bar{m}$, consists of an MMP species, produced by cancer cells, and a nutritional species, produced by the ECNE. These species may diffuse throughout the domain and will be produced, as stated above, as defined by their production term $\bar{\Phi}_m$ and will be naturally degraded. Finally, the drug populations, $\bar{p}$, are given by BRAFi and MEKi and may diffuse throughout the domain; will be artificially injected into the system, as defined by the function $\bar{theta}$; and will be degraded as they induce apoptosis among the cancer cells.

In order to explore the paradigm of drug resistance, using the pseudo spectral Chebyshev polynomial methods, we recall the system used in Section 3.2, given by

$$\begin{cases} \dfrac{\partial c}{\partial t} = \underbrace{\nabla_x \cdot \left[D_c \nabla_x c + c(1-\rho(c,v))\left(\nabla_x(\bar{\chi}_m \cdot \bar{m}) + \nabla_x \chi_v v\right)\right]}_{\text{Spatial Flux}} \\ \qquad + \underbrace{\nabla_y \cdot \Sigma(y,\bar{m},\bar{p})\nabla_y c - r_\mu \nabla_y \cdot \Psi(y,\bar{m},\bar{p})c}_{\text{Structural Flux}} + \underbrace{\Phi_c(y,\bar{m},c,v)c}_{\text{Growth}} - \underbrace{\delta_c \bar{\mathfrak{f}}(y)\cdot \bar{p} c}_{\text{Drug Influence}} \\ \dfrac{\partial v}{\partial t} = \underbrace{\Phi_v(c,v)v}_{\text{ECNE Remodelling}} - \underbrace{\bar{\delta}_v \cdot \bar{m} v}_{\text{MMP Degradation}} \\ \dfrac{\partial \bar{m}}{\partial t} = \underbrace{\nabla_x \cdot \mathrm{diag}(\bar{D}_m)\nabla_x \bar{m}}_{\text{Spatial Diffusion}} + \underbrace{\int_{\mathcal{P}} \bar{\Phi}_m(y,\bar{m},c,v)\,dy}_{\text{Chemical Synthesis}} - \underbrace{\mathrm{diag}(\bar{\delta}_m)\bar{m}}_{\text{Natural Degradation}} \\ \dfrac{\partial \bar{p}}{\partial t} = \underbrace{\nabla_x \cdot \mathrm{diag}(\bar{D}_p)\nabla_x \bar{p}}_{\text{Spatial Diffusion}} + \underbrace{\bar{\theta}(t,x)}_{\text{Drug Input}} - \underbrace{\mathrm{diag}(\bar{\delta}_p)\bar{p}\int_{\mathcal{P}} c\,dy}_{\text{Drug Degradation}}. \end{cases} \tag{6.1}$$

This system of equations (6.1) is considered together with no-flux boundary

conditions in c, m, and $\bar{p}$. In the case of c we consider zero spatial fluxes, and zero structural fluxes on the boundaries of the spatial and structural domains, respectively.

6.1.2 Oncological co-invasion

Biological paradigms involving mixtures of heterogeneous subpopulations of cells have become the subject of increased scrutiny in recent years. Beginning from problems of cell sorting [132], cellular interactions now have a field of automata devoted to their exploration. One problem of significance is the change in behaviour of ordinarily non-invading proliferative cells ($\text{MITF}^{\text{HIGH}}$) in the presence of highly invasive, non-proliferative cells (MITF^{LOW}). Injection of these cellular populations, *in vivo*, in isolation yielded ordinary pathological behaviour whereas co-injection of disparate species led to the co-invasion of the local stroma by $\text{MITF}^{\text{HIGH}}$ cells, on a substrate altered by leading MITF^{LOW} cells [58].

This also gives cause to discuss more general problems in invasion. One methodology of cellular invasion involves the utilisation of 'microtracks', or spaces of reduced ECM concentration, by cells in order to gain a competitive advantage, travelling at increased speeds by direct comparison with those cells forced to travel through the dense ECM [51]. This increase in migration through native microtracks was shown, using time-lapse photography, to occur within the 3D collagen matrix. These microtracks have further been shown to have varying mean width and variance [193] which may be as a result of underlying matrix structuring and varying collagen densities across a given region. Importantly, the cells were shown to exhibit patterns of actin recruitment that were not discernible from those found in migratory cells out with microtracks [193].

The discrete Cellular Potts models which have been proposed model the cell moving through a grid-like structure, however fine, guided by a mechanistic, stochastic function [132]. Indeed, these have great power in reproducing qualitatively realistic results and can model even relatively complex systems [322].

These models exist in a discrete space where the implementation of behaviours is dependent on a delta probability function rather than the continuous machinery of the cell. This means that they lack the ability to, for example, explain or describe microtrack motility or to fully explain any emergent phenomena due to the model's reliance on stochastic dynamics.

One particular model which does not study the cell mechanics themselves, demonstrates that one can take a more physical interpretation of the tumour and its environment [349]. This model, again, chooses to describe a cellular population as a non-autonomous series of ball-like structures in arbitrary space acting under the standard forces (drag, traction, *et cetera*). The complexity of membrane-dependent biological interactions requires the creation of a novel cellular automata model who describes not only the position of the cells but endows them with some physical form which mediates its interaction with its environment.

6.2 Pseudo-Spectral, Chebyshev Polynomial-Based Modelling

6.2.1 The Mathematics of Chebyshev Polynomials

The most fundamental Chebyshev formulation is derived from the dilated inverse transformation through the trigonometric cosine function, given by

$$T_k(x) := \cos(k \cos^{-1} x), \qquad \forall k = 0, 1, 2, \ldots, \tag{6.2}$$

and for values of $x \in [-1, 1]$. Of course, the inverse cosine transformation of x yields values in $[0, \pi]$ such that the dilation by k serves to increase the periodicity of the function within the domain, or the number of rotations in the function (Fig. 6.1). In this way, k yields the 'degree' of the Chebyshev polynomial in its traditional sense; with a degree k polynomial having a maximal integer power of k and having k roots.

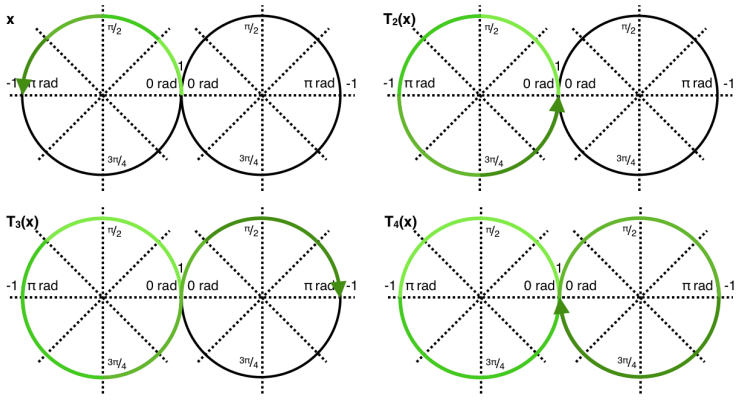

Figure 6.1: By pictorially representing the domain of $x \in [-1, 1]$ in terms of its sinusoidal transform $\cos^{-1} x$, we notice that the successive Chebyshev expansions represent an internal dilation on the circle and increase the number of minima/maxima by 1 each time.

Furthermore, setting $x := \cos z$ we arrive at the usual sinusoidal expression of the polynomial as $T_k(x) = \cos kz$. In order to simplify this notation and remove the sinusoidal terms from our Chebyshev system, notice that

$$\begin{aligned} T_{k-1}(x) + T_{k+1}(x) &= \cos(k-1)z + \cos(k+1)z \\ &= \cos(kz - z) + \cos(kz + z)\,. \end{aligned} \tag{6.3}$$

Then, using the trigonometric identity $\cos(A + B) = \cos A \cos B - \sin A \sin B$, we arrive at

$$\begin{aligned} T_{k-1}(x) + T_{k+1}(x) &= \cos kz \cos z + \sin kz \sin z + \cos kz \cos z - \sin kz \sin z \\ &= 2 \cos kz \cos z \\ &= 2x T_k(x), \end{aligned} \tag{6.4}$$

which, using $k \mapsto k - 1$, yields the recurrence relation

$$T_k(x) = 2x T_{k-1}(x) - T_{k-2}(x) \tag{6.5}$$

for generation of k^{th}-degree Chebyshev polynomials. Moreover, since the the two primary Chebyshev polynomials are arrived at by definition, $T_0(x) = 1$ and

$T_1(x) = x$, we may derive the entire sequence of Chebyshev polynomials by iteration (Table 6.1).

Next, we acknowledge that the direct sum of any of these two polynomials is of no great use or consequence, directly, where the weighted infinite sum of such polynomials, on the other hand, is capable of representing any given function, on the domain $[-1, 1]$. Therefore, each i^{th} polynomial given a weighting of α_i, we may write the complete polynomial as the sum of its constituent parts;

$$p_N(x) = \sum_{i=0}^{N} \alpha_i T_i(x)\,. \tag{6.6}$$

Moreover, in order to avoid the Runge phenomena which result from a equi-spaced discretisation of x on its domain[287], we use the Gauss-Lobatto points given by

$$x_i = \cos\left(\frac{\pi i}{N}\right), \qquad \forall i \in \{0, ..., N\}. \tag{6.7}$$

since the evaluation of our solution, $g(x)$, at these points, $g_i := g(x_i)$, shall guarantee that the Chebyshev collocation is capturing the most extreme behaviours of our solution. The Gauss-Lobatto points, after all, are chosen to coincide with the x-coordinates at which the N^{th} Chebyshev polynomial takes its extreme values, ± 1.

Multiplication of Chebyshev terms has been throughly discussed in several existing works and so we shall begin by acknowledging the forms of such a

Index	Approximated	T-notation	Polynomial
0	1	$T_0(x)$	1
1	$\cos x$	$T_1(x)$	x
2	$\cos 2x$	$T_2(x)$	$2x^2 - 1$
3	$\cos 3x$	$T_3(x)$	$4x^3 - 3x$
4	$\cos 4x$	$T_4(x)$	$8x^4 - 8x^2 + 1$
5	$\cos 5x$	$T_5(x)$	$16x^5 - 20x^3 + 5x$
6	$\cos 6x$	$T_6(x)$	$32x^6 - 48x^4 + 18x^2 - 1$

Table 6.1: Example of the first 6 Chebyshev polynomials and their approximated functions, calculated using (6.5).

multiplication as

$$T_i(x)T_j(x) = \frac{1}{2}\left(T_{i+j}(x) + T_{|i-j|}(x)\right) . \tag{6.8}$$

Therefore, the multiplication of 2 sums of such polynomials to degree $d-1$ can be given by

$$\left(\sum_{i=1}^{d} \alpha_i T_{i-1}(x)\right)\left(\sum_{j=1}^{d} \beta_j T_{j-1}(x)\right) = \sum_{i=1}^{d}\sum_{j=1}^{d} \tfrac{1}{2}\alpha_i\beta_j\left(T_{i+j-2}(x) + T_{|i-j|}(x)\right) \tag{6.9}$$

Therefore, the 1-dimensional change in any one coefficient can be given by

$$\begin{aligned} \left(\sum_{i=1}^{B} \alpha_i T_i(x)\right)\left(\sum_{j=1}^{B} \beta_j T_j(x)\right) &= \sum_{i=1}^{2B} \gamma_i T_i(x) \\ \gamma_m &= \sum_{i=q\left(\frac{m}{2}\right)}^{m} \tfrac{1}{2}\alpha_i\beta_{m-i} + \sum_{j=m}^{2B} \tfrac{1}{2}\alpha_j\beta_{|m-j|} \end{aligned} \tag{6.10}$$

where $q(\cdot) := \text{ceil}(\cdot)$ is the upwards, integer rounding function.

Following this methodology, one can write the multiplication of 2 summed N-dimensional Chebyshev polynomials as

$$\begin{aligned} &\left[\sum_{(i_1,\ldots,i_N)} \alpha_{i_1,\ldots,i_N} T_{i_1-1}(x)\ldots T_{i_N-1}(x)\right]\left[\sum_{(j_1,\ldots,j_N)} \beta_{j_1,\ldots,j_N} T_{j_1-1}(x)\ldots T_{j_N-1}(x)\right] \\ &= \sum_{(i_1,\ldots,i_N,j_1,\ldots,j_N)} \frac{1}{2}\alpha_{i_1,\ldots,i_N}\beta_{j_1,\ldots,j_N}\left(T_{i_1+j_1-2,\ldots,i_N+j_N-2}(x) + T_{|i_1-j_1|,\ldots,|i_N-j_N|}(x)\right) . \end{aligned} \tag{6.11}$$

In order to computationally implement this, however, would require a double iteration of the nested loops such that, for a 5-dimensional system, one would implement $(10^5)^2 = 10^{10}$ or 10bn iterations and would require two scalar multiplication operations per iteration giving 20bn operations.

This would make a straight implementation of an N-dimensional Chebyshev polynomial multiplication less efficient than that of a finite difference scheme. Therefore, one must derive an implementation scheme that takes advantage of the linear algebraic computational regimes in order to reduce the number of

necessary operations. For this substantive reason, we choose to implement a pseudo-spectral method in which we switch between finite difference grid and Chebyshev representations as necessary.

From trigonometric theory, the derivative of a single Chebyshev polynomial is given by

$$\begin{aligned}\frac{dT_n(x)}{dx} =& n \cdot \frac{\sin nz}{\sin z} = n \cdot U_{n-1}(x) \\ =& 2n \sum_{\substack{i=0 \\ n-i \text{ odd}}}^{n-1}{}' T_i(x)\end{aligned} \tag{6.12}$$

Further, the derivative of a Chebyshev sum is then given by

$$\nabla_x \sum_{i=0}^{B} \alpha_i T_i(x) = \sum_{i=0}^{B} 2i\alpha_i \sum_{\substack{j=0 \\ i-j \text{ odd}}}^{i-1}{}' Tj \tag{6.13}$$

Therefore, we write the resulting expression as

$$\nabla_x \sum_{i=0}^{B} \alpha_i T_i(x) = \sum_{i=0}^{B} \gamma_i T_i(x) \tag{6.14}$$

where the individual coefficients to this polynomial are given by the collected terms

$$\begin{cases} \gamma_0 = \dfrac{1}{2} \displaystyle\sum_{\substack{i=h \\ h\in\{0,2,4,6,\dots\}}}^{B} 2i\alpha_i \,, & \gamma_m = \displaystyle\sum_{\substack{i=H_m+h \\ h\in\{0,2,4,6,\dots\}}}^{B} 2i\alpha_i \,, \\ H_m = 2\left(\dfrac{m}{2} + 1 - q\left(\dfrac{m}{2}\right)\right), & m \in \{1,2,3,...,B\}, \end{cases} \tag{6.15}$$

where $q(\cdot) := \text{ceil}(\cdot)$ is the upwards, integer rounding function.

Moreover, using the trigonometric relation

$$x = \cos z \implies dx = -\sin z \, dz \tag{6.16}$$

and the standard definition for the expression of the Chebyshev polynomial

$T_k(x)$ in trigonometric form, we have that

$$\begin{aligned}\int_{-1}^{x} T_k(x)\,dx &= -\int_{-1}^{\cos z} \cos kz \sin z\,dz \\ &= -\frac{1}{2}\int_{-1}^{\cos z} \left[\sin(k+1)z - \sin(k-1)z\right]\,d\theta \\ &= \frac{1}{2}\left[\frac{\cos(k+1)z}{k+1} - \frac{\cos(k-1)z}{k-1}\right].\end{aligned} \tag{6.17}$$

Finally, using the inverse substitution, one finds that

$$\int_{-1}^{x} T_k(x) = \frac{T_{k+1}(x)}{2(k+1)} - \frac{T_{k-1}(x)}{2(k-1)}\,. \tag{6.18}$$

such that we may use a similar reasoning to that which was used for products of Chebyshev polynomials.

Finally, one must establish a methodology to go between the finite difference grid, in which we wish to store solutions, and the Chebyshev polynomials, which we wish to utilise in order to increase the accuracy of our calculations on this system. In order to retrieve the values in the finite difference grid, from the polynomial in question, we may simply evaluate the polynomial at these points. The remaining operation, then, is that of interpolating coefficients from a discrete set of points which we wish to represent.

The standard method of interpolation of a given function $g(x)$, where $i \in \{0, \ldots, N\}$ discrete values for this function are given by $g_i = g(x_i)$, is to use

$$\gamma_k = \frac{2}{\bar{c}_k N}\sum_{i=0}^{N}\frac{1}{\bar{c}_i} g_i \cos\left(\frac{k\pi i}{N}\right)\,, \tag{6.19}$$

where

$$\bar{c}_k = \begin{cases} 2 & \text{if } k \in \{0, N\} \\ 1 & \text{otherwise}\,. \end{cases} \tag{6.20}$$

Beyond these basic operations, one must define the aliasing operator which is used for numerically reducing the problem to that of a base B problem. This is necessary as the multiplication operator alone takes a polynomial of base B, $p_B(x)$, and returns a polynomial of base $2B$, $\bar{p}_{2B}(x)$. Aliasing uses the roots of the $B+1^{\text{th}}$ chebyshev polynomial, $T_{B+1}(x)$, to reflect higher degree polynomial degrees with those with degree $< B+1$. In order to alias, we use the property that certain cosinusoidal functions are similar to write the coefficients of the aliasing Chebyshev polynomial, $\breve{\alpha}_i$, as

$$\breve{\alpha}_i \quad = \quad \alpha_i - \alpha_{2B+2+i} - \alpha_{2B+2-i}\,, \qquad \forall i \in 0,1,2,...,B\,. \tag{6.21}$$

6.2.2 An Algorithm for Pseudo-Spectral Chebyshev Polynomial Methods

In order to achieve the decomposition of this process, we separate its entirety into 6 steps which, when iterated, shall yield the solution for a single time step in a finite temporal marching methodology. These steps may be described schematically (fig. 6.2) or are given explicitly as:

1. Simplification; evaluate the local addition, subtraction, multiplication, and division operations terms in order to reduce the number of Chebyshev operations.

2. Reorientation; rotate and reorient the solutions around the origin to bring the dimension of interest in line with the x-direction.

3. Interpolation; use the reorientation to determine the values of the coefficients for 1D Chebyshev polynomials in the x-direction, at the Gauss-Lobatto points through remaining dimensions.

4. Computation; compute the values of the operations of interest analytically, using the generated Chebyshev polynomials.

5. Reification; evaluate the 1D Chebyshev polynomials at their respective

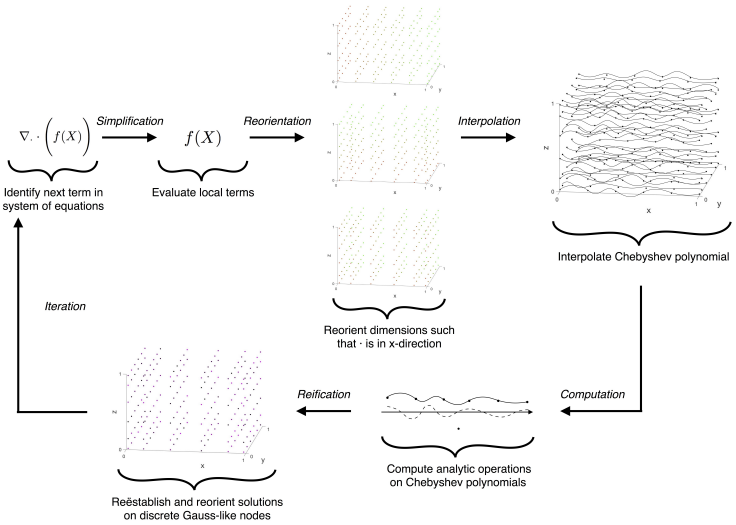

Figure 6.2: Schematic representation of the numerical Chebyshev polynomial scheme implemented, with individual steps given by simplification; reorientation; interpolation; computation; reification; iteration. Diagrams are given in a maximum of 3 dimensions in order to simplify their interpretation.

Gauss-Lobatto points and appropriately reorient the solutions, inversely with their earlier reorientation.

6. Iteration; continue by repeating the above steps for the next term in one's system of PDEs.

To expand upon these steps, begin with simplification. In this step, we aim to reduce the number of operation which must be computed using the Chebyshev polynomials, since these operations end to involve iterative processes without a concurrent or guaranteed increase in accuracy. Therefore, we take locally calculated terms, operations which require the comparison or interaction only of quantities evaluated both at the same location, within the super-term of interest. It is also necessary only to precompute local terms which would not be affected by collocation, since the Chebyshev results are analytic and should be given ultimate preference. For example, the addition of two quantities prior to collocation yield the same resultant polynomial and applying addition posterior

to collocation, since the addition of the solutions happens locally.

The process of reorientation may seem somewhat arbitrary and, rather than being mathematically necessary, serves to simplify the numerical and algorithmic implementation of the Chebyshev system by certifying the dimension of interest. To do this, we observe the dimension of interest in the current term and perform a rotational transformation upon the entire set of relevant solutions, in order that the dimension of interest now aligns with the x-dimension, formerly. Posterior to the reorientation, and by definition of the process itself, all subsequent operations are to take place upon Chebyshev polynomials whose coefficients have been evaluated for an x-directional polynomial system. This reduces numerical complexity and the need for iterative checking or reorientation within substages.

The next step is interpolation and requires that the coefficients be obtained for Chebyshev polynomials oriented in the x-direction. In this way, we use the Gauss-Lobatto points at which we are currently storing our solutions, in the form of a finite difference grid, to obtain the coefficients of polynomials up to degree $2N - 1$, where N is the number of Gauss-Lobatto points. This must be done across all points in the x-direction but upon all such points in all remaining dimensions, such that the number of values stored shall, in fact, increase; the idea being that the Gauss-Lobatto points, themselves, are too sparse to yield sufficiently high resolution calculations on non-local terms (such as derivatives) where the Chebyshev systems will yield analytic results. The subsequent step, then, is calculation wherein the term of interest is calculated with absolute accuracy and using the formulæ provided above (Section 6.2.1).

Finally, the solutions must go through a process of reification such that they reflect the form of the solutions from which they were derived. In order to do this, we evaluate the Chebyshev polynomials at their respective Gauss-Lobatto points and reassign these to a finite difference grid. This grid must then be reoriented, through the reverse transformation to that utilised above, such that they bare comparison to earlier generated solution and that the time stepping may continue. This step gives rise to a finalised calculation (although further

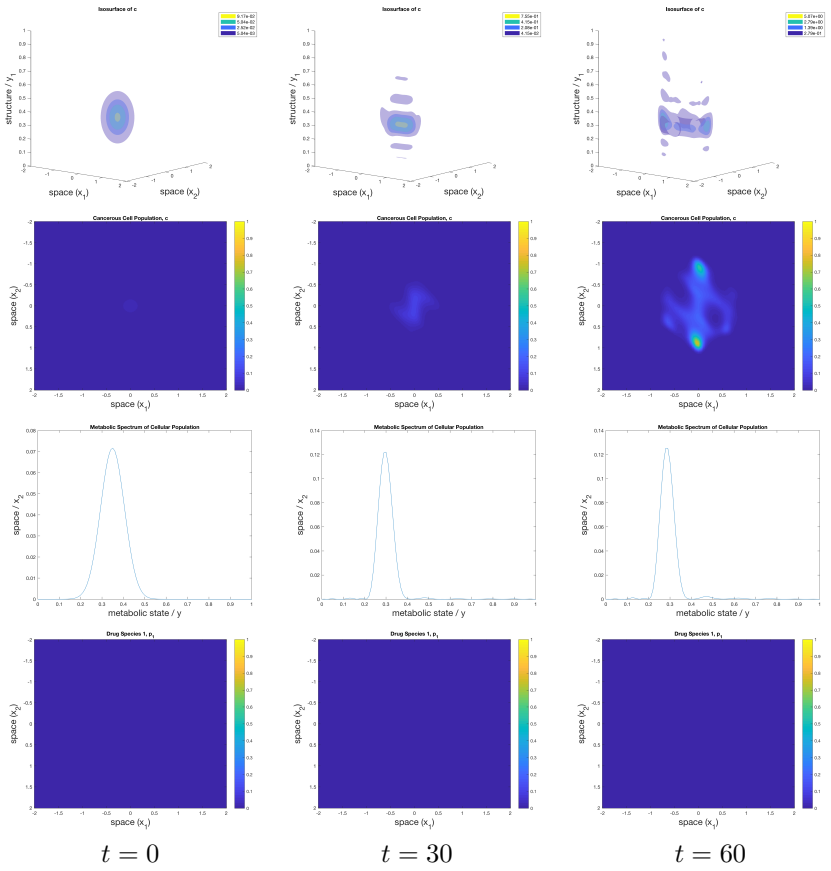

Figure 6.3: Results of the numerical simulations for the phenotypically evolving tumour model, using pseudo-spectral Chebyshev polynomial methods, are given. Panels displaying (*top*) the structured cellular population with space across the lower plane and mutational state given along the vertical axis; (*middle*) the spatial cellular distribution; and (*bottom*) the ECNE density, where ipilimumab treatment is given at $t = 40$ and BRAFi treatment is given at $t = 100$, for time points $t \in \{0, 30, 60\}$ are shown.

steps may, in fact, require the calculation of super-terms to this one) and the iteration step, requiring one to repeat the above procedure until all terms in the system of equations are exhausted.

6.2.3 Results & Conclusions

All of our solutions are generated using the above described methodology and using degree 20 Chebyshev polynomials, which should produce an interpolative error on the scale 10^{-6}. The initial condition for our solutions are given

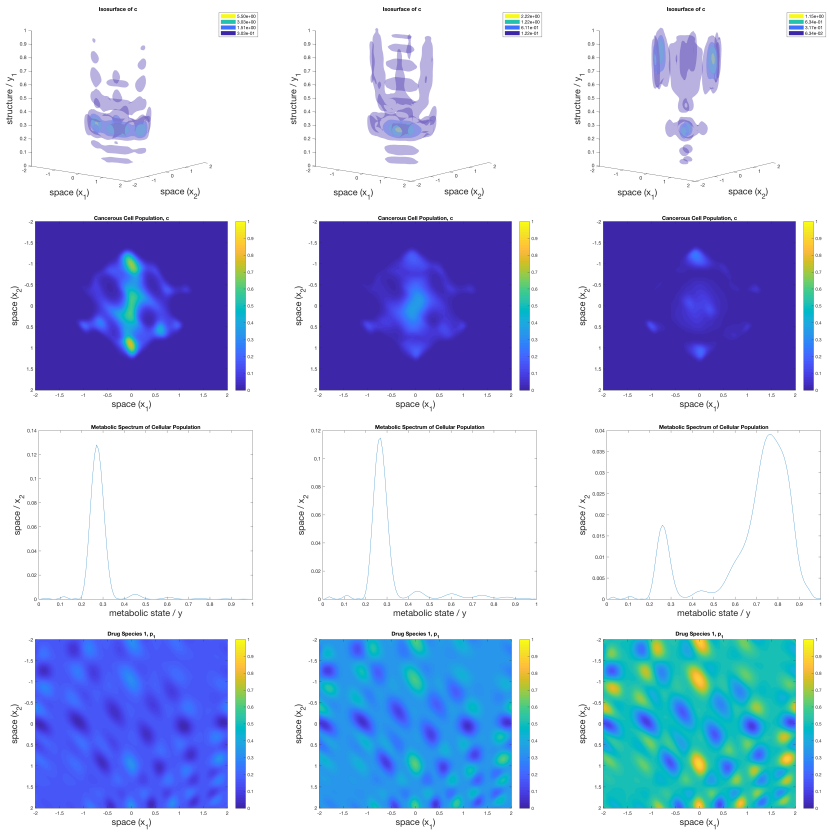

Figure 6.4: Results of the numerical simulations for the phenotypically evolving tumour model, using pseudo-spectral Chebyshev polynomial methods, are given. Panels displaying (*top*) the structured cellular population with space across the lower plane and mutational state given along the vertical axis; (*middle*) the spatial cellular distribution; and (*bottom*) the ECNE density, where ipilimumab treatment is given at $t = 40$ and BRAFi treatment is given at $t = 100$, for time points $t \in \{90, 100, 110\}$ are shown.

by the order 20 Chebyshev approximation of a Gaussian distribution across the spatial and structural domains, centred around $(0, 0, \frac{7}{20})$ as in [160]. Results of numerical simulations are displayed in three forms: The first displays higher dimensional variables, such as the IFN producer cells, as a 3-dimensional isosurface where space is given along the lower plane and the metabolic state (y) value is given along the vertical axis. Yellow isosurfaces indicate regions of maximal values for the cellular population, whilst blue isosurfaces indicate regions of $(1/100)^{\text{th}}$ the maximal value, at any given time point. The second

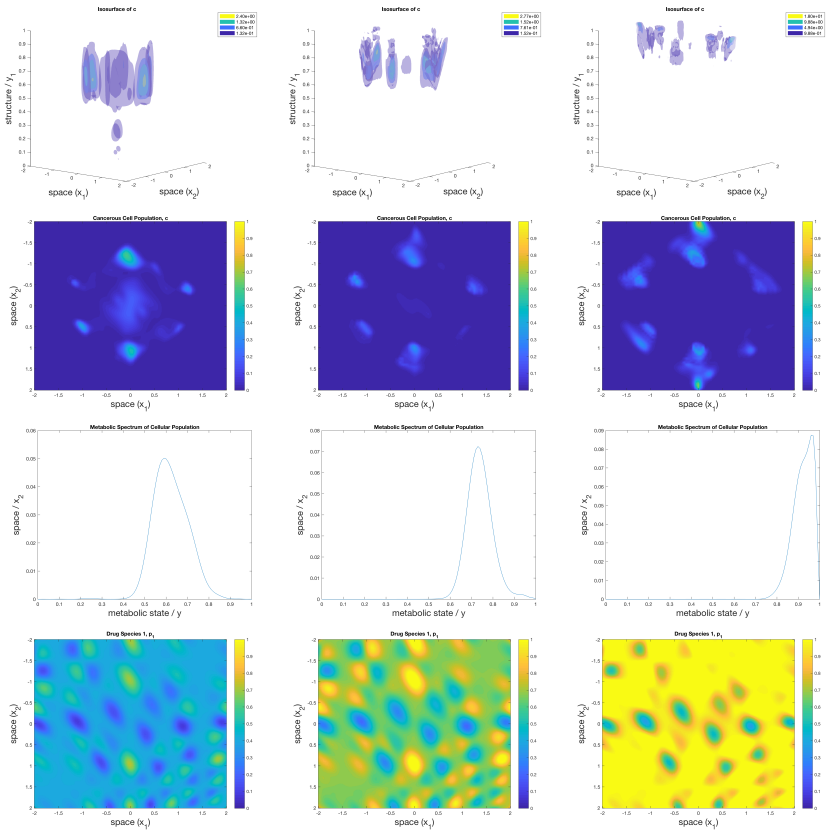

Figure 6.5: Results of the numerical simulations for the phenotypically evolving tumour model, using pseudo-spectral Chebyshev polynomial methods, are given. Panels displaying (*top*) the structured cellular population with space across the lower plane and mutational state given along the vertical axis; (*middle*) the spatial cellular distribution; and (*bottom*) the ECNE density, where ipilimumab treatment is given at $t = 40$ and BRAFi treatment is given at $t = 100$, for time points $t \in \{120, 150, 180\}$ are shown.

represents a spatial distribution of quantities of cells, or drug molecules, as a colour-mapping on a 2-dimensional axis between dark blue representing low values (near 0) and yellow representing high values (near 1). The third, and last, represents a quantitative probability density function (PDF) of the cell population in the metabolic dimension (y), for a higher-resolution depiction of the tumour's metabolic status.

The initial dynamics of the tumour cell population, free of drugs, displays a migration towards its genetically favourable metabolic state, $\omega = \frac{1}{4}$, but

quickly develops smaller but significant populations of cells at more disparate locations in the metabolic space (Fig. 6.3, 1^{st} *&* 3^{rd} *rows*). This appears to be as a direct result of the inhomogeneous of flux rates for populations spread across the metabolic space; where populations close to the genetically favourable metabolic position, ω, have relatively low flux rates in y whereas populations far from this positions may have a significant fold-difference in their flux rate. Given that the Chebyshev polynomials, by definition and necessarily, have real values at all locations in y, this, when combined with no-flux boundary conditions, artificially amplifies populations closer to the boundaries of the domain with respect to those nearer to ω.

After an initial tumour growth period, we applied targeted BRAFi + MEKi treatment to the tumour at $t = 80$, resulting in a decline in the tumour population over the time period $t \in [90, 120)$ (Fig. 6.4). In the meantime, small oxphos subpopulations, generated prior to treatment and who were decreasingly forced to compete for resources with faster growing glycolytic populations, were able to proliferate and became the more dominant population within the tumour (Fig. 6.4, 1^{st} *&* 3^{rd} *rows*), resulting in a phenotypic switch. It is worth remembering, at this stage that we assume that our targetted therapies are aimed at eradicating cancerous glycolytic cells, rather than oxphos cells, such that the dominant population within the tumour has rapidly become the more resistant subpopulation.

One clear benefit of this method is that one may run simulations in a much greater number of dimensions at a fraction of the memory costs, the major limitation of finite difference methods. On the other hand, the cancer cell populations generated using finite difference methods and representations display a slower rate in generating resistance, supported by *in vivo* experimentation [328, 296, 267]; follow, more strictly, the dynamics implied by the governing system of equations, which are occasionally violated by pseudo-spectral methods due to superordinate constraints; and allow for recapitulation of experiments that display clear resensitisation of a melanoma tumour to treatment [278]. Although the numerical methods had been rigorously tested on functions for which

known analytic solutions exist, displaying significant agreement, it is possible that these discrepancies reflect either genuine differences in resolution between these two approaches. It is also possible, however, that these discrepancies are manifestations of the fact that linear interpolation between finite grid points are a better approximation of a gaussian initial condition, given analytic agreement at grid points, than cosinusoidal interpolants of the same order.

6.3 A Novel Cellular Automata Framework for Cancer Cell Invasion and Micro-Environmental Interaction

Firstly, we choose to express the environmental system in standard Cartesian coordinates and the radial equations for the radial distance of the membrane from the nucleus. We then have that the standard coordinate conversion from polar to Cartesian is given by $x = \mathbf{r}\cos\theta$, $y = \mathbf{r}\sin\theta$ and we write $\mathbf{x} := [x, y]^T$. Therefore, let $\mathcal{I} = [0, T)$ be the time domain on which the system exists and $\mathcal{D} \subseteq \mathbb{R}^2$ be the spatial domain.

Secondly, let $\mathbf{r}(t, \theta)$, be a 2π periodic function such that $\mathbf{r}(t, \theta + 2n\pi) = \mathbf{r}(t, \theta)$, $\forall n \in \mathbb{N}$, and let it further define the perimeter of a cell with the brief notation $\mathbf{r} := \mathbf{r}(\theta) := \mathbf{r}(t, \theta)$. Let $\Theta = [0, 2\pi)$ be the domain for the nucleus-centred radius and let $\mathcal{R} \subseteq \mathbb{R}$ be the domain for the radius of the cell such that $\mathbf{r} : \mathcal{I} \times \Theta \to \mathcal{R}$. For cell i, we denote the radius $\mathbf{r}_i$. Finally, let $v : \mathcal{I} \times \mathcal{D} \to \mathbb{R}$ define the extracellular matrix (ECM) density and let $\mathbf{m} : \mathcal{I} \times \mathcal{D} \to \mathbb{R}^q$ define the q molecular species densities on the domain.

On Cell-Cell Bonding and Associated Field Equations

6.3.1 Development of a Novel Cellular Automata Model

We begin by reposing every cell-cell interaction problem as a generic problem between two cells situated a given distance d from one another and with both

of their respective centres at $y = 0$. First, let the vector $\mathbf{p}(c_i, c_j)$ be the vector in polar coordinates such that

$$||\mathbf{p}|| := \sqrt{(\bar{c}_{i,x} - \bar{c}_{j,x})^2 + (\bar{c}_{i,x} + \bar{c}_{j,x})^2}\,, \qquad \mathbf{p}_\theta := \tan^{-1}\left(\frac{\bar{c}_{j,y} - \bar{c}_{i,y}}{\bar{c}_{j,x} - \bar{c}_{i,x}}\right) \tag{6.22}$$

where $\bar{c}_i$ denotes the centre of mass for the cell c_i, then call this the pointing vector and perform the transforms $(r_j, \theta_j) \to \left(r_j, \theta_j - \mathbf{p}_\theta + \frac{\pi}{2}\right)$ and $(\bar{c}_{j,x}, \bar{c}_{j,y}) \to (0, ||\mathbf{p}||)$, in order to move cell j onto the x-axis and to rotate the cell such that the same are aligned as was the case prior to the coordinate transform.

Then, from simple algebraic reasoning, one has that the distance between any two points on the membranes of these cells, with respect to θ, is given by

$$d(\theta) = \sqrt{(c_{i,r}\cos(\theta) - c_{j,r}\cos(\theta))^2 + (c_{i,r}\sin(\theta) - c_{j,r}\sin(-\theta) + ||\mathbf{p}||)^2} \tag{6.23}$$

and this means that the contribution to a given radius can be calculated by the force at that point, multiplied by the appropriate elongation factor which is given by the trigonometric relation $\bar{d} = d\cos\left(\theta - \frac{\pi}{2}\right)$, where $\frac{\pi}{2}$ is a factor which accounts for the reorientation of the cells.

Let us now look at the attractive intercellular force, $F_A(d)$. There is evidence to suggest that, below some limiting distance, the negative charges on repeat 3 of α-actinin and positive charges on intercellular adhesion molecule (ICAM)-1 dominate the interaction. Above this distance, the contribution of the positive-positive interaction is increased between the acidic centre of the α-actinin domain and Lys acids on ICAM1 [52, 251]. We model this by introducing some constant imaginary distance, i, between the two membranes.

The repulsive Coulomb force, $F_R(d)$, emanates from the addition of pressure to the membrane reducing the spacing between membranous lipids, producing a restorative force. Therefore, we calculate the distance at which the centre of charge of the membrane sits, with respect to the cell radius. For a circle of uniform radius $r(\theta) = r$, the radial centre of charge is approximated by $\bar{r} \approx \frac{4}{3\pi}r$, which shall serve as a positioning of the internal charge.

We can then write the overall field equation as

$$F(d) = \frac{1}{(d-d_A)^2+1} - \frac{1}{\left(d+\frac{4}{3\pi}\right)^2+\frac{1}{Q_s}} \tag{6.24}$$

where Q_s gives the ratio of charge separation for the protein complex, with respect to the separation of the charges in the lipid bilayer of the melanoma cells themselves. Biological precedents for this force distribution exists, with physical measurement being taken between staphylococcus aureus cells and biofilms [153]

On Cell-ECM Bonding and Associated Field Equations

The dissociation rate of one protein from another is widely considered [180, 46] to have the form $k = k_0 \exp(fx/k_bT)$, where k_0 is the zero rate of dissociation, f is the force applied in separating the proteins, x is the distance of separation, and k_BT gives the thermal energy of the system. Now, consider an arbitrary force that brings the proteins of the cell and the ECM together, then their normalised association rate, $\bar{k}$, would be given by $\bar{k} = [1 - (k_0/K)\exp(-fx/k_bT)]$ where the maximal rate of dissociation is given by K.

The force on the cell from the ECM is proportional to the density of the ECM itself and therefore we write $|F_c^+| = \bar{k}v$. We also have that the direction of association is from lower to higher densities of protein, which follows directly from their proportionality. As for the force equation for pressure, we assume the field generated scales with the square of the ECM density, and acts in the opposite direction. Therefore, we can write the entirety of the force equation as

$$|F| = \left[1 - \frac{k_0}{K}\exp\left(-\frac{fx}{k_bT}\right)\right] v - k_P v^2\,, \qquad \hat{F} = \tan^{-1}\left(\frac{\partial v}{\partial y}\frac{\partial x}{\partial v}\right)\,. \tag{6.25}$$

Molecular Species on the Boundary — Chemotaxis

The chemotaxis of a cell is dependent on the molecular species concentration $m(t,x)$ on the immediate boundary of the cell, since it is not endocytosis but simply sensory response that is necessary for this stimulus.

Using the standard definition of a line integral, we can write the line integral of the molecular species concentration $m_i(x, y)$ over the boundary of the cell and with surface element σ as

$$I = \int\limits_{\partial\Omega_i} m_i(\bar{x})\, d\sigma\,, \qquad d\sigma = \sqrt{\mathbf{r}(\theta)^2 \sin^2\theta + \mathbf{r}(\theta)^2 \cos^2\theta}\, d\theta = \mathbf{r}(\theta)\, d\theta\,. \tag{6.26}$$

It is then trivial to rewrite the line integral with respect to the individual cell and a specific molecular species, $m_j(t, x)$, to obtain the overall molecular species concentration on the boundary, and the bias of such a concentration.

Taking the biased molecular concentrations and extract from them the optimal direction, in terms of chemical attractants, the mean biased chemotaxis is be given by

$$\overset{\circ}{\chi} = \frac{1}{\sum\limits_{j=1}^{q} \chi_{m_j}} \begin{pmatrix} \chi_{m_1} \\ \vdots \\ \chi_{m_q} \end{pmatrix} \cdot \begin{pmatrix} \tan^{-1}\left(\frac{\int_\Theta m_1(\mathbf{r}(\theta)\cos\theta, \mathbf{r}(\theta)\sin\theta)\cos\theta\, d\theta}{\int_\Theta m_1(\mathbf{r}(\theta)\cos\theta, \mathbf{r}(\theta)\sin\theta)\sin\theta\, d\theta}\right) \\ \vdots \\ \tan^{-1}\left(\frac{\int_\Theta m_q(\mathbf{r}(\theta)\cos\theta, \mathbf{r}(\theta)\sin\theta)\cos\theta\, d\theta}{\int_\Theta m_q(\mathbf{r}(\theta)\cos\theta, \mathbf{r}(\theta)\sin\theta)\sin\theta\, d\theta}\right) \end{pmatrix} \tag{6.27}$$

where the chemotactic constant for any given molecular species $m_j(t, x)$ is given by χ_{m_j}.

Temporal Changes in Intracellular Properties

We must, further, have a means by which the cell's interior can reposition itself with respect to the environment. A sensible candidate for this movement can simply be taken as a result of the net forces which move the membrane of the cell having direct and proportionate effect on the position of the nucleus such that we can write

$$\frac{\partial x_1}{\partial t} = \int\limits_{[0,2\pi)} \frac{\partial}{\partial t}\mathbf{r}(\tilde{\theta}) \cdot \cos\tilde{\theta}\, d\tilde{\theta}\,, \qquad \frac{\partial x_2}{\partial t} = \int\limits_{[0,2\pi)} \frac{\partial}{\partial t}\mathbf{r}(\tilde{\theta}) \cdot \sin\tilde{\theta}\, d\tilde{\theta}\,, \tag{6.28}$$

reflecting a mechanical movement of the nucleus with the membrane.

Consider the overall change in the polarisation, ϕ, of the cell and that the cell is capable of rearranging its internal infrastructure in response to the attraction of chemicals and in order to maximise its potential for utilising the byproducts of this infrastructure. Then we assume that the cell will attempt to reorient itself to the optimal direction

$$\bar{\phi} = \frac{1}{\omega_F+\omega_\chi}\left(\omega_F \tan^{-1}\left(\frac{\partial x_2}{\partial t}\frac{\partial t}{\partial x_1}\right) + \omega_\chi \overset{\circ}{\chi}\right), \tag{6.29}$$

given the weightings ω_F, ω_χ for the force and chemotactically mediated polarity preferences, respectively.

Then consider that the cell will have more success in achieving small angular reorientation than in large angular reorientations. Therefore, we make the assumption that the polarisation may only change through small changes around the perimeter of the cell and that $\ln(\partial\phi/\partial t) \propto -\left(\bar{\phi}-\phi\right)^2$. We write that the change in polarisation can be given by

$$\frac{\partial\phi}{\partial t} = \exp\left[-\left(\left(\frac{\partial x_1}{\partial t}\right)^2 + \left(\frac{\partial x_2}{\partial t}\right)^2\right)^{-\frac{1}{2}} \cdot \left(\bar{\phi}-\phi\right)^2\right]. \tag{6.30}$$

6.3.2 Numerical Aspects of Cellular Automata Modelling

Movement of the nucleus: A simple translation method

The current methodology for reassignment, or mathematical translation, of the position of a radial function $\mathbf{r}(\theta)$ to a differing position is given as follows

$$\mathbf{r}_1 = \sqrt{\mathbf{r}^2+\mathbf{r}_0^2+2\mathbf{r}\mathbf{r}_0\cos(\theta_0-\theta)}, \qquad \theta_1 = \cos^{-1}\left(\frac{\mathbf{r}\cos\theta+\mathbf{r}_0\cos\theta_0}{\mathbf{r}_1}\right), \tag{6.31}$$

where $(\mathbf{r},\theta)$ gives the original solution in polar coordinates; $(\mathbf{r}_0,\theta_0)$ gives the magnitude and direction of the translation; and $(\mathbf{r}_1,\theta_1)$ gives the translated set of solutions. Then observe the following simplification:

Theorem 6.3.1. *Let the space $\mathcal{N} \subseteq \mathbb{R}^2$ define the cartesian plane on which the nucleus of a given 2-dimensional cell is defined, and the space $\mathcal{Q} \subseteq \mathbb{R}\times[0,2\pi)$*

define the polar domain centred at $(x, y) \in \mathcal{N}$ on which the membrane of the cell is defined. Then we can define a cell as some $[(x_0, y_0), (\mathbf{r}_0(\theta_0), \theta_0)] \in \mathcal{N} \times \mathcal{Q}$, where $\mathbf{r}(\theta) : [0, 2\pi) \to \mathbb{R}$ is the radial membrane distance as measured from the centre of the cell. Define further a formula for translation of the nucleus of this cell, given by $(x, y) \to (x + \xi, y)$, where the membrane of the cell retains its position in the cartesian space and dependence on θ_0, given by

$$\mathbf{r}_1(\theta_0) = \mathbf{r}_0(\theta_0) - \xi \cos(\theta_0)\,.$$

Then the error for this translation is given by

$$E_r \leq \left(1 - \sin\left(\frac{1}{2}\cos^{-1}\left(\frac{-\mathbf{r}(\hat{\theta}) + \sqrt{\mathbf{r}(\hat{\theta})^2 + 8\xi^2}}{4\xi}\right)\right)\right)\left(\frac{-\mathbf{r}(\hat{\theta}) + \sqrt{\mathbf{r}(\hat{\theta})^2 + 8\xi^2}}{4\xi}\right)\xi,$$

where $\mathbf{r}(\hat{\theta}) = \max\limits_{\theta \in [0,2\pi)} \mathbf{r}(\theta)$.

Proof. Recall the coordinate relations given by $x_0 = \mathbf{r}(\theta)\cos\theta$, $y_0 = \mathbf{r}(\theta)\sin\theta$ and the counter-relation $\mathbf{r}(\theta)^2 = x^2 + y^2$. Consider, further, the translation in only the cartesian x-direction, of magnitude ξ, corresponding to a linear progression in an aligned set of polar axes given by $x_1 = \mathbf{r}(\theta)\cos\theta - \xi$, $y_1 = \mathbf{r}(\theta)\sin\theta$.

Using the translation approximation $\mathbf{r}_1(\theta_0) = \mathbf{r}_0(\theta_0) - \xi\cos(\theta_0)$ and allowing that the maximal error for this approximation is given at $\theta_0 = \hat{\theta}$, defined by $\mathbf{r}(\hat{\theta}) := \max\limits_{\theta \in [0,2\pi)} \mathbf{r}(\theta)$, the maximal error is given by

$$\bar{E} = \underbrace{(\mathbf{r}(\hat{\theta}) + \xi\cos\hat{\theta})\sin\hat{\theta}}_{\text{approximation}} - \underbrace{(\mathbf{r}(\hat{\theta})^2 - (\mathbf{r}(\hat{\theta})\sin\hat{\theta} - \xi)^2)^{\frac{1}{2}}}_{\text{absolute calculation}}\,. \tag{6.32}$$

We can then find this maximum at $\hat{\theta}$ by considering the derivative of the term for the translation approximation, which simplifies to

$$\tilde{E}' = \mathbf{r}(\hat{\theta})\cos\hat{\theta} + \xi\cos 2\hat{\theta} = 0 \tag{6.33}$$

and by further using the trigonometric relation $\cos 2\theta = 2\cos^2\theta - 1$ we can write

$$\mathbf{r}(\hat{\theta})\cos\hat{\theta} + 2\xi\cos^2\hat{\theta} - \xi = 0 \tag{6.34}$$

who is a quadratic in $\cos\hat{\theta}$, such that the solution for $\hat{\theta}$ is given by

$$\cos\hat{\theta} = \frac{-\mathbf{r}(\hat{\theta}) \pm \sqrt{\mathbf{r}(\hat{\theta})^2 + 8\xi^2}}{4\xi} \quad \Longrightarrow \quad \hat{\theta} = \cos^{-1}\left(\frac{-\mathbf{r}(\hat{\theta}) + \sqrt{\mathbf{r}(\hat{\theta})^2 + 8\xi^2}}{4\xi}\right). \tag{6.35}$$

Substituting this into the original equation, and recognising that the negative term in the error is minimised at $x = \xi$, one has that the maximal error is written

$$\bar{E} = \mathbf{r}\left(\cos^{-1}\left(\frac{-\mathbf{r}(\hat{\theta}) + \sqrt{\mathbf{r}(\hat{\theta})^2 + 8\xi^2}}{4\xi}\right)\right) + \left(\frac{-\mathbf{r}(\hat{\theta}) + \sqrt{\mathbf{r}(\hat{\theta})^2 + 8\xi^2}}{4\xi}\right)\xi - \mathbf{r}(\hat{\theta})\,. \tag{6.36}$$

Then the precise value of $y(\hat{\tilde{\theta}})$ is given at $y(\hat{\tilde{\theta}}) = \mathbf{r}(\frac{1}{2}\hat{\theta})\sin(\frac{1}{2}\hat{\theta})$, such that the maximal error can be given precisely by

$$\bar{E} = \left(1 - \sin\left(\tfrac{1}{2}\cos^{-1}\left(\frac{-\mathbf{r}(\hat{\theta}) + \sqrt{\mathbf{r}(\hat{\theta})^2 + 8\xi^2}}{4\xi}\right)\right)\right)\left(\frac{-\mathbf{r}(\hat{\theta}) + \sqrt{\mathbf{r}(\hat{\theta})^2 + 8\xi^2}}{4\xi}\right)\xi\,. \tag{6.37}$$

□

In this case, using Theorem 6.3.1, the error for values of $\xi \leq 0.1$ is such that $E_r < \frac{1}{2}\xi^2$ and ξ is proportional with the time step such that $\xi \propto \delta\tau$. Thus, for sufficiently small time steps one is able to discern that the error is sufficiently small, and non-cumulative, and that this may be acceptable within the bounds of expected numerical error.

Numerical approximations of line integrals

We begin by recalling that the analytic, single-variable line integral for a radial function is given by $I = \int_{\mathcal{S}} r(\theta)\, d\sigma$, where $\mathcal{S}$ is used to denote the surface of the cell and σ is some surface element on $\mathcal{S}$. Discretisation of this system leads us to derive a metric on the basis of maximal efficacy on the discrete radial

interval, $(\tilde{\theta}, \tilde{\theta} + \delta\theta)$. Begin by considering the true arc length in this portion of the radius of a given cell and notice that this can be approximated by sketching a line between the two extreme radii, $r(\tilde{\theta}), r(\tilde{\theta} + \delta\theta)$.

Theorem 6.3.2. *Let Ω be the internal cell space of a cell whose radius is is given by $\mathbf{r} : \mathcal{I} \times \Theta \to \mathcal{R}$. Further, let the perimeter length of the cell be given by $I_c = \int\limits_{\partial\Omega} \mathbf{r}(t, \theta)\, d\sigma_{\partial\Omega}$, where $\sigma_{\partial\Omega}$ is a surface element on $\partial\Omega$, and let $\widetilde{I}_c$ be given by the numerical approximation*

$$\widetilde{I} = \sum_{\tilde{\theta} \in \{0, \delta\theta, \ldots, 2\pi - \delta\theta\}} \delta\theta \cdot \left(\left(\min(r(\tilde{\theta}), r(\tilde{\theta} + \delta\theta)) \delta\theta \right)^2 + \left| r(\tilde{\theta}) - r(\tilde{\theta} + \delta\theta) \right|^2 \right)^{\frac{1}{2}} .$$

Then, for a discrete step length, h, the error, E_L, for this approximation is of order $\mathcal{O}(h^2)$ and is given explicitly by

$$E_L \leq \int\limits_{\partial\Omega} \left[\frac{h^2}{2} \frac{\partial^2}{\partial\theta^2} \mathbf{r}(\theta_i + \eta) + \mathcal{O}(h^3) \right] d\sigma_{\partial\Omega}$$

Proof. Begin by noticing that our approximation is given precisely by the length of the line connecting the points $\mathbf{r}(\theta_i)$ and $\mathbf{r}(\theta_i + h)$ such that

$$\tilde{\mathbf{r}}(\eta) = \tfrac{\mathbf{r}(\theta_i + h) - \mathbf{r}(\theta_i)}{h} \eta + \mathbf{r}(\theta_i) \tag{6.38}$$

for $\eta \in (0, h)$ and centred around the point θ_i and where we are interested in values in the interval $(\theta_i, \theta_i + h)$.

Further, write the analytic function as the Taylor series

$$I_c(\theta_i + \eta) \approx \quad \mathbf{r}\,(\theta_i + \eta) + \eta \tfrac{\partial}{\partial\theta} \mathbf{r}(\theta_i + \eta) + \tfrac{\eta^2}{2} \tfrac{\partial^2}{\partial\theta^2} \mathbf{r}(\theta_i + \eta) + \mathcal{O}(\eta^3) \tag{6.39}$$

then from the intermediate value theorem, we can choose η such that it satisfies

$$\tfrac{\partial}{\partial\theta} \mathbf{r}(\theta_i + \eta) = \tfrac{\mathbf{r}(\theta_i + h) - \mathbf{r}(\theta_i)}{h} . \tag{6.40}$$

Next, we take the difference between the two line integrals to find the analytic

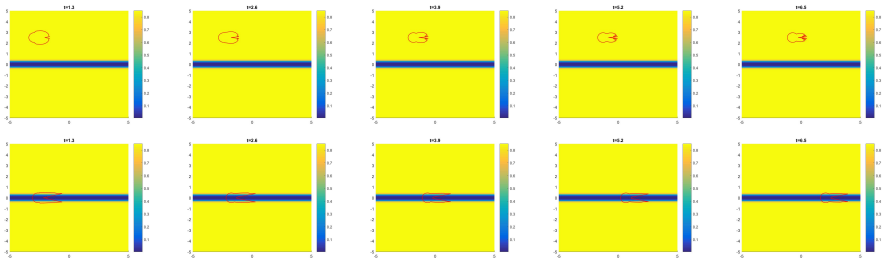

$t = 2$ $t = 4$ $t = 6$ $t = 8$ $t = 10$

Figure 6.6: Snapshots of simulated cells migrating through the ECM for the initial condition for the nucleus of the cell given within the ECM itself (*top*) or within an artificial microtrack (*bottom*) at times $t' \in \{2, 4, 6, 8, 10\}$.

error in our approximation

$$E_L = \int\limits_{\partial\Omega} \left[\mathbf{r}\left(\theta_i + \eta\right) + \eta \frac{\partial}{\partial\theta}\mathbf{r}(\theta_i + \eta) + \frac{\eta^2}{2}\frac{\partial^2}{\partial\theta^2}\mathbf{r}(\theta_i + \eta) + \mathcal{O}(h^3) \right] d\sigma_{\partial\Omega} - \int\limits_{\partial\Omega} \left[\frac{\mathbf{r}(\theta_i + h) - \mathbf{r}(\theta_i)}{h}\eta + \mathbf{r}(\theta_i) \right] d\sigma_{\partial\Omega} \tag{6.41}$$

and since the linear terms for the Taylor expansion and the approximation (6.40) describes straight lines between two equidistant points, their magnitudes are equal. Therefore, considering that we have $h \geq \eta$, we obtain the maximal error bound

$$E_L \leq \int\limits_{\partial\Omega} \left[\frac{h^2}{2}\frac{\partial^2}{\partial\theta^2}\mathbf{r}(\theta_i + \eta) + \mathcal{O}(h^3) \right] d\sigma_{\partial\Omega}\,. \tag{6.42}$$

□

6.3.3 Results & Conclusions

In order to attempt the sorting experiment, we began with high affinity cells as the outer cells of a cellular Bravais lattice and low affinity cells in the centre, repeating the results of Garner *et al.* [132] (*data not shown*), which provided some base validation of the model. Counterintuitively, cells who have high cell-cell binding coefficients quickly separate into a web like structure whereas low binding constant scenarios tend to instead form a 2-dimensional hexagonal

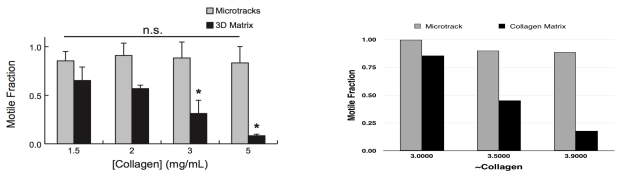

Figure 6.7: Results of cell microtrack experiments from the biological literature [51] (*left*) and from the numerical simulations (*right*).

lattice.

In our second experiment we wanted a testable scenario to measure the migration of simulated cancerous cells through the ECM. For this we chose the scenario of microtracks since this presents to unique and measurably distinguishable scenarios in which to place our cells. We endow each with a polarisation of $\theta_p = 0$ and with the initial conditions $r^0(\theta) = \text{const.}$ such that they are represented as circular cells in the 2D domain.

The first thing to notice is that although the membranes of cells within the microtracks start partially submerged in the ECM, they retract their membranes and conform entirely to the width of the microtrack (Fig. 6.6 *bottom*), as in the biological case [51]. Moreover, elongation in the microtrack cell is marked compared with those who remain within the ECM (Fig. 6.6).

Travel through the ECM also appears to be more conducive to the extension of lamellipodia (Fig. 6.6 *top*), whereas travel through the microtrack appears to be more conducive to the extension of longer, thinner, and more directive filopodia (Fig. 6.6 *bottom*). Not only this but the heterogeneity of the environment, alone, is sufficient to give rise to differing rates of travel within or without microtracks. Moreover, for increasing ECM density, one observes a decrease in velocity for cells within the ECM but no such changes in velocity for those within the microtrack (Fig. 6.7).

Our final experiment involves the interaction between two different metabolic phenotypes of cell: Highly proliferative, non-invasive ($\text{MITF}^{\text{HIGH}}$) cells and highly invasive, non-proliferative (MITF^{LOW}) cells. We begin with a heterogeneous distribution of v_1 and $v_2(t, x) = 0$. $\text{MITF}^{\text{HIGH}}$ cells are attracted to

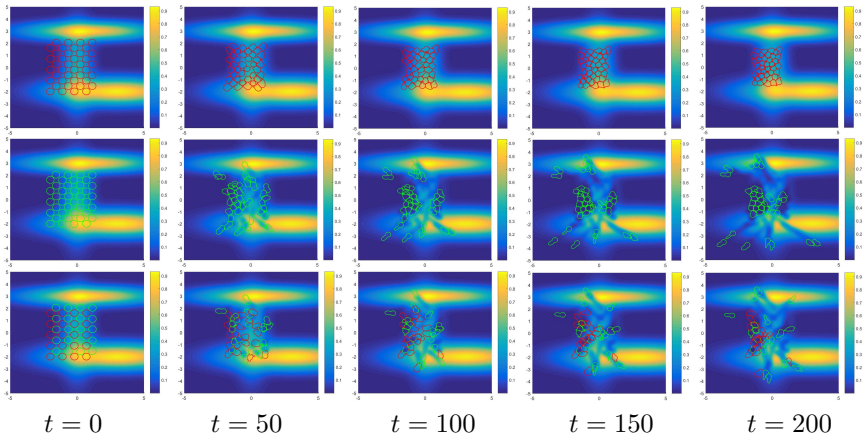

Figure 6.8: Experimental *in silico* injection of *red* $\text{MITF}^{\text{HIGH}}$ cells (*top*); *green* MITF^{LOW} cells (*middle*); or both cell types (*bottom*) onto a heterogeneous density function for v_1 coloured *blue* through *yellow*, at time points $t \in \{0, 50, 100, 150, 200\}$.

v_2 but not v_1 and MITF^{LOW} cells are attracted to v_1 but not v_2 and convert $v_1 \to v_2$ [58].

Injection of $\text{MITF}^{\text{HIGH}}$ cells, alone (and in the absence of mitosis), reveals and extremely non-invasive behaviour with dominating cell-cell adhesive dynamics (Fig. 6.8 *top*). Injection of MITF^{LOW} cells, alone, one observes a highly invasive dynamic (Fig. 6.8 *middle*). Co-injection of the two disparate populations displays a mixture of behaviours between cell-cell binding and cell-ECM motility and one observes a co-invasion of $\text{MITF}^{\text{HIGH}}$ cells in the wake of invading MITF^{LOW} cells (Fig. 6.8 *bottom*). Again, one can identify the production of filopodia by cells who have elongated upon the heterogeneous substrate for invasion (Fig. 6.8).

We have derived a modelling framework to solve problems which previous frameworks [132, 322] were unable to approach. Errors for the numerical implementation of estimates for these models are small and, as such, allow one to be confident in their predictive power. This novel modelling framework has also shown practical promise; recreating the cell sorting experiment before predicting the outcomes of biological microtrack [51] and co-invasion [58] experiments. Moreover, this model may explain emergent phenomena, such as cellular elon-

gation and filo- or lamellipodia extension, could be explained through simple physical interactions between the cellular membrane and the homo- or heterogeneous ECM. Future work should aim to extend this model through the addition of microscale boundary interactions and look to explore more complex biological phenomena. This cellular automata model could also be useful in other contexts where one requires a nuanced interaction between automata and their environment.

Chapter 7

Conclusion

Heterogeneity invariably leads to the vast unpredictability of biological systems and, yet, remains in need of formal methods whose generality is capable of fully exploring the domains of this variation – whether this heterogeneity be temporal, spatial, or structural. The major focus of this investigation was to produce and expound new modelling methodologies, particular to the circumstances in which they were required, capable of grappling with the dynamic complexities of population or cell biology and oncology. We have rigorously explored the possibilities of modelling biological systems in higher-dimensions, although much remains to be explored, and have sought to expand this method as far as was necessary in our particular case and beyond. Through this investigation, it has also been necessary to explore novel methods of generating solutions to such systems and conducting analysis but many important results have been produced on the basis of the organic heterogeneity of the systems considered.

7.1 Particular Conclusions

We begin from the assumptions of the continuity equation to establish a methodology capable of capturing the complex biological dynamics of cell-based systems. After deriving a novel mathematical framework for the generation of

systems of PDEs appropriate for application to biological systems with dynamics in time; space; surface receptors; binding ligands; and intracellular metabolic pathways, we have proceeded to demonstrate the vast potential for the application of these framework across various scenarios [158, 161, 160]. These applications have spanned the fields of oncology, pharmacodynamics, immunology, evolutionary ecology, and cellular biology to reach general conclusions about the behaviour of biological systems as well as precise hypotheses concerning the nature of the system in question. As such, we compare and contrast several such conclusions, in order to clarify their contribution to the work as a whole.

From first principles, we derived in Chapter 1 a novel higher-dimensional mathematical framework, for the specific purpose of scientifically scrutinising biological systems, and generated source terms for this framework specific to continuous population-level mitotic events, accounting for cell cycle dynamics. We then went on to apply these source terms in Section 2.2, Section 4.2 and Section 5.2.1, demonstrating the applicability of these functions to the natural sciences. We also provide a clarification of the numerical scheme that we use through the generation of numerical solutions to the problems set out in Chapter 2 through Chapter 5 and provide a novel theorem for the stability of the non-local, central difference, gradient operator in linear analysis. These methods and theorems are applicable not only within the current framework but across all numerical schemes currently utilising the finite difference approach to approximating solutions to nonlocal PDEs, making their reach extensive.

The first biological paradigm that we analyse is then an application of the predecessor to this framework, given in Section 2.2, and involves the urokinase plasminogen activator (uPA) system of cancer invasion. Herein, we present the first numerical solutions of their kind in higher-dimensional biology and demonstrate the ability to generate such frameworks in coming applications. These results also show the propensity for structurally heterogeneous models to generate spatial heterogeneities in concentration time profiles. Here we also reflect that the discontinuities produced by the system given in Section 2.2 have since been rectified by the source term given in Section 1.3.1 [161].

Previously, both spatial [248, 82, 333, 203] and structural [212] models had been used to investigate the interaction between anti-cancer drugs and a given cancer cell population but we provide the first spatio-structural model of this interaction and provide a basis for the importance of its consideration. In the first instance (Section 3.2), we generated a theoretical drug resistance model on the basis of observations in the literature that targeted therapies (namely BRAF and MEK inhibitors) tend to target genes upstream of those coding for glycolytic enzymes. This allowed us to describe and explain the process of an initial resistance episode and, posteriorly, the partial resensitisation to those drugs, in a spatially heterogeneous tumour. Following this, in Section 3.3 we apply the same model to the case of an *in vivo* murine tumour, for which we obtained temporally resolved single-cell RNA-sequencing data received from Dr. Jean-Christophe Marine [278]. In this instance we were able to couple the population level RNA-seq dynamics to a spatial tumour model in order to generate a hypothesis on the spatial organisation of the biologically heterogeneous tumour; namely, that highly resistant cells on the outside of the tumour would protect those sensitive cells within the tumour, allowing even a partially sensitive tumour to continue to grow unimpeded by treatment.

The application of this model to both the theoretical model-driven situation and, alternatively, the single cell RNA-seq data-driven situation poses an interesting comparative. There is no direct comparison to be drawn in this case, of course, since the biological scenarios considered are disparate but comparisons may be drawn as to the approach and success of these approaches. Firstly, the success of each is roughly equal, in that the theoretical models generate solutions which possess at least persuasive power over the biological community, whist the data-driven models were capable of generating sensible and testable hypotheses for a particularly complex, *in vivo* system. In terms of laboriousness, however, the theoretical model presents as far more elegant approach and required far less human interpretative effort in comparison to the single cell RNA-seq based models. As time goes on, however, perhaps computational resources will increasingly be allocated to such tasks and labour will be reserved

for the interpretation of model outputs.

The ways in which cancer cells evolve and behave are not well known and are frequently the subject of controversy in biology; therefore, in order to conduct a fundamental investigation using our framework, in Chapter 4 we chose a biological problem in immunology for which the parameters were better defined. The particular immunological circumstance that that we wished to answer to was the seemingly paradoxical existence of both high and low affinity variants of the interferon (IFN) molecule – a ligand used for intercellular communication upon infection with a virus. Firstly, we found that whilst high affinity molecules were good at inducing and sustaining a local response to the virus, low affinity molecules were poor at achieving this but better equipped to travel through the biological system and prime farther molecules for the incoming viral infection. This novel hypothesis answers this pertinent question directly and also reveals a role for this type of mathematical modelling in systems where receptors, binding ligands, and genetic/metabolic responses are simultaneously orchestrating a particular behaviour.

Answering a less fundamental – although equally prescient – question, we wanted to use our modelling technique to discover how these two ligands would come into existence, in the first instance. Whenever ontology is invoked in biology, evolution will generally feature in the response. We, therefore, investigated the influence of an additional low affinity ligand, to a system with only high or medium affinity molecules, in the response to a localised viral inflection. We found that systems with additional low affinity ligands would respond significantly faster than those without and, in an analogous case to that found in humans, systems with 1 high and 10 medium affinity ligands increased their ability to reduce a viral load by $\sim 23\%$ in the presence of 2 additional low affinity ligands. Low affinity ligands, then, may grant the host of a viral infection a significant survival advantage over their counterparts without such a ligand. This was in line with empirical studies which found that the *Rosettus ægyptiacus* bat, who has significantly greater numbers of IFN species than his cousins, is immune to a particularly lethal mammalian virus – namely the Marburg virus.

In order to then investigate whether factors that impact survival are solely the arbitrators of evolutionary progress, in Chapter 5 we study a ecosystem in which populations may evolve through trait spaces for survival, sexual selectivity, and sexually attractive elaboration. Within the mathematical analysis of this system, wherein selective females over-select for elaborate males and elaborate males have a predatory survival disadvantage, we present new approaches to obtaining analytic solutions to systems whose spatial dynamics are not based on flux in the unstructured, discrete-structured, and quasi-continuous cases. These methods may be useful in other cases where source terms are formed of nested integral operations. We establish the validity of our model by observing that completely advantageous traits are always selected for, before finding that, even in the case where male elaboration is costly to survival, evolution will sexually select for male elaborations; indicating that beauty is an evolutionary end in itself. These models also support a hypothesis that selection for a disadvantageous trait will aid selection, in the non-expressive children, for orthogonal advantageous traits, in certain particular cases.

The main scientific difference between the studies conducted in oncology, immunology, and evolution is the abundance of evidence for each. In the presence of the overwhelming evidence that graces the field of evolutionary biology, it is possible to rigorously test hypotheses against the natural world, since any modelling inconsistencies will necessarily come into contradiction with this natural order of things. This has been the case with the handicap and honest signalling principles, for example, which have been criticised for their lack of natural adherence [310, 311]. In the case of immunology, their exists a wealth of knowledge [40, 177, 111] around the mechanisms of action pertaining to this system but the experiments necessary to test or validate our spatially dependent hypotheses are not yet possible. The oncological scenarios that we attempted to scrutinise, on the other hand, are neither well-defined, in terms of the essential mechanics involved, nor are they easily tractable or testable, at least in the *in vivo* context for which they are most relevant. We find, therefore, that our modelling in evolution is far more verifiable than either of our other studies, al-

though certain degrees of validation still exist for each of our other approaches. One such method of validation for the oncological model is to carry out cross-sectional rainbow cell barcoding [16] on *in vivo* obtained tumour sections, as is currently being carried out on the tumours used by Rambow *et al.* [278], where a comparison will clarify the validity of our model-based conclusions.

One of the major practical limitations of generating solutions for models, built with the framework used throughout this paper, is that the discrete finite difference tensors (described in Section 3.2) require large dedications of accessible memory and increasingly long processing times. This limited our ability to increase the number of dimensions beyond 5 (or 4 plus time) and, in order to remedy this, we investigated the use of spectral methods. In Chapter 6 we expound a pseudo-spectral Chebyshev polynomial-based method for the generation of solutions to higher-dimensional problems. We apply this to our theoretical oncological model [160], presented first in section 3.2, and find that the pseudo-spectral representation of the tumour is not capable of showing sufficient sensitivity to treatment so as to elicit a response to any conceivable drug species. It was unclear as to whether this insufficiency stemmed from the implementation or from the methodology itself but extensive testing was carried out on the individual operations within the model to attempt to validate their behaviour.

The comparison between those solutions generated through finite difference schemes and through pseudo-spectral Chebyshev polynomial-based methods makes for a discursive interaction between discreteness and continuity. The original intention for generating this novel cancer resistance model was to explore the biological problem of cancer within a more continuous representation and, yet, the extension to the fully continuous paradigm of polynomials has resulted in the dissolution of the very phenomenon that we had hoped to reproduce. It seems that, in this case, the errors in using the polynomial-based methods stem from the inherent discreteness of the natural system, on the scale at which we consider the problem. This is not always true and, in cases where the indivisible unit of the system (the cell in the case of tumour population

modelling) is insignificant with respect to the domain over which the problem is considered, poynomial-based methods may be more appropriate. For example, Chebyshev polynomials are commonly used in the simulation of solutions to fluid dynamical problems but, in this case, the scale of the domain is usually several billion orders greater than the order of the individual fluid molecules, themselves. Perhaps this realisation of scales is a factor which must be more quantitatively considered in the choice of numerical approach.

As with the limitation in the number of accessible dimensions, one particular biological problem whose mathematical representation remained elusive was that of cancer cell co-invasion; where formerly non-invasive cancer cells ($\text{MITF}^{\text{HIGH}}$) would co-invade the stroma in the presence of naturally invasive cancer (MITF^{LOW}) cells. After attempting to solve this problem using a spatio-temporal PDE approach, and failing to establish a system parameterisation with sufficient biological realism and inter-situational heterogeneity, in Chapter 6 we build a novel agent-based cellular automata approach to solving this problem. In solving this problem, we derived a generic framework capable of accounting for not only the intra-cellular mechanics but also the dynamics at the cellular membrane and the interactions of this membrane with the cellular environment. In order to simulate cells using this framework, we develop several numerical error bound theorems for mathematical substitutions designed to computationally simplify simulations. We found that this model was able to recapitulate the results of experiments wherein cells migrate through artificial ECM microtracks [51] and the co-injection experiments of Chapman *et al.* [58].

Although spatial heterogeneity has come under recent focus within the biological community, our modelling approaches and results show that a far greater emphasis deserves to be placed on correlated changes across time, space, and bio-dynamics of these complicated systems. We have shown that coupling the dynamics of resistance to the spatial dynamics of drug infiltration allows one to understand the mechanisms, by which resistance develops and sustains itself, and make predictions concerning the behaviour of the system during and after the development of resistance. Using the same techniques in immunology

and evolution, we have managed to develop sensible hypotheses interesting to both theoretical and experimental biologists, demonstrating at least the power of this approach to capture complicated and intricate biological systems. Our greatest contribution, then, may be that of a tool which is now able to capture true covariants of biological reality and, in the age of big-data, provide models capable of utilising biological data more fully.

7.2 Perspectives

The work stemming from this document could potentially be used across 3 major streams: Firstly, it seems that this higher-dimensional modelling technique will likely be used to further our theoretical knowledge and understanding of systems with dynamic, spatio-structural heterogeneity. Secondly, the application of this model to extrapolating further results from high-resolution singe cell data was intriguing and is certainly worthy of further exploration. Thirdly, the agent-based cellular automata methods developed herein are powerful and may well be used for descriptive and demonstrative purposes in the field of cell biology.

There are also very important questions to be answered about how cancer cells interact with the immune system, both of which are structured populations. For instance, oncolytic viruses gained much celebrity during their inception, for their potential ability to preferentially degrade tumours, but failed to produce the expected results as the immune system reacted to the incoming threat of viral infection. This process is importantly mediated by the IFN signalling system and the interaction of these two systems – cancer and IFN – is an important and logical next step in the utilisation of this higher-dimensional framework.

Another particular application of this modelling framework has been to problems involving the stochastic dynamics of genetic transcription and protein synthesis [176], from the resultant RNA. In the same line, there exists an exceptional potential to use such a framework for the conversion of systems of governing ODEs for genetic, metabolic, or alternative intra-cellular pathways and mod-

elling these pathways on the population level, and indeed through space. This has not yet been done and would certainly represent a desirable stage in the development of these modelling approaches, which could prove invaluable to the associated biological experimentalists.

Moreover, there are scientific advances which allow both the theoretical model-driven and data-driven approaches to be utilised simultaneously, through the use of modern computer scientific deep learning techniques. Currently, we are looking at the potential for genetically barcoded, and simultaneously metabolically marked, tumours to be experimentally imaged in a spatial context which, using deep learning trained to the model framework, would allow for concurrent data-driven model improvement. Ideally this would be achieved through time and in the presence of various, clinically relevant drugs. In the clinical context this databased model could then be used to make important predictions about the behaviour of *in situ* biopsied tumours in response to a drug or, indeed, to suggest drug-dose regimens.

Bibliography

[1] Abraham, A.K., Kagan, L., Kumar, S., Mager, D.E.: Type i interferon receptor is a primary regulator of target-mediated drug disposition of interferon-β in mice. The Journal of Pharmacology and Experimental Therapeutics **334**, 327–332 (2010)

[2] Ackerman, A., Klein, O., McDermott, D.F., Wang, W., Ibrahim, N., Lawrence, D.P., Gunturi, A., Flaherty, K.T., Hodi, F.S., Kefford, R., Menzies, A.M., Atkins, M.B., Long, G.V., Sullivan, R.J.: Outcomes of patients with metastatic melanoma treated with immunotherapy prior to or after BRAF inhibitors. Cancer **120**(11), 1695–1701 (2014)

[3] Ackerman, A., McDermott, D.F., Lawrence, D.P., Gunturi, A., Flaherty, K.T., Giobbie-Hurder, A., Hodi, F.S., Ibrahim, N., Atkins, M.B., Cho, D.C., Sullivan, R.J.: Outcomes of patients with malignant melanoma treated with immunotherapy prior to or after vemurafenib. Journal of Clinical Oncology **30**, 8569–8569 (2012)

[4] Adam, J., Bellomo, N.: A Survey of Models for Tumor-Immune System Dynamics. Birkhäuser, Boston (1996)

[5] Adam, L., Mazumdar, A., Sharma, T., Jones, T.R., Kumar, R.: A three-dimensional and temporo-spatial model to study invasiveness of cancer cells by heregulin and prostaglandin e_2. Cancer Research **61**, 81–87 (2001)

[6] Agarwala, S.S., Lee, S.J., Flaherty, L.E., Smylie, M., Kefford, R.F., Carson, W.E., Cohen, G., Kirkwood, J.M.: Randomized phase iii trial of high-dose interferon alfa-2b (hdi) for 4 weeks induction only in patients with intermediate- and high-risk melanoma (intergroup trial e 1697). Journal of Clinical Oncology **29**(15), 8505 (2011)

[7] Ajmone Marsan, G., Bellomo, N., Gibelli, L.: Stochastic evolutionary differential games toward a systems theory of behavioral social dynamics. Mathematical Models and Methods in Applied Sciences **26**(6), 1051–1093 (2017)

[8] Al-Omari, J., Gourley, S.: Monotone travelling fronts in an age-structured reaction-diffusion model of a single species. Journal of Mathematical Biology **45**(4), 294–312 (2002). DOI 10.1007/s002850200159

[9] Alarcon, T., Byrne, H., Maini, P.K.: A multiple scale model for tumor growth. Multiscale Modelling & Simulation **3**(2), 440–475 (2005)

[10] Alcalá, A.M., Flaherty, K.T.: BRAF inhibitors for the treatment of metastatic melanoma: Clinical trials and mechanisms of resistance. Clinical Cancer Research **18**(1), 33–39 (2012)

[11] Allen, E.J.: Derivation of stochastic partial differential equations for size- and age-structured populations. Journal of Biological Dynamics **3**(1), 73–86 (2009). DOI 10.1080/17513750802162754

[12] Altan-Bonnet, G., Mukherjee, R.: Cytokine-mediated communication: a quantitative appraisal of immune complexity. Nature Reviews Immunology **19**, 205–217 (2019)

[13] Andasari, V., Gerisch, A., Lolas, G., South, A.P., Chaplain, M.A.J.: Mathematical modeling of cancer cell invasion of tissue: biological insight from mathematical analysis and computational simulation. Journal of Mathematical Biology **63**(1), 141–171 (2011). DOI 10.1007/s00285-010-0369-1

[14] Anderson, A., Chaplain, M.A.J.: Continuous and Discrete Mathematical Models of Tumor-induced Angiogenesis. Bulletin of Mathematical Biology **60**(5), 857–899 (1998)

[15] Anderson, A.R.A., Chaplain, M.A.J., Newman, E.L., et al.: Mathematical Modelling of Tumour Invasion and Metastasis. Journal of Theoretical Medicine **2**(2), 129–154 (2000)

[16] Andreiuk, B., Reisch, A., Lindecker, M., Follain, G., Peyriéras, N., Goetz, J.G., Klymchenko, A.S.: Fluorescent polymer nanoparticles for cell barcoding *in vitro* and *in vivo*. Small **13**(38), 1701,582 (2017)

[17] Aplin, A.E., Kaplan, F.M., Shao, Y.: Mechanisms of resistance to raf inhibitors in melanoma. Journal of Investigative Dermatology **131**(1817-1820) (2011)

[18] Arimoto, K.i., L'ochte, S., Stoner, S.A., Burkart, C., Zhang, Y., Miyauchi, S., Wilmes, S., Fan, J.B., Heinisch, J.J., Li, Z., Yan, M., Sandra Pellegrini, S., Colland, F., Piehler, J., Zhang, D.E.: Stat2 is an essential adaptor in usp18-mediated suppression of type i interferon signaling. Natural Structural Molecular Biology **24**(3), 279–289 (2017)

[19] Armitage, P., Doll, R.: The age distribution of cancer and a multi-stage theory of carcinogenesis. British journal of cancer **8**(1), 1 (1954)

[20] Arnold, S.J.: Mate Choice, chap. 4. Sexual Selection: the interface of theory and empiricism. Cambridge University Press (1983)

[21] Ayati, B.P.: A structured-population model of proteus mirabilis swarm-colony development. Journal of Mathematical Biology **52**(1), 93–114 (2006). DOI 10.1007/s00285-005-0345-3

[22] Baca, S.C., Prandi, D., Lawrence, M.S., Mosquera, J.M., Romanel, A., Drier, Y., Kyung Park, K., Kitabayashi, N., MacDonald, T.Y., Ghandi, M., van Allen, E., Kryukov, G.V., Sboner, A., Theurillat, J.P., Soong,

T.D., Nickerson, E., Auclair, D., Tewari, A., Beltran, H., Onofrio, R.C., Gunther Boysen, G., Guiducci, C., Barbieri, C.E., Cibulskis, K., Sivachenko, A., Carter, S.L., Saksena, G., Voet, D., Ramos, A.H., Winckler, W., Cipicchio, M., Ardlie, K., Kantoff, P.W., Berger, M.F., Gabriel, S.B., Golub, T.R., Meyerson, M., Lander, E.S., Elemento, O., Getz, G., Demichelis, F., Rubin, M.A., Garraway, L.A.: Punctuated evolution of prostate cancer genomes. Cell **153**, 666–677 (2013)

[23] Baker, R.R., Parker, G.A.: The evolution of bird coloration. Philosophical Transactions of the Royal Society of London B **287**(1018), 63–130 (1979)

[24] Barinka, C., Parry, G., Callahan, J., et al.: Structural Basis of Interaction between Urokinase-type Plasminogen Activator and its Receptor. Journal of Molecular Biology **363**(2), 482–495 (2006)

[25] Barkai, N., Rose, M.D., Wingreen, N.S.: Protease helps yeast find mating partners. Nature **396**(6710), 422 (1998)

[26] Barton, N.H., Etheridge, A.M., Véber, A.: Modelling evolution in a spatial continuum. Journal of Statistical Mechanics: Theory and Experiment p. P01002 (2013)

[27] Basse, B., Ubezio, P.: A Generalised Age- and Phase-Structured Model of Human Tumour Cell Populations Both Unperturbed and Exposed to a Range of Cancer Therapies. Bulletin of Mathematical Biology **69**(5), 1673–1690 (2007)

[28] Beckman, R.A., Schemmann, G.S., Yeang, C.H.: Impact of genetic dynamics and single-cell heterogeneity on development of nonstandard personalized medicine strategies for cancer. Proceedings of the National Academy of Sciences **109**(36), 14,586–14,591 (2012)

[29] Bekkal Brikci, F., Clairambault, J., Ribba, B., Perthame, B.: An age-and-cyclin-structured cell population model for healthy and tumoral tissues.

Journal of Mathematical Biology **57**(1), 91–110 (2008). DOI 10.1007/s00285-007-0147-x

[30] Bellomo, N., Li, N.K., Maini, P.K.: On the foundations of cancer modelling: Selected topics, speculations, and perspectives. Mathematical Models and Methods in Applied Sciences **18**(4), 593–646 (2008)

[31] Bellomo, N., Preziosi, L.: Modelling and mathematical problems related to tumor evolution and its interaction with the immune system. Mathematical and Computer Modelling **32**, 413–452 (2000)

[32] Benzekry, S., Lamont, C., Beheshti, A., et al.: Classical Mathematical Models for Description and Prediction of Experimental Tumor Growth. PLoS Computational Biology **10**(8), e1003,800 (2014)

[33] Bertuzzi, A., D'Onofrio, A., Fasano, A., Gandolfi, A.: Modelling cell populations with spatial structure: Steady state and treatment-induced evolution of tumour cords. Discrete and Continuous Dynamical Systems - Series B **4**(1), 161–186 (2004)

[34] Bhuvarahamurthy, V., Schroeder, J., Kristiansen, G., et al.: Differential gene expression of urokinase-type plasminogen activator and its receptor in human renal cell carcinoma. Oncology Reports **14**(3), 777–782 (2005)

[35] Bianchi, E., Ferrero, E., Fazioli, F., Mangili, F., Wang, J., Bender, J.R., Blasi, F., Pardi, R.: Integrin-dependent induction of functional urokinase receptors in primary t lymphocytes. Journal of Clinical Investigation **98**(5), 1133–1141 (1996)

[36] Binder, B.R., Mihaly, J., Prager, G.W.: uPAR - uPA - uPAI-1 interactions and signalling: A vascular biologist's view. International Journal for Vascular Biology and Medicine **97**, 336 – 342 (2007)

[37] Bollag, G., Hirth, P., Tsai, J., Zhang, J., Ibrahim, P.N., Cho, H., Spevak, W., Zhang, C., Zhang, Y., Habets, G., Burton, E.A., Wong, B., Tsang,

G., West, B.L., Powell, B., Shellooe, R., Marimuthu, A., Nguyen, H., Zhang, K.Y.J., Artis, D.R., Schlessinger, J., Su, F., Higgins, B., Iyer, R., D'Andrea, K., Koehler, A., Stumm, M., Lin, P.S., Lee, R.J., Grippo, J., Puzanov, I., Kim, K.B., Ribas, A., McArthur, G.A., Sosman, J.A., Chapman, P.B., Flaherty, K.T., Xu, X., Nathanson, K.L., Nolop, K.: Clinical efficacy of a RAF inhibitor needs broad target blockade in BRAF-mutant melanoma. Nature **467**, 596–599 (2010)

[38] Bollag, G., Tsai, J., Zhang, J., Zhang, C., Ibrahim, P., Nolop, K., Hirth, P.: Vemurafenib: the first drug approved for BRAF-mutant cancer. Nature Reviews Drug Discovery **11**(11), 873–886 (2012)

[39] Bomze, I.M.: Lotka-volterra equation and replicator dynamics: A two-dimensional classification. Biological Cybernetics **48**, 201–211 (1983)

[40] Borden, E.C., Sen, G.C., Uzé, G., Silverman, R.H., Ransohoff, R.M., Foster, G.R., Stark, G.R.: Interferons at age 50: past, current and future impact on biomedicine. Nature Reviews Drug Discovery **6**, 975–990 (2007)

[41] Bosc, C., Selak, M.A., Sarry, J.E.: Resistance is futile: Targeting mitochondrial energetics and metabolism to overcome drug resistance in cancer treatment. Cell Metabolism **26**, 705–707 (2017)

[42] Bozic, I., Nowak, M.A.: Timing and heterogeneity of mutations associated with drug resistance in metastatic cancers. Proceedings of the National Academy of Sciences of the United States of America **111**(45), 15,964–8 (2014)

[43] Bunin, G.: Ecological communities with lotka-volterra dynamics. Physical Review E **95**(4), 042,414 (2017)

[44] Burrell, R.A., McGranahan, N., Bartek, J., Swanton, C.: The causes and consequences of genetic heterogeneity in cancer evolution. Nature **501**, 338–345 (2013)

[45] Busenberg, S., Iannelli, M.: A class of nonlinear diffusion problems in age-dependent population dynamics. Nonlinear Analysis: Theory, Methods & Applications **7**(5), 501 – 529 (1983). DOI 10.1016/0362-546X(83)90041-X

[46] Buxboim, A., Ivanovska, I.L., Discher, D.E.: Matrix elasticity, cytoskeletal forces and physics of the nucleus: how deeply do cells 'feel' outside and in? J Cell Sci **123**(Pt 3), 297–308 (2010)

[47] Byrne, H.M., Owen, M.R., Alarcon, T., Murphy, J., Maini, P.K.: Modelling the response of vascular tumours to chemotherapy: A multiscale approach. Mathematical Models and Methods in Applied Sciences **16**(supp01), 1219–1241 (2006)

[48] Cairns, J.: Mutation selection and the natural history of cancer. Nature **255**(5505), 197 (1975)

[49] Calsina, À., Saldaña, J.: A model of physiologically structured population dynamics with a nonlinear individual growth rate. Journal of Mathematical Biology **33**(4), 335–364 (1995). DOI 10.1007/BF00176377

[50] Cardano, G.: Artis Magnæ, Sive de Regulis Algebraicis Liber Unus (1545)

[51] Carey, S.P., Rahman, A., Kraning-Rush, C.M., Romero, B., Somasegar, S., Torre, O.M., Williams, R.M., Reinhart-King, C.A.: Comparative mechanisms of cancer cell migration through 3D matrix and physiological microtracks. Am J Physiol Cell Physiol **308**(6), C436–47 (2014)

[52] Carpen, O., Pallai, P., Staunton, D.E., Springer A, T.: Association of Intercellular Adhesion Molecule-1 (ICAM-1) with Actin-containing Cytoskeleton and -actinin. J Cell Biol **118**(5), 1223–1234 (1992)

[53] Castilla, A.M., Bauwens, D.: Observations on the natural history, present status, and conservation of the insular lizard *Podarcis hispanica atrata* on the columbretes archipelago, spain. Biological Conservation **58**, 69–84 (1991)

[54] Chaplain, M.A.J., Ganesh, M., Graham, I.G.: Spatio-temporal pattern formation on spherical surfaces: numerical simulation and application to solid tumour growth. Journal of Mathematical Biology **42**(5), 387–423 (2001)

[55] Chaplain, M.A.J., Lolas, G.: Mathematical modelling of cancer cell invasion of tissue: the role of the urokinase plasminogen activation system. Mathematical Models and Methods in Applied Sciences **11**(2005), 1685–1734 (2005)

[56] Chaplain, M.A.J., Lolas, G.: Mathematical modelling of cancer invasion of tissue: Dynamic heterogeneity. Networks and Heterogeneous Media **1**(3), 399–439 (2006)

[57] Chaplain, M.A.J., Lolas, G.: Mathematical modelling of cancer cell invasion of tissue: The role of the urokinase plasminogen activation system. Mathematical Models and Methods in Applied Sciences (2011)

[58] Chapman, A., del Ama, L.F., Ferguson, J., Kamarashev, J., Wellbrock, C., Huristone, A.: Heterogeneous tumour subpopulations cooperate to drive invasion. Cell Reports **8**, 688–695 (2014)

[59] Chapman, P.B., Hauschild, A., Robert, C., Haanen, J.B., Ascierto, P., Larkin, J., Dummer, R., Garbe, C., Testori, A., Maio, M., Hogg, D., Lorigan, P., Lebbe, C., Jouary, T., Schadendorf, D., Ribas, A., O'Day, S.J., Sosman, J.A., Kirkwood, J.M., Eggermont, A.M.M., Dreno, B., Nolop, K., Li, J., Nelson, B., Hou, J., Lee, R.J., Flaherty, K.T., McArthur, G.A.: Improved survival with vemurafenib in melanoma with BRAF V600E mutation. N Eng J Med **364**(26), 2507–2516 (2011)

[60] Chapman, S.J., Plank, M.J., James, A., Basse, B.: A nonlinear model of age and size-structured populations with applications to cell cycles. The ANZIAM Journal **49**(02), 151 (2007)

[61] Chaurasia, P., Aguirre-Ghiso, J.A., Liang, O.D., et al.: A Region in Urokinase Plasminogen Receptor Domain III Controlling a Functional Association with 5beta1 Integrin and Tumor Growth. Journal of Biological Chemistry **281**(21), 14,852–14,863 (2006)

[62] Clarke, B.L.: Stoichiometric network analysis. Cell Biochemistry and Biophysics **12**(1), 237–253 (1988)

[63] Clayton, D., Schifflers, E.: Models for temporal variation in cancer rates. I: Age–period and age–cohort models. Statistics in Medicine **6**(4), 449–467 (1987)

[64] Coccia, E.M., Severa, M., Giacomini, E., le Monneron, D., Remoli, M.E., Julkunen, I., Cella, M., Lande, R., Uzé, G.: Viral infection and Toll-like receptor agonists induce a differential expression of type I and λ interferons in human plasmacytoid and monocyte-derived dendritic cells. European Journal of Immunology **34**, 796–805 (2004)

[65] Colina, R., Mauro Costa-Mattioli, M., Dowling, R.J.O., Jaramillo, M., Tai, L.H., Breitbach, C.J., Martineau, Y., Larsson, O., Rong, L., Svitkin, Y.V., Makrigiannis, A.P., Bell, J.C., Sonenberg, N.: Translational control of the innate immune response through irf-7. Nature **452**, 323–329 (2008)

[66] Cott, H.B.: Adaptive Coloration in Animals. Methuen & Co Ltd (1940)

[67] Cressman, R., Garay, J.: Evolutionary stability in lotka–volterra systems. Journal of Theoretical Biology **2**(21), 233–245 (2003)

[68] Cross, W.C.H., Graham, T.A., Wright, N.A.: New paradigms in clonal evolution: punctuated equilibrium in cancer. Journal of Pathology **240**(2), 126–136 (2016)

[69] Cuadrado, M., Mawin, J., Lopez, P.: Camouflage and escape decisions in the common chameleon *Chamaeleo chamaeleon*. Biological Journal of the Linnean Society **72**, 547–554 (2001)

[70] Cushing, J.M.: An Introduction to Structured Population Dynamics, *CBMS-NSF Regional Conference Series in Applied Mathematics*, vol. 71. SIAM (1998). DOI 10.1137/1.9781611970005.ch2

[71] Cusulin, C., Iannelli, M., Marinoschi, G.: Age-structured diffusion in a multi-layer environment. Nonlinear Analysis: Real World Applications **6**(1), 207 – 223 (2005). DOI 10.1016/j.nonrwa.2004.08.006

[72] Dakin, R., Montgomerie, R.: Peahens prefer peacocks displaying more eyespots, but rarely. Animal Behaviour **82**, 21–28 (2011)

[73] Danø, K., Andreasen, P., Grøndahl-Hansen, J., et al.: Plasminogen Activators, Tissue Degradation, and Cancer. Advances in Cancer Research **44**, 139–266 (1985)

[74] Danø, K., Rømer, J., NIELSEN BOYE S., B.S., et al.: Cancer invasion and tissue remodeling-cooperation of protease systems and cell types. APMIS **107**(1-6), 120–127 (1999)

[75] Darwin, C.: On the Origin of Species by Means of Natural Selection. John Murray (1859)

[76] Darwin, C.: The descent of man: and selection in relation to sex. John Murray, Washington DC (1871)

[77] Das Thakur, M., Salangsang, F., Landman, A.S., Sellers, W.R., Pryer, N.K., Levesque, M.P., Dummer, R., McMahon, M., Stuart, D.D.: Modelling vemurafenib resistance in melanoma reveals a strategy to forestall drug resistance. Nature **494**(7436), 251–255 (2013)

[78] Das Thakur, M., Stuart, D.D.: The evolution of melanoma resistance reveals therapeutic opportunities. Cancer Research **73**(20), 6106–6111 (2013)

[79] Davies, H., Bignell, G.R., Cox, C., Stephens, P., Edkins, S., Clegg, S., Teague, J., Woffendin, H., Garnett, M.J., Bottomley, W., Davis, N., Dicks,

E., Ewing, R., Floyd, Y., Gray, K., Hall, S., Hawes, R., Hughes, J., Kosmidou, V., Menzies, A., Mould, C., Parker, A., Stevens, C., Watt, S., Hooper, S., Wilson, R., Jayatilake, H., Gusterson, B.a., Cooper, C., Shipley, J., Hargrave, D., Pritchard-Jones, K., Maitland, N., Chenevix-Trench, G., Riggins, G.J., Bigner, D.D., Palmieri, G., Cossu, A., Flanagan, A., Nicholson, A., Ho, J.W.C., Leung, S.Y., Yuen, S.T., Weber, B.L., Seigler, H.F., Darrow, T.L., Paterson, H., Marais, R., Marshall, C.J., Wooster, R., Stratton, M.R., Futreal, P.A.: Mutations of the BRAF gene in human cancer. Nature **417**(6892), 949–954 (2002)

[80] Davis, A., Gao, R., Navin, N.: Tumor Evolution: Linear, Branching, Neutral or Punctuated? Biochimica et Biophysica Acta (BBA) - Reviews on Cancer (2017)

[81] Dawkins, R., Krebs, J.R.: Arms races between and within species. Proceedings of the Royal Society B **205**(1161) (1979)

[82] Débarre, F., Lenormand, T., Gandon, S.: Evolutionary epidemiology of drug-resistance in space. PLoS Computational Biology **5**(4), e1000,337 (2009)

[83] Delgado, M., Molina-Becerra, M., Suárez, A.: A nonlinear age-dependent model with spatial diffusion. Journal of Mathematical Analysis and Applications **313**(1), 366 – 380 (2006). DOI 10.1016/j.jmaa.2005.09.042

[84] Delgado-Goni, T., Miniotis, M.F., Wantuch, S., Parkes, H.G., Marais, R., Workman, P., Leach, M.O., Beloueche-Babari, M.: Cancer Biology and Signal Transduction The BRAF Inhibitor Vemurafenib Activates Mitochondrial Metabolism and Inhibits Hyperpolarized Pyruvate–Lactate Exchange in BRAF-Mutant Human Melanoma Cells. Molecular Cancer Therapeutics **15**(12), 2987–2999 (2016)

[85] Delitala, M., Lorenzi, T.: Asymptotic dynamics in continuous structured populations with mutations, competition and mutualism. Journal

of Mathematical Analysis and Applications **389**, 439–451 (2012). DOI 10.1016/j.jmaa.2011.11.076

[86] Delitala, M., Lorenzi, T., Melensi, M.: Competition between cancer cells and t cells under im- munotherapy: a structured population approach. ITM Web of Conferences **5**, 5p (2015). DOI 10.1051/itmconf/20150500005

[87] Deng, Q., Hallam, T.G.: An age structured population model in a spatially heterogeneous environment: Existence and uniqueness theory. Nonlinear Analysis: Theory, Methods & Applications **65**(2), 379 – 394 (2006). DOI 10.1016/j.na.2005.06.019

[88] Dhomen, N., Reis-Filho, J.S., da Rocha Dias, S., Hayward, R., Savage, K., Delmas, V., Larue, L., Pritchard, C., Marais, R.: Oncogenic Braf Induces Melanocyte Senescence and Melanoma in Mice. Cancer Cell **15**(4), 294–303 (2009)

[89] Di Blasio, G.: Non-linear age-dependent population diffusion. Journal of Mathematical Biology **8**(3), 265–284 (1979). DOI 10.1007/BF00276312

[90] Diekmann, O., Gyllenberg, M., Metz, J.A.J., Thieme, H.: The 'Cumulative' Formulation of (Physiologically) Structured Population Models. CWI (1992)

[91] Diekmann, O., Heijmans, H.J.A.M., Thieme, H.R.: On the stability of the cell size distribution. Journal Of Mathematical Biology **19**(2), 227–248 (1984)

[92] Diekmann, O., Metz, J.A.J.: On the Reciprocal Relationship Between Life Histories and Population Dynamics, *Lecture Notes in Biomathematics*, vol. 100, chap. Frontiers in Mathematical Biology, pp. 263–279. Springer Berlin Heidelberg (1994)

[93] Diekmann, O., Temme, N.M. (eds.): Nonlinear Diffusion Problems. No. 28 in MC Syllabus. Mathematisch Centrum, Amsterdam (1982)

[94] Doherty, Jr., P.F., Sorci, G., Royle, J.A., Hines, J.E., Nichols, J.D., Boulinier, T.: Sexual selection affects local extinction and turnover in bird communities. Proceedings of the National Academy of Sciences **100**(10), 5858–5862 (2003)

[95] Domschke, P., Trucu, D., Gerisch, A., et al.: Mathematical modelling of cancer invasion: Implications of cell adhesion variability for tumour infiltrative growth patterns. Journal of Theoretical Biology **361**, 41–60 (2014)

[96] Domschke, P., Trucu, D., Gerisch, A., Chaplain, M.A.J.: Structured models of cell migration incorporating molecular binding processes. Journal of Mathematical Biology **75**(6-7), 1517–1561 (2017)

[97] Domschke, P., Trucu, D., Gerisch, A., Chaplain, M.A.J.: Structured models of cell migration incorporating molecular binding processes. Journal of Mathematical Biology **75**(6-7), 1517–1561 (2017)

[98] Dubey, B., Zhao, T.G., Jonsson, M., Rahmanov, H.: A solution to the accelerated-predator-satiety lotka–volterra predator–prey problem using boubaker polynomial expansion scheme. Journal of Theoretical Biology **264**(1), 154–160 (2010)

[99] Dufau, I., Frongia, C., Sicard, F., Dedieu, L., et al.: Multicellular tumor spheroid model to evaluate spatio-temporal dynamics effect of chemotherapeutics: application to the gemcitabine/CHK1 inhibitor combination in pancreatic cancer. BMC Cancer **12**(1), 15 (2012)

[100] Duffy, M.J., Maguire, T.M., McDermott, E.W., et al.: Urokinase plasminogen activator: A prognostic marker in multiple types of cancer. Journal of Surgical Oncology **71**(2), 130–135 (1999)

[101] Dyson, J., Webb, G.: A nonlinear age and maturity structured model of population dynamics i. basic theory. Journal of Mathematical Analysis and Applications **242**, 93–104 (2000)

[102] Dyson, J., Webb, G.: A nonlinear age and maturity structured model of population dynamics ii. chaos. Journal of Mathematical Analysis and Applications **242**, 255–270 (2000)

[103] Eldredge, N., Gould, S.J.: Models in Paleobiology, chap. 5. Punctuated Equilibria: An Alternative to Phyletic Gradualism, pp. 82–115. Freeman, Cooper and Company (1972)

[104] Ellis, V., Danø, K.: Potentiation of plasminogen activation by an anti-urokinase monoclonal antibody due to ternary complex formation. A mechanistic model for receptor-mediated plasminogen activation. The Journal of biological chemistry **268**(7), 4806–13 (1993)

[105] Enbody, E.D., Lantz, S.M., Karubian, J.: Production of plumage ornaments among males and females of two closely related tropical passerine bird species. Ecology and Evolution **7**, 2024–2034 (2017)

[106] Feinerman, O., Jentsch, G., Tkach, K.E., Coward, J.W., Hathorn, M.M., Sneddon, M.W., Emonet, T., Smith, K.A., Altan-Bonnet, G.: Single-cell quantification of IL-2 response by effector and regulatory T cells reveals critical plasticity in immune response. Molecular Systems Biology **6**(437), 1–16 (2010). DOI 10.1038/msb.2010.90

[107] Ferretta, A., Maida, I., Guida, S., Azzariti, A., Porcelli, L., Tommasi, S., Zanna, P., Cocco, T., Michele Guida, M., Guida, G.: New insight into the role of metabolic reprogramming in melanoma cells harboring braf mutations. Biochimica et Biophysica Acta **1863**, 2710–2718 (2016)

[108] Figlin, R.A., Hutson, T.E., Tomczak, P., Michaelson, M.D., Bukowski, R.M., Négrier, S., Huang, X., Kim, S.T., Chen, I., Motzer, R.J.: Overall survival with sunitinib versus interferon (ifn)-α as first-line treatment of metastatic renal cell carcinoma (mrcc). Journal of Clinical Oncology **26**(15), 5024 (2008)

[109] Fitzgibbon, W., Parrott, M., Webb, G.: Diffusion epidemic models with incubation and crisscross dynamics. Mathematical Biosciences **128**(1–2), 131 – 155 (1995). DOI 10.1016/0025-5564(94)00070-G

[110] Fleisher, T.A., Shearer, W.T., Frew, A.J., Schroeder Jr., H.W., Weyand, C.M.: Clinical Immunology: Principles and Practice, 4^{th} edn. Elsevier Saunders (2013)

[111] François-Newton, V., de Freitas Almeida, G.M., Payelle-Brogard, B., Monneron, D., Pichard-Garcia, L., Piehler, J., Pellegrini, S., Uzé, G.: Usp18-based negative feedback control is induced by type i and type iii interferons and specifically inactivates interferon α response. PLoS One **6**(7), e22,200 (2011)

[112] François, P., Altan-bonnet, G.: The Case for Absolute Ligand Discrimination : Modeling Information Processing and Decision by Immune T Cells. Journal of Statistical Physics **162**(5), 1130–1152 (2016). DOI 10.1007/s10955-015-1444-1

[113] Galle, J., Hoffmann, M., Aust, G.: From single cells to tissue architecture—a bottom-up approach to modelling the spatio-temporal organisation of complex multi-cellular systems. Journal of Mathematical Biology **58**(1-2), 261–283 (2009)

[114] García-Navas, V., Ferrer, E.S., Sanz, J.J.: Plumage yellowness predicts foraging ability in the blue tit Cyanistes caeruleus. Biological Journal of the Linnean Society **106**, 418–429 (2012)

[115] Garroni, M.G., Langlais, M.: Age-dependent population diffusion with external constraint. Journal of Mathematical Biology **14**(1), 77–94 (1982). DOI 10.1007/BF02154754

[116] Gascoigne, N.R., Zal, T., Alam, S.M.: T-cell receptor binding kinetics in t-cell development and activation. Expert Reviews in Molecular Medicine **3**(6), 1–17 (2001)

[117] Gatenby, R.A., Gawlinski, E.T.: A Reaction-Diffusion Model of Cancer Invasion. Cancer Res. **56**(24), 5745–5753 (1996)

[118] Gavutis, M., Jaks, E., Lamken, P., Piehler, J.: Determination of the Two-Dimensional Interaction Rate Constants of a Cytokine Receptor Complex. Biophysical Journal **90**(9), 3345–3355 (2006). DOI 10.1529/biophysj.105.072546

[119] Gavutis, M., Lata, S., Lamken, P., Müller, P., Piehler, J.: Lateral Ligand-Receptor Interactions on Membranes Probed by Simultaneous Fluorescence-Interference Detection. Biophysical Journal **88**(6), 4289–4302 (2005). DOI 10.1529/biophysj.104.055855

[120] Gerisch, A., Chaplain, M.: Mathematical modelling of cancer cell invasion of tissue: Local and non-local models and the effect of adhesion. Journal of Theoretical Biology **250**(4), 684–704 (2008)

[121] Getty, T.: Handicap signalling: when fecundity and viability do not add up. Animal Behaviour **56**, 127–130 (1998)

[122] Ghang, W., Nowak, M.A.: Stochastic evolution of staying together. Journal of Theoretical Biology **360**, 129–136 (2014)

[123] Gibbert, K., Schlaak, J.F., Yang, D., Dittmer, U.: Ifn-a subtypes: distinct biological activities in anti-viral therapy. British Journal of Pharmacology **168**(1048-1058) (2013)

[124] Gluckman, T.L., Cardoso, G.C.: The dual function of barred plumage in birds: camouflage and communication. Journal of Evolutionary Biology **23**, 2501–2506 (2010)

[125] Godár, S., Hořejší, V., Weidle, U.H., et al.: M6P/IGFII-receptor complexes urokinase receptor and plasminogen for activation of transforming growth factor-β1. European Journal of Immunology **29**(3), 1004–1013 (1999)

[126] Goel, V.K., Lazar, A.J.F., Warneke, C.L., Redston, M.S., Haluska, F.G.: Examination of mutations in BRAF, NRAS, and PTEN in primary cutaneous melanoma. J Invest Dermatol **126**(1), 154–60 (2006)

[127] Gosden, T.P., Reddiex, A.J., Chenoweth, S.F.: Artificial selection reveals sex differences in the genetic basis of sexual attractiveness. Proceedings of the National Academy of Sciences **115**(21), 5498–5503 (2018)

[128] Götmark, F.: Anti-predator effect of conspicuous plumage in a male bird. Animal Behaviour **44**, 51–55 (1992)

[129] Götmark, F.: Conspicuous coloration in male birds is favoured by predation in some species and disfavoured in others. Proceedings of the Royal Society of London B **253**, 143–146 (1993)

[130] Grafen, A.: Biological signals as handicaps. Journal of Theoretical Biology **144**, 517–546 (1990)

[131] Grafen, A.: Sexual selection unhandicapped by the fisher process. Journal of Theoretical Biology **144**, 473–516 (1990)

[132] Graner, F., Glazier, J.A.: Simulation of biological cell sorting using a two-dimensional extended potts model. Phys Rev Lett **69**(13), 2013–2016 (1992)

[133] Grant, B.D., Donaldson, J.G.: Pathways and mechanisms of endocytic recycling. Nature reviews. Molecular cell biology **10**(9), 597 (2009)

[134] Graziani, G., Artuso, S., De Luca, A., Muzi, A., Rotili, D., Scimeca, M., Atzori, M.G., Ceci, C., Mai, A., Leonetti, C., Levati, L., Bonanno, E., Tentori, L., Caccuri, A.M.: A new water soluble MAPK activator exerts antitumor activity in melanoma cells resistant to the BRAF inhibitor vemurafenib. Biochemical Pharmacology **95**(1), 16–27 (2014)

[135] Günzl, P., Schabbauer, G.: Recent advances in the genetic analysis of PTEN and PI3K innate immune properties. Immunobiology **213**(9-10), 759–765 (2008)

[136] Gurdon, J.B.: A community effect in animal development. Nature **336**(6201), 772–774 (1988)

[137] Gurtin, M., MacCamy, R.: Diffusion models for age-structured populations. Mathematical Biosciences **54**(1–2), 49 – 59 (1981). DOI 10.1016/0025-5564(81)90075-4

[138] Gyilenberg, M., Webb, G.F.: A nonlinear structured population model of tumor growth with quiescence. Journal of Mathematical Biology **28**, 671–694 (1990)

[139] Gyllenberg, M.: Nonlinear age-dependent population dynamics in continuously propagated bacterial cultures. Mathematical Biosciences **62**(1), 45 – 74 (1982). DOI http://dx.doi.org/10.1016/0025-5564(82)90062-1

[140] Gyllenberg, M.: The size and scar distributions of the yeast saccharomyces cerevisiae. Journal of Mathematical Biology **24**(1), 81–101 (1986). DOI 10.1007/BF00275722

[141] Gyllenberg, M., Webb, G.: Age-size structure in populations with quiescence. Mathematical Biosciences **86**(1), 67 – 95 (1987). DOI 10.1016/0025-5564(87)90064-2

[142] Haller, O., Kochs, G., Weber, F.: The interferon response circuit : Induction and suppression by pathogenic viruses. Virology **344**, 119–130 (2006). DOI 10.1016/j.virol.2005.09.024

[143] Hammerstein, P., Selten, R.: Handbook of Game Theory with Economic Applications, vol. 2, chap. 28. Game theory and evolutionary biology, pp. 929–993. Elsevier (1994)

[144] Hanahan, D., Weinberg, R.A.: The hallmarks of cancer: The next generation. Cell **144**, 646–674 (2011)

[145] Haq, R., Shoag, J., Andreu-Perez, P., Yokoyama, S., Edelman, H., Rowe, G.C., Frederick, D.T., Hurley, A.D., Nellore, A., Kung, A.L., Wargo,

J.A., Song, J.S., Fisher, D.E., Arany, Z., Widlund, H.R.: Oncogenic braf regulates oxidative metabolism via pgc1a and mitf. Cancer Cell **23**, 302–315 (2013)

[146] Hardeman, K.N., Peng, C., Paudel, B.B., Meyer, C.T., Luong, T., Tyson, D.R., Young, J.D., Quaranta, V., Fessel, J.P.: Dependence On Glycolysis Sensitizes BRAF-mutated Melanomas For Increased Response To Targeted BRAF Inhibition. Scientific Reports **7**(October 2016), 42,604 (2017)

[147] Harris, D., Bullock, S.: Enhancing game theory with coevolutionary simulation models of honest signalling. Proceedings of the 2002 Congress on Evolutionary Computation (2002)

[148] Harrison, G.A., A, M.K., M, D.E.: Type i interferon genes from the egg-laying mammal, tachyglossus aculeatus (short-beaked echidna). Immunology and Cell Biology **82**(2), 112–118 (2004)

[149] Hart, Y., Reich-Zeliger, S., Antebi, Y.E., Zaretsky, I., Mayo, A.E., Alon, U., Friedman, N.: Paradoxical signaling by a secreted molecule leads to homeostasis of cell levels. Cell **158**(5), 1022–1032 (2014). DOI 10.1016/j.cell.2014.07.033

[150] Hata, R.I., Izukuri, K., Kato, Y., Sasaki, S., Mukaida, N., Maehata, Y., Miyamoto, C., Akasaka, T., Yang, X., Nagashima, Y., Takeda, K., Kiyono, T., Taniguchi, M.: Suppressed rate of carcinogenesis and decreases in tumour volume and lung metastasis in CXCL14/BRAK transgenic mice. Scientific Reports **5**, 9083 (2015)

[151] Hedrick, A.V.: Crickets with extravagant mating songs compensate for predation risk with extra caution. Proceedings of the Royal Society of London B **267**, 671–675 (2000)

[152] Henrique, D., Hirsinger, E., Adam, J., Le Roux, I., Pourquié, O., Ish-Horowicz, D., Lewis, J.: Maintenance of neuroepithelial progenitor cells

by delta–notch signalling in the embryonic chick retina. Current Biology **7**(9), 661–670 (1997)

[153] Herman-Bausier, P., El-Kirat-Chatel, S., Foster, T.J., Geoghegan, J.A., Dufrene, Y.F.: Staphylococcus aureus Fibronectin-Binding Protein A Mediates Cell-Cell Adhesion through Low-Affinity Homophilic Bonds. mBio **6**(3), e00,413–e00,415 (2015)

[154] Hess Michelini, R., Doedens, A.L., Goldrath, A.W., Hedrick, S.M.: Differentiation of CD8 memory T cells depends on Foxo1. The Journal of experimental medicine **210**(6), 1189–200 (2013)

[155] Hilkens, C.M.U., Schlaak, J.F., Kerr, I.M.: Differential responses to ifn-α subtypes in human t cells and dendritic cells. The Journal of Immunology **171**, 5255–5263 (2003)

[156] Hodgkinson, A.: Cellular Automata, chap. A Novel Cellular Automata Modelling Framework for Micro-Environmental Interaction and Co-Invasion. Springer (2018)

[157] Hodgkinson, A.: Beauty and survival traits are evolutionarily symbiotic p. (Submitted) (2019)

[158] Hodgkinson, A., Chaplain, M.A.J., Domschke, P., Trucu, D.: Computational approaches and analysis for a spatio-structural-temporal invasive carcinoma model. Bulletin of Mathematical Biology **80**(4), 701–737 (2018)

[159] Hodgkinson, A., G, U., Radulescu, O.: Both high and low affinity interferons are necessary for effective immune response. Journal of Unpublished Material p. *submitted* (2018)

[160] Hodgkinson, A., Le Cam, L., Trucu, D., Radulescu, O.: Spatio-genetic and phenotypic modelling elucidates resistance and re-sensitisation to treatment in heterogeneous melanoma. Journal of Theoretical Biology **466**, 84–105 (2019)

[161] Hodgkinson, A., Radulescu, O., Uzé, G., Trucu, D.: Signal propagation in sensing and reciprocating cellular systems with spatial and structural heterogeneity. Bulletin of Mathematical Biology **80**, 1900–1936 (2018). DOI https://doi.org/10.1007/s11538-018-0439-x

[162] Hodis, E., Watson, I.R., Kryukov, G.V., Arold, S.T., Imielinski, M., Theurillat, J.P., Nickerson, E., Auclair, D., Li, L., Place, C., DiCara, D., Ramos, A.H., Lawrence, M.S., Cibulskis, K., Sivachenko, A., Voet, D., Saksena, G., Stransky, N., Onofrio, R.C., Winckler, W., Ardlie, K., Wagle, N., Wargo, J., Chong, K., Morton, D.L., Stemke-Hale, K., Chen, G., Noble, M., Meyerson, M., Ladbury, J.E., Davies, M.A., Gershenwald, J.E., Wagner, S.N., Hoon, D.S.B., Schadendorf, D., Lander, E.S., Gabriel, S.B., Getz, G., Garraway, L.A., Chin, L.: A landscape of driver mutations in melanoma. Cell **150**, 251–263 (2012)

[163] Hoffmann, H.H., Schneider, W.M., Rice, C.M.: Interferons and viruses: an evolutionary arms race of molecular interactions. Trends in Immunology **36**(3), 124–138 (2015)

[164] Hou, J., Wang, P., Lin, L., Liu, X., Ma, F., An, H., Wang, Z., Cao, X.: Microrna-146a feedback inhibits rig-i-dependent type i ifn production in macrophages by targeting traf6, irak1, and irak2. The Journal of Immunology **183**, 2150–2158 (2009)

[165] Hoyos, E., Kim, K., Milloz, J., Barkoulas, M., Pénigault, J.B., Munro, E., Félix, M.A.: Quantitative variation in autocrine signaling and pathway crosstalk in the caenorhabditis vulval network. Current Biology **21**(7), 527–538 (2011)

[166] Hsieh, Y.H.: Altruistic population model with sex ifference. In: O. Arnino, D.E. Axelrod, M. Kimmel (eds.) Mathematical Population Dynamics, *Lecture Notes in Pure and Applied Mathematics*, vol. 131. Marcel Dekker, Inc. (1991)

[167] Hu, G., Wang, K.: Stability in distribution of competitive lotka–volterra system with markovian switching. Applied Mathematical Modelling **35**, 3189–3200 (2011)

[168] Huai, Q., Mazar, A.P., Kuo, A., Parry, G.C., et al.: Structure of human urokinase plasminogen activator in complex with its receptor. Science (New York, N.Y.) **311**(5761), 656–9 (2006)

[169] Huang, C.: An age-dependent population model with nonlinear diffusion in $\mathbf{R}^n$. Quart. Appl. Math. **52**, 377–398 (1994)

[170] Hughes, A.L.: The evolution of the type i interferon gene family in mammals. Journal of Molecular Evolution **41**(5), 539–548 (1995)

[171] Huhta, E., Rytkönen, S., Solonen, T.: Plumage brightness of prey increases predation risk: An among-species comparison. Ecology **84**(7), 1793–1799 (2003)

[172] Humplik, J., Hill, A.L., Nowak, M.A.: Evolutionary dynamics of infectious diseases in finite populations. Journal of Theoretical Biology **360**, 149–162 (2014)

[173] Hunt, G.: The relative importance of directional change, random walks, and stasis in the evolution of fossil lineages. Proceedings of the National Academy of Sciences **104**(47), 18,404–18,408 (2017)

[174] Hurd, P.L.: Communication in discrete action–response games. Journal of Theoretical Biology **174**, 217–222 (1995)

[175] Huyer, W.: A size-structured population-model with dispersion. Journal of Mathematical Analysis and Applications **181**(3), 716 – 754 (1994). DOI 10.1006/jmaa.1994.1054

[176] Innocentini, G.C.P., Hodgkinson, A., Radulescu, O.: Time dependent stochastic mrna and protein synthesis in piecewise-deterministic models of gene networks. Frontiers in Physics **6**(46), 1–16 (2018)

[177] Jaks, E., Gavutis, M., Uzé, G., Martal, J., Piehler, J.: Differential receptor subunit affinities of type i interferons govern differential signal activation. Journal of Molecular Biology **366**, 525–539 (2007)

[178] Jang, S., Atkins, M.B.: Which drug, And when, For patients with BRAF-mutant melanoma? The Lancet Oncology **14**(2), e60–e69 (2013)

[179] Johnson, A.E., Price, J.J., Pruett-Jones, S.: Different modes of evolution in males and females generate dichromatism in fairy-wrens (maluridae). Ecology and Evolution **3**(9), 3030–3046 (2013)

[180] Johnson, C.P., Tang, H.Y., Carag, C., Speicher, D.W., Discher, D.E.: Forced unfolding of proteins within cells. Science **317**(5838), 663–6 (2007)

[181] Journey, L., Drury, J.P., Haymer, M., Rose, K., Blumstein, D.T.: Vivid birds respond more to acoustic signals of predators. Behavioural Ecology and Sociobiology **67**, 1285–1293 (2013)

[182] Kamo, N., Ke, B., Busuttil, R.W., Kupiec-Weglinski, J.W.: PTEN-mediated akt/b-Catenin/foxo1 signaling regulates innate immune responses in mouse liver ischemia/reperfusion injury. Hepatology **57**(1), 289–298 (2013)

[183] Karreth, F.A., Tay, Y., Perna, D., Ala, U., Tan, S.M., Rust, A.G., Denicola, G., Webster, K.A., Weiss, D., Perez-Mancera, P.A., Krauthammer, M., Halaban, R., Provero, P., Adams, D.J., Tuveson, D.A., Pandolfi, P.P.: In vivo identification of tumor- suppressive PTEN ceRNAs in an oncogenic BRAF-induced mouse model of melanoma. Cell **147**(2), 382–395 (2011)

[184] Kersh, G.J., Kersh, E.N., Fremont, D.H., Allen, P.M., Louis, S.: High- and Low-Potency Ligands with Similar Affinities for the TCR : The Importance of Kinetics in TCR Signaling. Immunity **9**, 817–826 (1998)

[185] Khanna, M., Wang, F., Jo, I., et al.: Targeting multiple conformations leads to small molecule inhibitors of the upar·upa protein–protein interaction that block cancer cell invasion. ACS Chemical Biology (2011)

[186] Kim, M., Ouyang, W., Liao, W., Zhang, M., Li, M.: The transcription factor foxo1 controls central-memory CD8+ T cell responses to infection. Immunity **39**(2), 286–297 (2013)

[187] Kimmel, M., Darzynkiewicz, Z., Arino, O., Traganos, F.: Analysis of a cell cycle model based on unequal division of metabolic constituents to daughter cells during cytokinesis. Journal of Theoretical Biology **637-664** (1984)

[188] Kirkpatrick, M., Ravigné, V.: Speciation by natural and sexual selection: Models and experiments. The American Naturalist **159**(S3), 22–35 (2002)

[189] Kleinman, A.: The mathematics of random mutation and natural selection for multiple simultaneous selection pressures and the evolution of antimicrobial drug resistance. Statistics in Medicine **35**(29), 5391–5400 (2016)

[190] Knobler, R.L., Panitch, H.S., Braheny, S.L., Sipe, J.C., Rice, G.P.A., Huddlestone, J.R., Francis, G.S., Hooper, C.J., Kamin-Lewis, R.M., Johnson, K.P., Oldstone, M.B.A., Merigan, T.C.: Systemic alpha-interferon therapy of multiple sclerosis. Neurology **34**(10), 1273 (1984)

[191] Knudson, A.G.: Mutation and cancer: statistical study of retinoblastoma. Proceedings of the National Academy of Sciences **68**(4), 820–823 (1971)

[192] Kondraganti, S., Gondi, C.S., McCutcheon, I., et al.: RNAi-mediated downregulation of urokinase plasminogen activator and its receptor in human meningioma cells inhibits tumor invasion and growth. International Journal of Oncology **28**(6), 1353–1360 (2006)

[193] Kraning-Rush, C.M., Carey, S.P., Lampi, M.C., Reinhart-King, C.A.: Microfabricated collagen tracks facilitate single cell metastatic invasion in 3D. Integr Biol **5**(3), 606–16 (2013)

[194] Kunisch, K., Schappacher, W., Webb, G.: Nonlinear age-dependent population dynamics with random diffusion. Computers & Mathematics with Applications **11**(1-3), 155–173 (1985)

[195] Lachmann, M., Számadó, S., Bergstrom, C.T.: Cost and conflict in animal signals and human language. Proceedings of the National Academy of Sciences **98**(23), 13,189–13,194 (2001)

[196] Lambert, J.D.: Numerical Methods for Ordinary Differential Systems: The Initial Value Problem. John Wiley & Sons, Inc. (1991)

[197] Landis, M.J., Schraiber, J.G.: Pulsed evolution shaped modern vertebrate body sizes. Proceedings of the National Academy of Sciences **114**(50), 13,224–13,229 (2017)

[198] Langlais, M.: Large time behavior in a nonlinear age-dependent population dynamics problem with spatial diffusion. Journal of Mathematical Biology **26**(3), 319–346 (1988). DOI 10.1007/BF00277394

[199] Langlais, M., Milner, F.A.: Existence and uniqueness of solutions for a diffusion model of host–parasite dynamics. Journal of Mathematical Analysis and Applications **279**(2), 463 – 474 (2003). DOI 10.1016/S0022-247X(03)00020-9

[200] Larkin, J., del Vecchio, M., Ascierto, P.A., Krajsova, I., Schachter, J., Neyns, B., Espinosa, E., Garbe, C., Sileni, V.C., Gogas, H., Miller Jr, W.H., Mandalà, M., Hospers, G.A.P., Arance, A., Queirolo, P., Hauschild, A., Brown, M.P., Mitchell, L., Veronese, L., Blank, C.U.: Vemurafenib in patients with brafv600 mutated metastatic melanoma: an open-label, multicentre, safety study. The Lancet Oncology **15**, 436–444 (2014)

[201] Lavoie, T.B., Kalie, E., Crisafulli-Cabatu, S., Abramovich, R., DiGioia, G., Moolchan, K., Pestka, S., Schreiber, G.: Binding and activity of all human alpha interferon subtypes. Cytokine **56**, 282–289 (2011)

[202] Lavoie, T.B., Kalie, E., Crisafulli-cabatu, S., Abramovich, R., Digioia, G., Moolchan, K., Pestka, S., Schreiber, G.: Cytokine Binding and activity of all human alpha interferon subtypes. Cytokine **56**(2), 282–289 (2011). DOI 10.1016/j.cyto.2011.07.019

[203] Lefebvre, G., Cornelis, F., Cumsille, P., Colin, T., Poignard, C., Saut, O.: Spatial modelling of tumour drug resistance: the case of gist liver metastases. Mathematical Medicine and Biology **34**(2), 151–176 (2017)

[204] Leksa, V., Godar, S., Cebecauer, M., et al.: The N Terminus of Mannose 6-Phosphate/Insulin-like Growth Factor 2 Receptor in Regulation of Fibrinolysis and Cell Migration. Journal of Biological Chemistry **277**(43), 40,575–40,582 (2002)

[205] Levy, D.E., Marié, I., Prakash, A.: Ringing the interferon alarm: differential regulation of gene expression at the interface between innate and adaptive immunity. Current Opinion in Immunology **15**(1), 52–58 (2003)

[206] Li, Y., Cozzi, P.: Targeting uPA/uPAR in prostate cancer. Cancer Treatment Reviews **33**(6), 521–527 (2007)

[207] Liang, X., Yang, X., Tang, Y., et al.: RNAi-mediated downregulation of urokinase plasminogen activator receptor inhibits proliferation, adhesion, migration and invasion in oral cancer cells. Oral Oncology **44**(12), 1172–1180 (2008)

[208] Lieberman, B.S., Eldredge, N.: What is punctuated equilibrium? What is macroevolution? A response to Pennell et al. Trends in Ecology and Evolution **29**(4), 185–186 (2014)

[209] Lin, R., Heylbroeck, C., Pitha, P.M., Hiscott, J.: Virus-Dependent Phosphorylation of the IRF-3 Transcription Factor Regulates Nuclear Translo-

cation, Transactivation Potential, and Proteasome-Mediated Degradation. Molecular and Cellular Biology **18**(5), 2986–2996 (1998). DOI 10.1128/MCB.18.5.2986

[210] Liu, D., Ghiso, J.A., Estrada, Y., et al.: EGFR is a transducer of the urokinase receptor initiated signal that is required for in vivo growth of a human carcinoma. Cancer Cell **1**(5), 445–457 (2002)

[211] Löchte, S., Waichman, S., Beutel, O., You, C., Piehler, J.: Live cell micropatterning reveals the dynamics of signaling complexes at the plasma membrane. Journal of Cell Biology **207**(3), 407–418 (2014). DOI 10.1083/jcb.201406032

[212] Lorz, A., Lorenzi, T., Clairambault, J., Escargueil, A., Perthame, B.: Modeling the Effects of Space Structure and Combination Therapies on Phenotypic Heterogeneity and Drug Resistance in Solid Tumors. Bulletin of Mathematical Biology **77**(1), 1–22 (2015)

[213] Lorz, A., Lorenzi, T., Hochberg, M.E., Clairambault, J., Perthame, B.: Populational adaptive evolution, chemotherapeutic resistance and multiple anti-cancer therapy. ESAIM: Mathematical Modelling and Numerical Analysis **47**, 377–399 (2012)

[214] Lorz, A., Lorenzi, T., Hochberg, M.E., Clairambault, J., Perthame, B.: Populational adaptive evolution, chemotherapeutic resistance and multiple anti-cancer therapies. ESAIM: Mathematical Modelling and Numerical Analysis **47**, 377–399 (2013). DOI 10.1051/m2an/2012031

[215] Lotka, A.J.: Analytical note on certain rhythmic relations in organic systems. Proceedings of the National Academy of Sciences **6**, 410–415 (1920)

[216] Lotka, A.J.: Undamped oscillations derived from the law of mass action. Journal of the American Chemical Society **42**(8), 1595–1599 (1920)

[217] Lotka, A.J.: Elements of Physical Biology. Williams & Wilkins, Baltimore (1925)

[218] Loyau, A., Jalme, M.S., Cagniant, C., Sorci, G.: Multiple sexual advertisements honestly reflect health status in peacocks (Pavo cristatus). Behavioural Ecology and Sociobiology **58**, 552–557 (2005)

[219] Ma, Y., Zhang, Q.: Stationary distribution and extinction of a three-species food chain stochastic model. Transactions of A. Razmadze Mathematical Institute **172**, 251–264 (2018)

[220] MacCamy, R.: A population model with nonlinear diffusion. Journal of Differential Equations **39**(1), 52 – 72 (1981). DOI 10.1016/0022-0396(81)90083-8

[221] MacCormack, R.: 23$^{\text{rd}}$ Aerospace Sciences Meeting, chap. Current status of numerical solutions of the Navier-Stokes equations. American Institute of Aeronautics and Astronautics (1985)

[222] Mackay, C.R.: Chemokine receptors and t cell chemotaxis. Journal of Experimental Medicine **184**(3), 799–802 (1996)

[223] Macnamara, C., Eftimie, R.: Memory versus effector immune responses in oncolytic virotherapies. Journal of Theoretical Biology **377**, 1–9 (2015)

[224] Madsen, D.H., Engelholm, L.H., Ingvarsen, S., et al.: Extracellular Collagenases and the Endocytic Receptor, Urokinase Plasminogen Activator Receptor-associated Protein/Endo180, Cooperate in Fibroblast-mediated Collagen Degradation. Journal of Biological Chemistry **282**(37), 27,037–27,045 (2007)

[225] Magal, P., Ruan, S. (eds.): Structured Population Models in Biology and Epidemiology. Springer-Verlag (2008)

[226] Mahasa, K.J., Eladdadi, A., de Pillis, L., Ouifki, R.: Oncolytic potency and reduced virus tumor- specificity in oncolytic virotherapy. a mathematical modelling approach. PLoS ONE **12**(9), e0184,347 (2017)

[227] Maher, S.G., Sheikh, F., Scarzello, A.J., Romero-Weaver, A.L., Baker, D.P., Donnelly, R.P., Gamero, A.M.: Ifn-α and ifn-λ differ in their antiproliferative effects and duration of jak/stat signaling activity. Cancer Biology & Therapy **7**(7), 1109–1115 (2008)

[228] Maire, T., Youk, H.: Molecular-Level Tuning of Cellular Autonomy Controls the Collective Behaviors of Cell Populations Article Molecular-Level Tuning of Cellular Autonomy Controls the Collective Behaviors of Cell Populations. Cell Systems **1**, 349–360 (2015). DOI 10.1016/j.cels.2015.10.012

[229] Makinoshima, H., Takita, M., Saruwatari, K., Umemura, S., Obata, Y., Ishii, G., Matsumoto, S., Sugiyama, E., Ochiai, A., Abe, R., Goto, K., Esumi, H., Tsuchihara, K.: Signaling through the phosphatidylinositol 3-kinase (PI3K)/mammalian target of rapamycin (mTOR) axis is responsible for aerobic glycolysis mediated by glucose transporter in epidermal growth factor receptor (EGFR)-mutated lung adenocarcinoma. Journal of Biological Chemistry **290**(28), 17,495–17,504 (2015)

[230] Manry, J., Laval, G., Patin, E., Fornarino, S., Itan, Y., Fumagalli, M., Sironi, M., Tichit, M., Bouchier, C., Casanova, J.L., Barreiro, L.B., Quintana-Murci, L.: Evolutionary genetic dissection of human interferons. The Journal of Experimental Medicine **208**(13), 2747–2759 (2011)

[231] Martz, C.A., Ottina, K.A., Singleton, K.R., Jasper, J.S., Wardell, S.E., Peraza-Penton, A., Anderson, G.R., Winter, P.S., Wang, T., Alley, H.M., Kwong, L.N., Cooper, Z.A., Tetzlaff, M., Chen, P.L., Rathmell, J.C., Flaherty, K.T., Wargo, J.A., McDonnell, D.P., Sabatini, D.M., Wood, K.C.: Systematic identification of signaling pathways with potential to confer anticancer drug resistance. Science Signalling **57**(6), 742–768 (2015)

[232] Mayr, E.: Change of genetic environment and evolution (1954)

[233] Mazor, T., Pankov, A., Song, J.S., Costello, J.F.: Intratumoral heterogeneity of the epigenome. Cancer Cell **29**, 440–451 (2016)

[234] McGranahan, N., Swanton, C.: Biological and therapeutic impact of intratumor heterogeneity in cancer evolution. Cancer Cell **12**, 15–26 (2015)

[235] Meinzer, H., Sandblad, B.: A simulation model for studies of intestine cell dynamics. Computer Methods and Programs in Biomedicine **21**(2), 89–98 (1985)

[236] Melchor, L., Brioli, A., Wardell, C., Murison, A., Potter, N., Kaiser, M., Fryer, R., Johnson, D., Begum, D., Wilson, S.H., et al.: Single-cell genetic analysis reveals the composition of initiating clones and phylogenetic patterns of branching and parallel evolution in myeloma. Leukemia **28**(8), 1705 (2014)

[237] Merilaita, S., Lind, J.: Background-matching and disruptive coloration, and the evolution of cryptic coloration. Proceedings of the Royal Society of London B **272**, 665–670 (2005)

[238] Mesterton-Gibbons, M., Adams, E.S.: Animal contests as evolutionary games. American Scientist **86**(4), 334–341 (1998)

[239] Metz, J.A.J., Diekmann, O.: A Gentle Introduction to Structured Population Models: Three Worked Examples, *Lecture Notes in Biomethamatics*, vol. 68, chap. The Dynamics of Physiologically Structured Populations, pp. 3–45. Springer Berlin Heidelberg (1986)

[240] Meyerson, M., Pellman, D.: Cancer genomes evolve by pulverizing single chromosomes. Cell **144**(1), 9–10 (2011)

[241] Møller, A.P., Christiansen, S.S., Mousseau, T.A.: Sexual signals, risk of predation and escape behavior. Behavioral Ecology pp. 800–807 (2011)

[242] Møller, A.P., Nielsen, J.T.: Prey vulnerability in relation to sexual coloration of prey. Behavioural Ecology and Sociobiology **60**, 227–233 (2006)

[243] Murray, J.D., Oster, G.F.: Cell traction models for generating pattern and form in morphogenesis. Journal of Mathematical Biology **19**(3), 265–279 (1984)

[244] Nazarian, R., Shi, H., Wang, Q., Kong, X., Koya, R.C., Lee, H., Chen, Z., Lee, M.K., Attar, N., Sazegar, H., Chodon, T., Nelson, S.F., McArthur, G., Sosman, J.A., Ribas, A., Lo, R.S.: Melanomas acquire resistance to b-raf(v600e) inhibition by rtk or n-ras upregulation. Nature **468**, 973–977 (2010)

[245] Ng, C.T., Mendoza, J.L., Garcia, K.C., Oldstone, M.B.A.: Alpha and beta type 1 interferon signaling: Passage for diverse biologic outcomes. Cell **164**, 349–352 (2016)

[246] Ng, C.T., Sullivan, B.M., Teijaro, J.R., Lee, A.M., Welch, M., Rice, S., Sheehan, K.C.F., Schreiber, R.D., Oldstone, M.B.A.: Blockade of interferon beta, but not interferon alpha, signaling controls persistent viral infection. Cell Host & Microbe **17**, 653–661 (2015)

[247] Ng, W.L., Bassler, B.L.: Bacterial Quorum-Sensing Network Architectures. Annual Review of Genetics **43**(1), 197–222 (2009). DOI 10.1146/annurev-genet-102108-134304

[248] Norris, E.S., King, J.R., Byrne, H.M.: Modelling the response of spatially structured tumours to chemotherapy: Drug kinetics. Mathematical and Computer Modelling **43**, 820–837 (2006)

[249] Notta, F., Chan-Seng-Yue, M., Lemire, M., Li, Y., Wilson, G.W., Connor, A.A., Denroche, R.E., Liang, S.B., Brown, A.M.K., Kim, J.C., Wang, T., Simpson, J.T., Beck, T., Borgida, A., Buchner, N., Chadwick, D., Hafezi-Bakhtiari, S., Dick, J.E., Heisler, L., Hollingsworth, M.A., Ibrahimov, E., Jang, G.H., Johns, J., Jorgensen, L.G.T., Law, C., Ludkovski, O., Lungu, I., Ng, K., Pasternack, D., Petersen, G.M., Shlush, L.I., Timms, L., Tsao, M.S., Wilson, J.M., Yung, C.K., Zogopoulos, G., Bartlett, J.M.S., Alexandrov, L.B., Real, F.X., Cleary, S.P., Roehrl, M.H., McPherson, J.D., Stein, L.D., Hudson, T.J., Campbell, P.J., Gallinger, S.: A renewed model of pancreatic cancer evolution based on genomic rearrangement patterns. Nature **538**(7625), 378–382 (2016)

[250] Nowell, P.C.: The clonal evolution of tumor cell populations. Science **194**(4260), 23–28 (1976)

[251] Nyman-Huttunen, H., Tian, L., Ning, L., Gahmberg, C.G.: α-Actinin-dependent cytoskeletal anchorage is important for ICAM-5-mediated neuritic outgrowth. J Cell Sci **119**(Pt 15), 3057–3066 (2006)

[252] Olimpio, E.P., Youk, H.: Out-of-equilibrium statistical dynamics of spatial pattern generating cellular automata Kavli Institute of Nanoscience , Departments of Applied Physics and Bionanoscience , Delft University of Technology , Delft 2629HZ , the Netherlands Correspondence to. bioRxiv (2017)

[253] Otero-Muras, I., Yordanov, P., Stelling, J.: Chemical reaction network theory elucidates sources of multistability in interferon signaling. PLoS Computational Biology **13**(4), e1005,454 (2017)

[254] Ouyang, W., Beckett, O., Flavell, R.A., Li, M.O.: An Essential Role of the Forkhead-Box Transcription Factor Foxo1 in Control of T Cell Homeostasis and Tolerance. Immunity **30**(3), 358–371 (2009)

[255] Oyler-Yaniv, A., Oyler-Yaniv, J., Whitlock, B.M., Liu, Z., Germain, R.N., Huse, M., Altan-Bonnet, G., Krichevsky, O.: A Tunable Diffusion-Consumption Mechanism of Cytokine Propagation Enables Plasticity in Cell-to-Cell Communication in the Immune System. Immunity **46**(4), 609–620 (2017). DOI 10.1016/j.immuni.2017.03.011

[256] Paraiso, K.H., Fedorenko, I.V., Cantini, L.P., Munko, A.C., Hall, M., Sondak, V.K., Messina, J.L., Flaherty, K.T., Smalley, K.S.: Recovery of phospho-ERK activity allows melanoma cells to escape from BRAF inhibitor therapy. Br J Cancer **102**(12), 1724–1730 (2010)

[257] Paraiso, K.H.T., Xiang, Y., Rebecca, V.W., Abel, E.V., Chen, Y.A., Munko, A.C., Wood, E., Fedorenko, I.V., Sondak, V.K., Anderson, A.R.A., Ribas, A., Palma, M.D., Nathanson, K.L., Koomen, J.M.,

Messina, J.L., Smalley, K.S.M.: PTEN loss confers BRAF inhibitor resistance to melanoma cells through the suppression of BIM expression. Cancer Research **71**(7), 2750–2760 (2011)

[258] Park, C., Suzanne Li, S., Cha, E., Schindler, C.: Immune response in stat2 knockout mice. Immunity **13**, 795–804 (2000)

[259] Parmenter, T.J., Kleinschmidt, M., Kathryn M. Kinross, Bond, S.T., Li, J., Kaadige, M.R., Rao, A., Sheppard, K.E., Hugo, W., Pupo, G.M., Pearson, R.B., McGee, S.L., Long, G.V., Scolyer, R.A., Rizos, H., Lo, R.S., Cullinane, C., Ayer, D.E., Ribas, A., Johnstone, R.W., Hicks, R.J., McArthur, G.A.: Response of BRAF mutant melanoma to BRAF inhibition is mediated by a network of transcriptional regulators of glycolysis. Cancer Discovery **4**(4), 423–433 (2014). DOI 10.1117/1.3103783.Extended-working-distance

[260] Parupudia, A., Gruiaa, F., Kormana, S.A., Dragulin-Ottoa, S., Srab, K., Remmele Jr., R.L., Bee, J.S.: Biophysical characterization of influenza a virions. Journal of Virological Methods **247**, 91–98 (2017)

[261] Passalacqua, R., Caminiti, C., Buti, S., Porta, C., Camisa, R., Braglia, L., Tomasello, G., Vaglio, A., Labianca, R., Rondini, E., Sabbatini, R., Nastasi, G., Artioli, F., Prati, A., Potenzoni, M., Pezzuolo, D., Oliva, E., Alberici, F., Buzio, C.: Adjuvant low-dose interleukin-2 (il-2) plus interferon-α (ifn-α) in operable renal cell carcinoma (rcc): A phase iii, randomized, multicentre trial of the italian oncology group for clinical research (goirc). Journal of Immunotherapy **37**(9), 440–447 (2014)

[262] Pavlovich, S.S., Lovett, S.P., Koroleva, G., Guito, J.C., Arnold, C.E., Nagle, E.R., Kulcsar, K., Lee, A., Thibaud-Nissen, F., Hume, A.J., Mühlberger, E., Uebelhoer, L.S., Towner, J.S., Rabadan, R., Sanchez-Lockhart, M., Kepler, T.B., Palacios, G.: The egyptian rousette genome reveals unexpected features of bat antiviral immunity. Cell **173**, 1–13 (2018)

[263] Pedersen, M.G., Bertram, R., Sherman, A.: Intra-and inter-islet synchronization of metabolically driven insulin secretion. Biophysical journal **89**(1), 107–119 (2005)

[264] Peng, L., Trucu, D., Lin, P., Thompson, A., Chaplain, M.A.J.: A multiscale mathematical model of tumour invasive growth. Bulletin of Mathematical Biology **79**(3), 389–429 (2016)

[265] Peng, P.L., Hsieh, Y.S., Wang, C.J., et al.: Inhibitory effect of berberine on the invasion of human lung cancer cells via decreased productions of urokinase-plasminogen activator and matrix metalloproteinase-2. Toxicology and Applied Pharmacology **214**(1), 8–15 (2006)

[266] Pennell, T.M., de Haas, F.J.H., Morrow, E.H., van Doorn, G.S.: Contrasting effects of intralocus sexual conflict on sexually antagonistic coevolution. Proceedings of the National Academy of Sciences **113**(8), E978–E986 (2016)

[267] Perna, D., Karreth, F.A., Rust, A.G., Perez-Mancera, P.A., Rashid, M., Iorio, F., Alifrangis, C., Arends, M.J., Bosenberg, M.W., Bollag, G., Tuveson, D.A., Adams, D.J.: BRAF inhibitor resistance mediated by the AKT pathway in an oncogenic BRAF mouse melanoma model. Proceedings of the National Academy of Sciences of the United States of America **112**(6), E536–45 (2015)

[268] Persson, M., Madsen, J., Østergaard, S., et al.: 68Ga-labeling and in vivo evaluation of a uPAR binding DOTA- and NODAGA-conjugated peptide for PET imaging of invasive cancers. Nuclear Medicine and Biology **39**(4), 560–569 (2012)

[269] Perthame, B.: Transport Equations in Biology, chap. Population balance equations: size structure, pp. 81–110. Birkhauser Basel, Basel (2007)

[270] Petrie, M.: Improved growth and survival of offspring of peacocks with more elaborate trains. Nature **371**, 598–599 (1994)

[271] Petrie, M., Halliday, T., Sanders, C.: Peahens prefer peacocks with elaborate trains. Animal Behaviour **41**(2), 323–331 (1991)

[272] Polnaszek, T.J., Stephens, D.W.: Why not lie? costs enforce honesty in an experimental signalling game. Proceedings of the Royal Society of London B **281**, 20132,457 (2014)

[273] Pomiankowski, A.: Sexual selection: The handicap principle does work – sometimes. Proceedings of the Royal Society of London B **231**(1262), 123–145 (1987)

[274] Pomiankowski, A., Iwasa, Y.: Runaway ornament diversity caused by Fisherian sexual selection. Proceedings of the National Academy of Sciences **95**, 5106–5111 (1998)

[275] Porterfield, J.S., Burke, D.C., Allison, A.C.: An estimate of the molecular weight of interferon as measured by its rate of diffusion through agar. Virology **12**(2), 197–203 (1960)

[276] Press, W.H., Flannery, B.P., Teukolsky, S.A., Vetterling, W.T.: Numerical Recipes in Fortran 77: The Art of Scientific Computing, 2$^{\text{nd}}$ edn. Cambridge University Press (1992)

[277] Prigogine, I., Lefever, R.: Stability problems in cancer growth and nucleation. Comparative Biochemistry and Physiology Part B: Comparative Biochemistry **67**(3), 389–393 (1980)

[278] Rambow, F., Rogiers, A., Marin-Bejar, O., Aibar, S., Femel, J., Dewaele, M., Karras, P., Brown, D., Chang, Y.H., Debiec-Rychter, M., Adriaens, C., Radaelli, E., Wolter, P., Bechter, O., Dummer, R., Levesque, M., Piris, A., Frederick, D.T., Marine, J.C.: Toward minimal residual disease-directed therapy in melanoma. Cell **174**(4), 843–855 (2018)

[279] Randall, G., Limin Chen, L., Panis, M., Fischer, A.K., Lindenbach, B.D., Sun, J., Heathcote, J., Rice, C.M., Edwards, A.M., Mcgilvray, I.D.: Si-

lencing of usp18 potentiates the antiviral activity of interferon against hepatitis c virus infection. Gastroenterology **131**, 1584–1591 (2006)

[280] Ratzke, C., Gore, J.: Shaping the crowd: The social life of cells. Cell Systems **1**, 310–312 (2015)

[281] Reichenbach, T., Mobilia, M., Frey, E.: Coexistence versus extinction in the stochastic cyclic lotka-volterra model. Physical Review E **74**(5), 051,907 (2006)

[282] Rhandi, A.: Positivity and stability for a population equation with diffusion on l^1. Positivity **2**(2), 101–113 (1998). DOI 10.1023/A:1009721915101

[283] Rijken, D.C.: 2 Plasminogen activators and plasminogen activator inhibitors: biochemical aspects. Bailliere's Clinical Haematology **8**(2), 291–312 (1995)

[284] Rodero, M.P., Crow, Y.J.: Type i interferon-mediated monogenic autoinflammation: The type i interferonopathies, a conceptual overview. The Journal of Experimental Medicine **213**(12), 2527–2538 (2016)

[285] de Roos, A.M.: A gentle introduction to physiologically structured population models. In: S. Tuljapurkar, H. Caswell (eds.) Structured-Population Models in Marine, Terrestrial, and Freshwater Systems, *Population and Community Biology Series*, vol. 18, pp. 119–204. Springer US (1997). DOI 10.1007/978-1-4615-5973-3_5

[286] Rubinstein, J.C., Sznol, M., Pavlick, A.C., Ariyan, S., Cheng, E., Bacchiocchi, A., Kluger, H.M., Narayan, D., Halaban, R.: Incidence of the V600K mutation among melanoma patients with BRAF mutations, and potential therapeutic response to the specific BRAF inhibitor PLX4032. Journal of translational medicine **8**, 67 (2010)

[287] Runge, C.: über empirische funktionen und die interpolation zwischen äquidistanten ordinaten. Zeitschrift für Mathematik und Physik **46**, 224–243 (1901)

[288] Samuel, C.E.: Antiviral Actions of Interferons.pdf. Clinical Microbiology Reviews **14**(4), 778–809 (2001). DOI 10.1128/CMR.14.4.778

[289] Sang, Y., Liu, Q., Lee, J., Miller, L.C., Ma, W., Blecha, F.: Cross-species comparison reveals molecular and functional novelty of porcine interferon-omega subtype. The Journal of Immunology **198**(1), Supp 226.6 (2017)

[290] Sato, F., Saji, S., Toi, M.: Genomic tumor evolution of breast cancer. Breast Cancer **23**(1), 4–11 (2016)

[291] Schilling, C.H., Letscher, D., Palsson, B.Ø.: Theory for the systemic definition of metabolic pathways and their use in interpreting metabolic function from a pathway-oriented perspective. Journal of theoretical biology **203**(3), 229–248 (2000)

[292] Schreiber, G., Piehler, J.: The molecular basis for functional plasticity in type I interferon signaling. Trends in Immunology **36**(3), 139–149 (2015). DOI 10.1016/j.it.2015.01.002

[293] Servedio, M.R., Bürger, R.: The counterintuitive role of sexual selection in species maintenance and speciation. Proceedings of the National Academy of Sciences **111**(22), 8113–8118 (2014)

[294] Shain, A.H., Yeh, I., Kovalyshyn, I., Sriharan, A., Talevich, E., Gagnon, A., Dummer, R., North, J., Pincus, L., Ruben, B., Rickaby, W., D'Arrigo, C., Robson, A., Bastian, B.C.: The genetic evolution of melanoma from precursor lesions. The New England Journal of Medicine **373**(20), 1926–1936 (2015)

[295] Shen, M.: Chromoplexy: A New Category of Complex Rearrangements in the Cancer Genome. Cancer Cell **23**(5), 567–569 (2013)

[296] Shi, H., Hong, A., Kong, X., Koya, R.C., Song, C., Moriceau, G., Hugo, W., Yu, C.C., Ng, C., Chodon, T., Scolyer, R.A., Kefford, R.F., Ribas, A., Long, G.V., Lo, R.S.: A novel AKT1 mutant amplifies an adaptive

melanoma response to BRAF inhibition. Cancer Discovery **4**(1), 69–79 (2014)

[297] Shtilerman, E., Kessler, D.A., Shnerb, N.M.: Emergence of structured communities through evolutionary dynamics. Journal of Theoretical Biology **383**, 138–144 (2015)

[298] Sinko, J.W., Streifer, W.: A new model for age-size structure of a population. Ecology **48**(6), 910–918 (1967). DOI 10.2307/1934533

[299] Slipicevic, A., Holm, R., Nguyen, M.T.P., Bøhler, P.J., Davidson, B., Flørenes, V.A.: Expression of activated Akt and PTEN in malignant Melanomas: Relationship with clinical outcome. American Journal of Clinical Pathology **124**(4), 528–536 (2005)

[300] Smalley, K.S.M., Lioni, M., Dalla Palma, M., Xiao, M., Desai, B., Egyhazi, S., Hansson, J., Wu, H., King, A.J., Belle, P.V., Elder, D.E., Flaherty, K.T., Herlyn, M., Nathanson, K.L.: Increased cyclin D1 expression can mediate BRAF inhibitor resistance in BRAF V600E–mutated melanomas. Mol Cancer Ther **7**(9), 2876–83 (2008)

[301] Smith, H.W., Marshall, C.J.: Regulation of cell signalling by uPAR. Nature Reviews Molecular Cell Biology **11**(1), 23–36 (2010)

[302] So, J.W.H., Wu, J., Zou, X.: A reaction–diffusion model for a single species with age structure. i travelling wavefronts on unbounded domains. Proceedings of the Royal Society of London. Series A: Mathematical, Physical and Engineering Sciences **457**(2012), 1841–1853 (2001). DOI 10.1098/rspa.2001.0789

[303] Sormani, M.P., De Stefano, N.: Defining and scoring response to ifn-β in multiple sclerosis. Nature Reviews Neurology **9**, 504–512 (2013)

[304] Stark, G.R., Kerr, I.M., Williams, B.R., Silverman, R.H., Schreiber, R.D.: How cells respond to interferons. Annual review of biochemistry **67**, 227–64 (1998). DOI 10.1146/annurev.biochem.67.1.227

[305] Stephens, P.J., Greenman, C.D., Fu, B., Yang, F., Bignell, G.R., Mudie, L.J., Pleasance, E.D., Lau, K.W., Beare, D., Stebbings, L.A., McLaren, S., Lin, M.L., McBride, D.J., Varela, I., Serena Nik-Zainal, S., Catherine Leroy, C., Jia, M., Andrew Menzies, A., Butler, A.P., Teague, J.W., Quail, M.A., Burton, J., Swerdlow, H., Carter, N.P., Morsberger, L.A., Iacobuzio-Donahue, C., Follows, G.A., Green, A.R., Flanagan, A.M., Stratton, M.R., Futreal, P.A., Campbell, P.J.: Massive genomic rearrangement acquired in a single catastrophic event during cancer development. Cell **144**, 27–40 (2011)

[306] Stevens, M., Merilaita, S.: Animal Camouflage: Mechanisms and Function. Cambridge University Press (2011)

[307] Stillfried, G.E., Saunders, D.N., Ranson, M., et al.: Plasminogen binding and activation at the breast cancer cell surface: the integral role of urokinase activity. Breast Cancer Research **9**(1), R14 (2007)

[308] Stojdl, D.F., Lichty, B., Knowles, S., Marius, R., Atkins, H., Sonenberg, N., Bell, J.C.: Exploiting tumor-specific defects in the interferon pathway with a previously unknown oncolytic virus. Nature **6**(7), 821–825 (2000)

[309] Sugioka, K., Kodama, A., Okada, K., et al.: TGF-β2 promotes RPE cell invasion into a collagen gel by mediating urokinase-type plasminogen activator (uPA) expression. Experimental Eye Research **115**, 13–21 (2013)

[310] Számadó, S.: The cost of honesty and the fallacy of the handicap principle. Animal Behaviour **81**, 3–10 (2011)

[311] Számadó, S., Penn, D.J.: Why does costly signalling evolve? challenges with testing the handicap hypothesis. Animal Behaviour **110**, e9–e12 (2015)

[312] Takahashi, M., Arita, H., Hiraiwa-Hasegawa, M., Hasegawa, T.: Peahens do not prefer peacocks with more elaborate trains. Animal Behaviour **75**(4), 1209 (2008)

[313] Tentori, L., Lacal, P.M., , Graziani, G.: Challenging resistance mechanisms to therapies for metastatic melanoma. Trends in Pharmacological Sciences **34**(12), 656–666 (2013)

[314] Tomasello, E., Pollet, E., Vu Manh, T.P., Uzé, G., Dalod, M.: Harnessing mechanistic knowledge on beneficial versus deleterious ifn-i effects to design innovative immunotherapies targeting cytokine activity to specific cell types. Frontiers in Immunology **5**, 526 (2014)

[315] Través, P.G., de Atauri, P., Marin, S., Pimentel-Santillana, M., Rodriguez-Prados, J.C., Marin de Mas, I., Selivanov, V.A., Martin-Sanz, P., Bosca, L., Cascante, M.: Relevance of the MEK/ERK Signaling Pathway in the Metabolism of Activated Macrophages: A Metabolomic Approach. The Journal of Immunology **188**(3), 1402–1410 (2012)

[316] Trucco, E.: Mathematical models for cellular systems the von foerster equation. part i. The bulletin of mathematical biophysics **27**(3), 285–304 (1965). DOI 10.1007/BF02478406

[317] Trucco, E.: Mathematical models for cellular systems. the von foerster equation. part ii. The bulletin of mathematical biophysics **27**(4), 449–471 (1965). DOI 10.1007/BF02476849

[318] Trucu, D., Domschke, P., Gerisch, A., Chaplain, M.A.J.: Multiscale computational modelling and analysis of cancer invasion. In: Mathematical Models and Methods for Living Systems, pp. 275–310. Springer (2016)

[319] Trucu, D., Lin, P., Chaplain, M.A.J., Wang, Y.: A multiscale moving boundary model arising in cancer invasion. Multiscale Model. Simul. **11**(1), 309–335 (2013)

[320] Tucker, S.L., Zimmerman, S.O.: A nonlinear model of population dynamics containing an arbitrary number of continuous structure variables. SIAM Journal on Applied Mathematics **48**(3), pp. 549–591 (1988)

[321] Turner, N.C., Reis-Filho, J.S.: Genetic heterogeneity and cancer drug resistance. Lancet Oncology **13**, e178–185 (2012)

[322] Turner, S., Sherratt, J.A.: Intercellular adhesion and cancer invasion: A discrete simulation using the extended potts model. J Theor Biol **216**, 85–100 (2002)

[323] Uzé, G., Mogensen, K.E., Aguet, M.: Receptor dynamics of closely related ligands: "fast' and "slow' interferons. EMBO Journal **4**(1), 65–70 (1985)

[324] Uzé, G., Schreiber, G., Piehler, J., Pellegrini, S.: The receptor of the type i interferon family. Current Topics in Microbiology and Immunology **316**, 71–95 (2007)

[325] Van Allen, E.M., Wagle, N., Sucker, A., Treacy, D.J., Johannessen, C.M., Goetz, E.M., Place, C.S., Taylor-Weiner, A., Whittaker, S., Kryukov, G.V., Hodis, E., Rosenberg, M., McKenna, A., Cibulskis, K., Farlow, D., Zimmer, L., Hillen, U., Gutzmer, R., Goldinger, S.M., Ugurel, S., Gogas, H.J., Egberts, F., Berking, C., Trefzer, U., Loquai, C., Weide, B., Hassel, J.C., Gabriel, S.B., Carter, S.L., Getz, G., Garraway, L.A., Dirk Schadendorf, D.: The genetic landscape of clinical resistance to raf inhibition in metastatic melanoma. Cancer Discovery **4**, 94–109 (2014)

[326] van Pesch, V., Lanaya, H., Renauld, J.C., Michiels, T.: Characterization of the murine alpha interferon gene family. Journal of Virology **78**(15), 8219–8228 (2004)

[327] Vega-Redondo, F., Hasson, O.: A game-theoretic model of predator-prey signalling. Journal of Theoretical Biology **162**, 309–319 (1993)

[328] Villanueva, J., Infante, J.R., Krepler, C., Reyes-Uribe, P., Samanta, M., Chen, H.Y., Li, B., Swoboda, R.K., Wilson, M., Vultur, A., Fukunaba-Kalabis, M., Wubbenhorst, B., Chen, T.Y., Liu, Q., Sproesser, K., DeMarini, D.J., Gilmer, T.M., Martin, A.M., Marmorstein, R., Schultz, D.C., Speicher, D.W., Karakousis, G.C., Xu, W., Amaravadi, R.K., Xu,

X., Schuchter, L.M., Herlyn, M., Nathanson, K.L.: Concurrent MEK2 Mutation and BRAF Amplification Confer Resistance to BRAF and MEK Inhibitors in Melanoma. Cell Reports **4**(6), 1090–1099 (2013)

[329] Viola, A., Lanzavecchia, A.: T cell activation determined by t cell receptor number and tunable thresholds. Science **273**(5271), 104–106 (1996)

[330] Volterra, V.: Fluctuations in the abundance of a species considered mathematically. Nature **118**(2972), 558–560 (1926)

[331] Volterra, V.: Variations and fluctuations of the number of individuals in animal species living together. Animal Ecology pp. 409–448 (1926)

[332] Waclaw, B.: Evolution of drug resistance in bacteria. Advances and Medicine and Biology **915**, 49–67 (2016)

[333] Waclaw, B., Bozic, I., Pittman, M.E., Hruban, R.H., Vogelstein, B., Nowak, M.A.: A spatial model predicts that dispersal and cell turnover limit intratumour heterogeneity. Nature **525**, 261–264 (2015)

[334] Wagle, N., Van Allen, E.M., Treacy, D.J., Frederick, D.T., Cooper, Z.A., Taylor-Weiner, A., Rosenberg, M., Goetz, E.M., Sullivan, R.J., Farlow4, D.N., Friedrich, D.C., Anderka, K., Perrin, D., Johannessen, C.M., McKenna, A., Cibulskis, K., Kryukov, G., Hodis, E., Lawrence, D.P., Fisher, S., Getz, G., Gabriel, S.B., Carter, S.L., Flaherty, K.T., Wargo, J.A., Garraway, L.A.: Map kinase pathway alterations in braf-mutant melanoma patients with acquired resistance to combined raf/mek inhibition. Cancer Discovery **4**, 61–68 (2014)

[335] Waltz, D.A., Chapman, H.A.: Reversible cellular adhesion to vitronectin linked to urokinase receptor occupancy. The Journal of biological chemistry **269**(20), 14,746–50 (1994)

[336] Waltz, D.A., Natkin, L.R., Fujita, R.M., et al.: Plasmin and plasminogen activator inhibitor type 1 promote cellular motility by regulating the in-

teraction between the urokinase receptor and vitronectin. The Journal of clinical investigation **100**(1), 58–67 (1997)

[337] Wang, G.D., Zhang, B.L., Zhou, W.W., Li, Y.X., Jin, J.Q., Shao, Y., Yang, H.c., Liu, Y.H., Yan, F., Chen, H.M., Jing, L., Gao, F., Zhang, Y., Li, H., Mao, B., Murphy, R.W., Wake, D.B., Zhang, Y.P., Che, J.: Selection and environmental adaptation along a path to speciation in the Tibetan frog Nanorana parkeri. Proceedings of the National Academy of Sciences **115**(22), E5056–5065 (2018)

[338] Warburg, O.: On the origin of cancer cells. Science **123**(3191), 309–314 (1956)

[339] Wei, Y., Waltz, D.A., Rao, N., et al.: Identification of the urokinase receptor as an adhesion receptor for vitronectin. The Journal of biological chemistry **269**(51), 32,380–8 (1994)

[340] Wilmes, S., Beutel, O., Li, Z., Francois-Newton, V., Richter, C.P., Janning, D., Kroll, C., Hanhart, P., Hötte, K., You, C., Uzé, G., Pellegrini, S., Piehler, J.: Receptor dimerization dynamics as a regulatory valve for plasticity of type i interferon signaling. The Journal of Cell Biology **209**(4), 579–593 (2014)

[341] Wilmes, S., Beutel, O., Li, Z., Francois-Newton, V., Richter, C.P., Janning, D., Kroll, C., Hanhart, P., H′otte, K., You, C., Uzé, G., Pellegrini, S., Piehler, J.: Receptor dimerization dynamics as a regulatory valve for plasticity of type i interferon signaling. Journal of Cell Biology **209**(4), 579–593 (2015)

[342] Yamaguchi, N., Mizutani, T., Kawabata, K., Haga, H.: Leader cells regulate collective cell migration via rac activation in the downstream signaling of integrin $\beta 1$ and pi3k. Scientific Reports **5**(7656), 1–8 (2015)

[343] Yasukawa, K., Butler, L.K., Enstrom, D.A.: Intersexual and intrasexual consequences of epaulet colour in male red-winged blackbirds: an experimental approach. Animal Behaviour **77**, 531–540 (2009)

[344] Youk, H., Lim, W.A.: Secreting and sensing the same molecule allows cells to achieve versatile social behaviors. Science **343**(6171), 1242,782 (2014). DOI 10.1126/science.1242782

[345] Yun, L., Chen, P.J., Kwok, K.E., Angell, C.S., Rundle, H.D., Agrawal, A.F.: Competition for mates and the improvement of nonsexual fitness. Proceedings of the National Academy of Sciences **115**(26), 6762–6767 (2018)

[346] Zahavi, A.: Mate selection-a selection for a handicap. Journal of Theoretical Biology **53**, 205–214 (1975)

[347] Zahavi, A.: The cost of honesty (further remarks on the handicap principle). Journal of Theoretical Biology **67**, 603–605 (1977)

[348] Zahavi, A.: Evolutionary Ecology, chap. Reliability in communication systems and the evolution of altruism, pp. 253–259. Palgrave, London (1977)

[349] Zaman, M.H., Kamm, R.D., Matsudaira, P., Lauffenburger, D.A.: Computational model for cell migration in three-dimensional matrices. Biophys J **89**(2), 1389–1397 (2005)

[350] Zhu, C., Yin, G.: On competitive lotka–volterra model in random environments. Journal of Mathematical Analysis and Applications **357**, 154–170 (2009)

[351] Ziegler, S., Beisel, C., Kathrin Sutter, K., Griesbeck, M., Hildebrandt, H., Hagen, S., Ulf Dittmer, U., Altfeld, M.: Human pdcs display sex-specific differences in type i interferon subtypes and interferon α/β receptor expression. European Journal of Immunology **47**, 251–256 (2016)

[352] Zitvogel, L., Galluzzi, L., Smyth, M.J., Kroemer, G.: Mechanism of action of conventional and targeted anticancer therapies: Reinstating immunosurveillance. Immunity **39**, 74–88 (2013)

[353] Zollman, K.J.S.: Finding alternatives to handicap theory. Biological Theory **8**(2), 127–132 (2013)